UNIVERSITI TEKNOLOGI MARA

SYNTHESIS, PERFORMANCE AND OPTIMIZATION STUDIES OF MELDRUM'S ACID DERIVATIVES FOR CORROSION INHIBITION: EMPLOYING RESPONSE SURFACE METHODOLOGY, SURFACE ANALYSIS AND COMPUTATIONAL STUDY

MUHAMMAD AZHAN ARIF BIN MANSOR

MSc

August 2026

UNIVERSITI TEKNOLOGI MARA

SYNTHESIS, PERFORMANCE AND OPTIMIZATION STUDIES OF MELDRUM'S ACID DERIVATIVES FOR CORROSION INHIBITION: EMPLOYING RESPONSE SURFACE METHODOLOGY, SURFACE ANALYSIS AND COMPUTATIONAL STUDY

MUHAMMAD AZHAN ARIF BIN MANSOR

Thesis submitted in fulfilment
of the requirements for the degree of
Master of Science
(Chemistry)

Faculty of Applied Sciences

August 2026

CONFIRMATION BY PANEL OF EXAMINERS

I certify that a Panel of Examiners has met on 9 July 2026 to conduct the final examination of Muhammad Azhan Arif Mansor on his Masters of Science thesis entitled “Synthesis, Performance and Optimization Studies of Meldrum's Acid Derivatives for Corrosion Inhibition: Employing Response Surface Methodology, Surface Analysis and Computational Study” in accordance with Universiti Teknologi MARA Act 1976 (Akta 173). The Panel of Examiner recommends that the student be awarded the relevant degree. The Panel of Examiners was as follows:

Mohd Lokman Ibrahim, PhD
Associate Professor
Faculty of Applied Sciences
Universiti Teknologi MARA
(Chairman)

Nur Rahimah Said, PhD
Senior Lecturer
Faculty of Applied Sciences
Universiti Teknologi MARA
(Internal Examiner)

Norazzizi Nordin, PhD
Senior Lecturer
School of Chemical Sciences
Universiti Sains Malaysia
(External Examiner)

PROF DR HJH ZURAEDA IBRAHIM
Dean
Institute of Postgraduates Studies
Universiti Teknologi MARA

Date: 14 August 2026

AUTHOR'S DECLARATION

I declare that the work in this thesis was carried out in accordance with the regulations of Universiti Teknologi MARA. It is original and is the results of my own work, unless otherwise indicated or acknowledged as referenced work. This thesis has not been submitted to any other academic institution or non-academic institution for any degree or qualification.

I, hereby, acknowledge that I have been supplied with the Academic Rules and Regulations for Postgraduate, Universiti Teknologi MARA, regulating the conduct of my study and research.

Name of Student	:	Muhammad Azhan Arif Bin Mansor
Student ID. No.	:	2024685464
Programme	:	Master of Science (Chemistry) – AS756
Faculty	:	Applied Sciences
Thesis Title	:	Synthesis, Performance and Optimization Studies of Meldrum's Acid Derivatives for Corrosion Inhibition: Employing Response Surface Methodology, Surface Analysis and Computational Study
Signature of Student	:	…….……..
Date	:	August 2026

ABSTRACT

Corrosion of mild steel in acidic environments is a serious industrial problem that causes material damage and high economic losses. This creates a strong need for effective, optimized, and environmentally friendly organic corrosion inhibitors. Meldrum's acid derivatives are considered promising inhibitors because its highly reactive and easier to react with other derivatives thus they can strongly interact with mild steel surfaces through heteroatoms and π-electron systems. In this study, four Meldrum's acid derivatives were successfully synthesized: 4-formylbenzonitrile Meldrum's acid (FBMA), *p*-tolualdehyde Meldrum's acid (TOMA), 2-thiophenecarboxyaldehyde Meldrum's acid (THMA), and 4-pyridinecarboxyaldehyde Meldrum's acid (PYMA). The synthesized compounds were characterized using Attenuated Total Reflectance–Fourier Transform Infrared (ATR-FTIR), ^{1}H and ^{13}C Nuclear Magnetic Resonance (NMR) spectroscopy, elemental analysis, and single-crystal X-ray crystallography. Corrosion inhibition performance was evaluated using the weight loss method, adsorption isotherms, and Gibbs free energy analysis in 1 M HCl solution. Among the four inhibitors, FBMA showed the highest inhibition efficiency of 81.48 % at an inhibitor concentration of 7 mM due to electron-withdrawing cyano (–C≡N) group, which increases the polarity of the molecule and enhances its interaction with the mild steel surface. Adsorption studies revealed that all inhibitors followed the Langmuir isotherm, indicating monolayer adsorption, while Gibbs free energy results showed that FBMA adsorbed mainly through chemisorption, whereas the other inhibitors exhibited mixed adsorption behavior. Surface analysis using scanning electron microscopy (SEM) showed a smoother mild steel surface in the presence of inhibitors compared to the blank solution. Energy-dispersive X-ray (EDX) mapping confirmed inhibitor adsorption through the detection of oxygen and nitrogen on the mild steel surface. Atomic force microscopy (AFM) further supported these findings, with the Meldrum's acid derivatives-protected surface showing significantly lower roughness than the blank sample. X-ray photoelectron spectroscopy (XPS) confirmed Fe–O and C=O interactions, indicating chemisorption through oxygen atoms. Density functional theory (DFT) calculations showed that PYMA possessed the most favorable electronic properties, while THMA exhibited the weakest performance. Molecular electrostatic potential (MEP) and Mulliken charge analyses identified oxygen, nitrogen, and aromatic rings as the main adsorption sites. Response Surface Methodology (RSM) optimization revealed that FBMA achieved a maximum inhibition efficiency of 90.02% at an inhibitor concentration of 5.96 mM, concentration acid 0.49M, immersion time of 19.98 h, and inhibitor-to-acid ratio of 3.99: 3.01 mL. The inhibition mechanism involves both chemisorption and physisorption, forming a dense and protective film that effectively reduces corrosion. Overall, FBMA, TOMA, THMA, and PYMA inhibit mild steel corrosion by adsorbing via electron-rich oxygen, nitrogen, and sulphur atoms, as well as protonated sites. This combined adsorption forms a compact and stable protective layer, blocking active corrosion sites and significantly improving corrosion resistance, highlighting their potential as efficient, eco-friendly inhibitors for industrial acidic systems.

ACKNOWLEDGEMENT

First and foremost, I would like to express my utmost gratitude to Allah SWT for His endless blessings, guidance, and strength throughout my Master's journey. Without His mercy and wisdom, I would not have had the perseverance and resilience to complete this research successfully.

I would also like to convey my deepest appreciation to my beloved family for their constant prayers, patience, unconditional love, and unwavering support. Their encouragement and understanding have been my greatest source of motivation and strength in overcoming every challenge faced during the completion of this thesis.

My sincere and heartfelt gratitude goes to my supervisor, Associate Professor ChM. Dr. Nur Nadia Dzulkifli, for her invaluable guidance, continuous support, patience, and constructive advice throughout the course of this research. Her expertise, dedication, and encouragement played a significant role in shaping this study and ensuring its successful completion

I am also sincerely thankful to my co-supervisors, Associate Professor Ts. ChM Dr. Sheikh Ahmad Izaddin bin Sheikh Md Ghazali and Dr. Nurul Auni Zainal Abidin, for their insightful comments, guidance, and willingness to share their knowledge throughout my Master's journey. Their contributions are greatly appreciated.

Lastly, I would like to extend my appreciation to my fellow postgraduate colleagues and laboratory mates, especially Muiz, Aiman, Aisyah, Jannah, and Najihah, for their assistance, meaningful academic discussions, and moral support. Their cooperation and friendship made this academic journey more enriching and memorable.

TABLE OF CONTENTS

		Page
CONFIRMATION BY PANEL OF EXAMINERS		**ii**
AUTHOR'S DECLARATION		**iii**
ABSTRACT		**iv**
ACKNOWLEDGEMENT		**v**
TABLE OF CONTENTS		**vi**
LIST OF TABLES		**xi**
LIST OF FIGURES		**xiv**
LIST OF SYMBOLS		**xviii**
LIST OF ABBREVIATIONS		**xix**
CHAPTER 1 INTRODUCTION		**1**
1.1	Research Background	1
	1.1.1 Corrosion and Corrosion Inhibitor	1
	1.1.2 Meldrum's acid	3
	1.1.3 Corrosion Inhibition Performance	4
	1.1.4 Computational Study	4
1.2	Problem Statement	5
1.3	Objectives of Study	6
1.4	Significance of Study	6
1.5	Scope and Limitations	7
CHAPTER 2 LITERATURE REVIEW		**9**
2.1	Corrosion Inhibitor	9
2.2	Meldrum's Acid	14
2.3	Meldrum's Acid as a Corrosion Inhibitor	15
	2.3.1 Weight Loss Method	16
2.4	Surface Analysis	17
	2.4.1 Scanning Electron Microscopy with Energy Dispersive X ray Spectroscopy (SEM/EDX)	17

2.4.2 Atomic Force Microscopy (AFM) 19
2.4.3 X-ray Photoelectron Spectroscopy (XPS) 20
2.4.4 Density Functional Theory (DFT) 22
2.4.4.1 Frontier Molecular Orbital (FMO) 23
2.4.4.2 Molecular Electrostatic Potential 25
2.4.4.3 Mulliken Population Analysis 26
2.4.5 Response Surface Methodology (RSM) 27
2.4.5.1 RSM on Corrosion Study 29

CHAPTER 3 RESEARCH METHODOLOGY 35
3.1 List of Apparatus and Chemicals 35
3.2 List of Instruments and Software 35
3.3 Synthesis of Meldrum's Acid Derivatives 35
3.4 Characterization of Meldrum's Acid Derivatives 37
3.4.1 Attenuated Total Reflectance (ATR) - Fourier Transform Infra-Red (FTIR) Analysis 37
3.4.2 Nuclear Magnetic Resonance (NMR) Analysis 37
3.4.3 Elemental Analysis 37
3.4.4 Single Crystal X-ray Diffraction 38
3.5 Weight Loss Method 38
3.5.1 Preparing Solution 38
3.5.2 Weight Loss Method for Performance Screening 38
3.5.2.1 Isotherms 39
3.5.2.2 Gibb's Free Energy 40
3.6 Surface Analysis 40
3.6.1 Scanning Electron Microscope with Energy Dispersive X-ray Spectroscopy (SEM-EDX) 40
3.6.2 Atomic Force Microscope (AFM) 41
3.6.3 X-ray Photoelectron Spectroscopy (XPS) 41
3.7 Density Functional Theory (DFT) 41
3.8 Response Surface Methodology (RSM) 41

CHAPTER 4 RESULTS AND DISCUSSION 43
4.1 Synthesis of Meldrum's Acid Derivatives 43

4.1.1 Reactions Mechanism 43
4.2 Characterisation of Synthesised Meldrum's Acid Compounds 49
4.2.1 Physicochemical Analysis 49
4.2.1.1 Melting Point Determination 49
4.2.1.2 Elemental Analysis 51
4.2.2 Attenuated Total Reflectance - Fourier Transform Infrared (ATR-FTIR) Analysis 52
4.2.3 Nuclear Magnetic Resonance (NMR) Analysis 58
4.2.3.1 ^{1}H and ^{13}C NMR 58
4.2.4 Single Crystal X-ray Diffraction 69
4.3 Weight Loss Measurement 78
4.3.1 Adsorption Isotherm 82
4.3.2 Gibb's Free Energy Calculation ($\Delta G°_{ads}$) 83
4.4 Surface Analysis 86
4.4.1 SEM-EDX 86
4.4.2 AFM 95
4.4.3 XPS Analysis 98
4.5 Density Functional Theory (DFT) 104
4.5.1 Frontier Molecular Orbital (FMO) Theory 105
4.5.1.1 HOMO and LUMO Discussion 105
4.5.1.2 Ionization Potential (IP) and Electron Affinity (EA) 110
4.5.1.3 Dipole Moment (D) 113
4.5.1.4 Electronegativity (χ) 114
4.5.1.5 Electronic Chemical Potential (μ) 115
4.5.1.6 Global Hardness (η) and Softness (S) 116
4.5.1.7 Electrophilicity (ω) and Nucleophilicity (ε) Index 118
4.5.1.8 Electron-Donating (ω^{-}) and Electron-Accepting (ω^{+}) Power 120
4.5.1.9 Number of Electrons Transferred (ΔN) 121
4.5.1.10 Back-Donation Energy (ΔE Back-Donation) 122
4.5.2 Molecular Electrostatic Potential (MEP) 124
4.5.2.1 MEP, Interpretation of FBMA 124
4.5.2.2 MEP, Interpretation of TOMA 125
4.5.2.3 MEP, Interpretation of THMA 126

4.5.2.4 MEP, Interpretation of PYMA 127
4.5.3 Mulliken Population Analysis 129
4.6 Corrosion Inhibition Mechanism 132
4.6.1 FBMA Inhibition Mechanism 133
4.6.2 TOMA Inhibition Mechanism 136
4.6.3 THMA Inhibition Mechanism 137
4.6.4 PYMA Inhibition Mechanism 139
4.7 Response Surface Methodology (RSM) 140
4.7.1 Optimization for FBMA 141
4.7.1.1 Determination of Selected Model 142
4.7.1.2 Identification of Model Accuracy 145
4.7.1.3 Analysis of Variance (ANOVA) 149
4.7.1.4 Three-Dimensional (3D) Surface 151
4.7.1.5 Verification Model 156
4.7.1.6 Optimum Condition for Corrosion Inhibition FBMA 156
4.7.2 Optimization for TOMA 158
4.7.2.1 Determination of Selected Model 160
4.7.2.2 Identification of Model Accuracy 162
4.7.2.3 Analysis of Variance (ANOVA) 166
4.7.2.4 Three-Dimensional (3D) surface 168
4.7.2.5 Verification Model 173
4.7.2.6 Optimum Condition for Corrosion Inhibition (TOMA) 173
4.7.3 Optimization for THMA 175
4.7.3.1 Determination of Selected Model 177
4.7.3.2 Identification of Model Accuracy 179
4.7.3.3 Analysis of Variance (ANOVA) 183
4.7.3.4 Three-Dimensional (3D) surface 185
4.7.3.5 Verification Model 190
4.7.3.6 Optimum Condition for Corrosion Inhibition (THMA) 190
4.7.4 Optimization for PYMA 192
4.7.4.1 Determination of Selected Model 194
4.7.4.2 Identification of Model Accuracy 196
4.7.4.3 Analysis of Variance (ANOVA) 200
4.7.4.4 Three-Dimensional (3D) surface 202

4.7.4.5 Verification Model 207
4.7.4.6 Optimum Condition for Corrosion Inhibition (PYMA) 207

CHAPTER 5 CONCLUSION **210**
5.1 Conclusion 210
5.2 Recommendations 212

REFERENCES **213**

APPENDICES **222**

AUTHOR'S PROFILE **236**

LIST OF TABLES

Tables	Title	Page
Table 2.1	Gravimetric Data for Carbon Steel in the Absence and Presence of Different Concentrations	17
Table 2.2	RSM Model Design	32
Table 2.3	Analysis of Variance for the Evaluation of the Quadratic Model	32
Table 3.1	Coded and Actual Variable Level for Each Parameter	42
Table 4.1	Reaction Routes and Percentage Yields	48
Table 4.2	Melting Point Data	50
Table 4.3	Elemental Analyzer Results	52
Table 4.4	Assignment and Comparison of ATR-FTIR Stretching Bands	58
Table 4.5	^{1}H NMR Data of TOMA	60
Table 4.6	^{13}C NMR Data of TOMA	61
Table 4.7	^{1}H NMR Data of FBMA	63
Table 4.8	^{13}C NMR Data of FBMA	64
Table 4.9	^{1}H NMR Data of THMA	66
Table 4.10	^{13}C NMR Data of THMA	66
Table 4.11	^{1}H NMR Data of PYMA	68
Table 4.12	^{13}C NMR Data of PYMA	68
Table 4.13	Crystal and Experiment Data of FBMA, TOMA and THMA	74
Table 4.14	Hydrogen Bonds for FBMA	74
Table 4.15	Hydrogen Bonds for TOMA	75
Table 4.16	Hydrogen Bonds for THMA	75
Table 4.17	Summary of Weight-loss Measurements for Mild Steel in 1.0 M HCl Containing Different Inhibitors	81
Table 4.18	R^2 Values for Various Adsorption Isotherms Obtained From the WL Method	83
Table 4.19	K_{ads} and $\Delta G°_{ads}$ Values Obtained from WL Analysis	85
Table 4.20	AFM Surface Roughness Parameters of Mild Steel in 1 M HCl with Different Inhibitors	97

Table 4.21	Quantum Chemical Parameters of the Investigated Inhibitors	104
Table 4.22	Experimental Runs from CCD Design and the Response of the FBMA	142
Table 4.23	Sequential Model Sum of Square for FBMA	143
Table 4.24	Lack of Fit Test FBMA	143
Table 4.25	Model Summary Statistics for FBMA	144
Table 4.26	ANOVA Analysis of the Model for FBMA	150
Table 4.27	ANOVA Analysis Factor for FBMA	151
Table 4.28	Table of Verification Model for FBMA	156
Table 4.29	Constraint Data of FBMA	157
Table 4.30	Actual Predicted Data for Optimum Condition FBMA	158
Table 4.31	Experimental Runs from CCD Design and the Response for TOMA	159
Table 4.32	Sequential Model Sum of Square for TOMA	160
Table 4.33	Lack of Fit Test for TOMA	161
Table 4.34	Model Summary Statistics for TOMA	162
Table 4.35	ANOVA Analysis of the Model for TOMA	167
Table 4.36	ANOVA Analysis Factor for TOMA	168
Table 4.37	Table of Verification Model TOMA	173
Table 4.38	Constraint Table Data TOMA	175
Table 4.39	Actual and Predicted Data for Optimum Condition TOMA	175
Table 4.40	Experimental Runs from CCD Design and the Response of THMA	176
Table 4.41	Sequential Model Sum of Square for THMA	177
Table 4.42	Lack of Fit Test THMA	177
Table 4.43	Model Summary Statistics for THMA	178
Table 4.44	ANOVA Analysis of the Model for THMA	184
Table 4.45	ANOVA Analysis Factor for THMA	185
Table 4.46	Table of Verification Model THMA	190
Table 4.47	Constraint Data of THMA	192
Table 4.48	Actual and Predicted Data for Optimum Condition THMA	192
Table 4.49	Experimental Runs from CCD Design and the Response of the PYMA	193
Table 4.50	Sequential Model Sum of Square for PYMA	194

Table 4.51	Lack of Fit Test (PYMA)	194
Table 4.52	Model Summary Statistics for PYMA	195
Table 4.53	ANOVA Analysis of the Model for PYMA	201
Table 4.54	ANOVA Analysis Factor for PYMA	202
Table 4.55	Table of Verification Model PYMA	207
Table 4.56	Constraint Table for PYMA	208
Table 4.57	Actual and Predicted Data for Optimum Condition PYMA	209

LIST OF FIGURES

Figures	Title	Page
Figure 2.1	Types of Corrosion	10
Figure 2.2	Mechanism of Physisorption and Chemisorption	13
Figure 2.3	Meldrum's Acid Structure	14
Figure 2.4	SEM Images of Mild Steel in (a) 1 M HCl (Blank), and Mild Steel (b) 0.1 mM Inhibitor	18
Figure 2.5	EDX Analysis of Elements On Mild Steel Surface After 24 Hours Immersion in 1 M HCl Without and With 0.1 mM Inhibitor	19
Figure 2.6	AFM Image (a) Polished (b) Blank and (c) Inhibitor of VanMA in 3D	20
Figure 2.7	High Resolution XPS Spectra of (a-c) Blank and (d-f) VanMA	22
Figure 2.8	Representation of MEP Maps and Their Corresponding Electrostatic Contours for the Two Studied Molecules in Neutral and Protonated States	26
Figure 2.9	The Mulliken Charge Population of Nicotinic Acid	27
Figure 2.10	Effect of Concentration Inhibitor [A] and Concentration Acid [B] on the Inhibition Efficiency Based on (a) Contour Plot and (b) Response Surface Plot	33
Figure 2.11	Effect of Concentration Inhibitor [A] and Immersion Time [C] on the Inhibition Efficiency Based on (a) Contour Plot and (b) Response Surface Plot	34
Figure 3.1	Flowchart Methodology	36
Figure 4.1	Proposed Mechanism for the Formation of PYMA	44
Figure 4.2	Proposed Mechanism for the Formation of FBMA (R = CN) and TOMA (R = CH_3)	45
Figure 4.3	Proposed Mechanism for the Formation of THMA	46
Figure 4.4	ATR-FTIR Spectrum of FBMA	54
Figure 4.5	ATR-FTIR Spectrum of TOMA	55
Figure 4.6	ATR-FTIR Spectrum of THMA	56

Figure 4.7	ATR-FTIR Spectrum of PYMA	57
Figure 4.8	^{1}H NMR Spectrum Analysis of TOMA	59
Figure 4.9	^{13}C NMR Spectrum Analysis of TOMA	60
Figure 4.10	^{1}H NMR Spectrum Analysis of FBMA	62
Figure 4.11	^{13}C NMR Spectrum Analysis of FBMA	63
Figure 4.12	^{1}H NMR Spectrum Analysis of THMA	65
Figure 4.13	^{13}C NMR Spectrum Analysis of THMA	65
Figure 4.14	^{1}H NMR Spectrum Analysis of PYMA	67
Figure 4.15	^{13}C NMR Spectrum Analysis of PYMA	68
Figure 4.16	ORTEP Structure of FBMA	75
Figure 4.17	ORTEP Structure of TOMA	76
Figure 4.18	ORTEP Structure of THMA	76
Figure 4.19	Packing Diagram of FBMA Showing a Centrosymmetric Viewed Along the a-Axis	77
Figure 4.20	Packing Diagram of TOMA Showing a Centrosymmetric Viewed Along the a-Axis	77
Figure 4.21	Packing Diagram of THMA Showing a Centrosymmetric Viewed Along the a-Axis	78
Figure 4.22	Langmuir Adsorption Isotherm for Each Inhibitors	82
Figure 4.23	SEM Images of Polished Mild Steel in 1M HCl (blank) (a), Mild Steel in 7 mM THMA Solution (b), Mild Steel in 7 mM FBMA Solution (c), Mild Steel in 7 mM TOMA Solution (d), and Mild Steel in 7 mM PYMA Solution (e)	89
Figure 4.24	EDX Data for Bare Mild Steel	90
Figure 4.25	EDX and Mapping for the Distribution of Element on Mild Steel Surface After 24 h in 1 M HCl with 7 mM THMA	91
Figure 4.26	EDX and Mapping for the Distribution of Element on Mild Steel Surface After 24 h in 1 M HCl with 7 mM TOMA	92
Figure 4.27	EDX and Mapping for the Distribution of Element on Mild Steel Surface After 24 h in 1 M HCl with 7 mM FBMA	93
Figure 4.28	EDX and Mapping for the Distribution of Element on Mild Steel Surface After 24 h in 1 M HCl with 7 mM PYMA	94

Figure 4.29	3D AFM Images of the Mild Steel Surface After Immersion in Blank Solution (a), THMA (b), PYMA (c), FBMA (d), and TOMA (e)	97
Figure 4.30	XPS Spectra for Blank Mild Steel (a) Fe (b) C (c) O	99
Figure 4.31	XPS Spectra of Mild Steel With FBMA (a) Fe (b) C (c) O (d) N	100
Figure 4.32	XPS Spectra of Mild Steel With THMA (a) Fe (b) C (c) O (d) S	101
Figure 4.33	XPS Spectra of Mild Steel With TOMA (a) Fe (b) C (c) O	102
Figure 4.34	XPS Spectra of Mild Steel With PYMA (a) Fe (b) C (c) O (d) N	103
Figure 4.35	Energy Band Gap at DFT Level for FBMA	107
Figure 4.36	Energy Band Gap at DFT Level for TOMA	108
Figure 4.37	Energy Band Gap at DFT Level for THMA	109
Figure 4.38	Energy Band Gap at DFT Level for PYMA	110
Figure 4.39	MEP Diagram for FBMA	125
Figure 4.40	MEP Diagram for TOMA	126
Figure 4.41	MEP Diagram for THMA	127
Figure 4.42	MEP Diagram for PYMA	129
Figure 4.43	Atomic Charge Distribution for Each Atom in FBMA	130
Figure 4.44	Atomic Charge Distribution for Each Atom in PYMA	131
Figure 4.45	Atomic Charge Distribution for Each Atom in THMA	131
Figure 4.46	Atomic Charge Distribution for Each Atom in TOMA	132
Figure 4.47	Corrosion Mechanism of HCl on Mild Steel Surface	133
Figure 4.48	Proposed Inhibition Mechanism For FBMA	135
Figure 4.49	Proposed Inhibition Mechanism For TOMA	137
Figure 4.50	Proposed Inhibition Mechanism For THMA	138
Figure 4.51	Proposed Inhibition Mechanism for PYMA	140
Figure 4.52	Normal Plot for FBMA	146
Figure 4.53	Residual vs Predicted FBMA	146
Figure 4.54	Predicted vs Actual for FBMA	147
Figure 4.55	Residual vs Run for FBMA	147
Figure 4.56	Cook’s Distance for FBMA	148
Figure 4.57	Box-Cox Plot for FBMA	148

Figure 4.58	3D Surface Plot FBMA for (a) AB (b) AC (c) AD (d) BC (e) BD and (f) CD	155
Figure 4.59	Optimum Ramp Data for FBMA	158
Figure 4.60	Normal Plot for TOMA	163
Figure 4.61	Residuals vs Predicted for TOMA	163
Figure 4.62	Predicted vs Actual for TOMA	164
Figure 4.63	Residual vs Run for TOMA	164
Figure 4.64	Cook's Distance for TOMA	165
Figure 4.65	Box-Cox Plot for TOMA	165
Figure 4.66	3D Surface Plot TOMA for (a) AB (b) AC (c) AD (d) BC (e) BD and (f) CD	172
Figure 4.67	Optimum Ramp Data for TOMA	175
Figure 4.68	Normal Plot for THMA	180
Figure 4.69	Residual vs Predicted for THMA	180
Figure 4.70	Predicted vs Actual for THMA	181
Figure 4.71	Residual vs Run for THMA	181
Figure 4.72	Cook's Distance for THMA	182
Figure 4.73	Box-Cox Plot for THMA	182
Figure 4.74	3D Surface Plot THMA for (a) AB (b) AC (c) AD (d) BC (e) BD and (f) CD	189
Figure 4.75	Optimum Ramp Data for THMA	192
Figure 4.76	Normal Plot for PYMA	197
Figure 4.77	Residual vs Predicted for PYMA	197
Figure 4.78	Predicted vs Actual for PYMA	198
Figure 4.79	Residual vs Run for PYMA	198
Figure 4.80	Cook's Distance for PYMA	199
Figure 4.81	Box-Cox Plot for PYMA	199
Figure 4.82	3D Surface Plot PYMA for (a) AB (b) AC (c) AD (d) BC (e) BD and (f) CD	206
Figure 4.83	Optimum Ramp Data for PYMA	209

LIST OF SYMBOLS

Symbols

E_{corr}	Corrosion Potential
i_{corr}	Corrosion Current Density
K_{ads}	Equilibrium Constant of the Adsorption Process
ΔE	Band Gap Energy
$\Delta G°$	Gibb's Free Energy
ΔN	Number of Transferred Electrons
ΔW	Weight Loss
η	Absolute Hardness
χ	Electronegativity
Θ	Degree of Surface Coverage

LIST OF ABBREVIATIONS

Abbreviations

AFM	Atomic Force Microscopy
ATR-FTIR	Attenuated Total Reflectance-Fourier Transform Infra-Red
CHNS	Carbon Hydrogen Nitrogen Sulphur
CN	Cyano
DFT	Density Functional Theory
EDG	Electron Donating Group
EWG	Electron Withdrawing Group
FBMA	4-formylbenzonitrle Meldrum's acid
FMO	Frontier Molecular Orbital
HOMO	Highest Occupied Molecular Orbital
IE	Inhibition efficiency
LUMO	Lowest Unoccupied Molecular Orbital
MEP	Molecular Electrostatic Potential
NMR	Nuclear Magnetic Resonance
PYMA	4-pyridinecarboxyaldehyde Meldrum's acid
SEM	Scanning Electron Microscopy
THMA	2-thiophenecarboxyaldehyde Meldrum's acid
TOMA	*p*-tolualdehyde Meldrum's acid

CHAPTER 1
INTRODUCTION

1.1 Research Background

This study focuses on the synthesis and characterization of new Meldrum's acid derivatives, as well as the evaluation and optimization of their corrosion performance. Surface analysis techniques such as scanning electron microscopy (SEM), X-ray photoelectron spectroscopy (XPS), Atomic Force Microscopy (AFM) are applied to characterize the protective layers formed by Meldrum's acid derivatives on mild steel surface. These techniques offer insights into surface morphology, chemical composition, confirming the material's effectiveness in corrosion mitigation. In addition, A detailed computational study Density Functional Theory (DFT) analysis complements the experimental work, revealing the electronic structure, adsorption behaviour, and binding affinity of Meldrum's acid derivatives on mild steel surfaces. Utilizing Response Surface Methodology (RSM), the research aims to fine-tune the synthesis parameters for maximum corrosion protection. RSM, a statistical tool, is employed to explore the interaction of key variables such as ratio, temperature, concentration acid, concentration inhibitor and immersion time, to determine the ideal conditions for developing effective corrosion-resistant coatings.

1.1.1 Corrosion and Corrosion Inhibitor

The natural processes that cause material to degrade over time, especially metals, due to exposure to environmental factors such as moisture, oxygen, and chemicals also known as corrosion (Revie & Uhlig, 2008). Lot of industries including construction, transportation, and manufacturing, facing significant challenges in dealing with this phenomenon, which can result in structural damage, reduced equipment lifespans, and significant economic losses. In addition to compromising the structural integrity of machinery and infrastructure, corrosion poses a safety risk by causing industrial equipment to malfunction or structures to fall. Moreover, contamination of soil and water, can be occurred from hazardous substances that leak from corroded

pipelines, that eventually affect the ecosystem and human health (Hussein Khalaf et al., 2024).

Material properties, environmental conditions such as humidity, temperature, and pH, and the presence of corrosive agents like salts and acids is an example of factors that influenced how this phenomenon occurred (Ahmed et al., 2024). These factors need to be well understood to develop more effective mitigation strategies. To developed effective mitigation strategies, industries must understand the mechanism and effects metal degradation. (Hussein Khalaf et al., 2024).

A corrosion inhibitor is a chemical agent that reduces or prevents the corrosion of metals when introduced in small amounts to a corrosive environment. By creating a protective coating on the metal surface or altering the surrounding environment to reduce its reactivity, corrosion inhibitor performs as an essential remedy. These materials are widely utilised in sectors like construction, water treatment, oil and gas (Ahmed et al., 2024; Yu et al., 2024), automotive manufacturing, and maritime applications, where they improve the robustness and functionality of infrastructure and metal parts.

Corrosion inhibitor can be classified to two types according to their chemical structure and mechanism. The corrosion inhibition mechanism of the inhibitor on mild steel is by adsorption onto the metal surface through both physisorption and chemisorption, resulting in mixed-type inhibition. In acidic solution, inhibitor molecules become protonated and are physically adsorbed onto the steel surface via electrostatic interactions, leading to the formation of an initial protective film that restricts the diffusion of corrosive species toward active anodic and cathodic sites. Simultaneously, chemisorption occurs through the donation of lone-pair electrons from heteroatoms such as nitrogen and oxygen, as well as π-electrons from unsaturated bonds to the vacant *d*-orbitals of iron atoms, forming strong coordinate bonds.

The combined physical and chemical adsorption processes reduce both anodic metal dissolution and cathodic hydrogen evolution or oxygen reduction reactions without causing a significant change in corrosion potential, confirming that the inhibitor acts as a mixed-type inhibitor. (Ahmed et al., 2024). Chemical inhibitors can further be divided into two type, organic or inorganic inhibitors. Inorganic inhibitors, such as chromates, phosphates, and silicates, are widely recognized for their high effectiveness and stability because they promote the formation of a compact, adherent passive oxide or insoluble protective film on the metal surface. This passive layer acts as a barrier that

limits the diffusion of corrosive species and suppresses both anodic metal dissolution and cathodic reactions, thereby enhancing corrosion resistance. In contrast, organic inhibitors are highly adaptable and contain heteroatoms such as oxygen, sulfur, and nitrogen, along with π-electron-rich functional groups, which facilitate adsorption onto the metal surface through physical or chemical interactions to form a protective barrier against corrosion (Elebo et al., 2024).

Because of their excellent effectiveness, even at low concentrations, and environmental adaptability, organic corrosion inhibitors are most preferred among others. These substances interact with metal surfaces by using functional group like hydroxyl, carboxyl, or amine to form a barrier that shields the metal from oxidation and other corrosive processes (Ahmed et al., 2024). Additionally, research into natural, green organic inhibitors that involve corrosion protection with environmental safety has increased due to the growing emphasis on sustainable practices. The comprehension and design of these inhibitors have been further enhanced by contemporary advancement in analytical methods and computational tools, guaranteeing their crucial part in tackling industrial corrosion issues while adhering to environmental standards (Ahmed et al., 2024).

1.1.2 Meldrum's acid

Meldrum's acid, also known as 2,2-dimethyl 1,3-dioxane, is a well-known organic molecule in synthetic chemistry that is highly reactive and has a distinctive structure. This *β*-dicarbonyl molecule is a useful precursor for several chemical transformation because it has two carbonyl groups on either side of a very acidic methylene group. Because of its acidity (pK_a ~ 4.8 in water), it readily forms enolates, which facilitates a variety of reactions like condensation, acylation and alkylation (Shaabani et al., 2001). Meldrum's acid is frequently employed in the synthesis of heterocyclic compounds, carboxylic acids, and esters. It is a vital tool for the synthesis of complex organic compounds, such as agrochemicals and pharmaceuticals, due to its versatility in nucleophilic substitution, cyclization and decarboxylation reactions (Idelfitri et al., 2023). Meldrum's acid derivatives have potential to act as a corrosion inhibitor by adsorbing onto metal surfaces through a combination of chemical and physical interactions, forming a protective barrier that prevents corrosion. Its conjugated system enhances surface coverage and adsorption efficiency, while its

electron-rich oxygen atoms facilitate strong interactions with the metal substrate, further improving its inhibitory performance (Baharin et al., 2024).

1.1.3 Corrosion Inhibition Performance

Validating corrosion inhibition performance is essential to evaluating inhibitor effectiveness and understanding their protective mechanisms on metal surfaces subjected to corrosive environments. Instead of employing pure metal, mild steel will be used for corrosion investigation. Surface analysis techniques are essential to the validation of mild steel performance because they offer detailed visual and chemical insights (Idelfitri et al., 2023). Atomic force microscopy (AFM), x-ray photoelectron spectroscopy (XPS) and scanning electron microscopy (SEM) are methods commonly employed in surface analysis to analyze the morphology of mild steel surfaces before and after inhibitor utilization. These methods provide crucial information on surface coverage, protective layer formation, and surface damage reduction, all of which have an impact on the inhibitor's effectiveness. SEM images can display uniform, smooth layers produced by an effective inhibitor at the surface mild steel, AFM to analyze the roughness of protective layer on the mild steel, and XPS used to determine the chemical composition, and element states at the surface level (Baharin et al., 2024).

1.1.4 Computational Study

Furthermore, computational studies are additional methods to validate the inhibition performance and mechanism. The inhibitor-metal interactions at the molecular level can be monitored with the help of methods like Density Functional Techniques (DFT). This computational method can be used to study the binding energies, active sites, and inhibitor adsorption behavior that led to the creation of protective films (Baharin et al., 2024; Idelfitri et al., 2023). DFT simulations make it possible to estimate the molecular orbitals and electron density distribution, which aids in the identification of inhibitors with potent adsorption properties (Idelfitri et al., 2023). By integrating surface analysis and computational studies, inhibition performance can be evaluated, and mechanism can be proposed. Surface analysis shows an experimental validation of protection, while computational tools allow inhibitor design optimization by predicting performance patterns and spotting possible mechanisms. This dual

approach is essential for advancing the development of effective, sustainable corrosion inhibitors tailored to various industrial applications.

A popular statistical and mathematical approach for examining interactions between several factors and optimizing complex process is response surface methodology (RSM) (Benyounis, 2019; Chahid et al., 2024). For research in a variety of domains, including corrosion investigations, its capacity to provide accurate predictive models while minimizing the number of experimental trials makes it very important. RSM makes it easier to identify the optimum conditions for desired results by methodically planning trials and examining the connections between inputs and outputs (Benyounis, 2019). RSM has shown itself to be a successful methodology for tackling important problems in corrosion research. It has been used, for example to forecast the long-term corrosion behaviour of cement and sulphur concretes used in sewer systems, allowing weight loss models to be derived from experimental data (Benyounis, 2019). RSMs accuracy and precision make it a vital tool for corrosion science process optimization and complex system analysis. By optimizing experimental designs and boosting the effectiveness of prediction models, this study seeks to use RSM strength to create novel approaches for corrosion mitigation (Mert et al., 2025).

1.2 Problem Statement

In many different industries, corrosion is still a major problem that leads to huge financial losses, environmental risks and safety issues. Despite their effectiveness, inorganic inhibitors have been employed extensively to reduce corrosion but due to their toxicity, bioaccumulation, and long-term environmental persistence, they frequently present health and environmental hazards. Consequently, environmentally benign organic inhibitors have emerged as promising alternatives due to their lower toxicity, biodegradability, and structural versatility. However, many reported organic inhibitors still exhibit limitations, including moderate inhibition efficiency, poor long-term stability under aggressive corrosive conditions, limited adsorption strength on metal surfaces, and insufficient optimization for practical industrial applications. These restrictions leave a big hole in the development of effective, secure and long-lasting corrosion inhibition. The experimental trial and error methods used in earlier corrosion inhibitor studies have been time consuming, resource intensive and limited in their ability to explore the detailed molecular interactions between inhibitors and metal

surfaces. Furthermore, a lot of research lacks systematic optimization framework to optimize inhibitor application conditions, which results in less than ideal performance in actual industrial settings (Vaidya et al., 2022). In addition, it is still unclear on investigated the adsorption mechanism, electronic properties, and structure–activity relationship of Meldrum's acid derivatives using an integrated experimental and computational approach. The influence of different functional groups on their adsorption behaviour and corrosion inhibition performance also remains insufficiently understood how Meldrum's acid derivatives interact with metal surfaces in a variety of environmental conditions. By using RSM and DFT to systematically designs, optimize and validate environmentally friendly Meldrum's acid derivative as efficient corrosions inhibitors, this study aims to overcome these limitations. This integrated approach is expected to enhance the understanding of inhibitor performance and adsorption behaviour while contributing to the development of long-lasting, high-performance corrosion protection systems suitable for various applications.

1.3 Objectives of Study

The main goals of this project were:

a) To synthesize and characterize four Meldrum's acid derivatives from *p*-tolualdehyde, 4-pyridinecarboxyaldehyde. 4-formylbenzonitrile and 2-thiophenecarboxyaldehyde.
b) To elucidate the corrosion inhibition performance and mechanism using a weight loss technique, surface analysis (SEM-EDX, AFM and XPS) and computational method (DFT).
c) To optimize corrosion inhibition condition of Meldrum's acid on different parameters using Response Surface Methodology (RSM).

1.4 Significance of Study

The development of corrosion inhibiting derivatives from Meldrum's acid has enormous potential for extending the durability and lifespan of critical infrastructure and machinery. Even under extreme circumstances like high acidity and high temperatures, these derivatives provide strong resistance against corrosion by forming protective coatings on metal surfaces. Organic inhibitors, such as Meldrum's acid

derivatives, are non-toxic, environmentally friendly and in compliance with ever higher regulatory criteria than conventional inorganic inhibitors. This supports resource efficiency, which is in line with SDG 12 (Responsible Consumption and Production) of the UN, and reduces harmful emissions and water pollution, which is in line SDG 13 (Climate action) and SDG 14 (Life below water).

Advanced techniques like density functional theory (DFT), Response Surface Methodology (RSM) have become valuable tools for corrosion studies. DFT provides molecular-level insights into the electronic properties and adsorption behaviour of corrosion inhibitors, while RSM is a statistical optimization technique used to evaluate the effects of experimental variables and determine the optimum conditions for maximum corrosion inhibition efficiency, RSM minimise experimental time and costs by carefully optimizing synthesis and supplication parameters. Meldrum's acid derivatives molecular interactions and binding affinities on metal surfaces are shown using DFT analysis, and their behaviour in actual environments, which improves inhibitor design precision. The goal of this research is to produce corrosion inhibitors that are effective, and sustainable by integrating surface characterisation, computer modelling, and experimental optimization. In addition to promoting resilience and industrial innovation (SDG 9: Industry, innovation, and infrastructure), these results also help create a cleaner, more sustainable environment.

1.5 Scope and Limitations

This study focuses on the synthesis, characterization, and evaluation of a Meldrum's Acid derivatives (4-formylbenzonitrile Meldrum's acid, *p*-tolualdehyde Meldrum's acid, 2-thiophenecarboxyaldehyde Meldrum's acid and 4-pyridinecarboxyaldehyde Meldrum's acid) as a corrosion inhibitor for mild steel in acidic medium. The inhibitor was synthesized via Knoevengel condensation reaction and characterized using Fourier Transform Infrared Spectroscopy (FTIR), Nuclear Magnetic Resonance (^{1}H and ^{13}C NMR), Elemental analyzer and Single Crystal X-ray Diffraction (XRD) analysis. The corrosion inhibition performance was investigated in 1.0 M hydrochloric acid (HCl) solution using the weight loss method. Adsorption behavior was analyzed using various adsorption isotherm models including Langmuir, Frumkin, Temkin, Freundlich, Flory–Huggins, and El-Awady. Surface morphology analysis was performed using Scanning Electron Microscopy (SEM), Atomic Force

Microscopy (AFM) and surface elemental composition was evaluated using X-ray Photoelectron Spectroscopy (XPS). In addition, quantum chemical calculations were conducted using Density Functional Theory (DFT) to correlate molecular properties with inhibition efficiency. The effects of concentration inhibitor, concentration acid, immersion time and ratio were studied and optimized using Response Surface Methodology (RSM).

The limitation of this study, the corrosion inhibition evaluation in 1.0 M HCl solution and does not investigate other corrosive media such as sulfuric acid (H_2SO_4) or basic environments. The corrosion performance was primarily evaluated using the weight loss technique, not using advanced electrochemical techniques such as Electrochemical Impedance Spectroscopy (EIS) and Potentiodynamic Polarization were not included. The temperature range and immersion time were restricted to controlled laboratory conditions, which may not fully represent long-term industrial environments. Although Response Surface Methodology (RSM) is a useful statistical tool for optimizing corrosion inhibition conditions, it is mainly based on experimental data and does not explain the actual mechanism of adsorption. The quadratic model used in RSM may oversimplify the complex and non-linear nature of electrochemical corrosion processes, and its predictions are only reliable within the selected experimental range. Therefore, RSM results should be supported by electrochemical 28 tests and surface analysis for better reliability. In addition, the DFT calculations in this study were performed using the neutral form of the inhibitor molecule. However, in strongly acidic media such as 1 M HCl, functional groups containing nitrogen or oxygen can become protonated. This protonation can change the molecule's structure, charge distribution, and energy levels, which may affect its adsorption behavior on the mild steel surface. As a result, the electronic parameters obtained from the neutral molecule may not fully represent the actual species present under experimental conditions. Future studies should consider protonated forms and solvent effects to provide a more accurate understanding of the corrosion inhibition mechanism

CHAPTER 2
LITERATURE REVIEW

2.1 Corrosion Inhibitor

Destructive degradation of metal through chemical or electrochemical reactions with environment known as corrosion. This process only occurs to metals, identifying it as distinct from other types of material degradation (Hussein Khalaf et al., 2024). For example, corrosion for iron or steel that resulting formation hydrous ferric oxides can be refer as rusting meanwhile for non-ferrous metal form other oxides or salts. This giving a new path to corrosion science to discover causes and mechanisms of this phenomenon, by the knowledge corrosion engineer can develop solution for its prevention. Both play a major role to ensure that the economic, safety, and environmental challenges from corrosion (Revie & Uhlig, 2008).

There are a lot of factors that can cause corrosion, which include environmental conditions, material properties, and electrochemical characteristics. The presence of oxygen, moisture, temperature, and contaminants like salts or acids was categorized as environmental conditions that significantly accelerate corrosion. The next factor is material composition, impurities in metal can serve as localized electrodes that promote galvanic corrosion (Alamri, 2020). As an example, the difference between commercial-grade aluminium and high-purity aluminium is big because commercial-grade aluminium is more prone to corrode due to impurities compared to high-purity aluminium (Revie & Uhlig, 2008). Corrosion can happen in many forms, each with distinct features and effects. The most common type of corrosion is uniform corrosion (Figure 2.1) (a). When a substance is continuously exposed to a corrosive environment, like air or water, its surface deteriorates uniformly over a wide region (Hussein Khalaf et al., 2024). Even though uniform corrosion causes predictable material loss, its effects can be taken into consideration during design and maintenance, making it frequently easier to control. In contrast, pitting corrosion occurs when small holes or cavities are formed on a metal surface due to rapid corrosion in small, localized locations (Figure 2.1) (b) (Revie & Uhlig, 2008). Even though the total material loss appears to be small, these pits have the potential to deeply erode the material, seriously impairing its

structural integrity. The breakdown of protective oxide coatings by chloride ions frequently causes pitting (Ahmad, 2006). Galvanic corrosion occurs when two dissimilar metals are electrically coupled in the presence of an electrolyte, like saltwater (Figure 2.1) (c). While the other metal (the cathode) is shielded, the anode corrodes preferentially. This type of rust is frequently found in mixed-metal assemblies (Ahmad, 2006; Harsimran et al., 2021). Crevice corrosion is kind of localized corrosion happens in tight areas, including behind gaskets or in the crevices between bolts and joints (Figure 2.1) (d). Aggressive chemicals, including chlorides, can build up inside fissures due to restricted environmental flow, producing a highly corrosive microenvironment (Ahmad, 2006).

This results in a focused assault inside the crack. Intergranular corrosion, usually seen in alloys, this type of corrosion targets the metals' grain boundaries (Figure 2.1) (e). It frequently happens because of incorrect welding or heat treatment, which makes the boundaries anodic in relation to the bulk material (Harsimran et al., 2021; Revie & Uhlig, 2008). As a result, the material's structure is weakened and may disintegrate without obvious surface damage. The combined effects of chemical assault and mechanical wear result in erosion-corrosion (Figure 2.1) (f). It happens in systems with moving fluids, including pumps or pipelines, and can cause material loss quickly in places with high flow rates or turbulence (Ahmad, 2006).

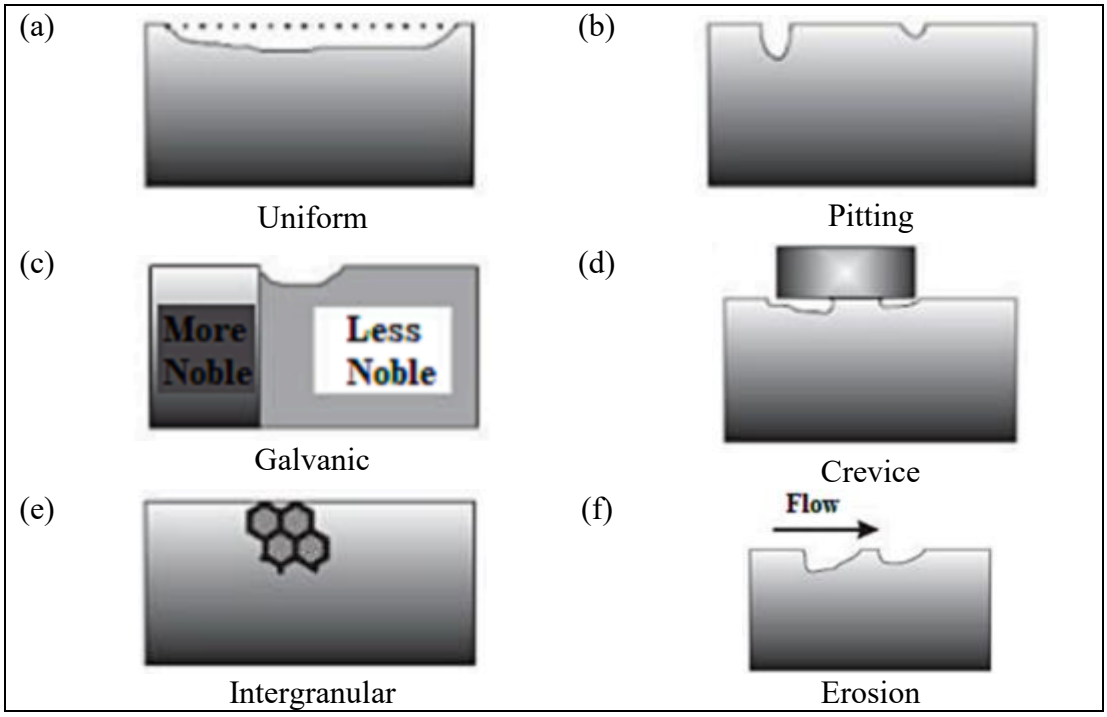


Figure 2.1 Types of Corrosion

The basic mechanism of corrosion is electrochemical and involves anodic and cathodic reactions. In the anodic reaction equation 2,1, metal atoms lose electrons and dissolve into the environment as ions (Harsimran et al., 2021)

$$Fe \rightarrow Fe^{2+} + 2e^{-} \quad (2.1)$$

Simultaneously, cathodic reactions equation (2.2) involves the reduction of species like oxygen or hydrogen ions in the surrounding environment.

$$O_2 + 4e^{-} + 2H_2O \rightarrow 4OH^{-} \quad (2.2)$$

These reactions take place locally, creating galvanic cells in which ions move through the electrolyte and electrons move through the metal. Temperature gradients, contaminants, and variations in oxygen content are some of the variables that affect the kinetics of these reactions and frequently speed up the corrosion process (Revie & Uhlig, 2008). The design of corrosion prevention solutions can be improved by comprehending how various types, mechanisms, and factors interact. To reduce the corrosion effect caused by unavoidable natural processes, techniques such as using inhibitors, cathodic protection, protective coatings, and corrosion-resistant materials will be applied to the steel (Harsimran et al., 2021).

The usage of corrosion inhibitors has become more popular among the available strategies because of its affordability, adaptability and suitability across diverse environments. To stop degradation, theses inhibitors work by altering the corrosive environment or by interacting with the metal surfaces (Al-Amiery et al., 2023; Idelfitri et al., 2023). As inhibitor technologies have advanced over time, more environmentally friendly and sustainable alternatives have been developed, bringing corrosion control methods into compliance with legal and environmental requirements. Based on their composition and functionality, corrosion inhibitors can be divided into two main categories: inorganic and organic inhibitors (Al-Amiery et al., 2023).

Due to their great effectiveness in creating passive oxide layers on metal surfaces, inorganic inhibitors including chromates, nitrites and molybdates have been widely used. These inhibitors lower corrosion rates by changing the electrochemical environment. For instance, nitrites oxidize ferrous ions into ferric ions, creating stable

protective layers, while molybdates enhance corrosion resistance by forming a thin molybdate-ferric oxide film (Al-Amiery et al., 2023). This statement was proved from studies by (Ahmed et al., 2024) that used sodium nitrite (used for carbon steel in 5 mM chloride solution) as an anodic inhibitor with 90% inhibition efficiency. However, the need better substitutes have been prompted by environmental worries about the toxicity of chemicals like chromates. Next, organic inhibitors depend on their molecular structure and functional group's ability to adsorb onto metal surfaces. Active sites in compounds like phosphonates and heterocyclic molecules interact with metal atoms to form a protective barrier. Because they prevent both corrosion and scaling, phosphonates are especially useful in water treatment systems (Ahmed et al., 2024). This is due to their nitrogen, sulphur or oxygen containing structure, heterocyclic compounds combine with metal ions to create stable complexes that offer excellent corrosion resistance. For example, from studies by (Ahmed et al., 2024) using1-benzylimidazole towards carbon steel in 1 M HCl with a mixed adsorption mechanism and 82% inhibition. Furthermore, natural resources such as plant extracts, biopolymers, and amino acids are often known as "green inhibitors." These inhibitors combine low toxicity and great efficiency to provide a sustainable substitute for traditional alternatives (Ahmed et al., 2024; Elebo et al., 2024).

The effectiveness of corrosion inhibitors lies in their ability to disrupt the electrochemical processes that drive corrosion or to physically block corrosive agents from interacting with metal surfaces. Two primary mechanisms that play a vital role are adsorption and electrochemical inhibition (Ahmed et al., 2024). Inhibitor molecules attach to the metals surface by adsorption process. This can happen by physisorption which involves weak van der Waals forces or electrostatics interactions between the inhibitor molecules and the metal surfaces. Because of its low adsorption energy (5–40 kJ/mol), this kind of adsorption is typically reversible and more noticeable at lower temperatures (Al Bahir et al., 2024). By forming multiple layers on the metal surfaces, inhibitor molecules in physisorption reduce direct contact with aggressive ions like chloride or oxygen. Particularly in neutral or acidic environments, organic inhibitors with functional groups like -OH, -NH_2, or -COOH frequently depend on physisorption for their early protective activity (Oguzie et al., 2011). Chemisorption, on the other hand, is the process by which inhibitor molecules and the metal surface create robust chemical interactions, usually covalent or coordinating bonds. These bonds are created when electrons are transferred or shared from the inhibitor's active sites such as lone

pairs on nitrogen (N), oxygen (O), or sulphur (S) atoms to the metal's empty orbitals (Al Bahir et al., 2024). Chemisorption is irreversible and preferable at higher temperatures due to its high adsorption energy (80–400 kJ/mol). In contrast to physisorption, chemisorption produces a persistent monolayer that blocks corrosive species from getting to the metal surface, offering strong and durable corrosion protection (Oguzie et al., 2011). Figure 2.2 shows example of mechanisms physisorption and chemisorption (Al Bahir et al., 2024).

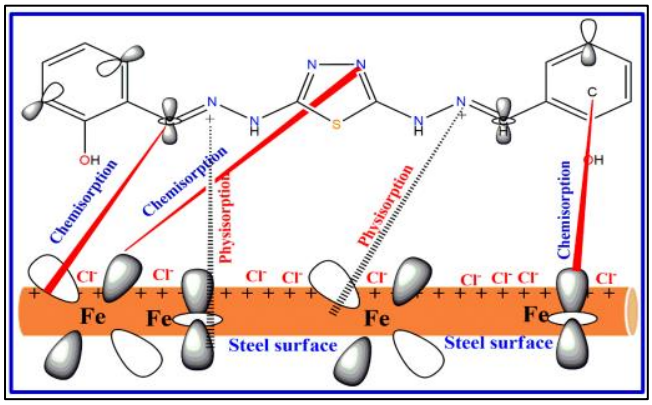


Figure 2.2 Mechanism of Physisorption and Chemisorption

Electrochemical inhibition works by altering the anodic or cathodic reactions in the corrosion process. Anodic inhibitors promote the formation of protective oxide films on the metal surface, effectively reducing the rate of metal dissolution. Cathodic inhibitors, on the other hand, deposit insoluble compounds at cathodic sites, lowering the availability of electrons needed for corrosion reactions. Together, these mechanisms help preserve the integrity of metal structures under various environmental conditions (Ahmed et al., 2024; Oguzie et al., 2011). To maintain the integrity of metallic structures and lower the financial and environmental costs associated with corrosion, corrosion inhibitors are essentials. The industry ability to contemporary issues is demonstrated by the transitions from conventional inorganic inhibitor to advanced, environmentally friendly alternatives. Researchers can create inhibitors that are more potent and long-lasting by utilising computational methods, synergistic mixes, and thermodynamic insights. Corrosion inhibitors will be essential in safeguarding infrastructure and guaranteeing environmental compliance as the sector continues to place a high priority on efficiency and sustainability. This will open the door for more robust and sustainable corrosion management techniques in the future.

2.2 Meldrum's Acid

Known by its chemical name 2,2-dimethyl-1,3-dioxane-4,6-dione, Meldrum's acid (Figure 2.3) is a cyclic β-ketoester that is highly reactive and versatile in organic synthesis. Because of its distinct structural and chemical characteristics, this molecule, which was first synthesised by Alexander Meldrum's in 1908, has found extensive application (Filho et al., 2020; Baharin et al., 2024). Meldrum's acid is a great reagent for a range of synthetic transformations because its highly electrophilic carbonyl groups and a stiff isopropylidene ring. It is useful for creating heterocyclic compounds, ketenes, and alkylidene derivatives because of its acidity (pK_a ~7.5), which allows it to take part in nucleophilic and electrophilic processes. Because of these characteristics, Meldrum's 's acid can be used to create functionalized organic molecules instead of malonic esters (Shaabani et al., 2001).

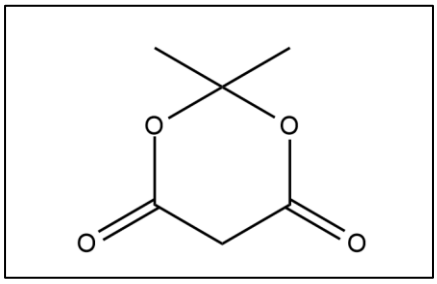


Figure 2.3 Meldrum's Acid Structure

Meldrum's acid is widely used in organic chemistry, but it has drawn interest particularly as a corrosion inhibitor. The potential of compounds, including Vanilin Meldrum's acid, 4-NitroMeldrum acid Thiosemicarbazone and Nitrobenzaldehyde Meldrum acid to protect metal from corrosive conditions like acidic solutions has been studied. Through a combination of chemical and physical adsorption processes, Meldrum's acid derivative adsorbs onto metal surfaces, creating protective barrier that prevent corrosion. These characteristics belong to the molecule conjugated systems, which increase surface coverage and adsorption efficiency, and its electron rich oxygen atoms which promotes its interaction with metal substrates (Baharin et al., 2024; Idelfitri et al., 2023). The extensive potential of Meldrum's acid in both synthetic and practical applications has been validated by studies that combine advanced computational approaches with experimental techniques like spectroscopy and crystallography (Baharin et al., 2024; Mansor et al., 2024). These studies show that

Meldrum’s 's acid is not only a fundamental component of synthetic chemistry but also a viable option for creating economical and ecologically friendly. Its joint contribution to the advancement of materials science and chemical synthesis emphasizes its adaptability and significance in contemporary study.

The FTIR spectrum analysis of Meldrum’s 's acid typically reveals its characteristic functional groups through distinct stretching bands. Meldrum’s acid exhibits strong absorption bands for the symmetric and asymmetric stretching vibrations of the carbonyl groups, ν(C=O). These bands are usually observed in the range of 1730–1790 cm^{-1}, reflecting the presence of two carbonyl functionalities within its cyclic structure. The methyl groups attached to the isopropylidene ring give rise to ν(C–H) stretching vibrations, typically seen in the range of 2800–3000 cm^{-1}. The ν(C–O) vibrations within the cyclic ester ring may appear in the 1100–1300 cm^{-1} region. Additional absorptions related to the cyclic structure of Meldrum’s acid, such as C–H bending or ring vibrations, may be present in the 1400–1500 cm^{-1} range (Baharin et al., 2024; Idelfitri et al., 2023; Mansor et al., 2024).

In NMR analysis the two methyl (CH_3) groups attached to the isopropylidene ring appear as a singlet around 1.6–1.8 ppm due to their equivalent chemical environment. The single proton on the methine carbon (CH) within the cyclic structure typically resonates downfield, though it is often masked or indistinct because the proton is highly acidic and can easily exchange with protons from water or the solvent, leading to a blurred or weakened signal in the NMR. Meanwhile, the two carbonyl (C=O) carbons resonate in the 165–175 ppm range, indicating their highly deshielded environment due to the electronegative oxygen atoms. The central quaternary carbon in the isopropylidene group appears in the 100–120 ppm range, reflecting its deshielded but less electronegative environment compared to carbonyl carbons. Lastly, the two methyl (CH_3) carbons resonate in the 25–30 ppm range, consistent with their shielding from the surrounding electron environment (Baharin et al., 2024; Mansor et al., 2024).

2.3 Meldrum’s Acid as a Corrosion Inhibitor

Formally known as 2,2-dimethyl-1,3-dioxane-4,6-dione, Meldrum’s acid is a cyclic diketone that is well known for its reactivity since it contains active methylene groups. Its distinctive structure two highly electrophilic carbonyl groups and a rigid isopropylidene ring makes it a crucial step in organic synthesis, especially for creating

ketenes and heterocyclic compounds. Meldrum's acid is also essential to studies on corrosion inhibition (Filho et al., 2020). Meldrum's acid can be mixed with other compounds such as vanillin, nitrobenzaldehyde and thiosemicarbazone to create new derivatives like vanillin Meldrum's acid (VanMa), which have demonstrated remarkable corrosion inhibiting capabilities. By adsorbing to metal surfaces, these inhibitors form a barrier that prevents exposure to corrosive agents (Baharin et al., 2024 ; Idelfitri et al., 2023).

Meldrum's acid derivatives' capacity to interact with the metal surface through both physical (physisorption) and chemical (chemisorption) adsorptions is what makes them effective at inhibiting corrosion, particularly in hostile situations like 1 M HCl. Electronegative oxygen atoms in the molecule and π-electrons from conjugated systems assist this interaction, which increases the stability of the protective barrier and encourages adsorption. By considerably reducing the corrosion rate at low concentrations, VanMA, for example, exhibits great inhibitory efficiency. Its adsorption mechanisms follow Freundlich isotherms and exhibit spontaneity, as shown by negative Gibbs free energy values (Baharin et al., 2024; Mansor et al., 2024).

The ability of Meldrum's acid derivative to reduce corrosion by creating homogenous, adsorbed coatings on metal surfaces could be validate by advanced methods such as weight loss studies and surface analysis, including SEM EDX, AFM and XPS. Additionally, computational method like Density Functional Theory (DFT) show that Meldrum's acid unique structural characteristics improve its capacity to interact with mild steel, making it a viable option for creating corrosion inhibitor that are both safe and efficient (Baharin et al., 2024; Idelfitri et al., 2023) corrosion inhibition performance.

2.3.1 Weight Loss Method

The weight loss method is a gravimetric technique used to determine the corrosion rate and inhibition efficiency of a given compound. The principle involves immersing metal samples in a corrosive environment with and without an inhibitor, measuring the weight loss over a specified period. This method to quantify corrosion rates and assess the protective effects of various inhibitors (Verma et al., 2018). Table 2.1 (Barrahi et al., 2025) shows results weight loss data associated with steel corrosion after a 6-hour immersion in 1 M HCl without and with a benzothiazole iodide (BTFI)

inhibitor. Based on the results shows that the corrosion rate (v) and inhibitory effectiveness (% ηw) change with BTFI concentrations. As BTFI concentration rises, W_{corr} significantly decreases, and ηw (%) increases.

Table 2.1
Gravimetric Data for Carbon Steel in the Absence and Presence of Different Concentrations

Medium	C (M)	W_{cor} (mg/cm^{2}h)	ηw (%)
1M HCl	00	1.800	-
BTFI	10^{-3}	0.060	97
	10^{-4}	0.094	95
	10^{-5}	0.180	90
	10^{-6}	0.270	85

2.4 Surface Analysis

2.4.1 Scanning Electron Microscopy with Energy Dispersive X ray Spectroscopy (SEM/EDX)

A crucial analytical technique for analyzing the surface morphology and elemental composition of metals exposed to corrosive environments, like mild steel in 1M HCl, both with and without the use of corrosion inhibitors, is scanning electron microscopy with energy dispersive x-ray spectroscopy (SEM-EDX) (Chahid et al., 2024; Mansor et al., 2024). This method was widely used to investigate the effectiveness of Meldrum's acid derivatives as corrosion inhibitor, such as vanillin Meldrum's acid (VanMA). High-resolution images of the mild steel surface were obtained using SEM, demonstrating the degree of surface deterioration. The SEM images of untreated mild steel exposed to HCl showed significant pitting, roughness, and fracture formation all of which are common signs of aggressive corrosion brought on by the acidic media. On the other hand, the VanMA-treated surfaces showed a noticeable improvement, seeming smoother and more consistent, which was a clear sign that a protective inhibitor layer had formed to reduce corrosion. An important factor was the inhibitor concentration; as VanMA concentration increased, surfaces were smoother and less eroded, indicating the inhibitor's dose-dependent action (Baharin et al., 2024).

By identifying and measuring the elements on the steel surface, EDX analysis added elemental insights to the morphological data. High concentrations of oxygen and

chloride ions, which are linked to corrosion products such iron oxides and chlorides, were found in untreated samples. The elemental composition was considerably changed by the addition of VanMA (Baharin et al., 2024), though as EDX revealed reduced chloride ions and carbon and oxygen coming from the inhibitor. This demonstrated that the inhibitor molecules had adsorbed onto the mild steel surfaces, forming a barrier that reduced the amount of contact between the mild steel and the corrosive chemicals (Idelfitri et al., 2023).

Moreover, by preventing oxidative processes that results in corrosion, the decrease in oxygen levels further confirmed VanMA protective effectiveness. Thus, SEM EDX analysis offered a dual viewpoint in which the inhibitor impact on reducing surface damage was visibly shown by SEM, while the adsorption of the inhibitor and the decrease in corrosive components were chemically verified by EDX. These results supported VanMA proposed missed adsorption mechanism, which combines chemical and physical interactions to enhance corrosion inhibitory actions. The study emphasised SEM-EDX as a formidable instrument to support Meldrum's acid derivatives' protective properties and their promise as economical and sustainable corrosion mitigation options in industrial settings. Figure 2.4 shows the SEM images of mild steel with and without inhibitor meanwhile Figure 2.5 shows the results of EDX analysis.

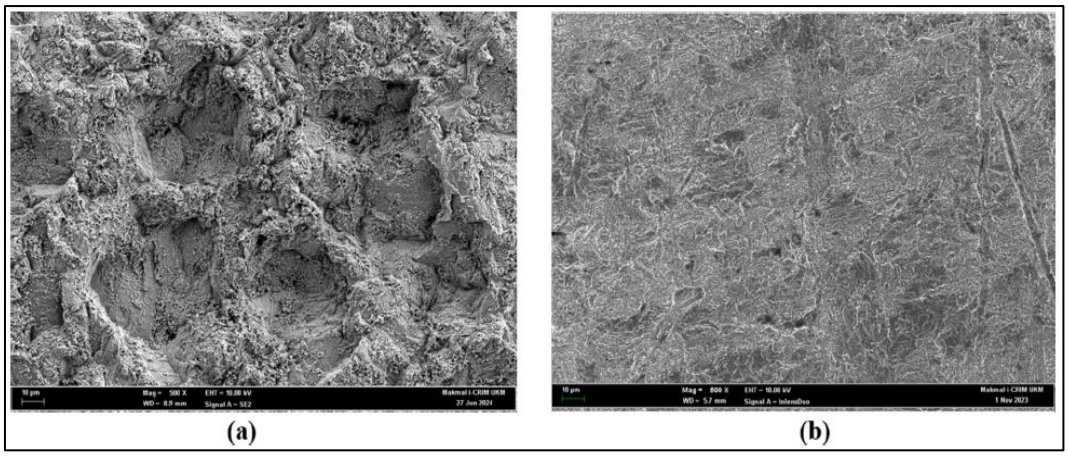


Figure 2.4 SEM Images of Mild Steel in (a) 1 M HCl (Blank), and Mild Steel (b) 0.1 mM Inhibitor

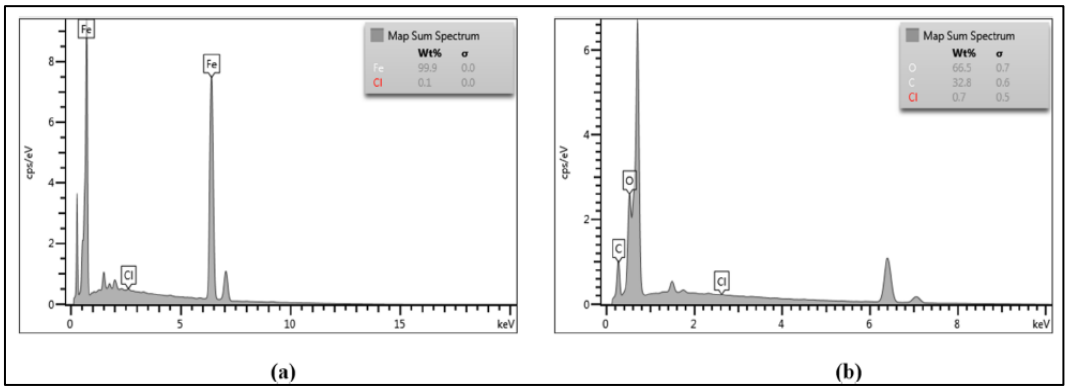


Figure 2.5 EDX Analysis of Elements On Mild Steel Surface After 24 Hours Immersion in 1 M HCl Without and With 0.1 mM Inhibitor

2.4.2 Atomic Force Microscopy (AFM)

Atomic Force Microscopy (AFM) played a crucial role in evaluating the surface roughness and topographical changes of mild steel in the study of Meldrum's acid derivatives, such as vanillin Meldrum's acid (VanMA), as corrosion inhibitors. AFM provides high-resolution, three-dimensional images of surface morphology at the nanometer scale, offering quantitative insights into the degree of surface damage caused by corrosion and the effectiveness of inhibitor protection (Yamin et al., 2020). The AFM analysis in this study was performed on three types of samples: untreated polished mild steel, corroded mild steel exposed to 1 M HCl without inhibitor, and corroded mild steel treated with VanMA at its optimal concentration (Baharin et al., 2024).

For the polished mild steel, the AFM images revealed a relatively smooth surface with minimal roughness, characteristic of a pristine sample. When exposed to the corrosive medium without any inhibitor, the surface displayed significant roughening with deeper grooves and pits, indicating severe damage due to metal dissolution and corrosion processes. This increased roughness was quantitatively measured and attributed to the aggressive action of HCl on the mild steel surface, which resulted in the formation of corrosion products and surface defects (Naseri et al., 2018).

In contrast, the AFM images of the mild steel samples treated with VanMA showed a markedly smoother surface, with a significant reduction in roughness compared to the untreated corroded sample. The smoother surface confirmed the formation of a protective film by VanMA, which acted as a physical barrier between the corrosive environment and the metal substrate. The quantitative roughness parameters, such as the root-mean-square (RMS) roughness, decreased substantially for

the inhibited samples, reflecting the ability of VanMA to adsorb onto the mild steel surface effectively. This adsorption likely involved both physisorption and chemisorption, as suggested by complementary studies in the same research (Baharin et al., 2024; Okewale et al., 2019). Figure 2.6 shows the results of mild steel image in polished conditions without inhibitor and with inhibitor.The AFM data not only visually demonstrated the inhibitor's ability to mitigate corrosion but also provided a quantitative measure of its performance (Idelfitri et al., 2023). The reduction in roughness indicated that VanMA effectively suppressed the formation of corrosion pits and minimized surface damage.

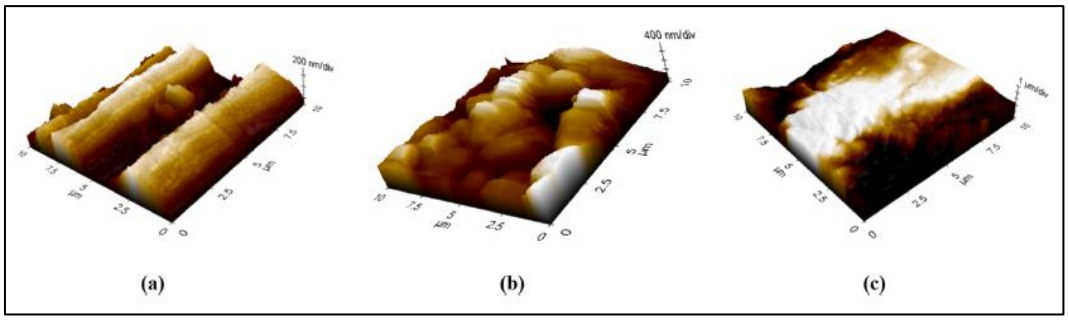


Figure 2.6 AFM Image (a) Polished (b) Blank and (c) Inhibitor of VanMA in 3D

2.4.3 X-ray Photoelectron Spectroscopy (XPS)

X-ray Photoelectron Spectroscopy (XPS) was employed in the study of Meldrum's acid derivatives, such as vanillin Meldrum's acid (VanMA), to analyze the chemical composition and binding states of mild steel surfaces treated with the inhibitor in a corrosive 1 M HCl environment (Figure 2.7). XPS provided surface-sensitive insights, revealing significant changes in the elemental composition and chemical states on the steel surface. For untreated mild steel exposed to the acidic medium, XPS spectra showed the presence of corrosion-related products, such as iron oxides (FeO, Fe_2O_3), and high levels of chloride ions, indicating severe metal dissolution (Al-Amiery et al., 2023; Baharin et al., 2024). However, in samples treated with VanMA, the spectra highlighted a substantial reduction in chloride ions and the appearance of peaks corresponding to carbon and oxygen from the inhibitor.

These peaks were associated with functional groups like carbonyl (C=O) and carbonyl (C–O), confirming the adsorption of VanMA onto the mild steel surface. The analysis further demonstrated the formation of Fe-O bonds, indicative of chemisorption,

while π-electron interactions from the aromatic structure suggested a contribution from physisorption. The combined effects of physisorption and chemisorption formed a robust protective film, reducing surface oxidation and blocking the penetration of aggressive ions (Baskar et al., 2023). This mixed adsorption mechanism was further supported by shifts in binding energy values, confirming strong interactions between VanMA and the metal surface. The XPS data provided compelling evidence of VanMA's ability to protect mild steel by forming a stable, adsorbed barrier layer, complementing results from SEM-EDX and AFM analyses (Baharin et al., 2024). These findings underscored the effectiveness of Meldrum's acid derivatives as efficient and environmentally friendly corrosion inhibitors in highly aggressive acidic environments.

Furthermore, XPS analysis has been extensively used to investigate the contribution of heteroatoms, particularly nitrogen (N) and sulfur (S), in the adsorption mechanism of organic corrosion inhibitors. The appearance of the N 1s peak, typically observed at binding energies between 398 and 401 eV, is attributed to nitrogen-containing functional groups such as pyridine, azomethine (C=N), amine, or amide groups. A shift in the N 1s binding energy after adsorption indicates coordination between the nitrogen lone pair electrons and the vacant 3d orbitals of iron, leading to the formation of Fe–N bonds and confirming chemisorption on the mild steel surface (Hashim et al., 2020). Likewise, sulfur-containing inhibitors exhibit characteristic S 2p peaks within the range of approximately 162–169 eV.

Peaks at lower binding energies (162–164 eV) are generally assigned to Fe–S coordination bonds, while peaks at higher binding energies (166–169 eV) correspond to oxidized sulfur species formed during exposure to the corrosive medium. Sulfur atoms possess higher polarizability and electron density than nitrogen atoms, enabling stronger interactions with the metal surface and promoting the formation of a more stable protective film. Therefore, the presence of N 1s and S 2p signals in XPS spectra provides direct evidence of the participation of nitrogen- and sulfur-containing active sites in the adsorption process, further enhancing the corrosion inhibition performance through a mixed chemisorption and physisorption mechanism.

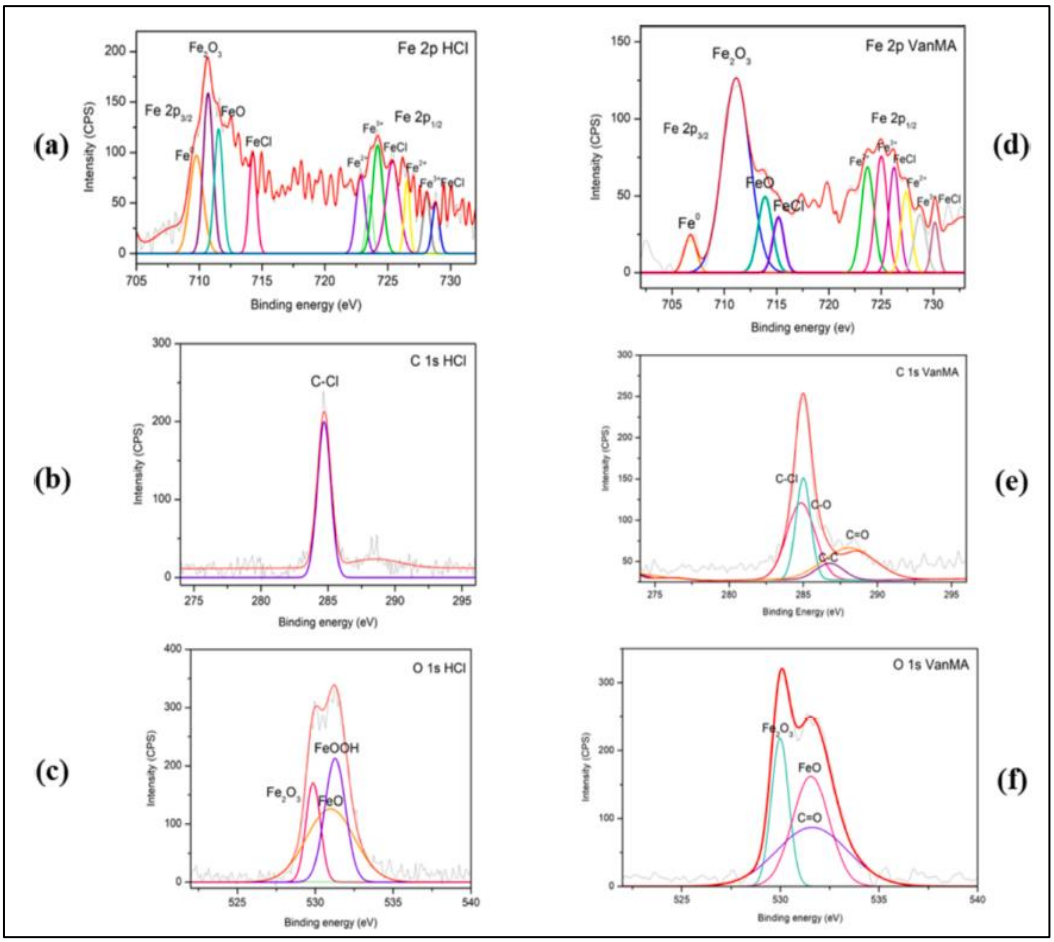


Figure 2.7 High Resolution XPS Spectra of (a-c) Blank and (d-f) VanMA

2.4.4 Density Functional Theory (DFT)

DFT is a computational modelling method used to investigate the electronic structure of molecules and materials. It helps in understanding the interaction between inhibitors and metal surfaces at the atomic level. In several disciplines, including chemistry and materials science.

In addition to illuminating the process of corrosion inhibitor-metal surface contact, DFT calculations can probe in-depth into minute features such electronic structure alterations and chemical bonding types during the adsorption phase. the findings of DFT calculations and research of inhibitors lowest unoccupied molecular orbital energy (LUMO) and highest occupied molecular orbital energy (HOMO). DFT simulations were used to identify theoretical properties such as electronegativity, molecular electrostatic potential (MEP), absolute hardness and softness, and frontier molecular orbital (FMO).

2.4.4.1 Frontier Molecular Orbital (FMO)

Frontier molecular orbital (FMO) theory is a crucial computational tool providing insight to the adsorption processes and reactivity of corrosion inhibitors on metal surfaces. The FMO focuses on the lowest unoccupied molecular orbital (LUMO) and highest occupied molecular orbital (HOMO) energies, which control the electron donation and acceptance capabilities of inhibitor molecules. While a lower LUMO energy implies the molecule can affectively accept back donated electrons from metal surface, a higher HOMO energy indicates a strong ability to donate electron to the vacant *d* orbitals (Ani et al., 2022; Baharin et al., 2024). This behaviour suggests that electron donation from the inhibitor molecule to the vacant d-orbitals of the iron surface, together with the back-donation of electrons from the metal to the inhibitor through the LUMO, contributes to the formation of a stable adsorbed layer. The simultaneous electron donation and back-donation interactions strengthen the adsorption process and enhance the corrosion inhibition performance (Baharin et al., 2024).

According to (Baharin et al., 2024), for example, in a study on vanillin Meldrum's acid (VanMA), the HOMO energy level allowed for strong interactions with mild steel surfaces, while the LUMO energy enabled electron acceptance, which led to effective adsorption and corrosion inhibition. The synergistic interaction between electron donation from the inhibitor to the metal and back-donation from the metal to the inhibitor strengthens the adsorption process and enhances the stability of the protective film formed on the mild steel surface. Furthermore, the energy gap ($\Delta E = E_{LUMO} - E_{HOMO}$) is a crucial indicator of chemical reactivity; smaller energy gaps are associated with more stable adsorption complexes and higher inhibition efficiency (Ani et al., 2022; Okewale et al., 2019).

The reported findings are consistent with previous studies on organic corrosion inhibitors. For example, VanMA exhibited favourable HOMO and LUMO energy levels that promoted effective electron donation and acceptance during adsorption on the mild steel surface (Baharin et al., 2024). Similarly, Oguzie et al. (2011) reported that plant-derived inhibitors containing oxygen, nitrogen, and sulphur atoms possessed relatively small energy gaps (ΔE), which facilitated electron transfer and enhanced adsorption on metal surfaces. These studies demonstrate that although the inhibitors differ in molecular structure, a higher HOMO energy together with a lower LUMO

energy generally contributes to stronger adsorption and improved corrosion inhibition performance.

For instance, molecules containing nitrogen, oxygen, and sulphur atoms with delocalised π-electrons showed low ΔE values in the case of plant extract inhibitors, resulting in enhanced inhibition performance (Oguzie et al., 2011). Additionally, HOMO and LUMO energies are used to create global reactivity descriptors that provide predictive information about the stability of adsorption interactions, such as chemical hardness (η) and chemical softness (S) (Obot et al., 2019).

For instance, inhibitors with higher softness are generally more reactive, facilitating electron transfer between the inhibitor molecule and the metal surface, which enhances adsorption and improves corrosion inhibition efficiency (Obot et al., 2019). Furthermore, the fractions of electron transfer (ΔN) between the inhibitor molecule and the metal surface are measured by Pearson's electronegativity principle. In addition to HOMO and LUMO energies, global reactivity descriptors provide further comparison between inhibitor molecules. Obot et al. (2019) reported that inhibitors with lower chemical hardness and higher softness generally exhibit greater chemical reactivity and stronger adsorption on metal surfaces. Likewise, positive ΔN values reported by Akalezi et al. (2013) indicate favourable electron donation from inhibitor molecules to iron atoms, supporting the formation of stable adsorption layers.

These findings suggest that the combined evaluation of HOMO, LUMO, ΔE, hardness, softness and ΔN provides a more comprehensive prediction of corrosion inhibition performance than relying on a single quantum chemical parameter. According to (Akalezi et al., 2013), positive ΔN values indicate that the inhibitor effectively donates electrons to the metal surface, stabilising the adsorption layer. The global reactivity descriptors are calculated using the following equations (2.3 – 2.14):

ΔE_{gap}	E_{LUMO}-E_{HOMO}	(2.3)
I	-E_{HOMO}	(2.4)
Global hardness	-E_{LUMO}	(2.5)
Global softness	$\eta = \frac{I-A}{2}$	(2.6)
Electronegativity	$S = \frac{1}{\eta}$	(2.7)
Chemical potential	$\chi = \frac{I+A}{2}$	(2.8)

Electrophilicity	$\omega = \frac{\mu^2}{2\eta}$	(2.9)
Nucleophilicity	$\varepsilon = 1\omega$	(2.10)
Electron donating ability	$\omega- = \frac{(A+3I)^2}{16(1-A)}$	(2.11)
Electron accepting ability	$\omega+ = \frac{(1+3A)^2}{16(1-A)}$	(2.12)
Δ Eback-donation	$-\frac{\eta}{4}$	(2.13)
Transferred electron	$\Delta N = \frac{\chi_{fe}-\chi_{inh}}{2(\eta_{fe}+\eta_{inh})}$	(2.14)

2.4.4.2 Molecular Electrostatic Potential

An essential visualisation tool in DFT for highlighting regions of electron density across inhibitor molecules is molecular electrostatic potential (MEP) mapping. By highlighting nucleophilic (electron-rich) and electrophilic (electron-deficient) areas that facilitate adsorption onto metal surfaces, these maps offer a three-dimensional representation of the charge distribution (Figure 2.8) (Ani et al., 2022b). For example, MEP maps often indicate atoms of oxygen, nitrogen, and sulphur as nucleophilic centres that can form coordinate bonds with vacant metal *d*-orbitals (Guendouz et al., 2024; Baharin et al., 2024). Furthermore, back-donation from the metal surface is facilitated by areas of low electron density, known as electrophilic zones, which improves the stability of the inhibitor-metal complex (Adindu et al., 2016). Because areas with high HOMO density frequently coincide with nucleophilic centres, MEP analysis supports the expectations of significant adsorption and enhances FMO results (Ani et al., 2022) According to (Guendouz et al., 2024) for Figure 2.8, the red colour indicated as negative charges, that localized near oxygen and nitrogen atoms, indicates regions of negative electrostatic potential that are sensitive to electrophilic attacks (Guendouz et al., 2024). Meanwhile blue colour represents positively charged region that situated around hydrogen and carbon atoms forming as region positive.

The MEP distributions reported in different studies show similar adsorption characteristics despite differences in inhibitor structure. Guendouz et al. (2024) observed that the oxygen and nitrogen atoms were mainly located within the regions of negative electrostatic potential, indicating their roles as the primary adsorption centres. Likewise, Baharin et al. (2024) reported that the oxygen atoms of VanMA exhibited the highest electron density, suggesting that these atoms preferentially interact with the

mild steel surface during adsorption. The consistency between these studies indicates that heteroatoms possessing high electron density play an essential role in the adsorption mechanism of organic corrosion inhibitors.

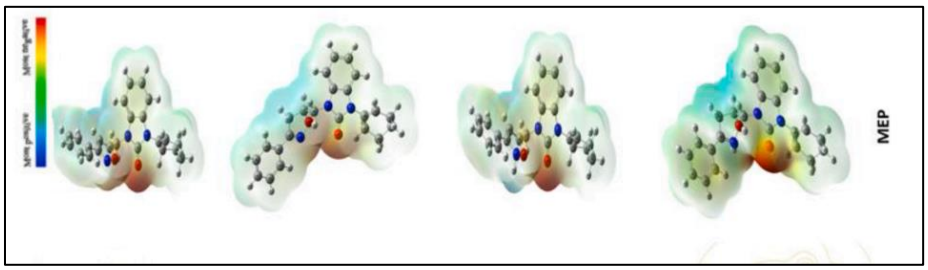


Figure 2.8 Representation of MEP Maps and Their Corresponding Electrostatic Contours for the Two Studied Molecules in Neutral and Protonated States

2.4.4.3 Mulliken Population Analysis

Mulliken Population Analysis (MPA) is used to quantify the distribution of electron densities and atomic charges among inhibitor molecules, offering important information on adsorption behaviour. Because they can donate lone pair electrons to metal surfaces, elements with larger negative Mulliken charge usually nitrogen, oxygen, and sulfur are identified as key adsorption centres in corrosion inhibition investigations (Baharin et al., 2024). Mulliken analysis, for example in Ju & Li, 2007, identified oxygen and nitrogen atoms as the main adsorption sites in nicotinic acid. Strong chemisorption on the surfaces of Zn and Zn-Al alloy was made possible by large negative charges, resulting in a 96.7% inhibitory efficiency. Similarly, derivatives of piperidin-4-one showed notable negative charges on nitrogen and oxygen atoms, which improved their interaction with mild steel surfaces and produced efficient inhibitory properties (Kathirvel et al., 2014).

A comparison of previous studies also indicates that oxygen, nitrogen and sulphur atoms consistently possess the highest negative Mulliken charges regardless of the molecular framework of the inhibitor. Ju and Li (2007) reported that the oxygen and nitrogen atoms of nicotinic acid acted as the principal adsorption centres on Zn and Zn–Al alloy surfaces, whereas Kathirvel et al. (2014) observed similar behaviour for piperidin-4-one derivatives during mild steel corrosion inhibition. Likewise, Baharin et al. (2024) demonstrated that the oxygen-containing functional groups of VanMA

exhibited the most negative charge distribution, confirming that these heteroatoms actively participate in adsorption through electron donation to the metal surface.

Additionally, Mulliken analysis offers insights into intramolecular charge transfer, particularly in aromatic rings and conjugated systems, where adsorption stability is improved by electron delocalisation (Adindu et al., 2016). The Mulliken charge distribution's agreement with HOMO and MEP results strengthens the accuracy of computer forecasts and closes the gap between theory and experimental observation. Figure 2.9 shows the population charge of nicotinic acid (Ju & Li, 2007).

Furthermore, the agreement between Mulliken population analysis, HOMO localisation and MEP mapping demonstrates the complementary nature of these DFT techniques. While Mulliken analysis identifies the atoms with the greatest tendency to donate electrons, FMO explains the electronic transitions responsible for adsorption, whereas MEP visualises the electron-rich and electron-deficient regions of the inhibitor molecule. Therefore, combining these approaches provides a more reliable prediction of adsorption behaviour and corrosion inhibition efficiency than using a single computational parameter alone (Adindu et al., 2016; Baharin et al., 2024).

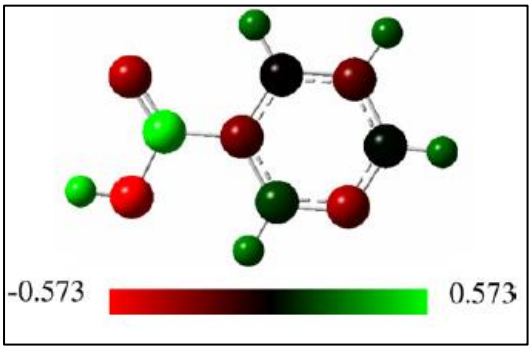


Figure 2.9 The Mulliken Charge Population of Nicotinic Acid

2.4.5 Response Surface Methodology (RSM)

A strong and adaptable statistical and mathematical method for modelling and optimizing processes impacted by numerous independent variables is Response Surface Methodology (RSM). Since its introduction by Box and Wilson in the 1950s, RSM has grown to be a crucial technique in several scientific and industrial domains, including as product development, engineering, manufacturing, and the natural sciences (Bezerra et al., 2008; Yolmeh & Jafari, 2017). Finding the connections between several

controllable input parameters and one or more quantifiable outputs is the main goal of RSM. This allows researchers to pinpoint the ideal circumstances for the intended results (Bezerra et al., 2008; Mansor et al., 2024). RSM provides a methodical and effective means of assessing the combined impacts of several variables and their interactions, in contrast to conventional experimental techniques like the one-variable-at-a-time (OVAT) method.

The RSM is frequently approximated using a second-order polynomial equation (Bezerra et al., 2008; Mansor et al., 2024). The Central Composite Design (CCD) and the Box-Behnken Design (BBD) are two popular experimental designs in RSM. By reducing the number of experimental runs needed, these designs enable the development of prediction models that capture quadratic and interaction effects (Bezerra et al., 2008; Mansor et al., 2024; Yolmeh & Jafari, 2017). Centre points and axial (or star) points are added to a factorial or fractional factorial design to create a CCD. This adds information for modelling curvature in the response surface (Bezerra et al., 2008). CCD works well for quadratic model estimation and usually employs five levels for each factor. BBD, on the other hand, is a three-level design that was created by fusing incomplete block designs, centre points, and two-level factorial designs (Yolmeh and Jafari, 2017). BBD is more effective when operating in a limited experimental area because it does not have axial points like CCD does. The positioning of the design elements in the two designs is a significant difference: BBD places points more compactly within the design space, whereas CCD's axial points extend beyond the factorial space, necessitating a wider experimental zone (Bezerra et al., 2008; Mansor et al., 2024).

Compared to CCD, which is more adaptable and offers higher prediction accuracy close to the centre of the design area, BBD is less resilient to missing data because of its compactness. Furthermore, CCD has the possibility to achieve rotatability, which is perfect for investigating broad response surfaces because it means that the variation of the anticipated response solely depends on the distance from the design centre (Mert et al., 2025). On the other hand, when the region of interest closely coincides with the zone of operability, BBD is frequently used due to its effectiveness and simplicity. Both designs are useful instruments in RSM, and the decision between CCD and BBD frequently comes down to the goals of the study, the resources at hand, and the limitations of the experimental setup (Bezerra et al., 2008).

RSM is especially helpful when there are intricate, nonlinear interactions between the variables that affect the result. A deeper understanding of the system under study is made possible by RSM's ability to generate response surfaces and contour plots, which visually depict how variables interact and affect the response. Additionally, to manage multi-response scenarios where several outcomes need to be balanced at once RSM integrates optimization approaches such desirability functions. This capacity is particularly useful in sectors where process optimization is necessary to raise quality, increase productivity, or satisfy performance standards (Bezerra et al., 2008; Mert et al., 2025).

Researchers can achieve more precise and dependable results while drastically cutting down on the time, money, and resources required for experimentation by incorporating RSM into experimental processes. The predictive power and flexibility of the methodology have made it a vital tool for decision-making and problem-solving in a variety of applications, from process optimisation and quality control to chemical synthesis and product creation (Mert et al., 2025). The use of RSM keeps growing as technology develops and problems in different sectors get more complicated because of its capacity to offer thorough insights and the best solutions in an organised and effective way.

2.4.5.1 RSM on Corrosion Study

The efficiency of RSM in the optimization of several corrosion inhibitors has been shown in recent studies. For example, studies on mild steels ability to withstand corrosion in acidic environment have demonstrated have highlighted the potential of heterocyclic compound. Compound such as 2-methyl-1,3-thiazole-4-carbothioamide and 4-aminothieno[2,3-*d*] pyrimidine-2-thiol had inhibitory efficiency of 98.96% and 98.66%, respectively, at a concentration of 5 mM following 48 hours of exposure, according to electrochemical experiments combined with RSM (Chahid et al., 2024). Also supported by compound isatin 4-ethyl-3-thiosemicarbazone that had inhibitory efficiency of 98% at a 5 mM acid sulphuric concentration for 24 hours exposure (Mansor et al., 2024). These findings were validated through RSM-based modelling, which accurately predicted the corrosion behaviour and inhibition efficiency across various experimental conditions. This method not only improved the experimental work

accuracy but also offered deeper insights into the interactions between inhibitor properties and environmental factors.

Although both studies employed Response Surface Methodology (RSM) to optimise corrosion inhibition performance, differences in the optimum conditions and inhibition efficiencies were observed due to variations in the molecular structures of the inhibitors and the experimental conditions. Chahid et al. (2024b) reported inhibition efficiencies of 98.96% and 98.66% for nitrogen- and sulphur-containing heterocyclic compounds after 48 h of immersion, whereas Mansor et al. (2024) reported a comparable inhibition efficiency of 98% for isatin 4-ethyl-3-thiosemicarbazone after only 24 h of immersion. The high inhibition efficiencies obtained in both studies demonstrate that RSM is capable of accurately predicting the optimum operating conditions while reducing the number of experimental trials required.

The assessment of organic dyes as corrosion inhibitors is another instance of the use of RSM. In a 1 M HCl solution, an azo compound called Congo Red dye (CRD) was shown to be able to prevent aluminium corrosion (Chahid et al., 2024). The findings of the experiment showed that at a dose of 1400 ppm, CRD had a maximum inhibitory efficiency of 87.5%. RSM was used to determine the best conditions for its use by analyzing the impacts of variables including temperature, immersion period, and dye concentration on corrosion rates and inhibition efficiency. Theoretical simulations that demonstrated the significant adsorption of CRD molecules on the aluminium surface, such as Density Functional Theory (DFT) and molecular dynamics, corroborated these findings. These investigations highlight the importance of RSM in connecting theoretical and experimental perspectives on corrosion research (Chahid et al., 2024).

Compared with the heterocyclic compounds reported by Chahid et al. (2024) and the isatin derivative investigated by Mansor et al. (2024), Congo Red dye exhibited a lower maximum inhibition efficiency of 87.5%. This difference may be attributed to the molecular structure of the dye, which possesses fewer highly active adsorption centres than heterocyclic compounds containing multiple nitrogen and sulphur atoms. Nevertheless, RSM successfully determined the optimum inhibitor concentration, immersion time, and operating conditions for all inhibitor systems, demonstrating its applicability to a wide range of organic corrosion inhibitors.

In addition to synthetic compounds and dyes, natural and green inhibitors have also been explored using RSM. For example, plant extracts like *Aspilia Africana*, known for their eco-friendly characteristics, have been investigated for their corrosion

inhibition properties. While such natural inhibitors face challenges related to variability in composition and performance, RSM has proven effective in optimizing their application. By systematically varying parameters, researchers have identified conditions that maximize their inhibition efficiency, providing valuable insights into the feasibility of green chemistry approaches for corrosion prevention (Chahid et al., 2024). Based on finding by Mansor et al., 2024 as shown in Table 2.2 and Table 2.3 are example of values RSM model and analysis of variance for evaluation of quadratic model and final image of 3D model that corelate with the parameters.

Similarly, the application of RSM to natural corrosion inhibitors demonstrates that the optimisation technique is not limited to synthetic compounds. Although plant extracts generally exhibit greater variation in chemical composition than synthetic inhibitors, RSM effectively evaluates the interaction between experimental variables and identifies the optimum conditions that maximise inhibition efficiency. Compared with synthetic inhibitors, natural inhibitors may exhibit slightly lower inhibition efficiencies; however, their biodegradability, low toxicity, and environmental friendliness make them attractive alternatives for sustainable corrosion protection (Chahid et al., 2024).

Table 2.2
RSM Model Design

Run	Concentration inhibitor (mM)	Concentration acid sulphuric (M)	Time immersion (hours)	Response IE (%)
1	4	0.50	14	65
2	6	0.25	19	97
3	4	0.50	14	63
4	4	0.50	14	66
5	6	0.75	9	75
6	4	0.50	14	62
7	0	0.50	14	0
8	2	0.25	9	42
9	4	0.50	14	63
10	2	0.75	19	62
11	4	0.50	14	64
12	2	0.25	19	85
13	4	1.00	14	64
14	6	0.25	9	68
15	4	0.50	24	75
16	6	0.75	19	64
17	4	0	14	0
18	8	0.50	14	98
19	4	0.50	4	45
20	2	0.75	9	67

Table 2.3
Analysis of Variance for the Evaluation of the Quadratic Model

Source	Sum of squares	Degree of freedom	Mean square	*F*-value	*p*-value
Model	3459.02	9	384.34	159.63	< 0.0001 significant
Residual	19.26	8	2.41		
Lack of fit	8.43	3	2.81	1.30	0.3720 not significant
Pure error	10.83	5	2.17		
Total	3478.28	7			

The statistical analysis presented by Mansor et al. (2024) further demonstrated the reliability of the quadratic model, where the model was highly significant ($p < 0.0001$) while the lack-of-fit remained insignificant ($p = 0.3720$). (Figure 2.10) These statistical indicators confirm that the predicted inhibition efficiencies were in good agreement with the experimental values. Similar observations were reported by Chahid et al. (2024), where RSM accurately predicted corrosion behaviour under different

experimental conditions, highlighting the robustness and predictive capability of RSM for corrosion inhibition studies.

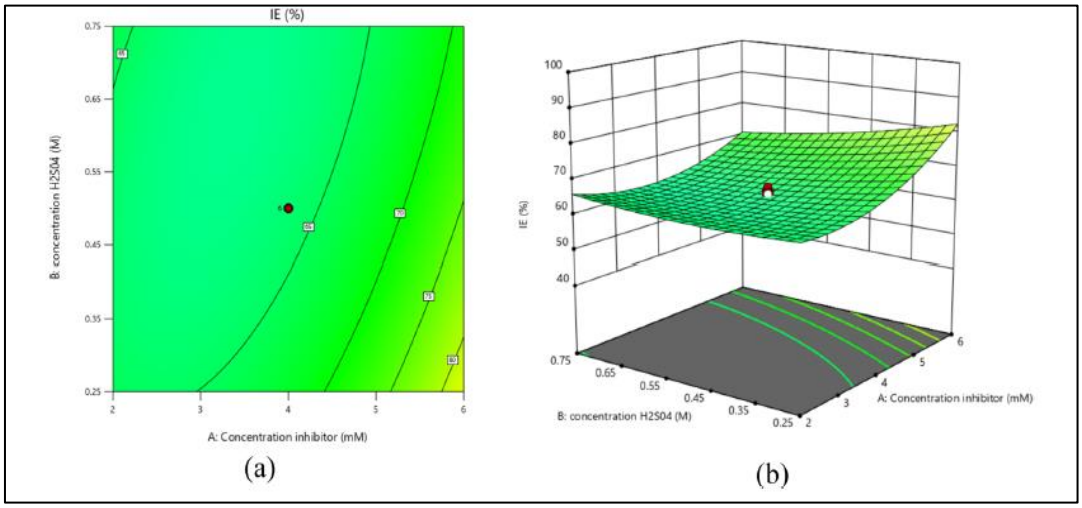


Figure 2.10 Effect of Concentration Inhibitor [A] and Concentration Acid [B] on the Inhibition Efficiency Based on (a) Contour Plot and (b) Response Surface Plot

All things considered, RSM has become a potent instrument in corrosion research, facilitating inhibitor optimisation and deepening our knowledge of corrosion mechanisms. Its capacity to model and forecast the behaviour of intricate systems improves the accuracy and dependability of results while lowering experimental effort and expense. Furthermore, researchers can create inhibitors that are both extremely effective and ecologically friendly by combining RSM with theoretical techniques like DFT and molecular dynamics. These developments have established (RSM) as a valuable tool for optimizing corrosion inhibition studies, supporting the continuous effort to mitigate corrosion in industrial and environmental applications. Furthermore, RSM aligns with the growing demand for environmentally sustainable and cost-effective corrosion protection strategies by reducing experimental time, material consumption, and operational costs.

Overall, the studies reported by Chahid et al. (2024) and Mansor et al. (2024) consistently demonstrate that RSM is an effective optimisation tool regardless of the type of corrosion inhibitor investigated (Figure 2.11). Whether applied to heterocyclic compounds, organic dyes, or environmentally friendly inhibitors, RSM provides reliable mathematical models that accurately predict corrosion inhibition performance while significantly reducing experimental effort. Furthermore, when combined with

Density Functional Theory (DFT) and Molecular Dynamics (MD) simulations, RSM provides a more comprehensive understanding of the adsorption mechanism by correlating experimental optimisation with molecular-level interactions.

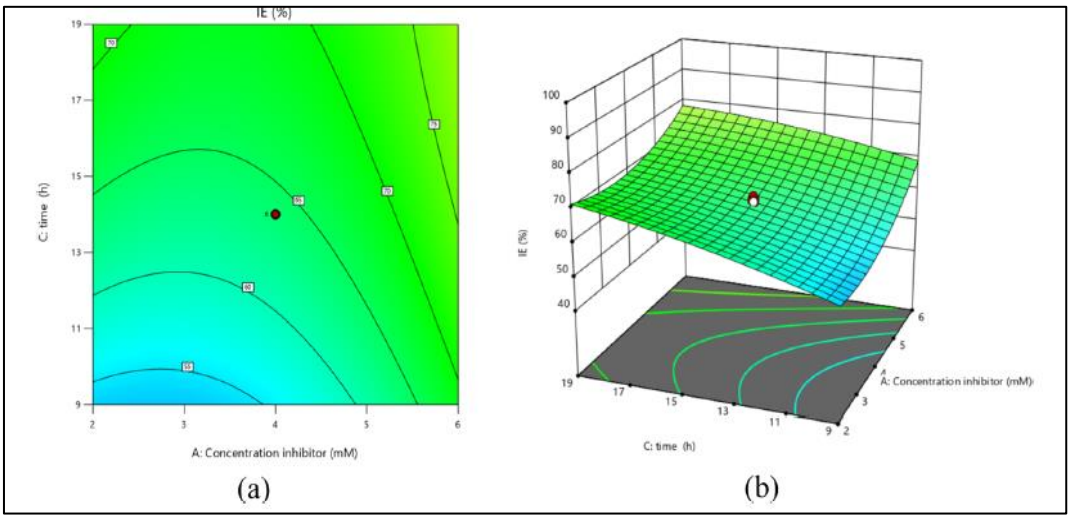


Figure 2.11 Effect of Concentration Inhibitor [A] and Immersion Time [C] on the Inhibition Efficiency Based on (a) Contour Plot and (b) Response Surface Plot

CHAPTER 3
RESEARCH METHODOLOGY

3.1 List of Apparatus and Chemicals

The apparatus used for the synthesis were hot plate, magnetic stirrer, vial, 25 mL beaker, filter paper, filter funnel, measuring cylinder, thermometer, dropper, desiccator, Liebig condenser, and 3-necks round bottom flask, mild steel (2.0 cm x 1.0 cm x 0.1 cm).

The chemicals used in the synthesis of the compounds were acetonitrile, ethanol, *p*-tolualdehyde, 4-pyridinecarboxyaldehyde, 2-thiophenecarboxyaldehyde, 4-formylbenzonitrile, Meldrum's acid, and hydrochloric acid (HCl) have purchased from MERCK and Sigma Aldrich.

3.2 List of Instruments and Software

The instruments have been used for characterization of compounds were Melting point Stuart SMP10 melting point apparatus, Fourier Transform Infrared Spectroscopy-Attenuated Total Reflectance (FTIR-ATR), Nuclear Magnetic Resonance (NMR), Single Crystal X-ray Diffractometer (SC-XRD), Scanning Electron Microscope (SEM) with Energy Dispersive X-ray Analyzer (EDX), X-ray Photoelectron Spectroscopy (XPS), Atomic Force Microscopy (AFM), and Elemental Analyzer (CHN). Response surface Methodology (RSM) was conducted using Design Expert 13 and Density Functional Theory (DFT) was conducted using Gaussian 16.

3.3 Synthesis of Meldrum's Acid Derivatives

Synthesis of Meldrum's acid derivatives: Meldrum's acid (0.154 g, 1.07 mmol) and the aldehyde derivative (1 mmol) were separately dissolved in ethanol (10 mL) in different beakers. The aldehyde derivative solution was then added to the Meldrum's acid solution in a conical flask, and the reaction mixture was heated for 80°C under reflux for 2 hours. The mixture was filtered to remove unreacted raw material, and the filtrate was left to precipitate at room temperature (24°C) to get the final product. The precipitate was rinsed using ethanol and dried in the desiccator. The precipitate was

characterized with elemental analyzer, FTIR-ATR and NMR to prove the structures were as expected. Table 4.1 shows the proposed structures, percentage yield and physical appearance of Meldrum's acid derivatives. Selected synthesized products were dissolved in acetonitrile to obtain suitable SC-XRD analysis, which was used to verify their molecular structure.

Figure 3.1 illustrates the workflow of the experiment, which was divided into three main parts based on the research objectives.The first part involved the synthesis of Meldrum's acid, followed by characterization of the synthesized compound using four analytical techniques: (ATR-FTIR), (NMR), Elemental analyzer (CHNS) and (SC-XRD). The second part consisted of corrosion inhibition evaluation. This evaluation was carried out through weight loss studies, which were further divided into three components: adsorption isotherm analysis, Free Gibbs Energy and surface analysis. The surface analysis was further divided into three techniques, namely (SEM–EDX), (AFM), and (XPS). Finally, the third part comprised the computational study, which included (DFT) calculations and (RSM) analysis.

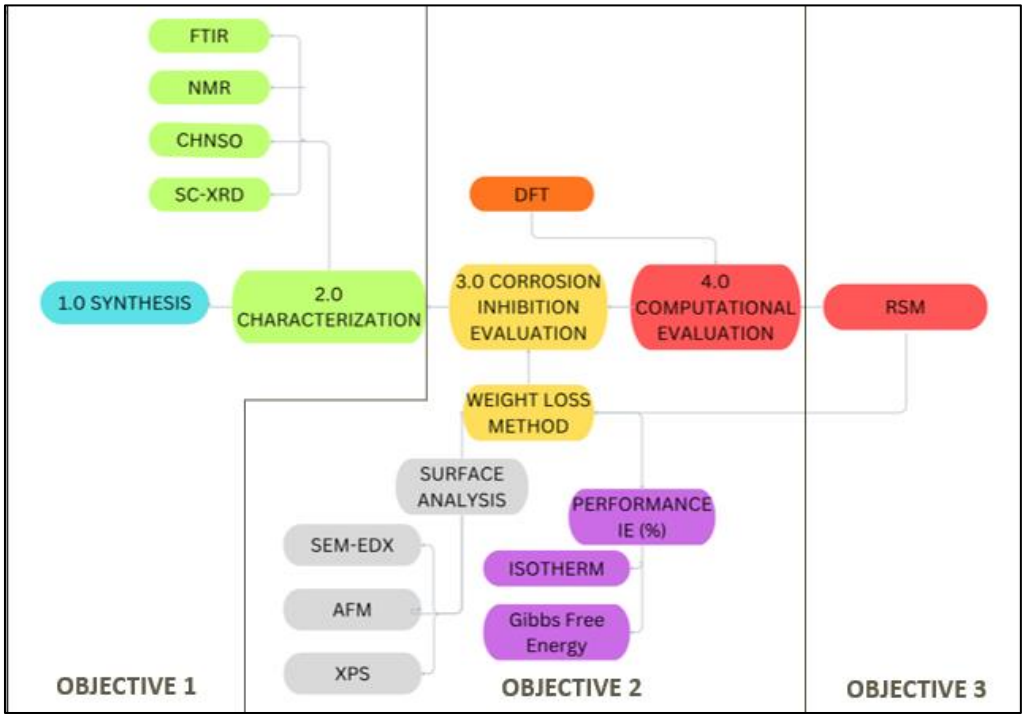


Figure 3.1 Flowchart Methodology

3.4 Characterization of Meldrum's Acid Derivatives

Four instruments have been used to characterize Meldrum's acid derivatives which were ATR FTIR, NMR, elemental analyzer and SC-XRD.

3.4.1 Attenuated Total Reflectance (ATR) - Fourier Transform Infra-Red (FTIR) Analysis

ATR-FTIR analysis was performed to identify functional groups and major stretching bands. The FTIR Perkin Elmer model GX spectrophotometer was used for this investigation, which covered the range of 4000 - 650 cm^{-1} with a resolution of 4.00 cm^{-1} and 32 scan numbers. The ATR-FTIR analysis was carried out on both the synthesized compounds and the starting materials. ATR-FTIR needed little sample preparation, which involved placing a small amount of the solid product of the chemicals onto the ATR crystal surface.

3.4.2 Nuclear Magnetic Resonance (NMR) Analysis

600 MHz Lambda JEOL FT-NMR spectrometer was used to determine the structure of the synthesized compounds, with a focus on two separate nuclei of interest: proton (^{1}H) and carbon (^{13}C). To prepare the sample for analysis, a few mg of compounds were dissolved in deuterated dimethyl sulfoxide (DMSO-d6) and carefully put into an NMR-specific tube. The analysis was carried out using a Bruker FT-NMR spectrophotometer model Avance III HD with a magnetic field strength of 600 MHz. The raw data from the equipment were then processed using the NMR TopSpin 4.3.0 software.

3.4.3 Elemental Analysis

The compounds were examined with an elemental analyzer to determine the amounts of carbon (C), hydrogen (H), nitrogen (N), sulphur (S), and oxygen (O) present. The analysis was conducted using the Thermo Scientific Elemental Analyzer, specifically the Flash Smart model. Approximately 5 mg of the sample intended for

analysis was properly prepared. The obtained percentages for each constituent were then compared to the calculated (theoretical) values.

3.4.4 Single Crystal X-ray Diffraction

Before going through exposure to an X-ray beam, a suitable single crystal was chosen with the support of a polarizing microscope, secured to a nylon loop, and positioned inside the diffractometer. The crystal and detector were positioned 40 mm apart. Using graphite monochromate Mo-Kα radiation (λ = 0.71073 Å) and a Bruker D8 QUEST CCD diffractometer fitted with a PHOTONIII detector, data were obtained at 300 K. The data were acquired using APEX4 software and interpreted using the SAINT program (Bruker, 2021). The Olex2 program was used to solve the structure using SHELXS software and Direct Methods. The XL refinement package was then used to minimize it using least squares. All non-hydrogen atoms were refined by anisotropic refinement, whereas all hydrogen atoms were refined as riding atoms with relative isotropic characteristics after being positioned in idealized positions.

3.5 Weight Loss Method

3.5.1 Preparing Solution

The synthesized FBMA, THMA, TOMA and PYMA compounds were dissolved in ethanol, to prepare a 10 mM solution in a 100 mL volumetric flask for the stock solution. Then, from the stock solution, the solution was diluted to 1 mM, 2 mM, 3 mM, 4 mM, 5 mM, 6 mM and 7 mM, respectively. Meanwhile, the 1 M HCl used for the screening purpose.

3.5.2 Weight Loss Method for Performance Screening

Mild steel (2.0 cm x 1.0 cm x 0.1 cm) was cleaned with emery paper, rinsed with distilled water and acetone. After that, the initial weight of the mild steel was determined using an analytical balance. The following stage was involved acid solutions 1 M HCl (3.5 mL) as a blank and inhibitor concentrations of 0, 1, 2, 3, 4, 5, 6 and 7 mM (3.5 mL) (screening purpose). The mild steels were cleaned with distilled water, then

immersed in room temperature for 24 hours. The experiment was repeat three times to determine the average masses, and the final weight of mild steel was recorded. Equations 3.1 – 3.3 were used to calculate the percentages of corrosion inhibition efficacy as an outcome:

ΔW	=	W1 – W2	(3.1)
Corrosion rate (CR)	=	$\Delta W/st$	(3.2)
% IE	=	$[(C^{o}_{RW} - C_{RW} / C_{RW})] \times 100$	(3.3)

Where,

W1 = Weight of mild steel before corrosion (g).

W2 = Weight of mild steel after corrosion (g).

ΔW = Weight loss (g).

s = Surface of mild steel.

t = Immersion time (h).

C°_{RW} = Corrosion rate with absence of inhibitor.

C_{RW} = Corrosion rate with presence of inhibitor.

%IE = Inhibition efficiency percentage.

3.5.2.1 Isotherms

The inhibition efficiency data obtained from the weight-loss measurements were fitted to the Langmuir (Equation 3.4), Freundlich (Equation 3.5), Frumkin (Equation 3.6), Temkin (Equation 3.7), El-Awady (Equation 3.8), and Flory–Huggins (Equation 3.9) adsorption isotherms to evaluate the adsorption behaviour and inhibition mechanism of the inhibitor on the mild steel surface.

Langmuir adsorption isotherm	$: \frac{C}{\theta} = \frac{1}{K} + C$	(3.4)
Freundlich adsorption isotherm	$: \log \theta = \log K_f + \frac{1}{n} \log C$	(3.5)
Frumkin adsorption isotherm	$: \ln (\frac{\theta}{1-\theta} C) = \ln K_{ads} + 2a\theta$	(3.6)

Temkin adsorption isotherm	: $\theta = \frac{1}{f} \ln (K_{ads} C)$	(3.7)
El-Awady adsorption isotherm	: $\log (\frac{\theta}{1-\theta}) = \log K + \frac{1}{Y} \log C$	(3.8)
Flory–Huggin's adsorption isotherm	: $\log (\theta/C) = \log(xK_{ads}) + x \log(1-\theta)$	(3.9)

3.5.2.2 Gibb's Free Energy

Equation 3.10 shows how to calculate the standard Gibb's free energy (ΔG_{ads}) from adsorption isotherm readings to determine the nature and effectiveness of adsorption.

$$(\Delta G^{\circ}_{ads}) = -RT \ln(55.5 \times K_{ads}) \quad (3.10)$$

When the Gibb's free energy (ΔG_{ads}) value is -20 kJ mol^{-1}, it implies physisorption, while a value of -40 kJ mol^{-1} or greater shows chemisorption. If the ΔG° value is between -20 kJ mol^{-1} to -40 kJ mol^{-1}, it indicates that the inhibitor is a mixed type of inhibitor that uses both physisorption and chemisorption methods.

3.6 Surface Analysis

3.6.1 Scanning Electron Microscope with Energy Dispersive X-ray Spectroscopy (SEM-EDX)

The mild steel that shows the highest corrosion inhibition efficacy at optimum condition, was carried out for SEM-EDX analysis. The surface morphology of the mild steel was explored in two ways: blank mild steel (immersed in 1 M HCl without inhibitor) and mild steel with inhibitor (immersed in 1 M HCl and inhibitor). This examination was carried out using a ZEISS MERLIN compact microscope equipped with a field emission gun. The distribution percentage of the elements on the surface of the mild steel was also visualized using Energy-Dispersive X-ray Spectroscopy (EDX).

3.6.2 Atomic Force Microscope (AFM)

The mild steel that shows the highest corrosion inhibition efficiency, was carried out for AFM analysis. The surface roughness of the mild steel samples was tested under two conditions: blank, and in the presence of Meldrum's acid derivative. This screening was carried out with the Park System XE-100 Atomic Force Microscope. The sample preparation technique for the AFM analysis is the same as for SEM.

3.6.3 X-ray Photoelectron Spectroscopy (XPS)

The mild steel that shows the highest corrosion inhibition efficiency was carried out for XPS analysis. Upon removal, the mild steel was dried and rinsed with deionized water. The surfaces of the polished, blank, and mild steel with inhibitor were analyzed using a Kratos AXIS Ultra DLD spectrometer (Kratos Analytical, United Kingdom [UK]) X-ray photoelectron spectroscope (XPS). The instrument will be set with a monochromatic Al K_α radiation source (hv = 1486.6 eV) operated at 150 W (15 kV × 10 mA).

3.7 Density Functional Theory (DFT)

Quantum chemical calculations were performed using the Gaussian 09 software package. The B3LYP functional with the 6-31G(d,p) basis set was employed for the crystal structure of the compound. Meanwhile, the B3LYP functional with the 6-31G(d,p)++ basis set was used for the non-crystal structure. The ground-state geometries of the Meldrum's acid derivatives were optimized using the density functional theory (DFT)

3.8 Response Surface Methodology (RSM)

Modelling and analysis of a corrosion inhibition study where responses are impacted by several factors were performed using RSM software (Design Expert 11). The independent variables were used for the optimization of Meldrum's acid derivatives on mild steel are A: Concentration inhibitor (X_a), B: Concentration acid (X_b), C: Time immersion (X_c) and D: Ratio acid and inhibitor (X_d). Inhibition efficiency (Y1) of the

gravimetric analysis was served as the responses (dependent variables). With many runs and three replications at the Centre spots, CCD was carried out. To prevent systematic mistakes, the run order for these trials were randomly. Table 3.1 shows the experimental range and variable levels that have been simplified by RSM.

Table 3.1
Coded and Actual Variable Level for Each Parameter

St. no	Parameter	Code	Unit	-1	0	+1
1	Concentration inhibitor	A	mM	0	4	8
2	Concentration acid	B	M	0	0.5	1
3	Time immersion	C	T	8	16	24
4	Ratio acid and inhibitor	D	mL	2	4	6

For RSM, Meldrum's acid derivatives were dissolved in acetonitrile to prepare a 1 M solution in a 100 mL volumetric flask. From the stock solution of inhibitor was diluted based on Table 4.22. Distilled water was used to dilute 98 % of HCl, respectively. 5.5 mL of 98 % HCl dissolved with distilled water in a 100 mL volumetric flask each. Same as weight loss method, the prepared acid and inhibitor followed the design of experiments (DoE), that was developed by RSM.

CHAPTER 4
RESULTS AND DISCUSSION

4.1 Synthesis of Meldrum's Acid Derivatives

Four Meldrum's acid derivatives were successfully synthesised. The synthesis was carried out through the Knoevenagel condensation method. This method occurred between carbon position C_5 of Meldrum's acid and the carbonyl group (C=O) from the aldehyde or ketone derivatives. Meldrum's acid, which has a high reactivity, attacked the carbonyl group in the derivative molecule nucleophilic, causing the reaction to occur as a nucleophilic addition (Sokov et al., 2024). Thus, forming new compounds with some can be observed to change colour, such as from a colourless solution to a brown or yellow precipitate.

4.1.1 Reactions Mechanism

Figure 4.1, Figure 4.2, Figure 4.3 shows the step-by-step mechanism for the formation of the *bis*-Meldrum's acid compounds. First, Meldrum's acid loses a hydrogen atom in the presence of ethanol, forming a reactive enolate ion. This enolate then attacks the carbonyl group of an aromatic aldehyde, creating an intermediate where the oxygen becomes negatively charged. The intermediate is then protonated by ethanol to form a β-hydroxy compound. Next, this compound loses a water molecule (dehydration), forming a double bond between the carbon atoms an α, β-unsaturated product. At this point, a second molecule of Meldrum's acid also becomes deprotonated and forms another enolate ion. During the Michael addition step, this second enolate attacks the β-carbon of the double bond in the α, β-unsaturated product, forming a new carbon-carbon bond (Sokov et al., 2024). This step links the two Meldrum's acid molecules together. Finally, proton transfer and rearrangement occur, stabilizing the product and forming the final bis-Meldrum's acid derivative, where two Meldrum's acid units are connected through the aromatic ring.

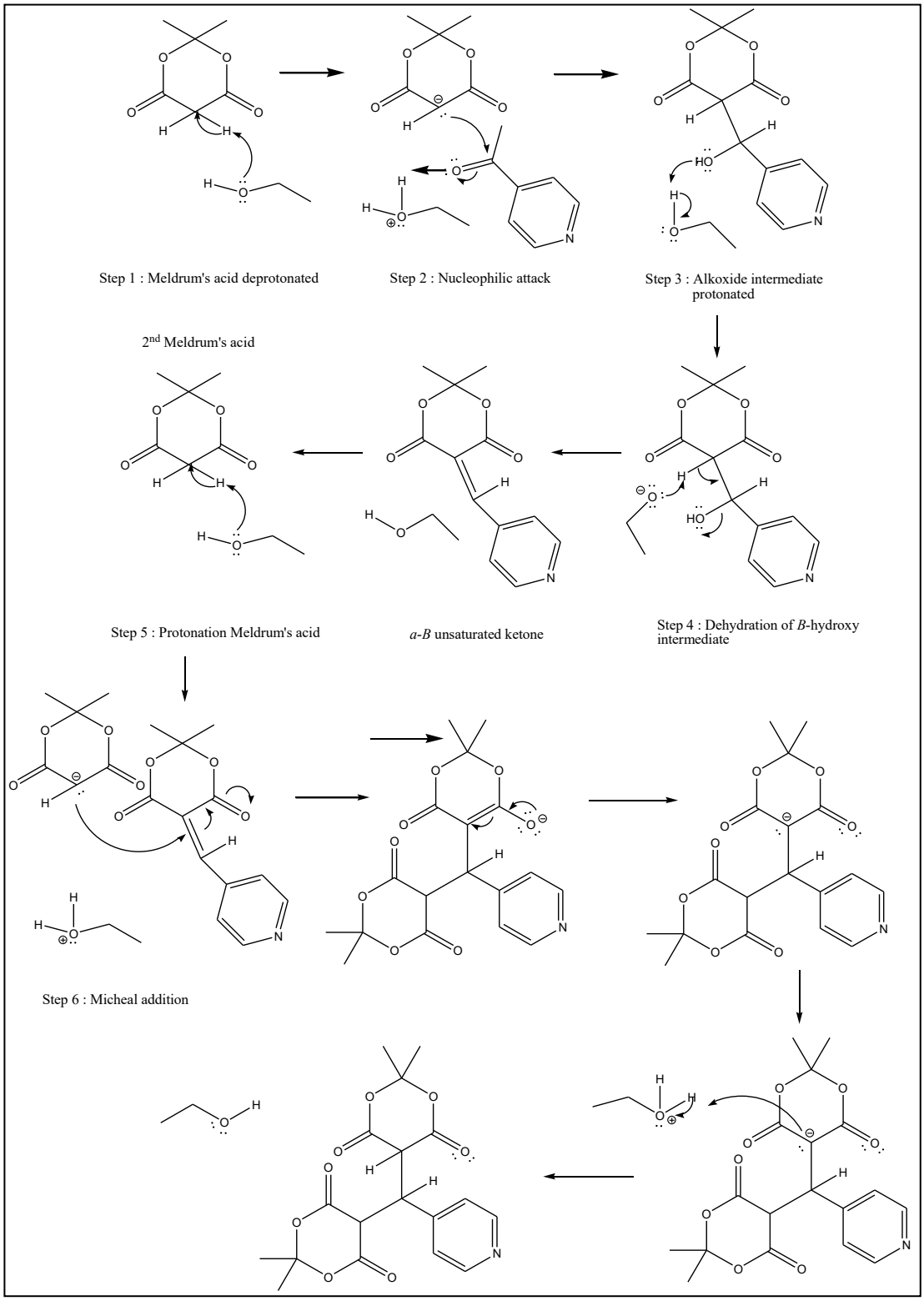


Figure 4.1Proposed Mechanism for the Formation of PYMA

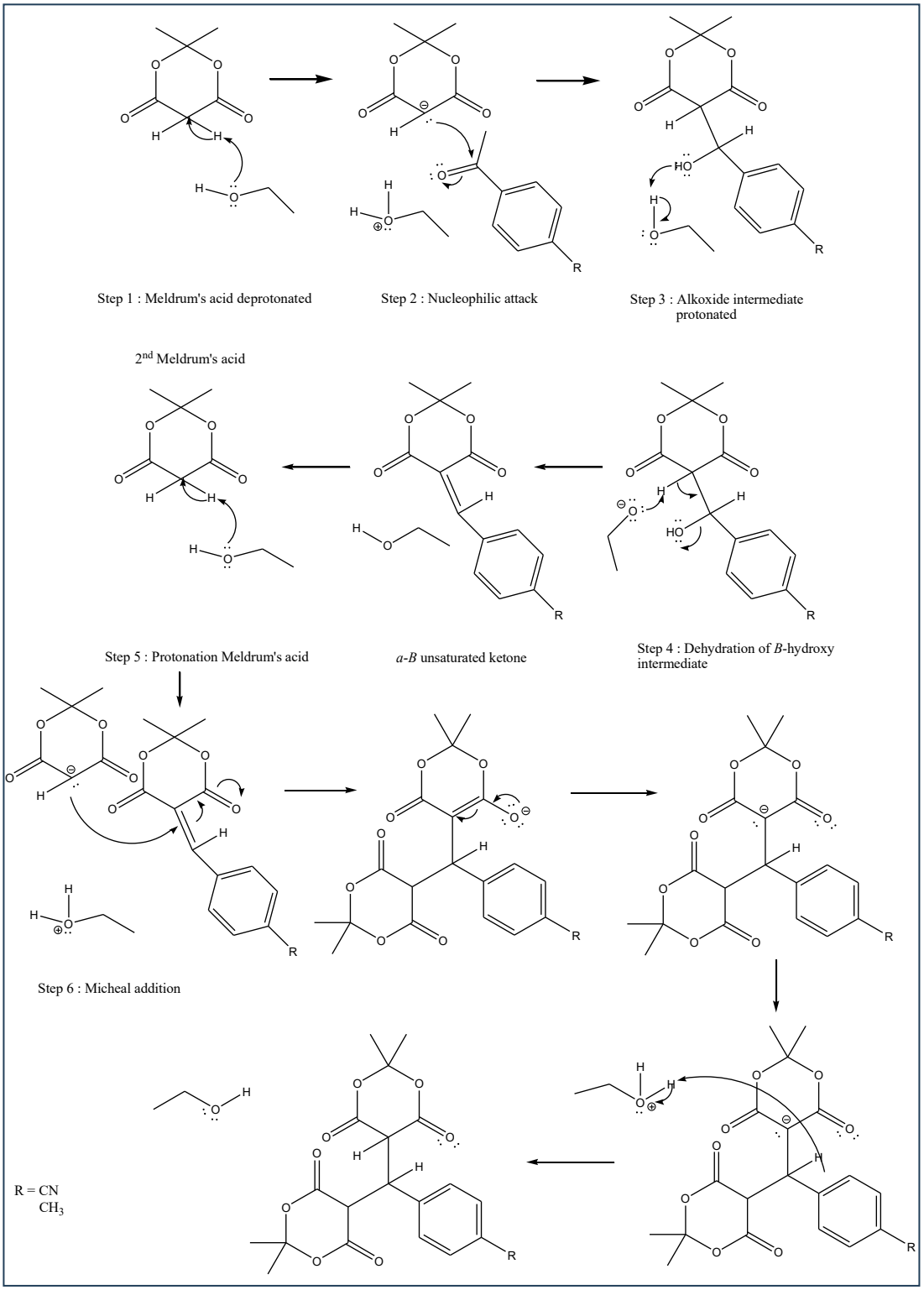


Figure 4.2 Proposed Mechanism for the Formation of FBMA (R = CN) and TOMA (R = CH_3)

Figure 4.3 illustrates the possible reaction mechanism for the formation of the single Meldrum's acid substitution product (THMA). The reaction begins in step (1), where Meldrum's acid, which is weakly acidic in ethanol and water, loses a proton and forms an enolate ion. In step (2), this enolate ion acts as a nucleophile and attacks the electrophilic carbonyl carbon of 2-thiophenecarboxaldehyde. Step (3) involves the formation of an alkoxide intermediate because of this nucleophilic attack, where the carbonyl group of the aldehyde is converted into an oxygen anion. The alkoxide intermediate is then protonated by methanol, producing a β-hydroxy compound and restoring the neutral oxygen atom. Finally, in step (4), the β-hydroxy intermediate undergoes dehydration, meaning it loses a water molecule, and this leads to the formation of a carbon–carbon double bond, producing the dioxanediones structure characteristic of THMA.

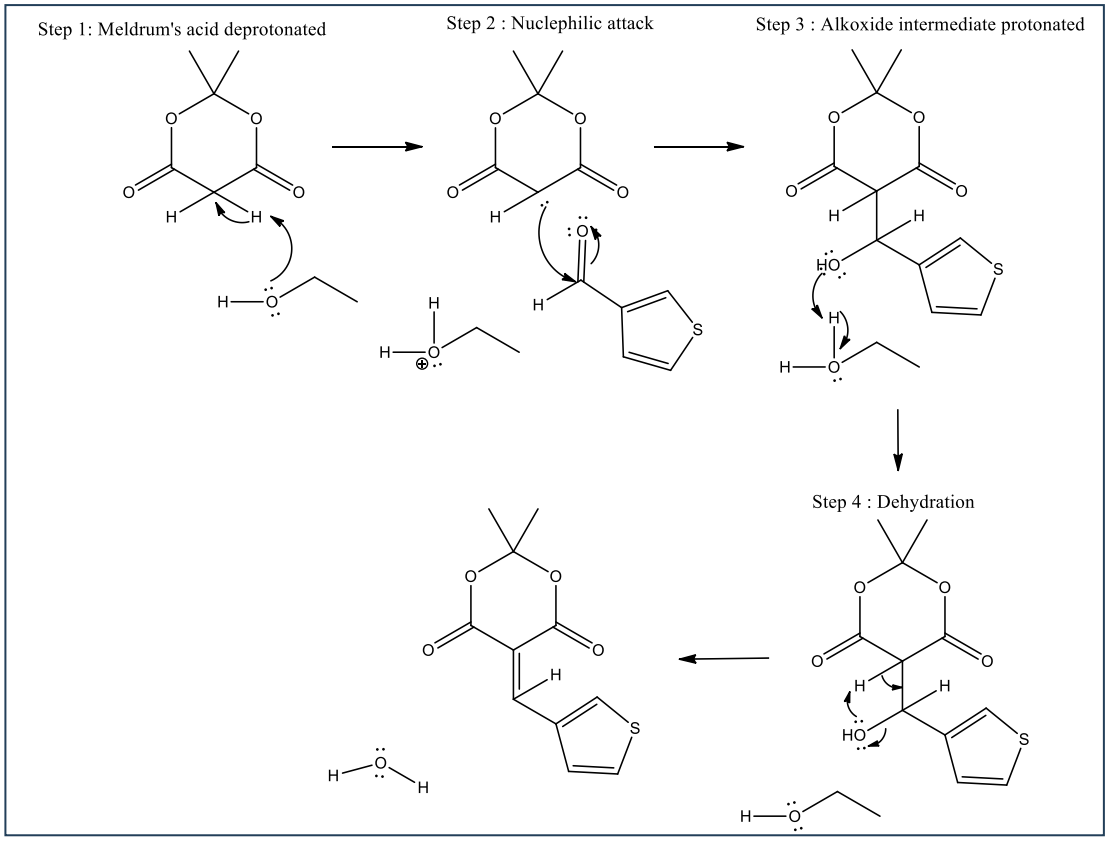
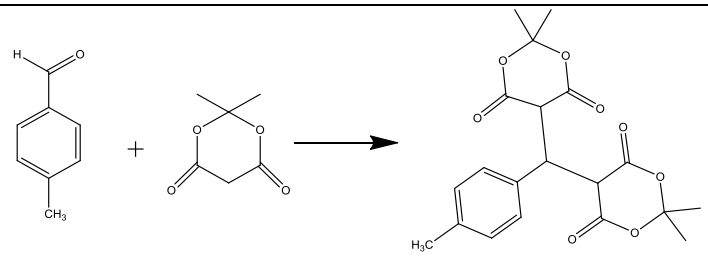
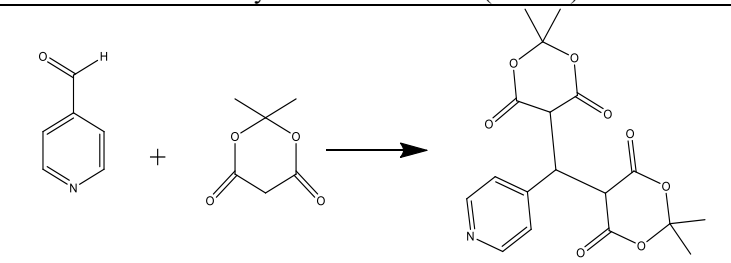
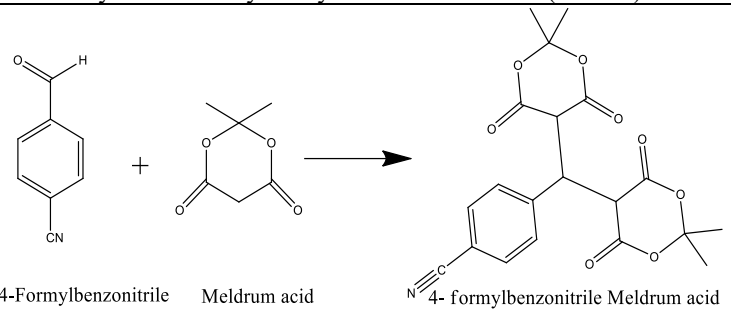
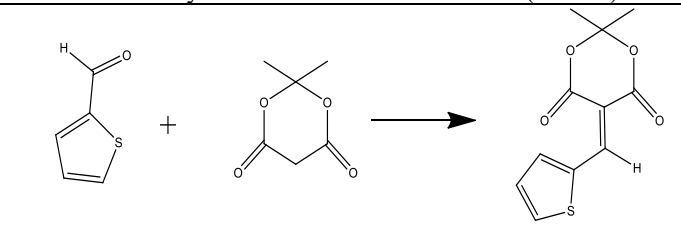


Figure 4.3Proposed Mechanism for the Formation of THMA

2-thiophenecarboxyaldehyde Meldrum's acid (THMA) only reacts once because the 2-thiophene ring shares a lot of its own electrons to form a new bond, making it stable. This stability prevented the second Meldrum's acid moiety from attach

into the structure (Cooper and Klymkowsky, 2020). On the other hand, 4-formylbenzonitrile and 4-pyridinecarboxaldehyde are electron withdrawing, that pulling electrons away from the bond, leaving it empty and reactive, this allows Meldrum's acid to attack and create a new bond. Meanwhile p-tolualdehyde reacted twice due to it cannot provide enough stabilization to stop the reaction at the first stage, leading to double addition of Meldrum's acid. Table 4.1 shows the reaction scheme, percentage yield and observations for all four Meldrum's acid and their derivatives.

Table 4.1
Reaction Routes and Percentage Yields

Reaction routes	Yield %	Observations
 p - Tolualdehyde Meldrum acid Tolualdehyde Meldrum acid Tolualdehyde Meldrum's Acid (TOMA)	78	Clear Crystal
 4-Pyridinecarboxyaldehyde Meldrum acid pyridinecarboxyaldehyde Meldrum acid Pyridinecarboxyaldehyde Meldrum's Acid (PYMA)	68	Yellow powder
 4-Formylbenzonitrile Meldrum acid 4- formylbenzonitrile Meldrum acid 4-Formylbenzonitrile Meldrum's Acid (FBMA)	79	Clear crystal
 2 - Thiophenecarboxyaldehyde Meldrum acid 2 - Thiophenecarboxyaldehyde Meldrum acid 2-Thiophenecarboxyaldehyde Meldrum's Acid (THMA)	78	Yellow crystal

4.2 Characterisation of Synthesised Meldrum's Acid Compounds

4.2.1 Physicochemical Analysis

The determination of melting points and elemental analysis were carried out in this study as an integral aspect of the physicochemical analysis of the synthesised compounds. These analyses play a vital role in evaluating the purity and confirmation of the proposed structures of synthesised compounds.

4.2.1.1 Melting Point Determination

Refer to the melting point Table 4.2 of the four synthesised Meldrum's acid derivatives which are FBMA, PYMA, THMA and TOMA were analysed to evaluate their thermal stability. The melting point is mainly influenced by molecular weight, molecular symmetry, planarity, polarity and how tightly the molecules can pack together in the solid state (Brosgé et al., 2021). Among them, PYMA exhibited the highest melting point (225-227°C) because of it has a rigid and planar pyridine ring that connect symmetrically with two Meldrum's acid units. The presence of a nitrogen atom in the aromatic ring increases polarity of molecule and allows strong dipole–dipole interactions and weak hydrogen bonding between molecules, these interactions make the molecules pack closely and form a stable structure (Hohenstein and Sherrill, 2009). Despite its moderate molecular weight (377.35 g/mol), its symmetrical and polar structure gives its high thermal resistance for melting due to it can form well-ordered structure that more energy needed to melt.

TOMA, which shares a similar symmetrical two Meldrum's rings attached to a phenyl ring, exhibited a slightly lower melting point (212-214 °C) than PYMA. This is primarily because TOMA lacks the pyridine nitrogen atom present in PYMA, resulting in weaker dipole–dipole interactions. In addition, the methyl group donates electrons and reduces the overall polarity of the molecule (Schulz et al., 2011). However, because TOMA is still rigid and symmetric, it maintains good crystal packing and therefore still melts at a relatively high temperature. Nevertheless, despite having a molecular weight (390.30 g/mol) comparable to that of PYMA, the weaker intermolecular interactions result in a slightly lower thermal stability and melting point.

In contrast, FBMA contains a benzonitrile core where two Meldrum's acid rings are attached at the para position. The nitrile group, is a strong electron-withdrawing group (EWG), making the molecule have a higher dipole moment and molecular polarity (Schulz et al., 2011). However, the uneven charge distribution in aromatic ring reduces the structural symmetry weaken crystal packing efficiency. This means the uneven charge resulting asymmetric or electronically unbalanced molecules, which tend to form less ordered crystals and therefore melt at lower temperatures. Thus, resulting lower melting point (185 °C) despite a higher molecular weight (401.37 g/mol).

Lastly, THMA, is only mono-substituted Meldrum's acid derivative, exhibited the lowest melting point (177 °C). Its relatively low molecular weight (238.35 g/mol), asymmetric molecular structure containing only one Meldrum's acid unit and reduced molecular rigidity contribute to weaker intermolecular interactions and poorer crystal packing efficiency. The sulphur atom in 2-thiophene is less electronegative than oxygen or nitrogen, so it forms weaker dipole interactions. The molecule is also slightly less planar, which reduces the ability of the molecules to stack efficiently in the solid state. These factors lead to weaker intermolecular forces and lower thermal stability.

In summary, the observed melting point (PYMA > TOMA > FBMA > THMA) is influenced not only by molecular mass and electronic effects but more critically by symmetry, polarity and the ability to form strong intermolecular interactions. These structural features collectively show how efficiently molecules pack in the solid state, directly affecting thermal behaviour and melting points.

Table 4.2
Melting Point Data

Compound	Molecular weight (g/mol)	Melting point (°C)
TOMA	390.37	212-214
FBMA	401.37	185-187
PYMA	377.35	225-227
THMA	238.35	177-179

4.2.1.2 Elemental Analysis

In general, the experimental results of elemental analysis show excellent agreement with the theoretical values, confirming that the compounds were successfully synthesised with high purity (Figure 4.3). This agreement supports the accuracy of the synthetic procedure and the reliability of the purification and drying processes.

Among the four compounds, PYMA shows the largest deviation, with the carbon content slightly lower (−0.65%) and oxygen content slightly higher (+0.64%) than the theoretical values. These differences exceed the acceptable range and may be attributed to several factors. One possible reason is the presence of trace solvent residues or moisture absorbed during drying or weighing. Even a small amount of residual water can increase the measured oxygen content, thus affecting the overall elemental balance. Another contributing factor could be incomplete combustion of the sample during elemental analysis, leading to minor underestimation of carbon. Additionally, experimental factors such as instrumental sensitivity or slight contamination of the sample holder can cause variations in measured values (Serpini et al., 2021). For the other compounds FBMA, TOMA and THMA the elemental composition matches closely with the calculated values, showing deviations well within the ±0.4% limit. This strong correlation demonstrates that these compounds were synthesised successfully and that their structures correspond to the expected molecular formulas. THMA, which contains a sulphur atom, shows an excellent match between theoretical and experimental sulphur percentages (13.49 % theoretical vs 13.45 % experimental), confirming the presence of the 2-thiophene moiety in the product.

Overall, the CHNSO elemental analysis validates the formation of the intended Meldrum's acid derivatives and confirms their chemical structures. The results indicate that the synthesis reactions proceeded efficiently, yielding products of high purity and correct elemental composition. The slight inconsistency observed for PYMA are minor and do not significantly affect the overall confirmation of compound identity. These findings are consistent with the expected molecular structures and support further spectroscopic analyses such as FTIR and NMR for structural verification.

Table 4.3
Elemental Analyzer Results

Compound	Element percentage (%)				
	% C	% H	% N	% O	% S
FBMA	59.85 (59.65)	4.77 (4.75)	3.49 (3.43)	31.89 (32.17)	-
TOMA	61.53 (61.53)	5.68 (5.68)	-	32.78 (32.78)	-
THMA	55.45 (55.14)	4.23 (4.18)	-	26.86 (27.17)	13.45 (13.49)
PYMA	57.29 (56.64)	5.08 (5.10)	3.71 (3.70)	33.92 (34.56)	-

Note: ( ) Actual value

4.2.2 Attenuated Total Reflectance - Fourier Transform Infrared (ATR-FTIR) Analysis

One method used to validate the success of the synthesis was Attenuated Total Reflectance - Fourier Transform Infrared (ATR-FTIR) spectroscopy. This technique enables the identification of functional groups by analyzing characteristics stretching bands, thereby confirming the formation of the desired compound and the presence of key chemical structures (Cunha and Santana, 2012). The synthesis of Meldrum's acid derivatives was confirmed, by comparing the starting raw material of Meldrum's acid (MA), 4-formylbenzonitrile (FBN), *p*-tolualdehyde (TOLA), 4-pyridinecarboxyaldehyde (PYCA) and 2-thiophenecarboxyaldehyde (THCA) with the final products which are FBMA, TOMA, THMA and PYMA.

The significant functional group frequencies considered in this study include the carbonyl stretching vibration, ν(C=O), which typically appears in the range of 1600–1800 cm^{-1} (Toledo et al., 2015). In addition, the stretching vibration of ν(C–O), is usually observed within the 1000–1300 cm^{-1} region. The presence of cyanide groups can be confirmed by the characteristic ν(C≡N) absorption band appearing around 2100–2250 cm^{-1}. Aromatic carbons, ν(C=C) vibrations are generally detected in the range of 1400–1600 cm^{-1}, indicating the presence of aromatic ring. Furthermore, the ν(C–S) vibration commonly occurs at lower frequencies, typically between 600–800 cm^{-1}, confirming the incorporation of sulfur-containing functional groups in the molecular structure (Silverstein et al., 2014). Since Meldrum's acid is the main compound in this study, its spectrum is discussed first. The spectrum shows two distinct carbonyl

stretching vibration bands, ν(C=O) appeared in 1749 and 1790 cm^{-1} which are characteristic of the two carbonyl groups presented in Meldrum acid structure. Additionally, an absorption band observed at 1303 cm^{-1} corresponds to the ν(C-O) stretching vibration. The presence of these key functional group frequencies confirms the identification and structure of Meldrum's acid used as starting material in this study (Adnan et al., 2021; Dey et al., 2015).

Figure 4.4 illustrates the ATR-FTIR spectrum of FBMA, As the features of Meldrum's acid have been discussed on previous section, the focus is now directed towards the second starting material, formylbenzonitrile (FBN). The spectrum of FBN displays two major diagnostic absorption bands. The sharp band observed at 2230 cm^{-1} is attributed to the ν(CN) vibration of nitrile group, while a strong vibration band at 1704 cm^{-1} correspond to the ν(C=O) of the carbonyl group. These characteristic bands confirm the presence and identity of formylbenzonitrile. For the synthesized FBMA compound, three major functional groups are observed, confirming that the reaction between Meldrum's acid and formylbenzonitrile was successfully achieved (Adnan et al., 2021; Dey et al., 2015). The absorption band at 2230 cm^{-1} confirms the presence of the ν(CN) cyanide group from formylbenzonitrile. Meanwhile, the two strong carbonyl stretching bands, ν(C=O) in 1770 and 1734 cm^{-1} indicate the retention of carbonyl groups from Meldrum's acid. In addition, the ν(C-O) vibration observed at 1317 cm^{-1} further supports the formation of the FBMA (Toledo et al., 2015). Based on these characteristic ATR-FTIR absorption bands, it can be concluded that FBMA was successfully synthesized.

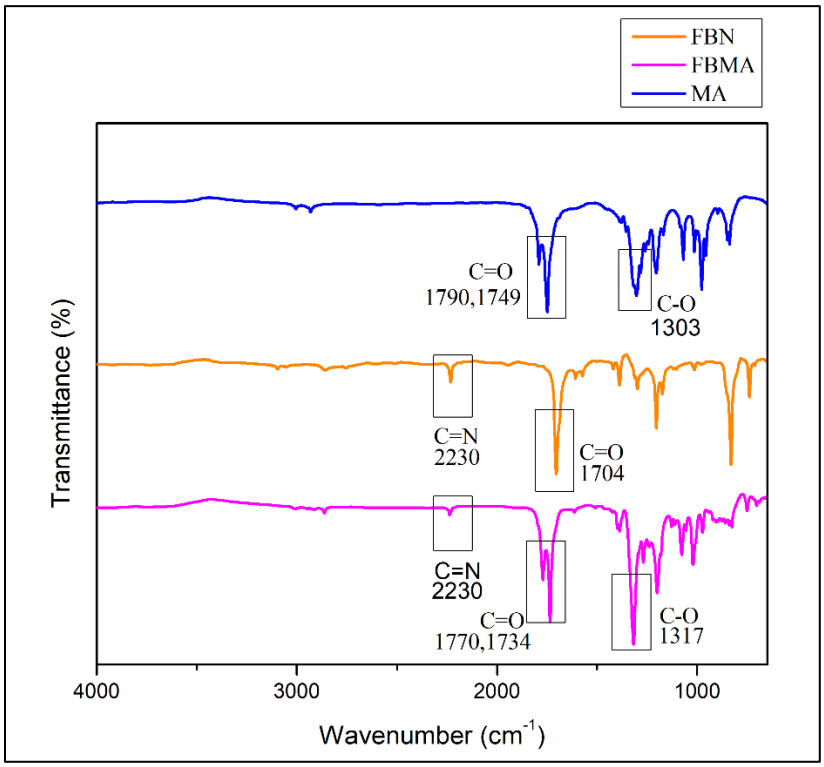


Figure 4.4ATR-FTIR Spectrum of FBMA

Figure 4.5 also illustrates the ATR-FTIR spectrum of TOMA, where tolualdehyde (TOLA) was used as the starting material. The ATR-FTIR spectrum of TOLA displays two prominent absorption bands a carbonyl stretching vibration, ν(C=O), at 1702 cm^{-1} (Silverstein et al., 2014) and a characteristic aromatic C=C stretching vibration at 1650 cm^{-1}, confirming the identity of *p*-tolualdehyde. In the ATR-FTIR spectrum of the synthesized TOMA compound, 2 important absorption bands were observed (Silverstein et al., 2014). The carbonyl stretching vibration at 1730 cm^{-1} and the C–O stretching vibration at 1311 cm^{-1} indicate that the Meldrum's acid structure remains intact after the reaction.

Notably, the original aromatic C=C stretching band of TOLA at 1650 cm^{-1} is no longer distinctly resolved in TOMA. Instead, it overlaps with the newly formed, highly conjugated alkenic C=C linker generated from the condensation (Dey et al., 2015). This broad overlap occurs because both the aromatic and the new alkene double bonds vibrate within the same spectral window. Furthermore, the extended electron delocalization across the aromatic ring, the new alkene linker and the carbonyls of the Meldrum's acid moiety increases the single-bond character of these double bonds. Consequently, this strong resonance stabilization causes the combined C=C absorption bands to merge, broaden and shift to a lower wavenumber (Toledo et al., 2015).

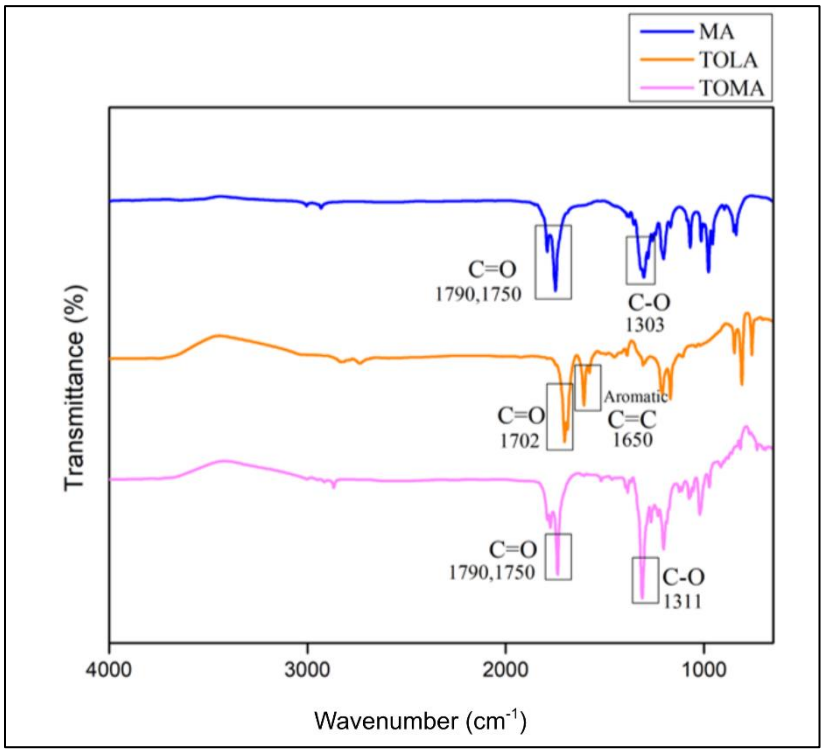


Figure 4.5 ATR-FTIR Spectrum of TOMA

The ATR-FTIR spectrum of THMA consists of characteristic features both Meldrum's acid and 2-thiophenecarboxyaldehyde (THCA). The spectrum of THCA shows two important absorption bands, 1672 cm^{-1}, indicating the presence of an aldehyde carbonyl group ν(C=O) (Silverstein et al., 2014) and a band at 863 cm^{-1} corresponding to the ν(C-S) vibration of the thiophne ring. These bands confirm the identity of the 2-thiophenecarboxyaldeyhde. In the spectrum of THMA, the presence of ν(C=O) vibration at 1713 cm^{-1} and ν(C-S) vibration observed at 866 cm^{-1} confirms the incorporation of 2-thiophenecarboxyaldehyde unit (Toledo et al., 2015). The presence of these three key absorption bands indicates that THMA was successfully synthesized.

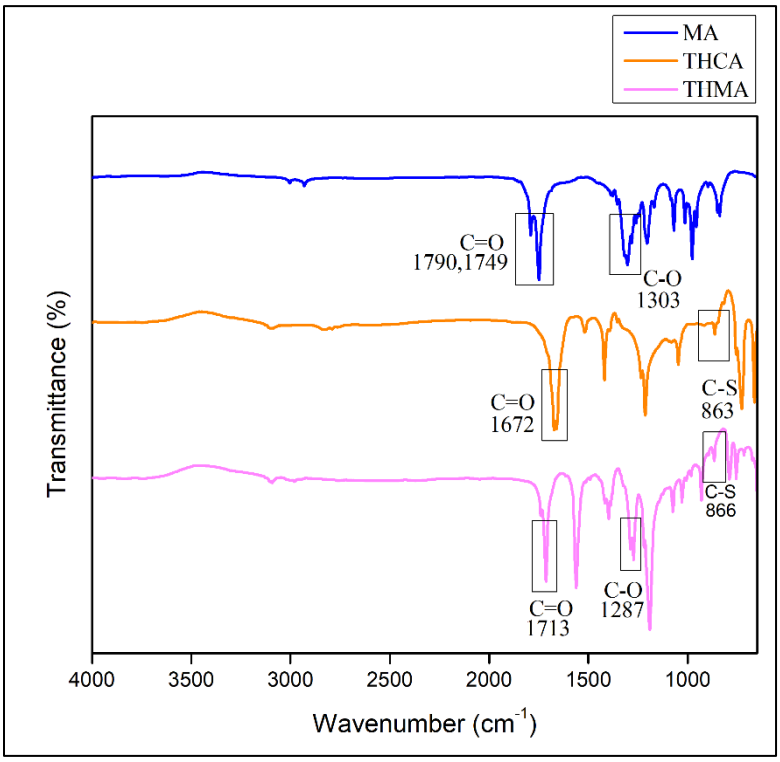


Figure 4.6ATR-FTIR Spectrum of THMA

The final ATR-FTIR spectrum corresponds to the reaction between Meldrum's acid and 4-pyridinecarboxyaldehyde (PYCA). PYCA contains both an aldehyde carbonyl, ν(C=O) and ν(C=N) groups within the pyridine ring. These functional groups were clearly observed in the spectrum of the raw material, with the ν(C=O) vibration band appeared at 1712 cm^{-1} and the ν(C=N) ring vibration observed at 1565 cm^{-1} confirming the identity of the compound (Silverstein et al., 2014), There are three key absorption bands are presented in the structure of PYMA. The ν(C=O) and ν(C-O) vibrations appeared at 1740 cm^{-1} and 1336 cm^{-1}, respectively confirm the presence of the Meldrum's acid moiety. Meanwhile, the ν(C=N) vibration at 1559 cm^{-1} confirms the incorporation of the pyridinecarboxaldehyde unit. These characteristic bands demonstrate that PYMA was successfully synthesized.

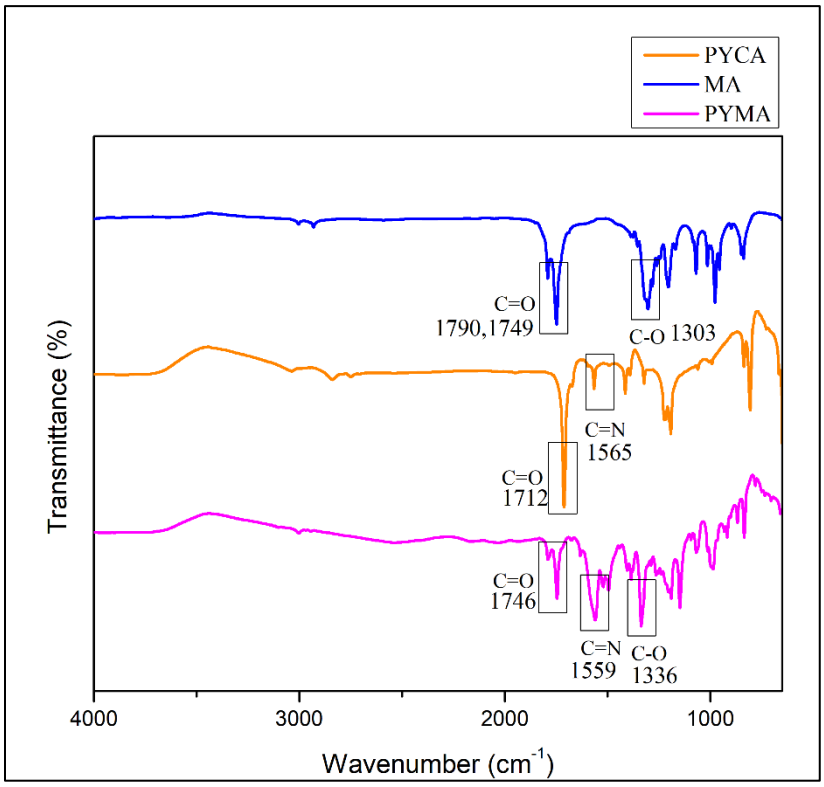


Figure 4.7 ATR-FTIR Spectrum of PYMA

The observed shifting of the C=O and C–O stretching bands in the FTIR spectra after synthesis indicates a change in the electronic environment of the Meldrum's acid (Toledo et al., 2015). In the parent Meldrum's acid, the carbonyl groups typically appear at higher wavenumbers due to their non-conjugated nature. However, after formation of the derivative, the carbonyl groups become conjugated with the newly formed C=C bond and/or aromatic ring system, resulting in increased electron delocalization. This conjugation reduces the effective bond order of the C=O bond, leading to a shift toward lower wavenumbers (Dey et al., 2015). Additionally, redistribution of electron density within the dioxane ring alters the C–O stretching frequency. These spectral changes confirm successful structural modification and formation of the intended Meldrum's acid derivative.

Table 4.4
Assignment and Comparison of ATR-FTIR Stretching Bands

Compounds	Wavenumber (cm^{-1})				
	ν(C=O)	ν(C-O)	ν(C=C) (ar)	ν(CN)	ν(C-S)
Meldrum's acid (MA)	1790, 1749	1303	-	-	-
4-formylbenzonitrile	1704	-	-	2230	-
p-Tolualdehyde	1702	-	1650	-	-
2-Thiophenecarboxyaldehyde	1672	-	-	-	863
4-Pyridinecarboxyaldehyde	1712	-	-	1565	-
FBMA	1770,1734	1317	-	2230	-
TOMA	1758, 1730	1311	-	-	-
THMA	1713, 1736	1287	-	-	866
PYMA	1746, 1734	1336	-	1559	-

4.2.3 Nuclear Magnetic Resonance (NMR) Analysis

4.2.3.1 ^{1}H and ^{13}C NMR

To confirm the structural of the synthesized compounds, both ^{1}H and ^{13}C NMR analysis were carried out in DMSO-d_6. Each spectrum exhibited distinct characteristic peaks that correspond well with the proposed molecular structures, confirming the presence of the expected functional groups and chemical environments.

The ^{1}H NMR spectrum (600 MHz) of the synthesized compound (Figure 4.8 and Table 4.5) is consistent with the proposed TOMA structure ($C_{20}H_{22}O_8$). Two aromatic doublets at 8.01- 7.98 ppm and 7.35-7.33 ppm (each integrating to 2H, $J \approx 8$ Hz) confirm the presence of a para-substituted benzene ring (Adnan et al., 2021; Dey et al., 2015). A singlet at δ 2.10 ppm (3H) corresponds to the aromatic methyl group. The central benzylic methine proton appears at 4.03 ppm as an apparent doublet integrating to one proton, likely due to weak vicinal coupling within the rigid bis-Meldrum. The adjacent methine protons resonate at δ 2.51–2.40 ppm as a triplet (2H) due to complex coupling within the rigid cyclic framework. A strong singlet at δ 1.75–1.71 ppm integrating to 12H is assigned to the four-equivalent gem-dimethyl groups of the two Meldrum's acid moieties, indicating molecular symmetry. The total integration of 22 protons matches the molecular formula, thereby confirming the structural integrity of the synthesized *bis*-Meldrum's acid derivative (Adnan et al., 2021; Dey et al., 2015).

^{13}C NMR spectrum of TOMA signals at 163.2 ppm correspond to the carbonyl carbons of the Meldrum's acid units, while the aromatic carbons of the *p*-tolyl ring

resonate in the range of 106.0–133.0 ppm, reflecting substitution and conjugation effects. The quaternary carbons of the $C(CH_3)_2$ groups were observed at 104.9 ppm and the acetal carbons (O–C–O) of the Meldrum's acid ring appear at 53.4 ppm (Dey et al., 2015). The gem-dimethyl methyl carbons resonate at 31.0–32.0 ppm, whereas the aromatic methyl carbon is detected at 21.8 ppm. The benzylic methine carbon connecting the aromatic ring to the Meldrum's acid units is observed at 27.4 ppm, confirming the successful formation of TOMA. Figure 4.9 and Table 4.6 present the representative ^{13}C NMR spectrum and carbon signal assignments of TOMA, respectively (Dey et al., 2015).

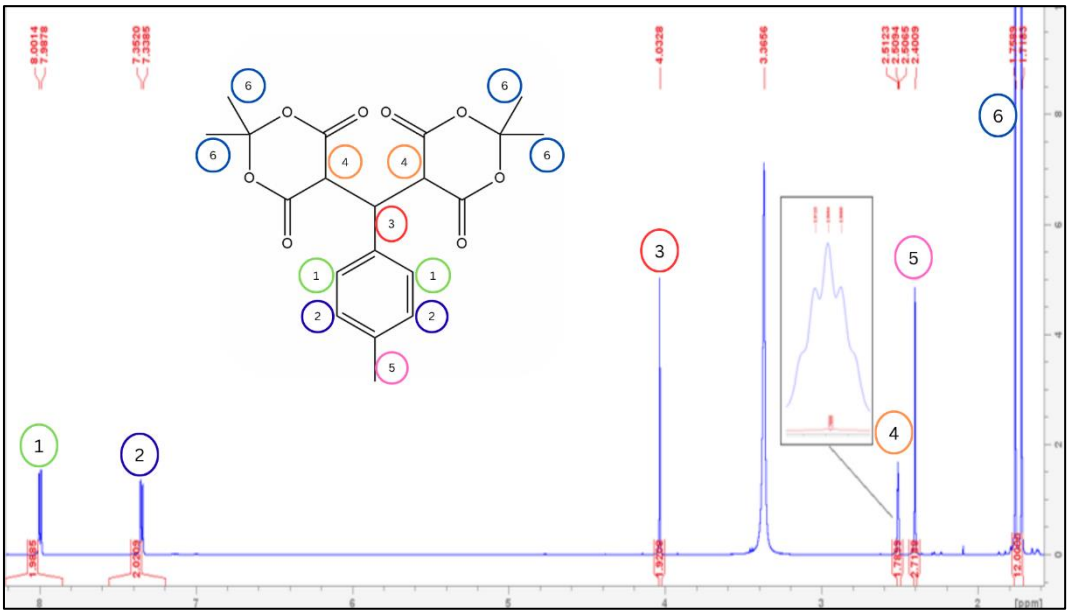


Figure 4.8 ^{1}H NMR Spectrum Analysis of TOMA

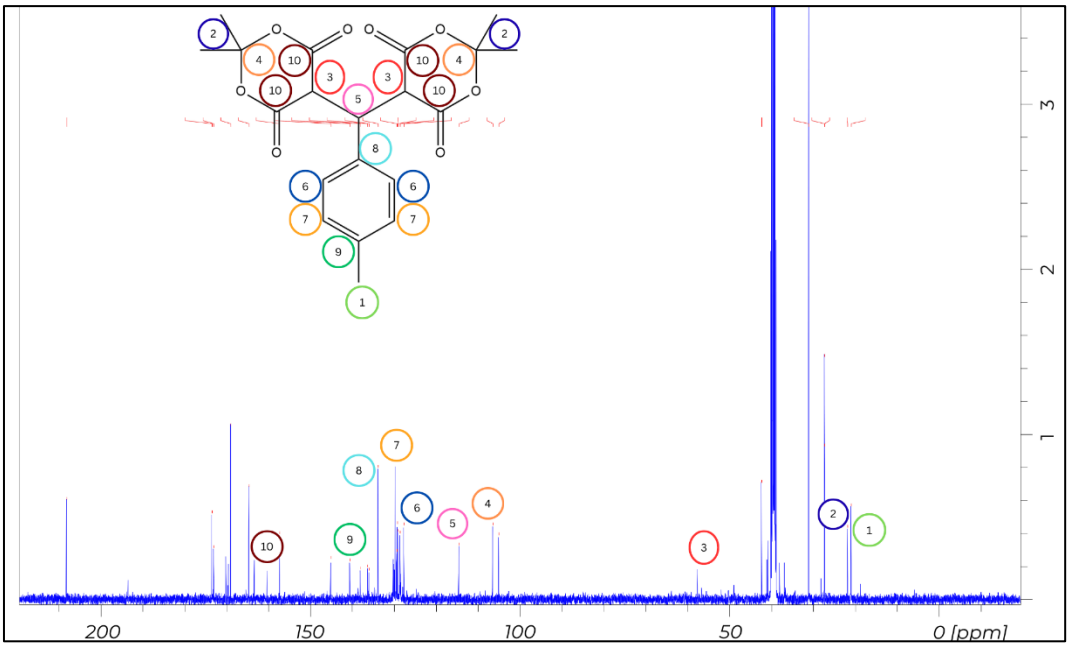


Figure 4.9 ^{13}C NMR Spectrum Analysis of TOMA

Table 4.5
^{1}H NMR Data of TOMA

No.	Fragment	No. of H	Multiplicity	δ (ppm)
1	Aromatic (ortho to benzylic carbon)	2	Doublet	8.07–7.98
2	Aromatic (meta)	2	Doublet	7.35 -7.33
3	CH–CH–CH (benzylic bridge)	2	Doublet	4.03
4	CH–CH–CH (benzylic bridge)	1	Triplet	2.51–2.40
5	Ar–CH_3	3	Singlet	2.10
6	$C(CH_3)_2$	12	Singlet	1.75 -1.71

Table 4.6
^{13}C NMR Data of TOMA

No.	Fragment	Carbon type	No. of C	δ (ppm)	Assignment
1	Ar–**C**H$_3$	Methyl C (aryl)	1	21.8	*p*-tolyl methyl carbon
2	**C**H$_3$ (gem)	Methyl C	4	27.4	Gem-dimethyl methyl carbons
3	O=**C**–O	Acetal C	2	53.4	Acetal carbons of Meldrum's acid ring
4	**C**(CH$_3$)$_2$	Quaternary C	2	105.3	Quaternary carbons of Meldrum's acid
5	CH-**C**H-CH	Quaternary C	1	111.9	Quaternary carbons of Meldrum's acid
6	Aromatic **C**	Aromatic CH	2	128.0	Conjugated aromatic carbons
7	Aromatic **C**	Aromatic CH	2	129.0	Electron-rich aromatic carbons
8	Bridge–**C**–(benzene)	Aromatic C-CH	1	135.5	Aromatic carbon
9	Benzene–**C**–CH$_3$	Quaternary aromatic C	1	138.0	Substituted aromatic carbon
10	O=**C**– (Meldrum's acid)	Carbonyl C	4	163.2	Meldrum's acid carbonyl carbons

The ^{1}H and ^{13}C NMR spectra of FBMA also support the expected bis-Meldrum's acid structure. The ^{1}H NMR spectrum (600 MHz, DMSO-d$_6$) of the FBMA agrees well with the proposed structure. Two doublets at 7.69–7.51 ppm (4H) confirm the presence of a para-substituted benzene ring and the slightly downfield position is due to the electron-withdrawing cyano (–C≡N) group (Bukhari et al., 2023). The central benzylic methine proton appears at 4.00 ppm as a singlet integrating to one proton. Although splitting might be expected, the rigid structure and the strong electron-withdrawing effects of the nitrile and carbonyl groups reduce the coupling, so the peak appears as a triplet. The two methine protons next to the Meldrum's acid rings appear as a singlet at 2.50 ppm (2H) because of complex interactions within the rigid framework. A strong singlet at 1.77 ppm (12H) corresponds to the four equivalent methyl groups of the two Meldrum's acid units. The total integration of 19 protons matches the molecular formula, confirming the structure of the synthesized compound.

In the ^{13}C NMR spectrum, confirms the structure of the carbonyl carbons of the Meldrum's acid units resonate at 164.6 ppm, corresponding to four C=O groups. The quaternary aromatic carbon of the para-substituted benzene ring appears at 159.5 ppm, while other aromatic carbons are observed at 131.8 and 129.0 ppm. The presence of the

cyano substituent is confirmed by the nitrile carbon signal at 118.0 ppm, with the adjacent aromatic carbon appearing at 106.2 ppm. The quaternary carbons of the $C(CH_3)_2$ groups resonate at 105.6 ppm and the secondary carbons adjacent to the carbonyl groups appear at 58.73 ppm. The gem-dimethyl methyl carbons are observed at 31.1 ppm. Collectively, the ^1H and ^{13}C NMR data confirm the successful formation of FBMA with two Meldrum's acid units symmetrically linked through a benzylic bridge to a para-cyanophenyl ring (Bukhari et al., 2023). Figures 4.10 and 4.11 present the representative ^1H and ^{13}C NMR spectra of FBMA, respectively, while Tables 4.7 and 4.8 provide the corresponding proton and carbon signal assignments, respectively.

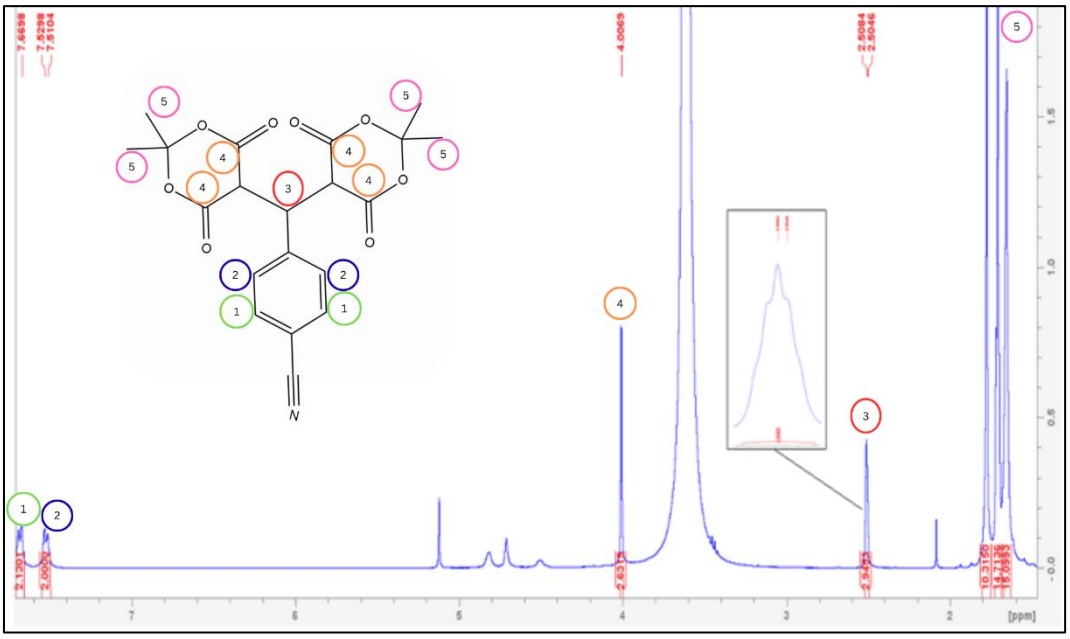


Figure 4.10 ^1H NMR Spectrum Analysis of FBMA

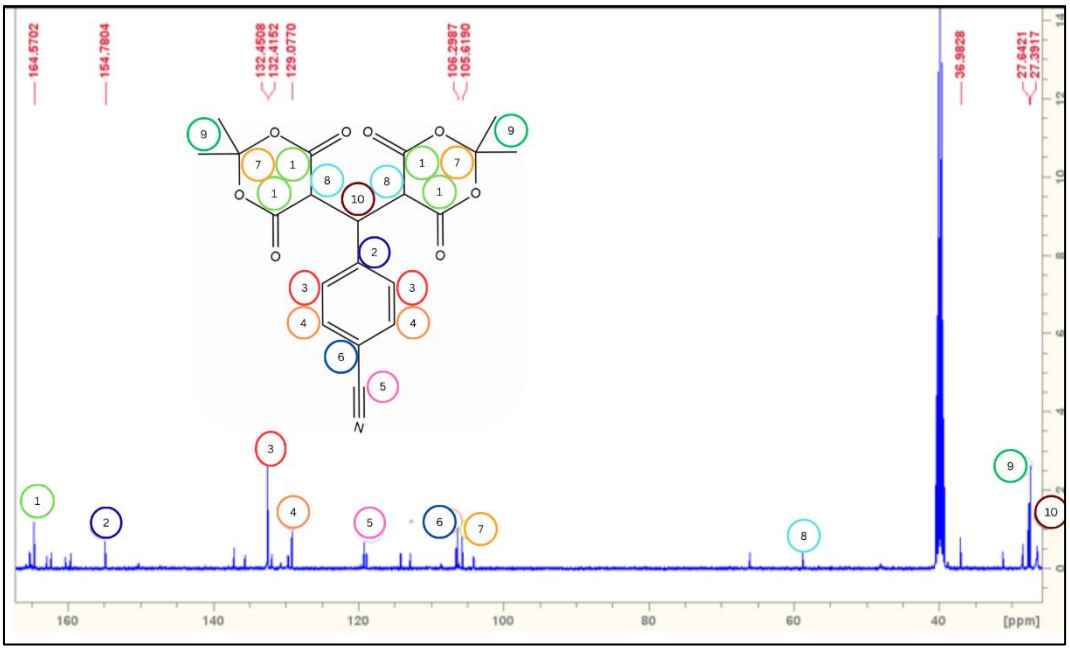


Figure 4.11 ^{13}C NMR Spectrum Analysis of FBMA

Table 4.7
^{1}H NMR Data of FBMA

No	Fragment	No. of H	Multiplicity	δ (ppm)
1	Pyridine aromatic protons ortho to CN	2	Doublet	7.68 -7.66
2	Pyridine aromatic proton	2	Doublet	7.52 -7.51
3	CH-CH-CH	1	Triplet	4.00
4	CH-CH-CH	2	Singlet	2.50
5	$C(CH_3)_2$	12	Singlet	1.70

Table 4.8
^{13}C NMR Data of FBMA

No	Fragment (formula)	Carbon type	No. of C	δ (ppm)	Assignment
1	O=C– (two per Meldrum ring)	Carbonyl C	4	164.6	Meldrum's acid carbonyl carbons
2	Aromatic–C– (bridge)	Quaternary aromatic C	1	159.5	Para-substituted aromatic carbon
3	Aromatic–CH near bridge	Aromatic CH	2	131.8	Aromatic carbons
4	Aromatic–CH near CN	Aromatic CH	2	129.0	Aromatic carbons
5	C≡N	Nitrile C	1	118.0	Benzonitrile carbon
6	Aromatic–C–CN	Aromatic C	1	106.2	Aromatic carbon bonded to CN
7	$C(CH_3)_2$	Quaternary C	2	105.6	Quaternary carbons of Meldrum's acid
8	–CH–C=O	Secondary C	2	58.73	Carbon adjacent to carbonyl
9	CH_3 (gem)	Methyl C	4	31.1	Gem-dimethyl methyl carbons
10	Aromatic-CH-	Bridge from aromatic	1	27.4	Bridge from aromatic

The ^{1}H NMR spectrum of THMA ($C_{11}H_{10}O_4S$) in DMSO-d_6 shows a singlet at 1.68 ppm integrating to six protons, corresponding to the gem-dimethyl groups of the Meldrum's acid moiety. In the downfield region, four distinct signals are observed between 8.65–7.34 ppm, assigned to three 2-thiophene protons and one exocyclic vinylic proton. The most deshielded signal at 8.65–8.61 ppm (1H) is attributed to the 2-thiophene proton adjacent to the sulfur atom, reflecting strong deshielding effects from the heteroatom and conjugation (Dey et al., 2015; Bukhari et al., 2023). The remaining 2-thiophene protons appear at 8.32–8.30 ppm doublet, 8.17–8.16 ppm as dtriplets due to typical vicinal coupling within the heteroaromatic ring. The exocyclic vinylic proton resonates at 7.37–7.34 ppm as a singlet, consistent with conjugation to the adjacent carbonyl groups and the thiophene ring. The overall integration of ten protons matches the molecular formula, confirming the proposed structure of THMA.

The ^{13}C NMR spectrum of THMA exhibits two carbonyl signals at 163.4 ppm corresponding to the ester carbonyl carbons of the Meldrum unit. Aromatic and vinylic carbons of the thiophene alkene system appear between 149.1–129.3 ppm, reflecting conjugation with the heteroaromatic ring and carbonyl groups. The characteristic acetal carbon of the Meldrum's acid ring is observed at 107.3 ppm, while the exocyclic alkene carbon resonates at 105.1 ppm (Adnan et al., 2021; Dey et al., 2015). The gem-dimethyl carbons appear at 27.3 ppm. The total number of carbon signals observed is consistent

with the eleven carbons in the molecular formula $C_{11}H_{10}O_4S$, supporting successful formation of the target compound. Figures 4.12 and 4.13 present the representative ^{1}H and ^{13}C NMR spectra of THMA, respectively, while Tables 4.9 and 4.10 provide the corresponding proton and carbon signal assignments, respectively.

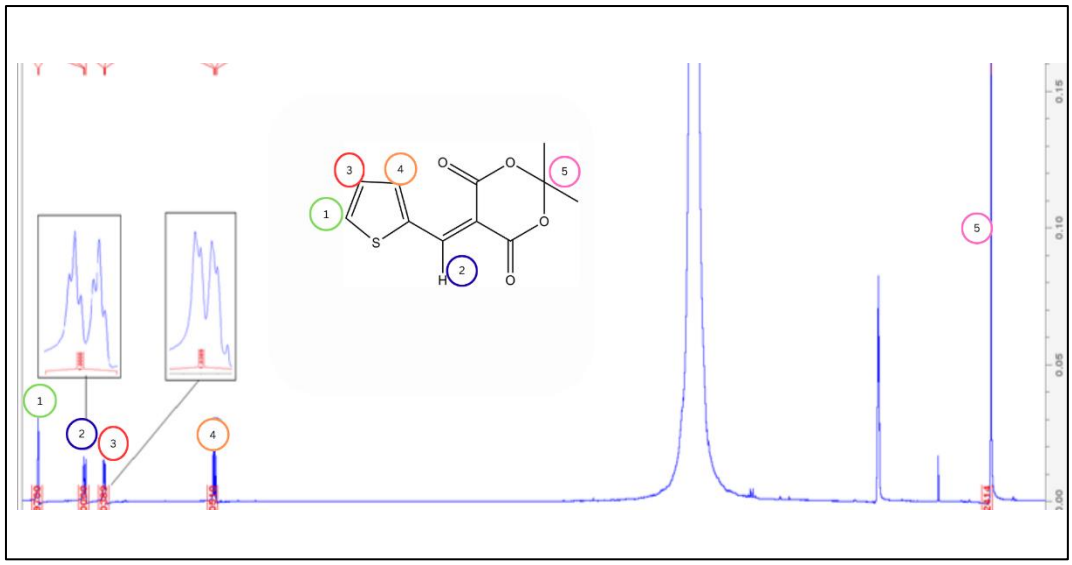


Figure 4.12 ^{1}H NMR Spectrum Analysis of THMA

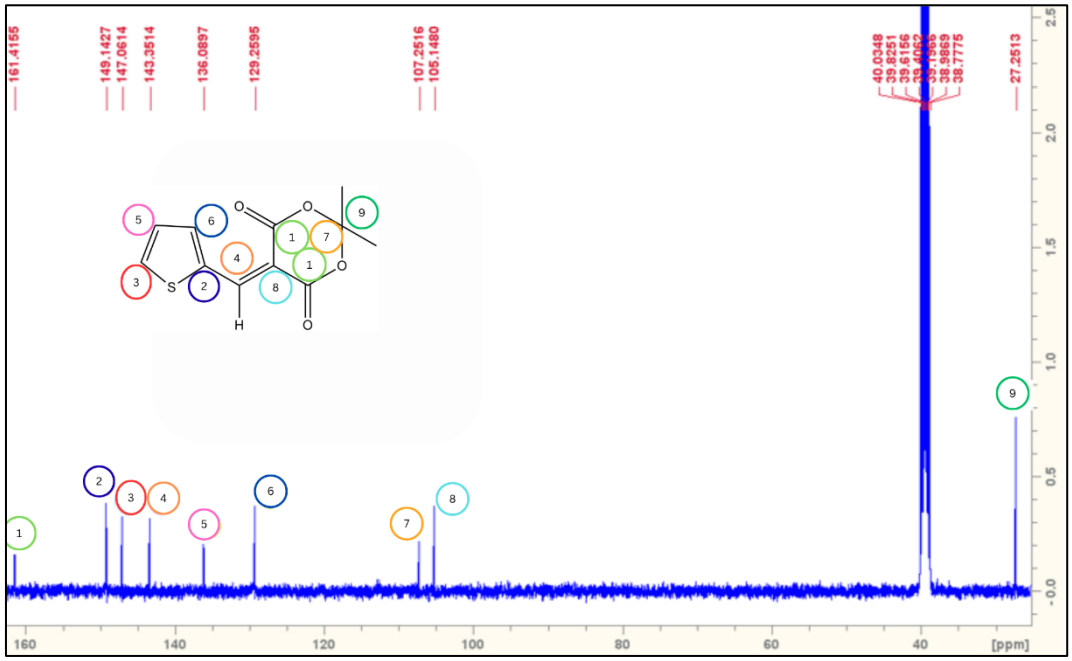


Figure 4.13 ^{13}C NMR Spectrum Analysis of THMA

Table 4.9
^{1}H NMR Data of THMA

No	Fragment	No. of H	Multiplicity	δ (ppm)
1	Thiophene–**H** (Ar), Near S	1	Doublet	8.65 -8.61
2	Thiophene proton	1	Doublet	8.32–8.30
3	Thiophene proton	1	Triplet	8.17–8.16
4	Vinylic H (C=C**H**–)	1	Singlet	7.37-7.35
5	$C(CH_3)_2$	6	Singlet	1.68

Table 4.10
^{13}C NMR Data of THMA

No	Fragment	Carbon type	No. of C	δ (ppm)	Assignment
1	O=C– (dioxane)	C=O	2	163.4	Carbonyls of dioxane ring
2	Thiophene C=C	Quaternary C	1	149.1	thiophene carbons
3	Thiophene-C-S	Quaternary C	1	147.3	Thiophene carbon adjacent to sulfur
4	(C=C–H)	Tertiary C	1	143.2	Exocyclic alkene carbon bearing proton
5	Thiophene-C-C	Aromatic	1	136.1	Thiophene protonated carbon
6	Thiophene-C-C	Aromatic	1	129.3	Thiophene protonated carbon
7	CH-CH	Quaternary C	1	107.3	Exocyclic alkene carbon attached to Meldrum
8	$C(CH_3)_2$ (quaternary)	Quaternary C	1	105.1	Gem dimethyl quaternary
9	$(CH_3)_2$	Methyl C	2	27.25	Gem-dimethyl methyls

The ^{1}H NMR spectrum of the PYMA ($C_{18}H_{19}NO_8$) confirms the proposed structure. The aromatic region between 7.42–7.37 ppm corresponds to four pyridine protons, with the most downfield signal at 7.35 -7.32 ppm assigned to the proton ortho to the nitrogen atom due to strong deshielding. The remaining pyridine protons appear as overlapping singlet because of ortho and meta coupling interactions within the heteroaromatic ring (Dey et al., 2015). The central benzylic methine proton is observed at 4.75 ppm as a singlet integrating to one proton, although coupling with adjacent methine protons is expected, the rigid *bis*-Meldrum framework and electron-withdrawing carbonyl groups reduce the coupling constant, resulting in unresolved splitting. The two methine protons adjacent to the Meldrum's acid units appear as a triplet at 2.60–2.45 ppm due to complex coupling effects (Adnan et al., 2021). A strong singlet at 2.10 ppm integrating to 12 protons corresponds to the four-equivalent gem-

dimethyl groups of the two Meldrum's units. The total integration of 19 protons matches the molecular formula, confirming successful formation of the target compound.

The ^{13}C NMR spectrum Meldrum's acid carbonyl carbons appear at 172.9 ppm, while the pyridine carbons resonate at 165.0 ppm (carbon adjacent to the bridge), 150.0 ppm (carbons near nitrogen) and 124.2 ppm (opposite pyridine carbons). The quaternary carbons of the gem-dimethyl groups appear at 102.5 ppm, with the corresponding methyl carbons at 32.7 ppm. The methylene carbons adjacent to carbonyls resonate at 27.0 ppm and the methine bridge carbon linking the pyridine ring to the Meldrum's acid units was observed at 27.3 ppm. These chemical shifts collectively confirm the successful formation of PYMA and are fully consistent with the expected bis-Meldrum's acid structure (Adnan et al., 2021; Dey et al., 2015; Bukhari et al., 2023). Figures 4.14 and 4.15 present the representative ^{1}H and ^{13}C NMR spectra of TOMA, respectively, while Tables 4.11 and 4.12 provide the corresponding proton and carbon signal assignments, respectively.

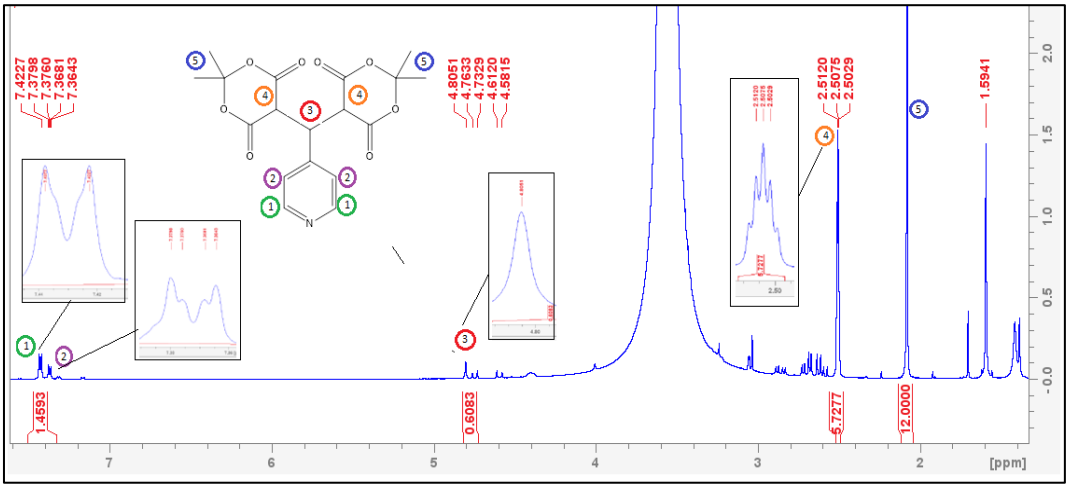


Figure 4.14 ^{1}H NMR Spectrum Analysis of PYMA

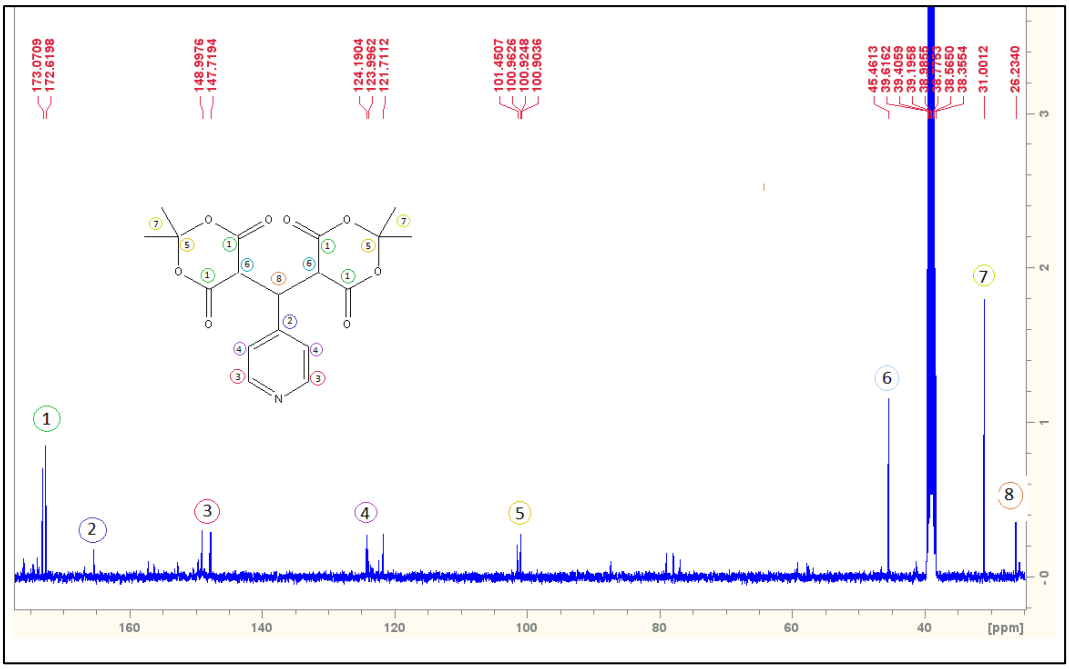


Figure 4.15 ^{13}C NMR Spectrum Analysis of PYMA

Table 4.11
^{1}H NMR Data of PYMA

No	Fragment	No. of H	Multiplicity	δ (ppm)
1	Pyridine–H near N	2	Doublet	7.42 -7.37
2	Pyridine–H near bridge	2	Doublet	7.35-7.32
3	Pyridine–CH–C(Meldrum)	1	Triplet	4.76
4	–CH–C=O	2	Singlet	2.60-2.45
5	$C(CH_3)_2$ (Meldrum)	12	Singlet	2.10

Table 4.12
^{13}C NMR Data of PYMA

No	Fragment	Carbon type	No. of C	δ (ppm)	Assignment
1	O=C– (Meldrum)	Carbonyl C	4	172.9	Carbonyl carbons of Meldrum rings
2	Pyridine C–CH	Quaternary aromatic C	1	165.0	Pyridine carbon adjacent to methine bridge
3	Pyridine C near N	Aromatic C	2	150.0	Pyridine carbons adjacent to N atom
4	Pyridine C near C	Aromatic C	2	124.2	Pyridine carbons opposite N
5	$C(CH_3)_2$	Quaternary C	2	102.5	Quaternary carbons of gem-dimethyl in Meldrum rings
6	–CH–C=O	Methine C	2	45.0	Carbons adjacent to Meldrum carbonyl
7	CH_3 (gem)	Methyl C	4	32.7	Methyl carbons of gem-dimethyl
8	Methine bridge	Methine C	1	27.3	Carbon linking pyridine to Meldrum units

4.2.4 Single Crystal X-ray Diffraction

Single crystal X-ray diffraction is determining the three-dimensional structure of molecules as it meets three key requirements which are (i) precisely determining the position of atoms even in large molecules, (ii) differentiating between different types of atoms and (iii) presenting views of the molecule from various directions. This approach reveals the molecular structure, including chirality, which is essential for explaining the behaviour of molecules. Moreover, XRD helps determine the molecular arrangement in crystals, which may differ depending on the crystallization conditions and affect characteristics like solubility and melting point (Gokhale & Mantri, 2017).

XRD analysis was used to reveal the structures of FBMA, TOMA and THMA using single crystals that were suitable. Acetonitrile solution kept at room temperature was slowly evaporated to produce white block crystals of FBMA, TOMA and yellow crystalline for THMA. Table 4.13 presents the crystallographic data and extensive structure refinement, including complete parameters significant to the symmetry and unit cell of each molecule. The FBMA, TOMA and THMA structures are represented using ORTEP (Oak Ridge Thermal Ellipsoid Plot) in Figure 4.16, Figure 4.17 and Figure 4.18, which use thermal ellipsoid representations to show atomic positions. These findings offer information about the molecular geometry and the implication for the compounds' corrosion-inhibiting and reactivity properties.

Table 4.13 shows the FBMA crystal has three molecules per unit cell and is categorised under the monoclinic $P2_1/c$ space group. Its lattice dimensions are a = 7.4605(3) Å, b = 10.9341(3) Å and c = 23.4696(9) Å and its unit cell parameters β = 97.448(2)°, A prominent Structurally, the FBMA molecule adopts a non-planar conformation due to the presence of bulky Meldrum's acid units, which induce steric hindrance and torsional distortion relative to the aromatic core. The aromatic ring exhibits typical C–C bond lengths in the range of 1.38–1.39 Å, confirming its aromatic character. The nitrile group is clearly identified by the short N≡C bond length of approximately 1.13 Å, indicative of a strong triple bond and significant electron-withdrawing character. This electron-withdrawing nature plays an important role in modulating the electronic distribution within the molecule, which is relevant to its adsorption behaviour.

The Meldrum's acid moieties are characterized by carbonyl C=O bond lengths ranging from 1.19 to 1.20 Å, consistent with highly polarized carbonyl groups. These

oxygen atoms act as potential electron-rich sites capable of interacting with metal surfaces through electrostatic attraction or donor–acceptor interactions. Figure 4.19 illustrate that the crystal packing of FBMA is stabilised by several weak but significant intramolecular hydrogen bonding interactions, primarily of the C–H···O and C–H···N type. Notably, intramolecular C7–H7···O8 and C8–H8···O7 hydrogen bonds are observed between hydrogen atoms of the aliphatic carbon framework and the carbonyl oxygen atoms of the Meldrum's acid moieties (Brosge et al., 2021).

In addition, a C13–H13···O5 interaction is formed between the hydrogen atom attached to the central carbon and a carbonyl oxygen atom, contributing to the conformational stabilization of the molecule. A further intramolecular interaction, C18-H18..N1, involves the nitrile nitrogen, highlighting its role as an additional hydrogen-bond acceptor within the molecular framework. As depicted in Figure 4.19 intermolecular hydrogen bonding interactions play a crucial role in linking FBMA molecules within the crystal lattice. C20-H20--O5 intermolecular hydrogen bonds connect adjacent molecules through interactions between alkyl hydrogen atoms and carbonyl oxygen atoms. These interactions arise from the trans orientation of the corresponding C–H bonds, enabling effective donor–acceptor overlap. Through centrosymmetric pairing of these C–H···O and C–H···N interactions, FBMA forms a two-dimensional supramolecular network within the crystal structure. Although classical hydrogen bonds are absent, the cumulative effect of these weak interactions significantly enhances the structural integrity and stability of the crystal packing (Brosge et al., 2021). Overall, the combination of intramolecular conformational locking and intermolecular hydrogen-bond-driven assembly governs the solid-state architecture of FBMA.

The molecular structure of TOMA Table 4.13 was confirmed by single-crystal X-ray diffraction analysis. TOMA crystallizes in the monoclinic crystal system with space group $P2_1/c$, indicating a centrosymmetric crystal lattice. The unit cell parameters and refinement indices demonstrate good data quality and reliable structure determination, confirming the successful synthesis of the targeted compound. The TOMA molecule consists of a toluene-derived aromatic ring substituted with two Meldrum's acid units. The aromatic ring exhibits typical C–C bond lengths ranging from 1.37 to 1.39 Å, consistent with a delocalized π-electron system.

The presence of the methyl substituent slightly distorts the molecular symmetry and introduces steric effects that influence the overall molecular conformation. Each

Meldrum's acid moiety is characterized by highly polarized carbonyl groups, with C=O bond lengths of approximately 1.19–1.21 Å, confirming strong double-bond character (Dey et al., 2015). These carbonyl oxygen atoms represent electron-rich sites that can interact with metal surfaces. The O–C–O bond angles within the dioxane-4,6-dione rings are close to 120°, indicating sp^2 hybridization and maintaining the rigidity of the cyclic structure. The overall molecular geometry of TOMA is non-planar due to steric hindrance between the bulky Meldrum's acid groups and the aromatic core (Dey et al., 2015).

This non-planarity is beneficial for corrosion inhibition, as it allows multiple functional groups to interact simultaneously with the metal surface, enhancing surface coverage and adsorption stability (Verma et al., 2018; Dey et al., 2015). Figure 4.20 show that the crystal packing of TOMA is dominated by several intramolecular C–H···O hydrogen bonds involving the carbonyl oxygen atoms of the Meldrum's acid units. Specifically, intramolecular interactions such as C6–H9···O5 and C5–H18···O8 are formed between hydrogen atoms of the aliphatic framework and the carbonyl oxygen atoms. These interactions assist in stabilizing the molecular conformation by maintaining the relative orientation of the Meldrum's acid moieties with respect to the aromatic ring.

As illustrated in Figure 4.20, intermolecular hydrogen bonds are essential for assembling the TOMA molecules within the crystal lattice. Notably, C10–H3···O8 and C4–H18···O8 intermolecular hydrogen bonds link neighbouring molecules through interactions between methyl or methylene hydrogen atoms and carbonyl oxygen atoms. These interactions are facilitated by the trans configuration of the corresponding C–H bonds, allowing favorable hydrogen-bond geometry. The observed H···O distances confirm the presence of weak yet directional hydrogen-bonding interactions. The cooperative effect of these intermolecular C–H···O hydrogen bonds lead to the formation of a two-dimensional hydrogen-bonded network within the crystal structure. Although π–π stacking interactions are absent due to steric hindrance from the methyl and Meldrum's acid substituents, the extensive hydrogen-bonding network plays a dominant role in stabilizing the crystal packing (Dey et al., 2015). Consequently, these hydrogen bonds collectively enhance the structural robustness and packing efficiency of TOMA in the solid state.

THMA (Table 4.13) crystallizes in the monoclinic $P2_1/c$ space group with four molecules per unit cell (Z = 4). The unit cell parameters are a = 6.0449(4) Å, b =

9.4012(7) Å and c = 19.1782(14) Å, with a monoclinic angle β = 95.353(2)°, while α and γ are fixed at 90°. These crystallographic parameters indicate a well-ordered molecular arrangement within the lattice. Distinctive single-bond features are observed throughout the THMA structure, confirming its molecular connectivity. The C–S bonds within the thiophene ring, S1–C1 (1.7406(12) Å) and S1–C2 (1.6975(15) Å), are consistent with typical thiophene-based single bonds. Additionally, the aliphatic C–C bonds involving the substituent groups, such as C8–C10 (1.513(2) Å) and C8–C11 (1.508(2) Å), together with constrained C–H bonds (0.96 Å), fall within the standard range for C–C single bonds (≈1.54–1.58 Å), validating the proposed THMA framework. The structural stability of THMA is strongly influenced by electron delocalisation within the aromatic thiophene ring. This is reflected in the intermediate bond lengths of C1–C4 (1.3836(18) Å) and C2–C3 (1.365(2) Å), which lie between typical single and double bond values, indicating partial double-bond character.

Such delocalisation enhances molecular rigidity and resonance stabilisation, contributing to the overall stability of the crystal structures also contains multiple oxygen-containing functional groups, which significantly define its geometry. The carbonyl bonds O3–C7 (1.2010(16) Å) and O4–C9 (1.2033(16) Å) confirm strong C=O double-bond character, while the ether linkages involving O1 and O2 exhibit bond angles characteristic of sp^2-hybridised carbonyl carbons (Gokhale & Mantri, 2017). These oxygen atoms act as electron-rich sites, which are structurally important for intermolecular interactions. Furthermore, the thiophene ring in THMA exhibits near-planarity, as evidenced by torsion angles close to 0° or 180°, such as C2–S1–C1–C4 (−0.04°) and C2–C3–C4–C1 (0.51°). This planarity promotes extended π-conjugation across the molecule, enhancing electronic stability. Overall, the experimentally determined bond lengths, bond angles and torsion parameters are in good agreement with optimised molecular models, confirming the reliability and accuracy of the THMA structural model.

Figure 4.21 illustrate that the crystal packing of THMA is influenced by several weak C–H···O hydrogen-bonding interactions involving the carbonyl oxygen atoms. Although classical intramolecular hydrogen bonds are absent, short intramolecular C–H···O contacts between the aliphatic and aromatic hydrogen atoms and nearby carbonyl oxygen atoms help to stabilize the molecular conformation. These interactions contribute to maintaining the relative orientation of the thiophene ring and the oxygen-rich functional groups within the molecule (Verma et al., 2018). As shown in Figure

4.21, intermolecular C–H···O hydrogen bonds play a dominant role in organizing THMA molecules within the crystal lattice. In particular, the C4–H4···O3 intermolecular interaction links adjacent molecules through contacts between aromatic hydrogen atoms and carbonyl oxygen atoms, generating a supramolecular association across symmetry-related molecules. These interactions arise from favorable molecular orientations within the monoclinic $P2_1/c$ space group and assist in propagating intermolecular connectivity throughout the crystal (Verma et al., 2018).

The cooperative nature of these hydrogen bonds promotes the formation of a three-dimensional hydrogen-bonded network, ensuring structural cohesion in the absence of strong classical hydrogen bonds. Although π–π stacking interactions are limited, likely due to the steric influence of substituent groups and the non-coplanar arrangement of neighbouring molecules, the cumulative effect of weak C–H···O hydrogen bonds and van der Waals interactions plays a crucial role in stabilizing the crystal packing of THMA. Overall, these non-covalent interactions enhance the packing efficiency and structural robustness of THMA in the solid state.

Table 4.13
Crystal and Experiment Data of FBMA, TOMA and THMA

Crystal data	FBMA	TOMA	THMA
Empirical formula	$C_{20}H_{19}NO_8$	$C_{20}H_{22}O_8$	$C_{11}H_{10}O_4S$
Formula weight	401.37	390.37	238.25
Temperature	303 K	303 K	303 K
Wavelength	0.71073 Å	0.71073 Å	0.71073 Å
Crystal system	Monoclinic	Monoclinic	Monoclinic
Space group	$P2_1/c$	$P2_1/c$	$P2_1/c$
Unit cell dimension	a = 7.4605 (3) Å	a = 7.5290 (3) Å	a = 6.0449 (4) Å
	b = 10.9341 (3) Å	b = 10.9954 (3) Å	b = 9.4012 (7) Å
	c = 23.4696 (9) Å	c = 22.9784 (8) Å	c = 19.1782 (14) Å
	α= 90°	α= 90°	α= 90°
	β= 97.448 (2)°	β= 98.234 (2)°	β= 95.353 (2)°
	γ = 90°.	γ = 90°	γ = 90°
Volume	1898.35 (12) Å^3	1882.64 (11) Å^3	1085.13 (13) Å^3
Z	8	4	4
Density	1.404 Mg m^{-3}	1.377 Mg m^{-3}	1.458 Mg m^{-3}
Absorption coefficient	0.110 mm^{-1}	0.110 mm^{-1}	0.110 mm^{-1}
F(000)	840	824	496
Crystal size	0.49 × 0.47 × 0.27 mm^3	0.02 x 0.19 x 0.29 mm^3	0.69 × 0.22 × 0.21 mm^3
Theta range for data collection	2.6–23.6°.	3.072 to 28.347°	3.072 to 28.347°
Reflections collected	61804	43622	43622
Independent reflections	4730 [R(int) = 0.0840]	3960 [R(int) = 0.070]	3960 [R(int) = 0.070]
Completeness to theta = 25.242°	99.7 %	99.8 %	99.8 %
Data/restraints / parameters	3311 / 0 / 199	4426 / 1 / 249	4426 / 1 / 249
Goodness-of-fit on F^2	1.017	0.989	0.989
Final R indices [I>2sigma(I)]	$R1$ = 0.0444, wR^2 = 0.1146	$R1$ = 0.0434, wR^2 = 0.0847	$R1$ = 0.0434, wR^2 = 0.0847
R indices (all data)	$R1$ = 0.0647, wR^2 = 0.1006	$R1$ = 0.789, wR^2 = 0.0927	$R1$ = 0.789, wR^2 = 0.0927

Table 4.14
Hydrogen Bonds for FBMA

Hydrogen bonds	D-H…A	d(D-H)	d(H…A)	d(D…A)
C7_1—H7_1···O8_1	112	0.98	2.34	2.853 (2)
C8_1 —H8_1···O7_1	112	0.98	2.36	2.885 (2)
C13_1—H13_1···O5_1	163	0.98	2.41	3.360 (2)
C18_1—H18*C*_1···N1_1	153	0.96	2.58	3.461 (4)

Table 4.15
Hydrogen Bonds for TOMA

Hydrogen bonds	D-H…A	d(D-H)	d(H…A)	d(D…A)
C10—H3···O8^{i}	163	0.96	2.49	3.417 (3)
C4—H18···O8^{i}	163	0.98	2.31	3.2596 (19)
C6—H9···O5	114	0.98	2.32	2.863 (2)
C5—H18···O8	111	0.98	2.37	2.867 (2)

Table 4.16
Hydrogen Bonds for THMA

Hydrogen bonds	D-H…A	d(D-H)	d(H…A)	d(D…A)
C4—H4···O3^{i}	149	0.93	2.48	3.3096 (17)
H5—O3···0.93	-	2.37	2.79 (1)	107

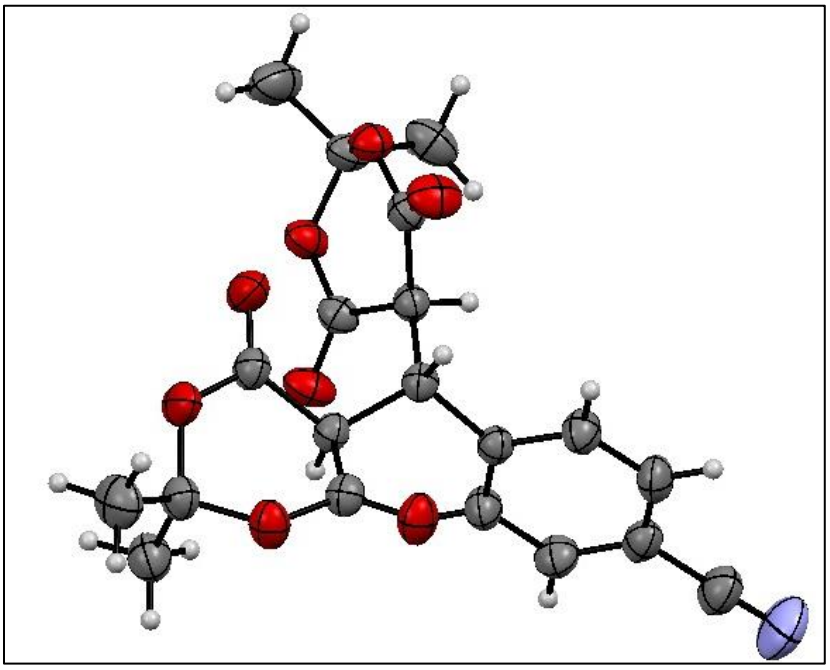


Figure 4.16 ORTEP Structure of FBMA

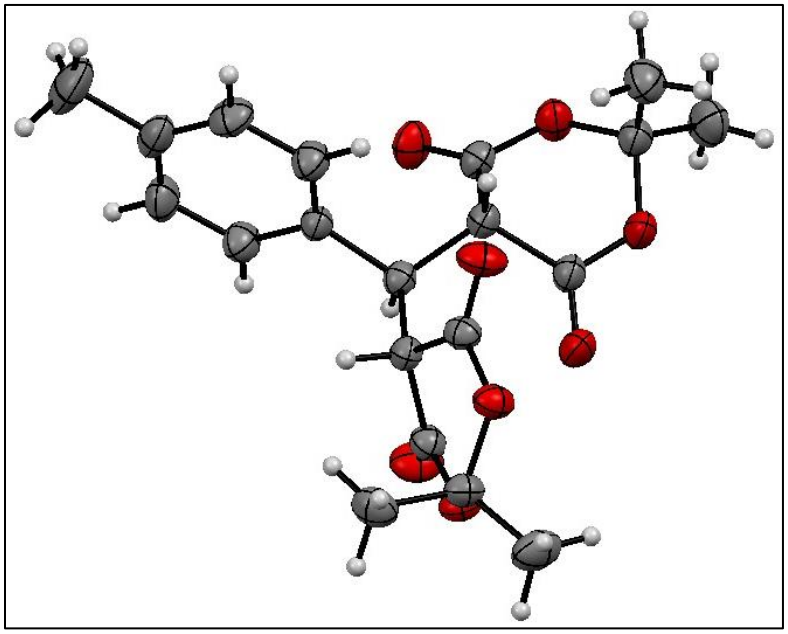


Figure 4.17 ORTEP Structure of TOMA

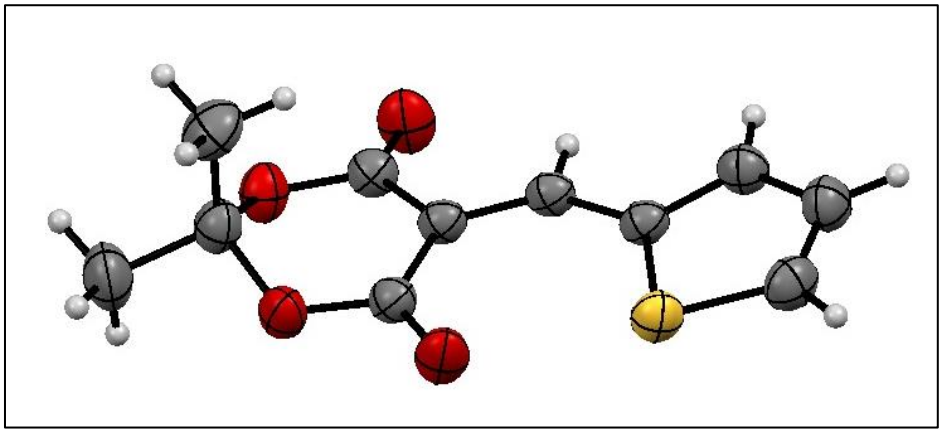


Figure 4.18 ORTEP Structure of THMA

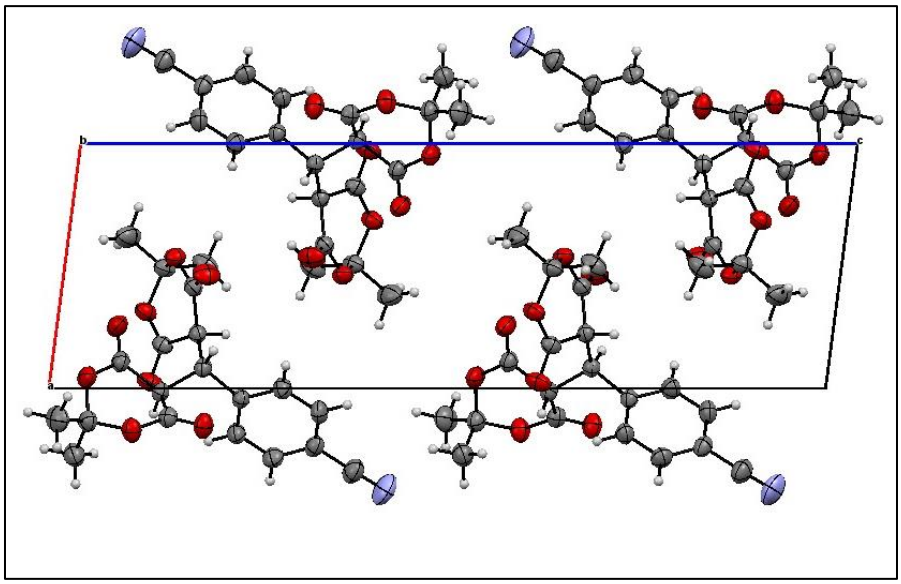


Figure 4.19 Packing Diagram of FBMA Showing a Centrosymmetric Viewed Along the a-Axis

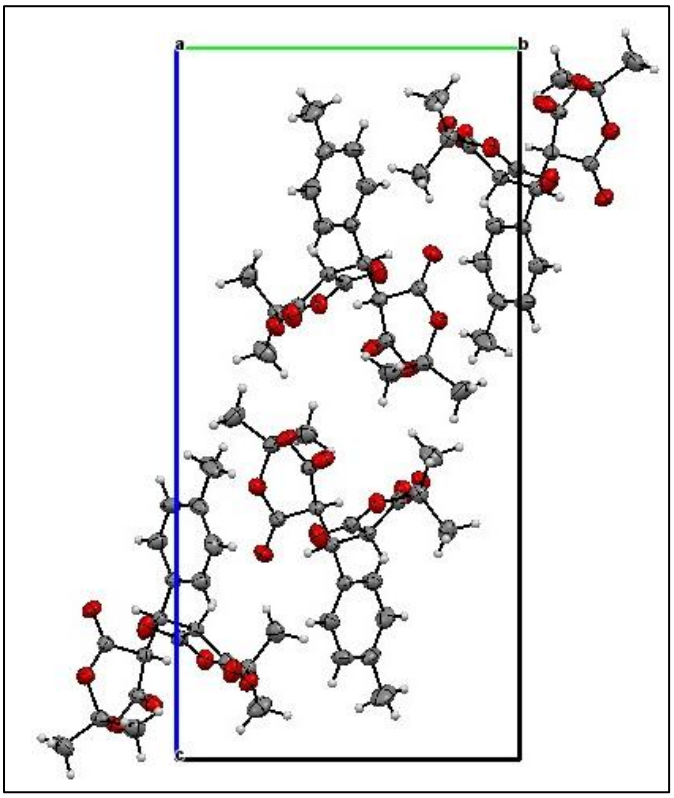


Figure 4.20 Packing Diagram of TOMA Showing a Centrosymmetric Viewed Along the a-Axis

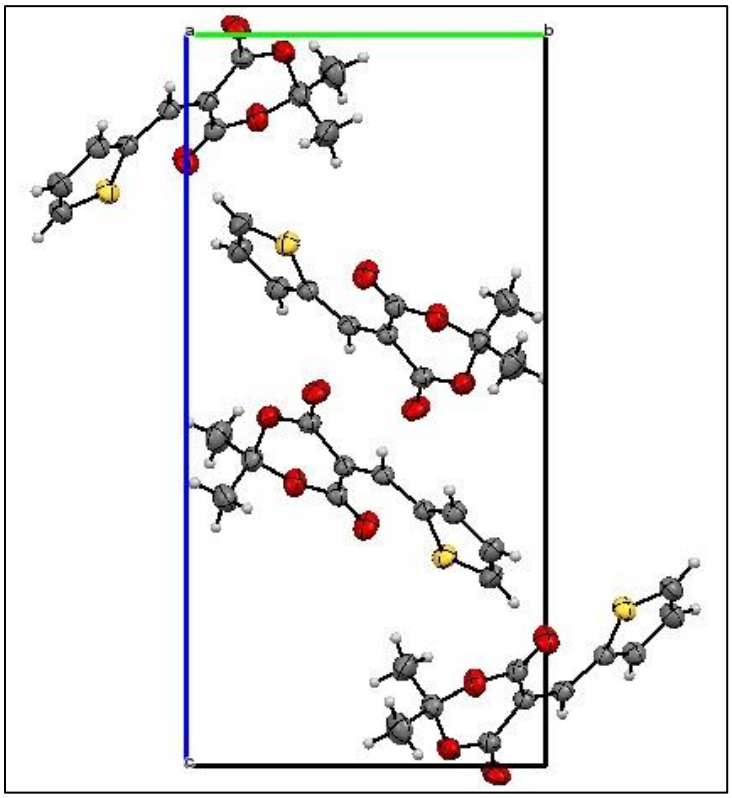


Figure 4.21 Packing Diagram of THMA Showing a Centrosymmetric Viewed Along the a-Axis

4.3 Weight Loss Measurement

The corrosion inhibition performance of the synthesized Meldrum's acid derivatives (FBMA, TOMA, THMA and PYMA) was evaluated using the weight loss method after 24 h immersion mild steel in 1M HCl at room temperature (Verma et al., 2018; Finšgar & Jackson, 2014). In this method, inhibition efficiency (IE%) represents the ability of an inhibitor to reduce mild steel dissolution compared to the blank solution. A higher IE% indicates better corrosion protection. Surface coverage (Θ) refers to the fraction of mild steel surface covered by inhibitor molecules, value closer to 1 indicate more complete coverage. The corrosion rate (CR) describes the speed at which mild steel corrodes and a lower CR value means slower metal degradation. These three parameters are closely related, as inhibitor increases, Θ and IE% increase, while CR decreases (Verma et al., 2018).

From the Table 4.17 experimental data, all inhibitors show a clear concentration dependent behaviour which were as the concentration increases from 1 to 7 mM, IE% and surface coverage increase steadily, while the corrosion rate decreases. This result confirms that higher concentrations, more inhibitor molecules are adsorbed onto mild

steel surface forming a protective film that reduces the contact between mild steel surfaces and the aggressive H^+ and Cl^- ions in the acidic medium (Gece, 2011). Among all inhibitors, FBMA exhibits the highest inhibition efficiency, reading about 81.48% at 7 mM, along with the lowest corrosion rate. This better performance can be explained by its molecular structure. FBMA contains an electron-withdrawing cyano (–C≡N) group, which increases the polarity of the molecule and enhances its interaction with the mild steel surface. The –C≡N group withdraws electron density from the aromatic ring, making it electron-deficient (Obot et al., 2014). This allows the aromatic π-system to act as a π-acceptor, facilitating back-donation from the iron d-orbitals to the inhibitor molecule. In addition, FBMA possesses two Meldrum's acid moieties, which increase molecular size, planarity and surface area. This larger and more planar structure allows FBMA to adsorb in a flat orientation on the steel surface, resulting in higher surface coverage and stronger protective film formation (Verma et al., 2018; Gece, 2011; Obot et al., 2014).

TOMA shows the second-highest inhibition efficiency after FBMA. Its performance is mainly attributed to the presence of an aromatic ring from tolualdehyde, which provides π-electrons that interact with the mild steel surface (Gece, 2011; Verma et al., 2018; Obot et al., 2014). However, TOMA contains a methyl group ($–CH_3$), which is an electron-donating group (EDG). While EDGs increase electron density, they do not enhance adsorption as effectively as strong electron-withdrawing groups (Gece, 2011). In addition, TOMA lacks highly electronegative heteroatoms compared to FBMA. As a result, its adsorption strength and surface coverage are slightly lower, leading to lower IE% and higher corrosion rate compared to FBMA. THMA exhibits lower inhibition efficiency compared to FBMA and TOMA. One important reason is its molecular structure: THMA contains only one Meldrum's acid unit attached to the thiophene ring, whereas FBMA and TOMA effectively benefit from larger conjugated systems. The presence of sulfur (S) in the thiophene ring contributes to corrosion inhibition because sulfur atoms have lone pair electrons that can coordinate with iron. However, the smaller molecular size and reduced planarity of THMA limit its surface coverage. With fewer adsorption sites and less steric protection, the inhibitor film formed by THMA is less compact, resulting in moderate inhibition efficiency (Verma et al., 2018; Finšgar & Jackson, 2014).

PYMA, THMA and TOMA shows inhibition behaviour comparable nearly the same but slightly lower than FBMA. The presence of a pyridine ring introduces a

nitrogen atom, which can donate lone-pair electrons to the mild steel surface and enhance adsorption. However, pyridine is relatively rigid and the molecule does not possess strong electron-withdrawing substituents like –C≡N (Komkov et al., 2022). In addition, the molecular structure of PYMA is slightly smaller, which reduces its ability to form a uniform and stable protective layer. Consequently, its surface coverage and inhibition efficiency are lower than FBMA. Overall, the inhibition efficiency follows the order: FBMA > TOMA > PYMA > THMA. This trend clearly shows that corrosion inhibition performance is strongly influenced by molecular structure, substituent effects and planarity. Compounds with larger molecular size, better planarity, strong electron-withdrawing groups and multiple adsorption centres show higher surface coverage and better protection. FBMA fulfils these criteria most effectively, leading to its better inhibition efficiency and lowest corrosion rate among the studied inhibitors.

In conclusion, the weight-loss results demonstrate that all synthesized Meldrum's acid derivatives act as effective corrosion inhibitors for mild steel in 1 M HCl. Their inhibition behaviour is governed by adsorption onto the steel surface, which increases with concentration. Structural factors such as the presence of electron-withdrawing groups, heteroatoms, planarity and the number of Meldrum's acid units play a crucial role in determining surface coverage and corrosion inhibition efficiency (Ahmed et al., 2024).

Table 4.17
Summary of Weight-loss Measurements for Mild Steel in 1.0 M HCl Containing Different Inhibitors

Inhibitor	Concentration (mM)	Ɵ	IE%	Corrosion rate, CR ($g\ cm^{-2}\ h^{-1}$)
Blank	-		-	8.4375×10^{-3}
FBMA	1	0.6617	66.17	2.8541×10^{-3}
	2	0.7012	70.12	2.5208×10^{-3}
	3	0.7679	76.79	1.9583×10^{-3}
	4	0.7703	77.03	1.9375×10^{-3}
	5	0.7876	78.76	1.7916×10^{-3}
	6	0.8074	80.74	1.6250×10^{-3}
	7	0.8148	81.48	1.5625×10^{-3}
TOMA	1	0.6814	68.14	2.6875×10^{-3}
	2	0.6839	68.39	2.6667×10^{-3}
	3	0.7111	71.11	2.4375×10^{-3}
	4	0.7185	71.85	2.3750×10^{-3}
	5	0.7234	72.34	2.3333×10^{-3}
	6	0.7432	74.32	2.1667×10^{-3}
	7	0.7555	75.55	2.0625×10^{-3}
THMA	1	0.6790	67.90	2.7083×10^{-3}
	2	0.6864	68.64	2.6458×10^{-3}
	3	0.7037	70.37	2.5000×10^{-3}
	4	0.7111	71.11	2.4375×10^{-3}
	5	0.7160	71.60	2.3958×10^{-3}
	6	0.7209	72.09	2.3541×10^{-3}
	7	0.7283	72.83	2.2916×10^{-3}
PYMA	1	0.6740	67.40	2.7500×10^{-3}
	2	0.6765	67.65	2.7291×10^{-3}
	3	0.6814	68.14	2.6875×10^{-3}
	4	0.7111	71.11	2.4375×10^{-3}
	5	0.7407	74.07	2.1875×10^{-3}
	6	0.7481	74.81	2.1250×10^{-3}
	7	0.7530	75.30	2.0833×10^{-3}

4.3.1 Adsorption Isotherm

The adsorption behaviour and thermodynamic properties of the Meldrum's acid inhibitors which are FBMA, PYMA, TOMA and THMA were examined using the weight-loss (WL) data to determine the interaction with the mild steel surface. Six adsorption isotherm models were applied: Langmuir, Frumkin, Temkin, Freundlich, El-Awady and Flory–Huggins. However, only the Langmuir and Frumkin isotherms provided the best correlation with the experimental results ($R^2 = 0.99$). The regression coefficient (R^2) was used as the main criterion to identify the most appropriate adsorption model, while the equilibrium constant (K_{ads}) and Gibbs free energy ($\Delta G°_{ads}$) were calculated to understand the strength and nature of adsorption. Since all compounds have a same isotherm, Figure 4.21 shows the Langmuir isotherm for each compound meanwhile other adsorption model graphs have shown in Appendices.

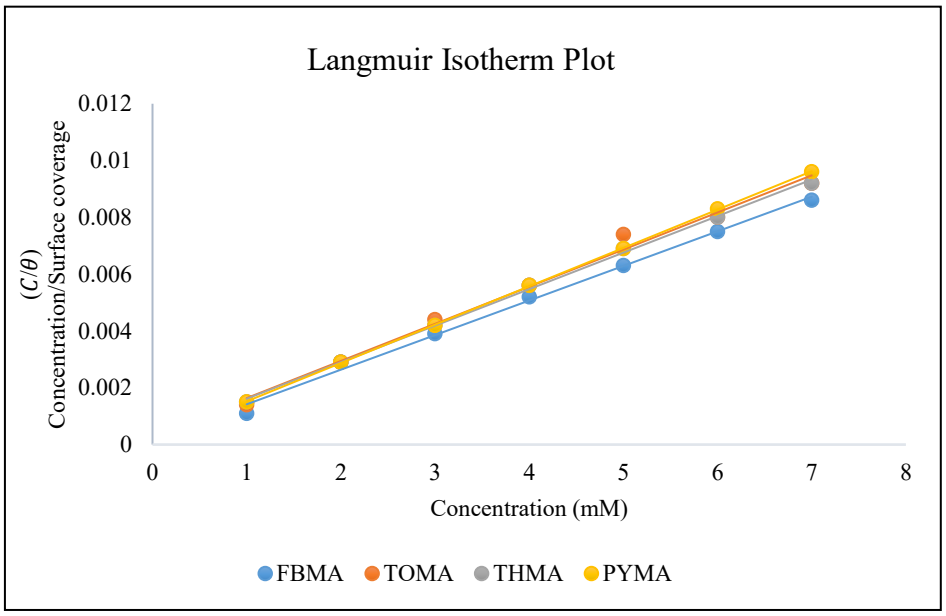


Figure 4.22 Langmuir Adsorption Isotherm for Each Inhibitors

From Table 4.18, the Langmuir isotherm shows the best correlation for all compound with R^2 values higher than 0.99, indicating that their adsorption follows a monolayer pattern on a homogeneous mild steel surface. This model assumes that each inhibitor molecule occupies one specific adsorption site without interaction between neighbouring molecules. Among the inhibitors, THMA displayed the highest R^2 value (0.9998). The adsorption equilibrium constant (K_{ads}) and Gibbs free energy ($\Delta G°_{ads}$) were calculated to further evaluate the strength and spontaneity of the adsorption

process. The K_{ads} value represents the strength of interaction between the inhibitor and the mild steel surface, while $\Delta G°_{ads}$ indicates whether the adsorption is spontaneous and what type of interaction (physical or chemical) dominates.

Table 4.18
R^2 Values for Various Adsorption Isotherms Obtained From the WL Method

Adsorption Isotherm	FBMA	PYMA	TOMA	THMA
Langmuir	0.9992	0.9975	0.9986	0.9998
Frumkin	0.9976	0.9951	0.9969	0.9935
Temkin	0.9779	0.9779	0.8821	0.9717
Freundlich	0.9762	0.8104	0.8879	0.9727
El-Awady	0.9794	0.9119	0.8720	0.9703
Flory–Huggins	0.9720	0.8015	0.8687	0.9660

4.3.2 Gibb's Free Energy Calculation ($\Delta G°_{ads}$)

Gibb's free energy, written as $\Delta G°_{ads}$, is a thermodynamic value that shows the maximum amount of useful work a system can perform when temperature and pressure remain constant. In corrosion inhibition study, $\Delta G°_{ads}$ is very important because it helps to understand the corrosion process and the effective of an inhibitor that can protect the mild steel surface. By calculating $\Delta G°_{ads}$, it is possible to identify the inhibitor molecules attach to the mild steel surface and determine the type of adsorption that occurs whether it is physical, chemical, or a combination of both (Ahmed et al., 2024).

According to the 20/40 rule (Vashishth et al., 2023), if $\Delta G°_{ads}$ is more positive than −20 kJ mol^{-1}, the adsorption is considered physical, meaning the inhibitor molecules are held to the mild steel surface by weak forces such as van der Waals interactions or electrostatic attraction. When $\Delta G°_{ads}$ is more negative than −40 kJ mol^{-1}, the adsorption is chemical, which involves the formation of stronger bonds where electrons are shared or transferred between the inhibitor and the Fe(II) on the mild steel surface. If the value lies between −20 and −40 kJ mol^{-1}, it indicates mixed adsorption, where both physical and chemical interactions occur together (Adamu et al., 2025; Cherif et al., 2024). Although these limits are only general guidelines, they are still very useful for understanding how inhibitors interact with the mild steel surface.

However, it is often difficult to make a direct connection between the inhibition efficiency and the $\Delta G°_{ads}$ value because other factors can also influence the process For

example, the size and shape of the inhibitor molecule can affect easily it attaches to the steel surface. Larger or bulkier molecules may cover more area but might not fit tightly on uneven parts of the metal. The presence of heteroatoms (such as oxygen, nitrogen, or sulfur) and π-electrons from aromatic rings also helps the inhibitor bond more strongly to the steel through electron donation or sharing. In addition, temperature and concentration can change how the molecules adsorb where a high temperature may weaken physical adsorption, while higher concentration can improve surface coverage. The surface roughness, purity of the metal and pH of the solution can also influence the evenly inhibitor spreads and binds to the steel surface. Because of these factors, the $\Delta G°_{ads}$ and inhibition efficiency may vary even when using the same type of inhibitor (Adamu et al., 2025; Cherif et al., 2024).

In this study, $\Delta G°_{ads}$ for each inhibitor was calculated using the formula as stated in the Chapter 3 The adsorption constant, K_{ads}, was determined from the adsorption isotherm that best fits the experimental data. Since the adsorption of the inhibitors on the mild steel surface mostly follows the Langmuir isotherm, the K_{ads} value was obtained from the reciprocal of the y-intercept (1/y-intercept) of the Langmuir plot. It is very important to ensure that the correct unit is used when calculating K_{ads}, which must always be expressed in the inverse of molarity (M^{-1}). This means that the y-intercept must be in molarity (M). The slope and regression coefficient (R^2) of the Langmuir plot will remain the same even if different concentration units are used, but using the wrong unit for the y-intercept can cause errors in the K_{ads} and $\Delta G°_{ads}$ values. This type of mistake can be quite large, especially for inhibitors with high molecular weights and may lead to an incorrect understanding of the type of interaction between the inhibitor and the metal surface.

Table 4.19 presents the calculated parameters used to determine $\Delta G°_{ads}$ based on the Langmuir isotherm plots. The K_{ads} and $\Delta G°_{ads}$ were used to study the strength and spontaneity of the adsorption process. A higher K_{ads} value shows a stronger interaction between the inhibitor and the mild steel surface, while a negative $\Delta G°_{ads}$ value indicates that the adsorption happens spontaneous and is thermodynamically favourable. In addition, ΔG_{ads} values also help in identifying whether the adsorption is mainly physical, chemical, or a combination of both.

Table 4.19
K_{ads} and $\Delta G°_{ads}$ Values Obtained from WL Analysis

Compound	Best Isotherm	Kads (M^{-1})	$\Delta G°_{ads}$ (kJ mol^{-1})	Type of adsorption
FBMA	Langmuir	2500	−19.4	physisorption
PYMA	Langmuir	3334	−20.1	Chemisorption & physisorption
TOMA	Langmuir	3334	−20.1	Chemisorption & physisorption
THMA	Langmuir	5000	−21.1	Chemisorption & physisorption

From Table 4.19 the calculated K_{ads} values increase in the order FBMA < PYMA ≈ TOMA < THMA, indicating that THMA exhibits the highest thermodynamic adsorption affinity toward the mild steel surface. Generally, a higher K_{ads} value reflects stronger adsorption and greater thermodynamic stability of the adsorbed layer. However, adsorption strength alone does not necessarily correspond to the highest corrosion inhibition efficiency, as the protective performance of an inhibitor also depends on factors such as molecular size, adsorption orientation, surface coverage, film compactness and intermolecular interactions within the adsorbed layer (Obot et al., 2015). Therefore, the adsorption constant should be interpreted together with the experimental corrosion data.

In this study, FBMA exhibited a $\Delta G°_{ads}$ value of −19.4 kJ mol^{-1}, suggesting that its adsorption predominantly involves physisorption. This interaction is mainly attributed to electrostatic attraction between the protonated inhibitor species and the charged steel surface, where the nitrogen and oxygen atoms (from nitrile and carbonyl groups) contribute through weak donor–acceptor and dipole–dipole interactions, characteristic of a physisorption-dominated adsorption process. Meanwhile, PYMA, TOMA and THMA displayed $\Delta G°_{ads}$ values between −20.1 and −21 kJ mol^{-1}, consistent with mixed adsorption. Their adsorption process likely begins with physisorption through weak van der Waals forces, followed by chemisorption via electron sharing or donation from heteroatoms and π-electron systems of the aromatic rings to the steel surface.

Overall, the adsorption of Meldrum's acid derivatives on mild steel follows the Langmuir isotherm, suggesting the formation of a uniform monolayer film on the metal surface. The slightly higher slope values from the Langmuir plots imply the presence of weak intermolecular interactions, which are common in practical corrosion systems. The increasing K_{ads} and more negative $\Delta G°_{ads}$ values from PYMA to THMA indicate stronger adsorption and a more stable protective film compared to FBMA. Among all

the inhibitors, THMA exhibited the highest K_{ads} (5000 M^{-1}) and the most negative $\Delta G°_{ads}$ (−21.1 kJ mol^{-1}), confirming it as the most effective inhibitor. This performance can be attributed to its aromatic structure and multiple heteroatoms, which enable efficient π-electron and lone-pair interactions with the steel surface, forming a stable and corrosion-resistant protective layer. Therefore, it can be concluded that all Meldrum's acid inhibitors adsorb spontaneously on mild steel through a mixed physical–chemical mechanism, with THMA showing the strongest and most stable adsorption behavior.

Although theoretical calculations predicted that THMA, which exhibits mixed adsorption, should be the more effective inhibitor, experimental results showed that FBMA, which adsorbs predominantly through physisorption, provided better corrosion inhibition. This can be explained by surface coverage and steric effects. Despite its bulky structure, FBMA molecules spread over the steel surface in a way that allows them to effectively block active sites, while also being flexible enough to adjust and fill gaps. In contrast, THMA, although capable of forming stronger chemisorption bonds, is smaller and more rigid, leading to less adaptable surface coverage. Therefore, under the experimental conditions, FBMA achieves better inhibition efficiency through a well-packed, physically adsorbed layer, even though its adsorption is mainly physisorption.

4.4 Surface Analysis

4.4.1 SEM-EDX

The surface morphology and elemental composition of mild steel after immersion in 1 M HCl for 24 hours, with and without 7 mM of inhibitors, were examined using SEM and EDX to understand the inhibitors protect the mild steel surface. The blank mild steel (without inhibitor) in Figure 4.23 (a) appeared very rough, uneven and covered with deep pits and cracks. This was caused by the strong attack of HCl, which reacted with the mild steel surface and formed corrosion products (Zaidon et al. 2020). The EDX spectrum of the blank sample mainly showed a high percentage of iron (Fe) also the presence of Cl at weightage of (0.9) %, confirming that the mild steel surface was destroyed because it was directly exposed to the acid hydrochloric. When inhibitors were added (Figure 4.26 (b-e)) the mild steel surfaces became

noticeably smoother and less damaged (Zaidon et al., 2021). The SEM micrographs clearly showed that all inhibitors formed protective films on the surface, reducing direct contact between the mild steel surface and the acid. The EDX spectra of the inhibited samples also showed new peaks for carbon (C), oxygen (O) and nitrogen (N), which come from the inhibitor molecules. The appearance of these new elements proves that the inhibitors successfully adsorbed on the steel surface.

Among the four inhibitors, the THMA-treated surface was the smoothest and most uniform, showing very few visible pits or corrosion spots. The EDX elemental spectrum confirmed the presence of the inhibitor, displaying prominent peaks for carbon (45.8%), oxygen (52.7%) and sulfur (1.5%). This compositional data supports the THMA's better inhibition performance, fundamentally governed by its high molecular planarity, which enables the molecule to adsorb in a flat configuration directly onto the mild steel substrate. A more planar molecule maximizes its contact area with the mild steel surface and can arrange itself more efficiently, allowing more molecules to pack tightly together. This results in a compact film with minimal gaps, blocking the penetration of chloride ions. The strong adsorption observed (reflected by high K_{ads} and the most negative $\Delta G°_{ads}$ value of –21.1 kJ mol^{-1}) is therefore a direct consequence of both its electronic properties and its structural planarity (Solomon, 2023).

The TOMA-treated surface appeared smooth but slightly rougher than THMA. Its EDX analysis revealed C (34%) and O (66%), confirming the adsorption of TOMA molecules on the mild steel surface. The presence of these elements indicates that TOMA formed a protective film through mixed adsorption, involving both weak electrostatic attraction and partial chemical bonding (occurs when atom share electrons unevenly or only limited degree) (Ahmed et al., 2021). This reduced surface coverage is attributed to its lower planarity and bulkier substituents, which limit the molecule’s ability to lie flat and pack efficiently. When molecular planarity is low, steric hindrance increases, leading to wider spacing between adjacent molecules on the steel surface. This creates empty regions that remain vulnerable to acid attack, explaining the presence of residual corrosion spots

The PYMA-treated surface was also smoother than the blank, but some small corrosion spots were still visible. Its EDX spectrum showed C (34.8%), O (63.4%) and a small amount of N (1.8%), confirming the presence of inhibitor molecules. The smaller nitrogen content compared to THMA and TOMA indicates a lower level of

chemical interaction with the metal surface. Structurally, PYMA possesses partial planarity and moderate steric size, allowing some degree of ordered packing but not as efficiently as THMA. As a result, the film formed is protective but less compact, permitting some acid penetration. The adsorption of PYMA occurs mainly through mixed adsorption, starting with weak physical attraction followed by partial electron donation which is when heteroatoms such as N, O, or S in the inhibitor transfer a limited amount of electron density to the mild steel surface, creating a mixed adsorption interaction that is stronger than physical adsorption but weaker than full chemisorption from the heteroatoms to the iron surface.

The FBMA-treated surface much smoother than the blank. The EDX data showed significant peaks for C (35.5%), O (61.9%) and N (2.60%), proving that FBMA was adsorbed onto the steel surface. The higher nitrogen content proving that FBMA interacts with the mild steel surface mainly through physisorption, driven by electrostatic attraction and weak physical interactions involving nitrogen and oxygen atoms (Ahmed et al., 2021). The bulky structure of FBMA prevents the molecules from arranging closely and evenly on the mild steel surface. Because of this steric hindrance, fewer inhibitor molecules can fit onto the surface and they tend to adopt irregular orientations. As a result, a physically adsorbed protective layer is formed that is stable but less compact, leading to incomplete coverage of the mild steel surface.

The SEM–EDX results show that the level of surface protection is strongly dependent on molecular planarity and steric effects. Molecules that are highly planar and have minimal steric hindrance (such as THMA) can pack more efficiently, allowing a greater number of inhibitor molecules to adsorb on the mild steel surface. This produces a dense, compact and uniform protective film, resulting in highly effective corrosion resistance. Conversely, molecules with reduced planarity or larger steric bulk (TOMA and FBMA) adsorb less efficiently, creating less uniform protective layers and leaving portions of the surface partially exposed. Figure 4.27 displays the EDX data of bare mild steel, meanwhile the Figures 4.28-4.31 display EDX and mapping for the distribution of element on mild steel surface after 24 h in 1 M HCl with 7 mM of Meldrum’s acid derivatives.

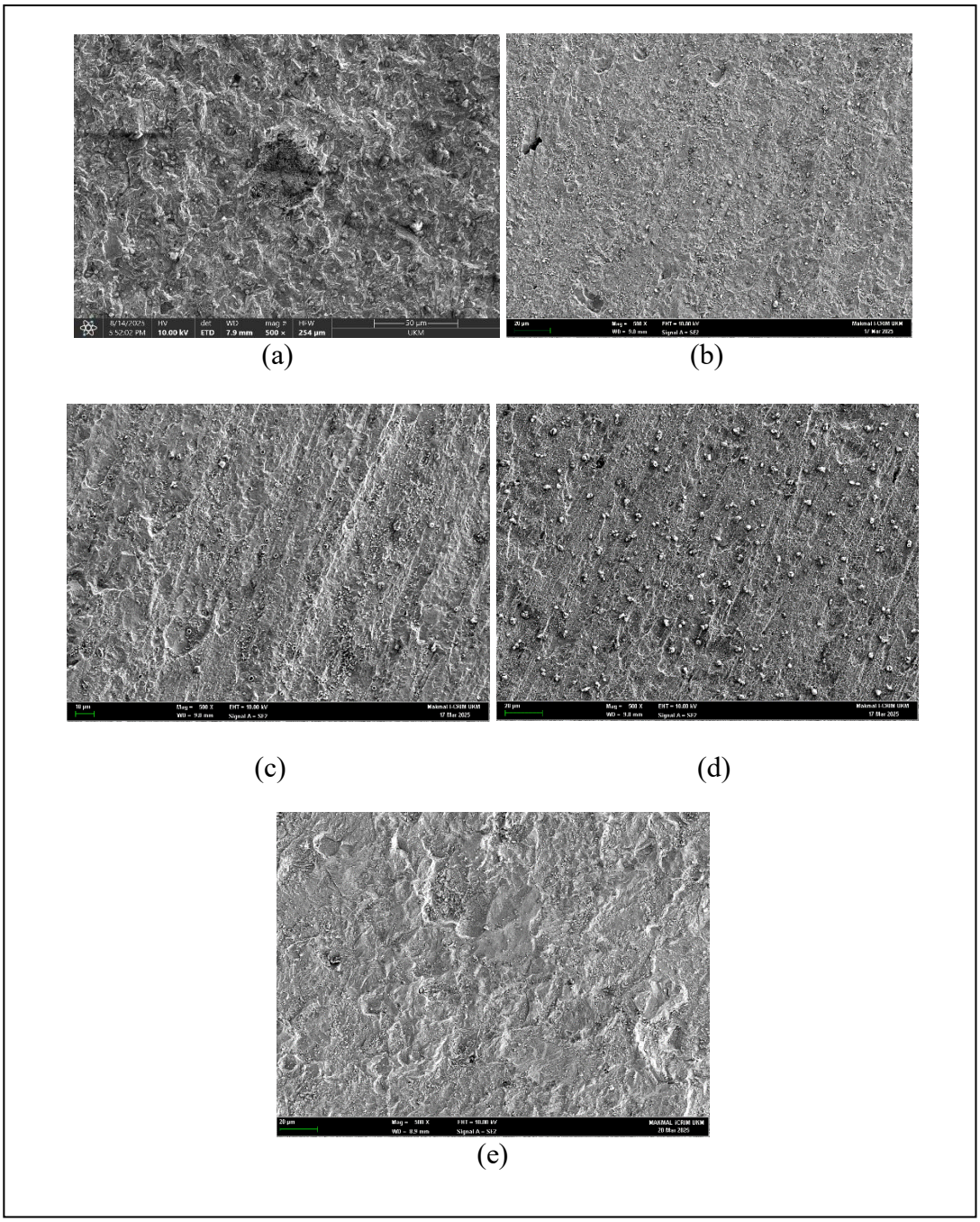
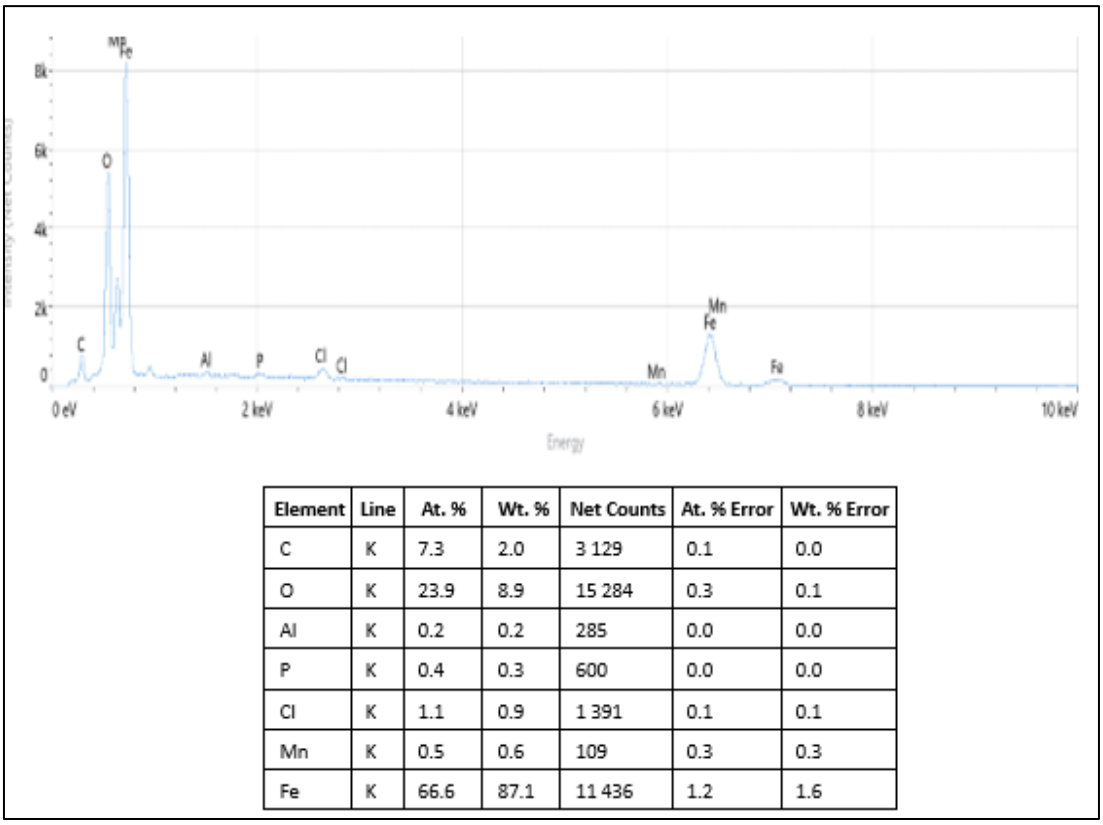


Figure 4.23 SEM Images of Polished Mild Steel in 1 M HCl (blank) (a), Mild Steel in 7 mM THMA Solution (b), Mild Steel in 7 mM FBMA Solution (c), Mild Steel in 7 mM TOMA Solution (d) and Mild Steel in 7 mM PYMA Solution (e)



Element	Line	At. %	Wt. %	Net Counts	At. % Error	Wt. % Error
C	K	7.3	2.0	3 129	0.1	0.0
O	K	23.9	8.9	15 284	0.3	0.1
Al	K	0.2	0.2	285	0.0	0.0
P	K	0.4	0.3	600	0.0	0.0
Cl	K	1.1	0.9	1 391	0.1	0.1
Mn	K	0.5	0.6	109	0.3	0.3
Fe	K	66.6	87.1	11 436	1.2	1.6

Figure 4.24 EDX Data for Bare Mild Steel

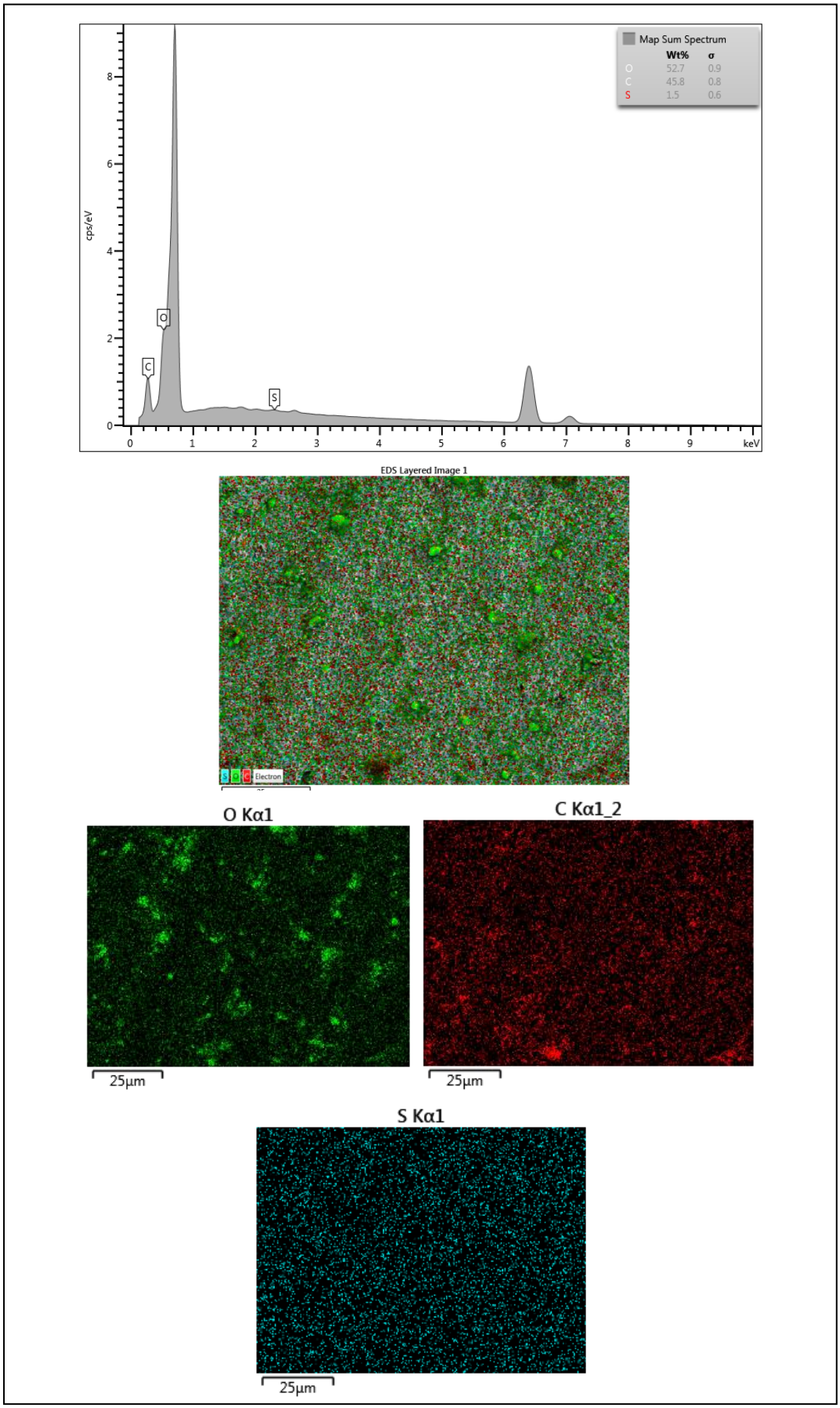


Figure 4.25 EDX and Mapping for the Distribution of Element on Mild Steel Surface After 24 h in 1 M HCl with 7 mM THMA

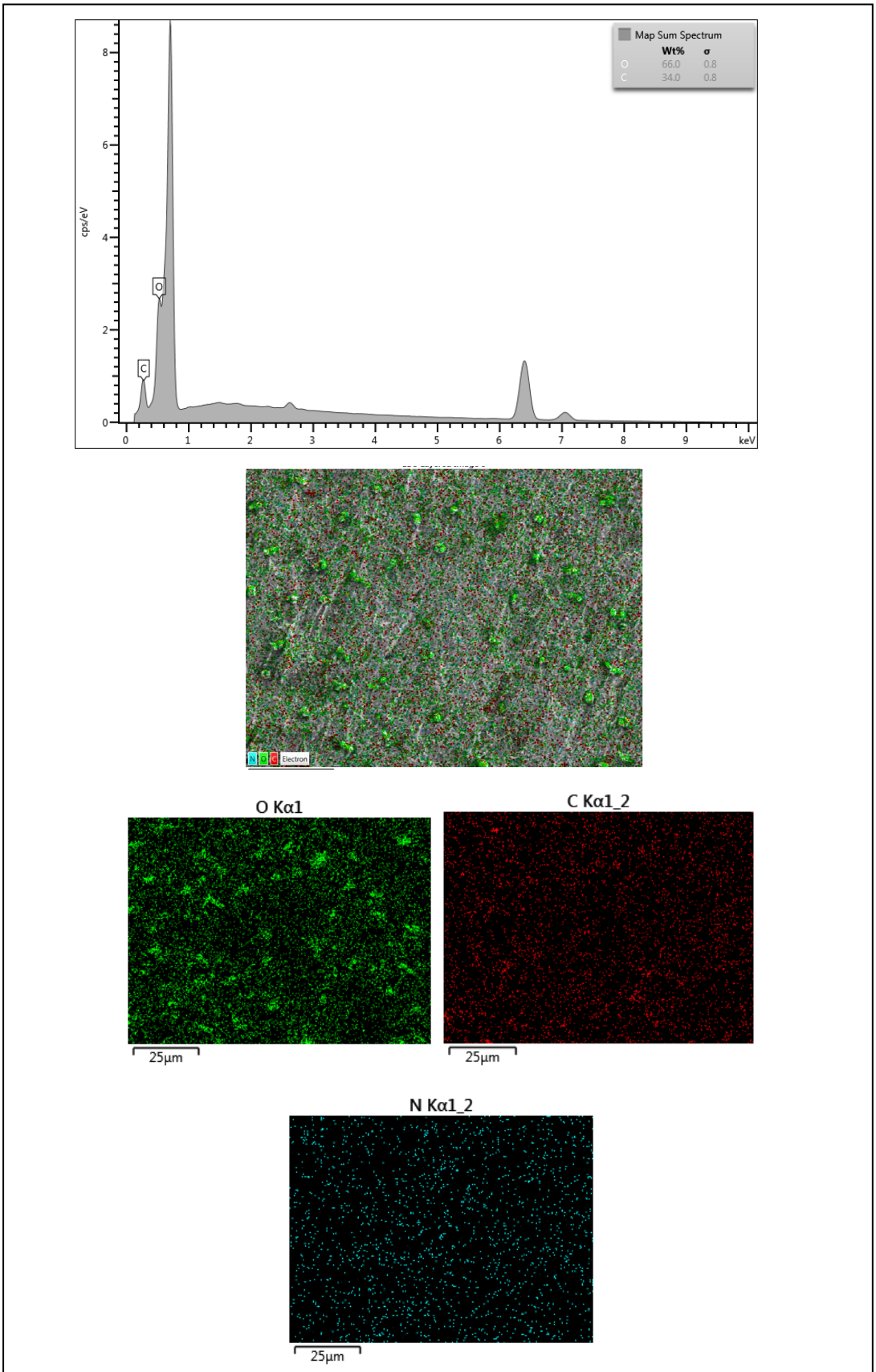


Figure 4.26 EDX and Mapping for the Distribution of Element on Mild Steel Surface After 24 h in 1 M HCl with 7 mM TOMA

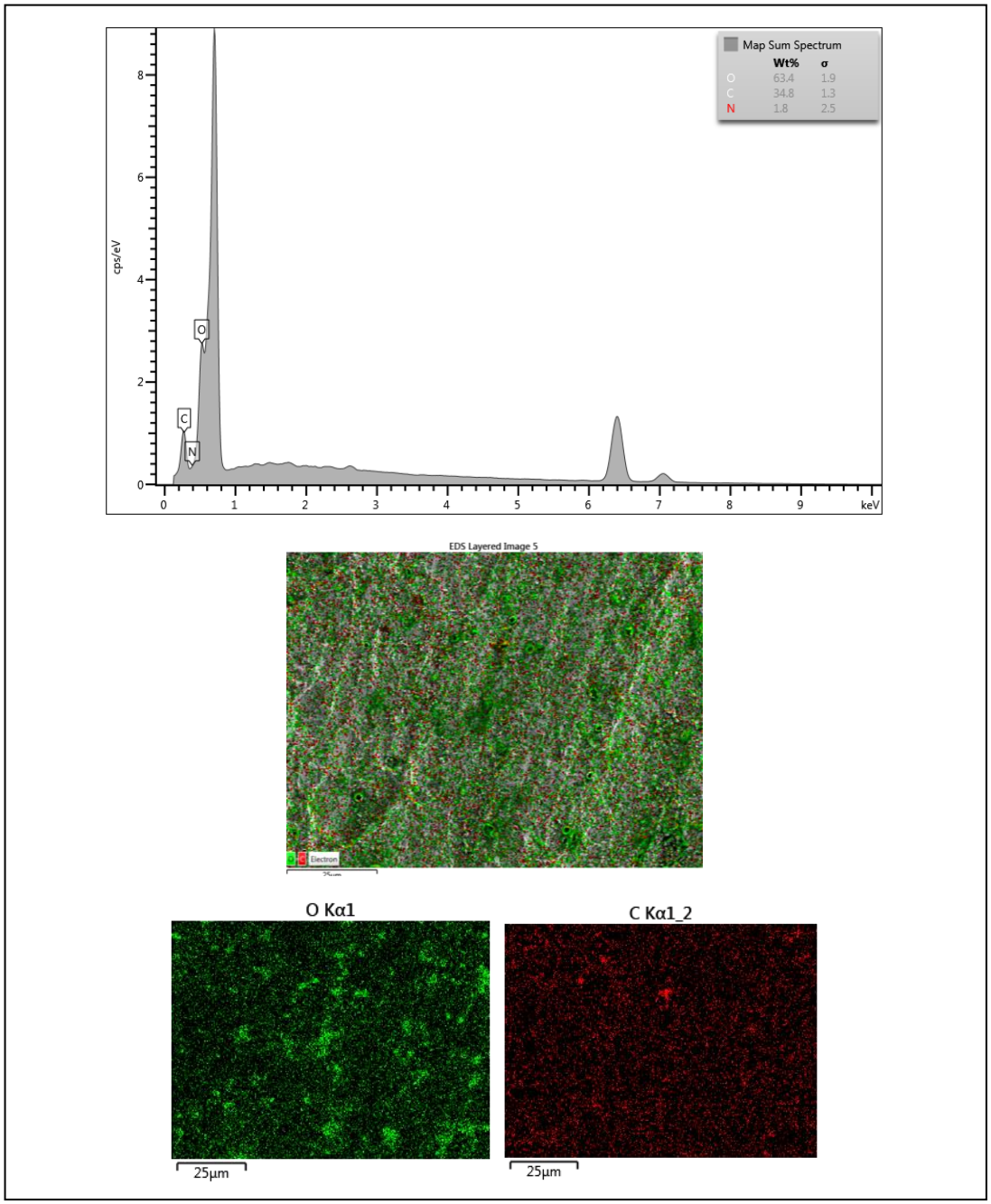


Figure 4.27 EDX and Mapping for the Distribution of Element on Mild Steel Surface After 24 h in 1 M HCl with 7 mM FBMA

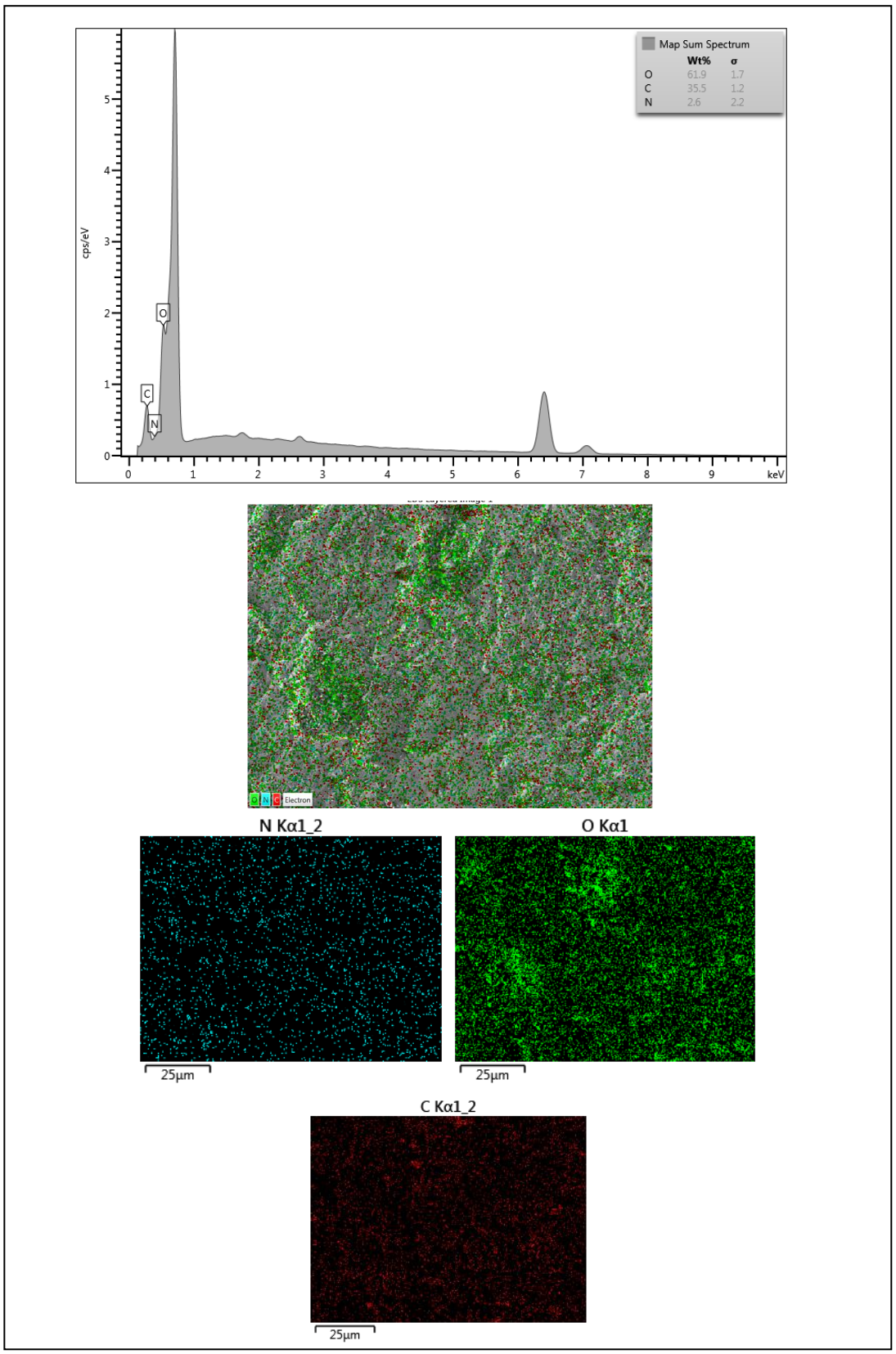


Figure 4.28 EDX and Mapping for the Distribution of Element on Mild Steel Surface After 24 h in 1 M HCl with 7 mM PYMA

4.4.2 AFM

Atomic Force Microscopy (AFM) was used to study the surface texture and roughness of mild steel after immersion in 1 M HCl solution, both with and without the presence of inhibitors. This technique gives a 3D image and measures the roughness metal surface. The key parameters obtained from AFM are the average roughness (S_a), root mean square roughness (S_q) and maximum valley depth (S_v). These parameters give important information about the surface condition. When the surface has high roughness values, it means the mild steel is more corroded and has a lot of uneven pits and holes. On the other hand, lower roughness values show that the surface is smoother, which indicates that an inhibitor film has successfully formed on the surface and protected it from acid attack (Monticelli, 2018). The blank mild steel sample (without inhibitor) was directly exposed to 1 M HCl, which caused heavy corrosion and surface damage. The AFM image showed a very uneven and rough surface, with S_a = 0.1859 µm, S_q = 0.2333 µm and S_v = 0.773 µm. The high values of S_a and S_q confirm that the acid strongly attacked the mild steel surface, forming deep pits and irregular shapes. This rough texture is typical for unprotected mild steel in an acidic environment, as the chloride (Cl^-) ions easily penetrate and destroy the surface layer of iron, leading to surface deterioration (Monticelli, 2018).

When inhibitors were added, the surface condition of mild steel improved significantly. The presence of inhibitor molecules helps form a protective layer that reduces the direct contact between the mild steel and the acid solution. Among all tested inhibitors, THMA produced the lowest roughness values (S_a = 0.1105 µm, S_q = 0.1401 µm, S_v = 0.4755 µm), indicating the formation of a smoother and more uniform protective layer. The better performance of THMA is closely related to its molecular planarity. A highly planar molecule can lie flat on the steel surface and establish stronger interactions over a larger contact area (Zaidon et al., 2021). This allows THMA molecules to pack closely together, minimizing gaps and creating a compact film that effectively isolates the steel from the acid. Its optimal steric size also prevents excessive crowding between molecules, enabling efficient alignment and complete surface coverage (Zaidon et al., 2021).

The TOMA-protected surface showed the highest roughness values among all inhibitor samples, with S_a = 0.1584 µm, S_q = 0.2114 µm and S_v = 0.8309 µm. The AFM image displayed a coarse and uneven surface, indicating that the inhibitor film was

loosely arranged and allowed continued acid penetration (Finšgar & Jackson, 2014). This poor performance is linked to TOMA's bulky substituents and low planarity. Molecules with large steric volume cannot lie flat on the steel surface and tend to adopt irregular orientations. This disrupts packing density and leaves unprotected regions through which corrosive ions can attack the mild steel. As a result, the protective layer becomes patchy, leading to higher roughness (Ahmed et al., 2024). PYMA demonstrated moderate inhibition effectiveness, with S_a = 0.1282 µm and S_q = 0.1781 µm. Its AFM surface showed noticeable smoothing compared to the blank but still contained some irregularities, indicating partial coverage. PYMA possesses intermediate planarity and steric dimensions; therefore, it can adsorb reasonably well but may not achieve the dense packing required for a fully uniform film. Some gaps likely remain between molecules, reducing the overall smoothness of the protected surface.

Similarly, FBMA provided a measurable improvement in surface morphology relative to the blank, with S_a = 0.1423 µm and S_q = 0.2008 µm. Although FBMA formed a continuous protective layer, the roughness remained slightly higher compared to THMA and PYMA. This behaviour can be attributed to FBMA's bulkier functional groups, which introduce steric hindrance and limit molecular planarity (Verma et al., 2018). When molecules cannot position themselves flat on the surface, their packing becomes less ordered, which reduces the overall compactness of the protective film., The AFM analysis confirms that all four synthesized inhibitors adsorb onto the mild steel surface and reduce surface roughness to varying degrees. The trend in surface smoothness and inferred film quality follows the order: THMA > PYMA > FBMA > TOMA.

This trend clearly reflects the influence of molecular structure. Molecules with high planarity and moderate steric size can pack efficiently on the steel surface, forming dense, uniform films that produce smoother AFM profiles (Ahmed et al., 2024; Gece, 2011). In contrast, bulky or non-planar molecules create loosely packed and irregular layers, resulting in higher surface roughness and lower protection efficiency. The AFM surface roughness parameters of mild steel immersed in 1 M HCl with and without Meldrum's acid derivatives are summarized in Table 4.20 and the three-dimensional AFM topographical images of the mild steel surfaces are shown in Figure 4.29.

Table 4.20
AFM Surface Roughness Parameters of Mild Steel in 1 M HCl with Different Inhibitors

Sample	Average Roughness, S_a (µm)	Root Mean Square Roughness, S_q (µm)	Maximum Valley Depth, S_v (µm)
Blank	0.1859	0.2333	0.773
THMA	0.1105	0.1401	0.4755
TOMA	0.1584	0.2114	0.8309
PYMA	0.1282	0.1781	0.8539
FBMA	0.1423	0.2008	0.6296

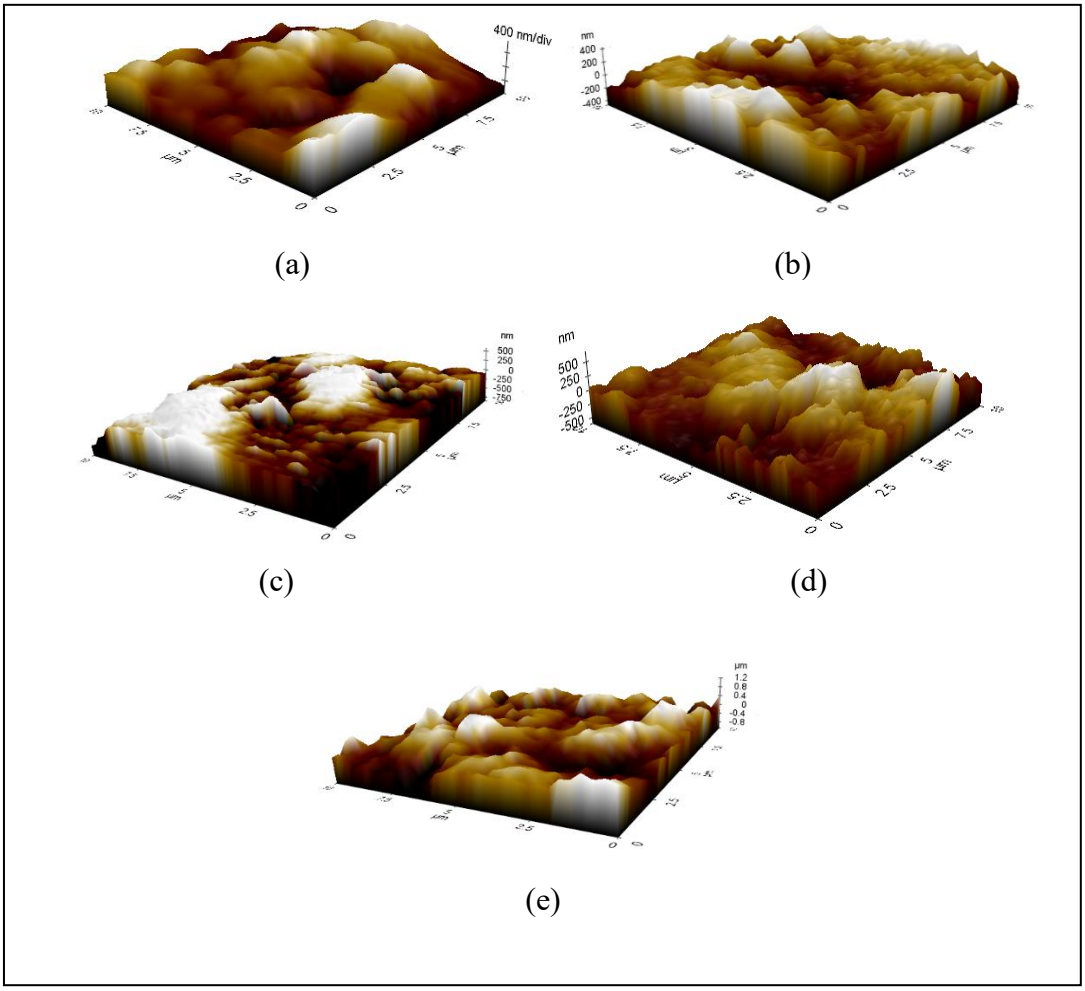


Figure 4.29 3D AFM Images of the Mild Steel Surface After Immersion in Blank Solution (a), THMA (b), PYMA (c), FBMA (d) and TOMA (e)

4.4.3 XPS Analysis

XPS technology in corrosion study was used to determine elemental composition, chemical state and electronic state of the adsorption inhibitor molecules on mild steel surface was evaluated (Biesinger, 2017). Full XPS spectra on surface layer of the mild steel is shown, which were Fe, O, C, N and S that related to component. To evaluate the interaction characteristic towards the mild steel, inhibitor FBMA, THMA, TOMA and PYMA were compared to the blank sample. 3 set of spectra (Fe, O and C) were compared side by side between mild steel with and without inhibitor. Fe-2p graph was used to monitor the binding of Fe with other compounds, for the O spectrum is to monitor the binding towards oxygen atom, while C spectrum to monitor binding towards carbon atom (Biesinger, 2017).

Blank mild steel Figure 4.30 surface displays typical features of an unprotected and naturally oxidized metal. The Fe 2p region shows two strong features between (725 eV) corresponding to iron in both Fe^{2+} and Fe^{3+} oxidation states, confirming that the steel is covered with iron oxide and hydroxyl layers (Biesinger, 2017). The O 1s region also confirms this, with peaks at 529 eV assigned to Fe-O (metal oxide) and (532) assigned to Fe-OH because of water adsorption. The Cl region only contains high peaks of Cl region at 285 eV indicates the iron from mild steel undergoes reaction towards HCl, meanwhile the C-O peaks indicate the reaction towards water in the HCl solution. Overall, the blank mild steel surface is dominated by iron oxide, hydroxy groups, chlorine groups and minor carbon contamination, indicating corrosion occurs on the surface mild steel.

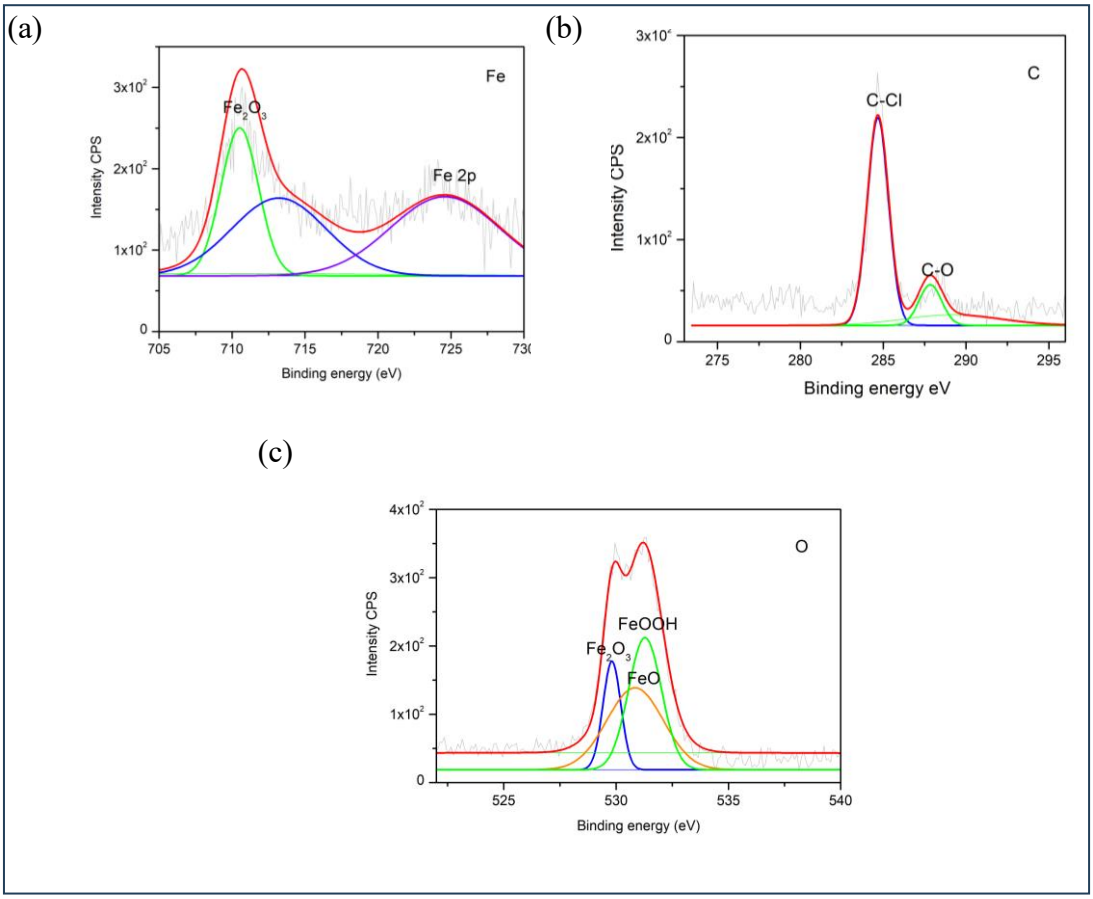


Figure 4.30 XPS Spectra for Blank Mild Steel (a) Fe (b) C (c) O

After treatment with inhibitor FBMA, the mild steel surface chemistry completely changes drastically. The C 1s region (Figure 4.31 (b)) develops three clear peaks at 284.73 eV (C-C/aromatic), 286.19 eV (C-O/C-N) and 289.97 eV (O-C=O), showing that FBMA forms a thick organic carbon layer on mild steel. The O 1s (Figure 4.31 (c)) peak at 531.03 eV (C=O) and 532.93 eV (C-O) indicate that oxygen now dominates the surface instead of iron oxide oxygen (Fe-O). A strong N 1s (Figure 4.31 (d)) peak appears at 401.41 eV (CN) (Aghamajidi et al., 2026), assigned to protonated or metal coordinated nitrogen, proving that nitrogen from FBMA is actively bonded to mild steel surface. The Fe 2p signal (Figure 4.31 (a)) is greatly suppressed, meaning the mild steel surface is almost completely covered by the inhibitor film. Chloride appears only in trace amounts, showing effective blocking of chloride ions. These results confirm that FBMA forms a dense, strongly adsorbed protective layer, with carbonyl and nitrogen groups playing the major roles in surface binding (Aghamajidi et al., 2026),

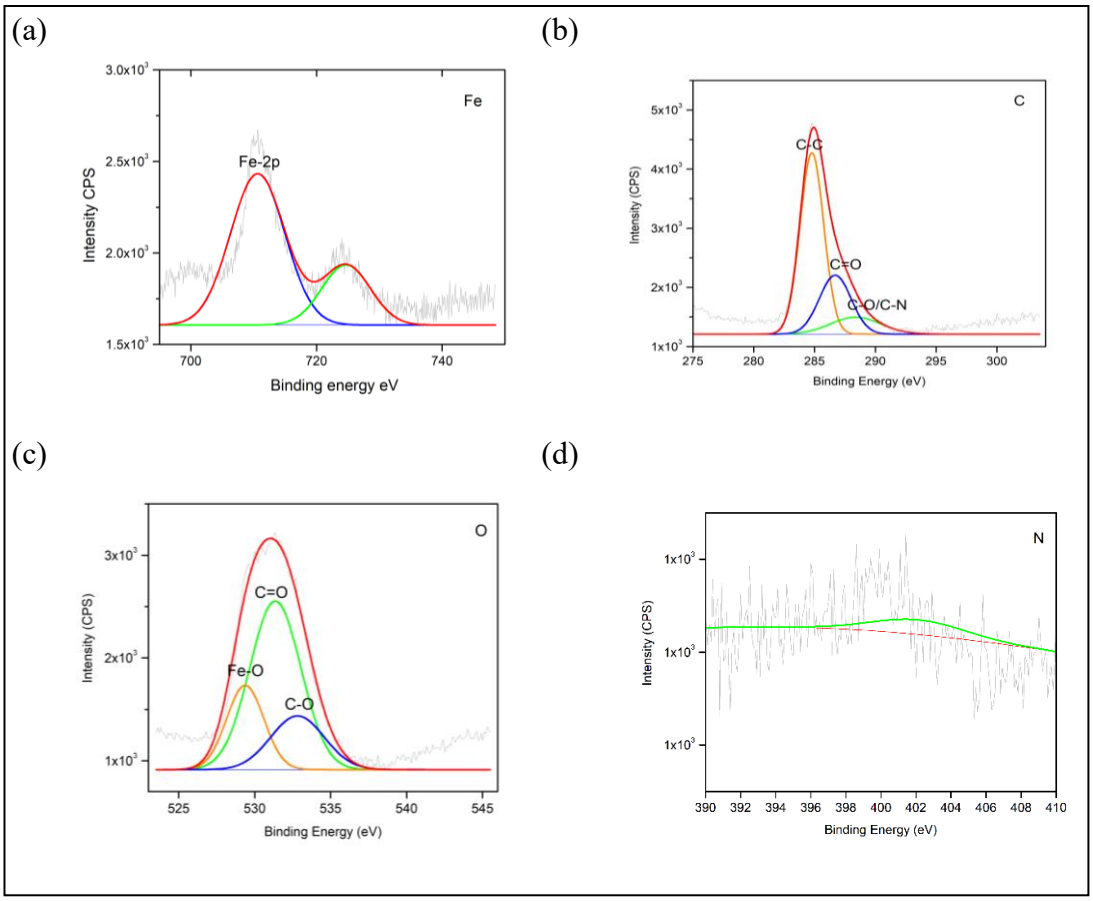


Figure 4.31 XPS Spectra of Mild Steel With FBMA (a) Fe (b) C (c) O (d) N

THMA, the C 1s (Figure 4.32 (b)) signal becomes much stronger, dominated by a peak at 285.19 eV that represents C-C groups from THMA's organic structure. This indicates that a substantial organic layer has formed on the mild steel surface (Verma et al., 2018). In the O 1s region (Figure 4.32 (c)), the contributions from C=O and C-O groups become more prominent, while the Fe-O signal becomes very small, this shows that THMA's oxygen containing groups are now covering the surface instead of metal oxide. A small but clear S 2p signal appears (Figure 4.32) (d), which indicates the presence of Fe-S bonding that may form by chemisorption (Gece, 2011; Obot et al., 2014; Aghamajidi et al., 2026). No chloride is detected, indicating that THMA prevents chloride ions from reaching the metal. Protective, these results show that THMA forms a compact, strongly attached protective film, where sulfur, carbonyl oxygen and the polar groups contribute to firm bonding with mild steel.

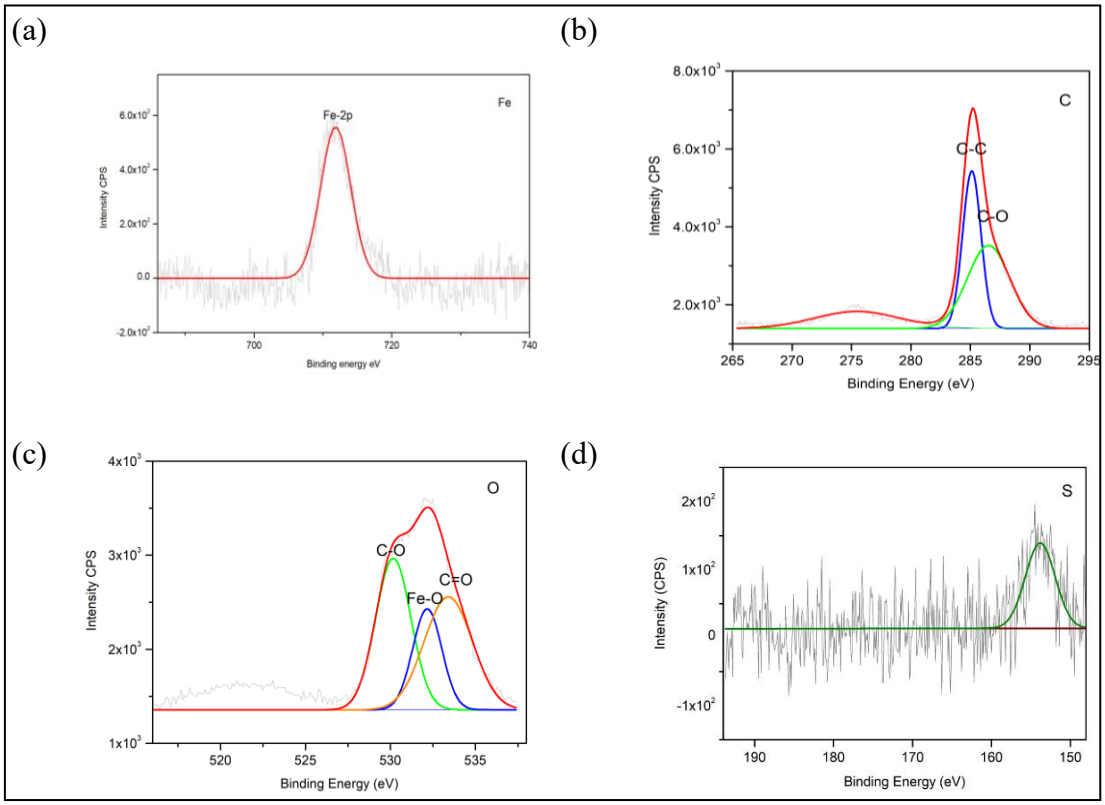


Figure 4.32 XPS Spectra of Mild Steel With THMA (a) Fe (b) C (c) O (d) S

The TOMA treated surface shows evidence of inhibition adsorption. The C 1s region (Figure 4.33 (b)) presents three components at 284.95 eV, 286.38 eV and 288.82 eV, indicating the presence of hydrocarbon groups, C-O functionalities and carbonyl groups from TOMA, while this confirms the presence of inhibitor, the O 1s region (Figure 4.33 (c)) still contains a noticeable Fe-O component at 530.33 eV, meaning that the oxide surface is not fully covered. There is no nitrogen signals due to the structure of the compounds doesn't have any nitrogen involved. More importantly, a significant amount of chloride (about 3.12%) is detected, indicating that TOMA does not completely block chloride ions from approaching the steel. The Fe 2p (Figure 4.33 (a)) peaks are still visible (5.71 at%), confirming that the inhibitor layer is thinner and does not fully conceal the substrate. These findings show that TOMA does adsorb on the steel, but the film is less uniform, less compact and less effective at preventing chloride penetration.

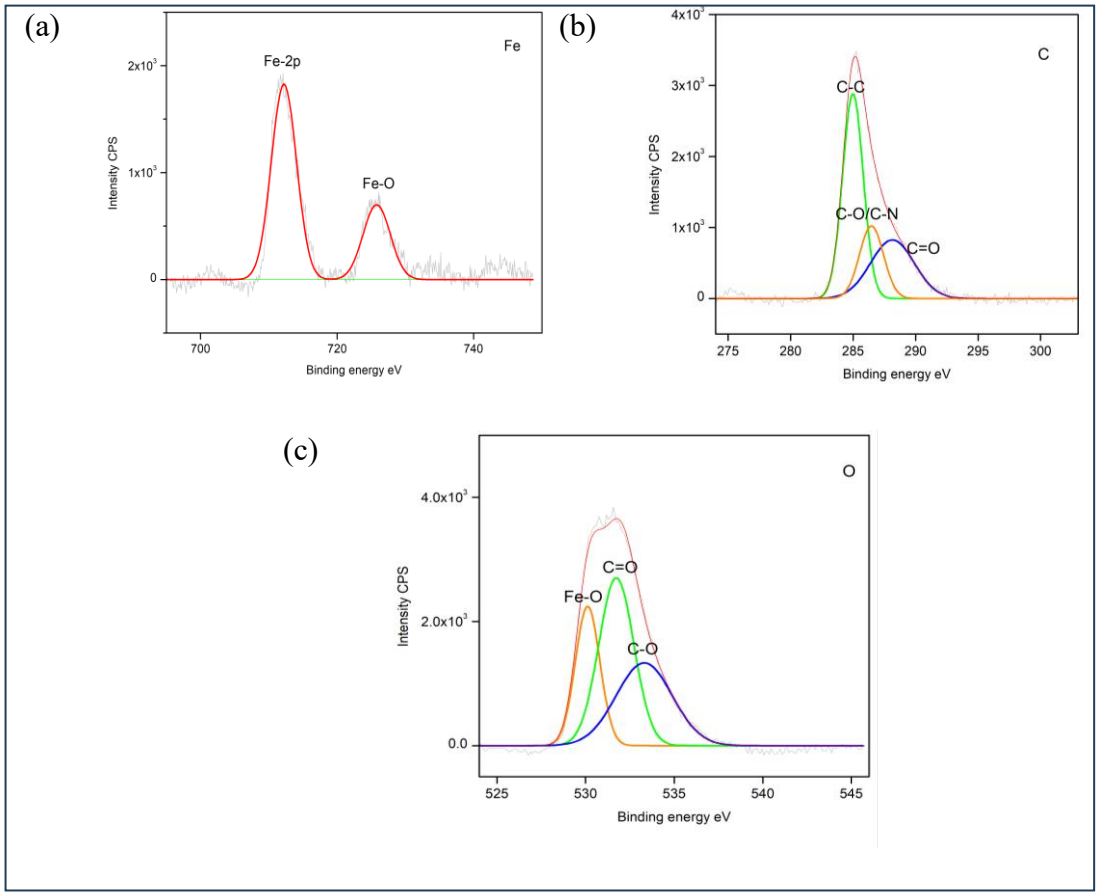


Figure 4.33 XPS Spectra of Mild Steel With TOMA (a) Fe (b) C (c) O

In contrast, the PYMA treated steel shows adsorption but with weaker protection. The C 1s (Figure 4.34 (b)) peak at 284.92 eV (C-C), 286.38 eV (C-O/C-N) and 288.50 eV (O-C=O) confirm the presence of the inhibitor on the mild steel surface. However, the O 1s region (Figure 4.34 (c)) still shows a significant Fe-O peak at 529.75 eV, indicating that parts of the metal oxide layer remain exposed. The nitrogen peak is very small, suggesting weak nitrogen metal interaction (Aghamajidi et al., 2026). The Fe 2p peak (Figure 4.34 (a)) remains visible, meaning the inhibitor film is thinner and does not bury the metal surface. The Cl 2p still presence indicates that chloride ions can still reach the surface through gaps in PYMA layer. These findings show that although PYMA provides some protection, the film it forms is less compact, less uniform and weaker in bonding.

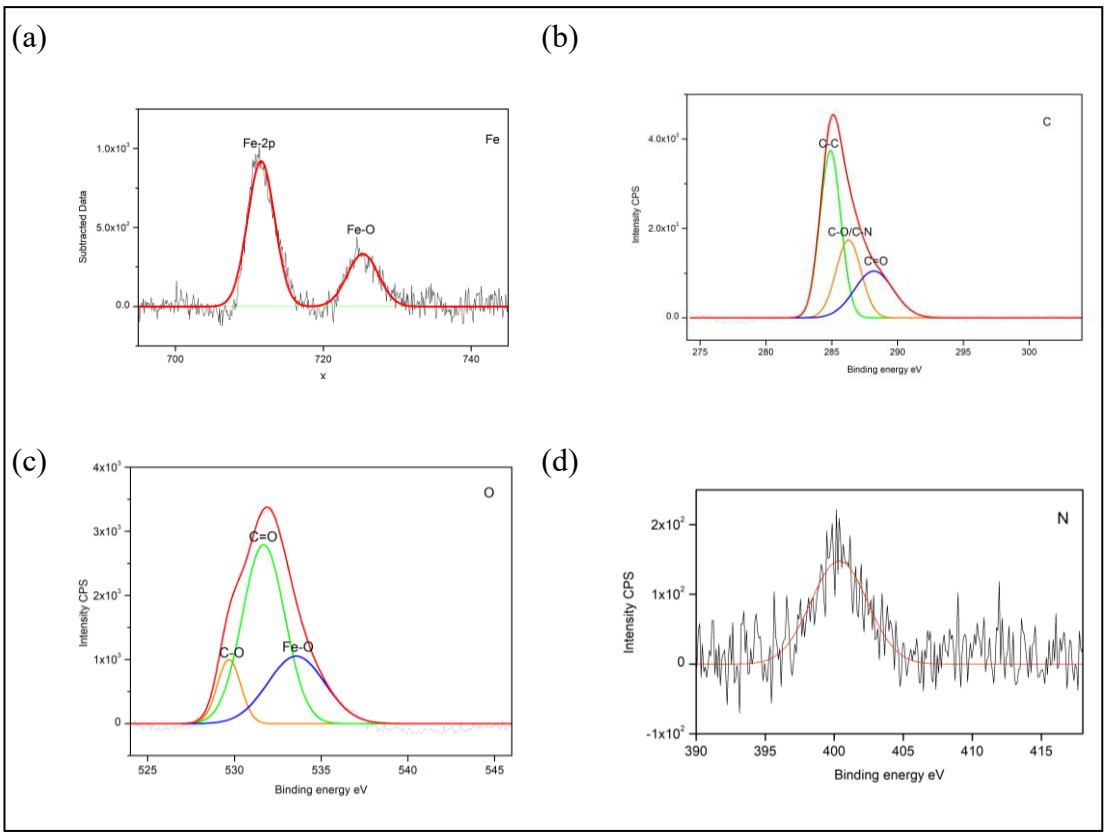


Figure 4.34 XPS Spectra of Mild Steel With PYMA (a) Fe (b) C (c) O (d) N

In conclusion, XPS analysis plays a crucial role in determining the effectiveness of corrosion inhibition by identifying the presence and relative intensity of surface elements and chemical bonds. The appearance of C–Cl peaks in the C 1s spectrum of the blank sample indicates that corrosion reactions occurred in the aggressive chloride medium, leading to the formation of corrosion-related species on the mild steel surface. In contrast, the inhibited sample shows a significant reduction or absence of C–Cl signals, demonstrating that the inhibitor effectively suppressed chloride interaction with the metal surface. Furthermore, the presence of characteristic bonds such as C–N and C=O in the inhibited sample confirms the adsorption of the organic inhibitor onto the mild steel surface. These functional groups contribute to the formation of a protective film that blocks active corrosion sites, thereby enhancing surface stability and significantly.

4.5 Density Functional Theory (DFT)

Quantum chemical studies are useful tools for evaluating the effectiveness of corrosion inhibitors and explaining the molecular and electronic properties of the investigated compounds (Sharma and Kumar et al., 2021). Density Functional Theory (DFT) calculations were used to explain the inhibition mechanism and the interaction between mild steel with four different inhibitors: FBMA, THMA, TOMA and PYMA. Although inhibitor molecules may become protonated in acidic solutions, only the neutral form of the molecules was considered in this work. Therefore, all calculated results are based on isolated neutral molecules in a vacuum.

In this studies PYMA result may be varies due to other inhibitor FBMA, THMA and TOMA were run in the program using data from single-crystal X-ray data meanwhile for PYMA the data was run based on initial structure only.

Table 4.21
Quantum Chemical Parameters of the Investigated Inhibitors

Parameters	FBMA	THMA	TOMA	PYMA
E_{HOMO} (eV)	-7.07	-6.54	-6.36	-9.72
E_{LUMO} (eV)	-1.47	-2.58	-0.60	-5.48
ΔE (eV)	5.60	3.96	5.76	4.24
IP (eV)	7.07	6.54	6.36	9.72
EA (eV)	1.47	2.58	0.60	5.48
Dipole moment (D)	4.27	4.56	3.48	7.6
χ (eV)	4.27	4.56	3.48	7.6
μ (eV)	-4.27	-4.56	-3.48	-7.6
η (eV)	2.80	1.98	2.88	2.12
S (eV^{-1})	0.35	0.51	0.36	0.47
ε (eV^{-1})	3.26	5.25	2.10	13.63
ω (eV)	5.60	3.96	5.76	20.2
ω^{+} (eV)	1.22	2.36	0.55	35.4
ω^{-} (eV)	9.74	11.44	7.93	−15.20
$\Delta \omega^{\pm}$ (eV)	−8.52	−9.08	−7.38	−0.66
ΔN	0.10	0.07	0.23	−0.53
$\Delta E_{back\text{-}donation}$ (eV)	−0.70	−0.50	−0.72	−0.53

4.5.1 Frontier Molecular Orbital (FMO) Theory

According to this theory, chemical reactivity depends on interaction between the highest occupied molecular orbital (HOMO) and the lowest unoccupied molecular orbital (LUMO) of both inhibitor and mild steel surface. The HOMO energy (E_{HOMO}) represents the ability of a molecule to donate electrons, while the LUMO energy (E_{LUMO}) indicates its ability to accept electrons. A higher (E_{HOMO}) value means that the inhibitor can easily donate electron to the metal surface, whereas a lower (E_{LUMO}) value suggest that the inhibitor can readily accept electrons from the metal. In theory, HOMO regions of inhibitor molecules act as electron-donating sites that transfer electrons into the empty or partially filled d orbitals of iron (Fe). At the same time, electrons from filled orbitals of Fe can be transferred to the LUMO regions of the inhibitor molecules through electron sharing (Alamiery, 2021).

4.5.1.1 HOMO and LUMO Discussion

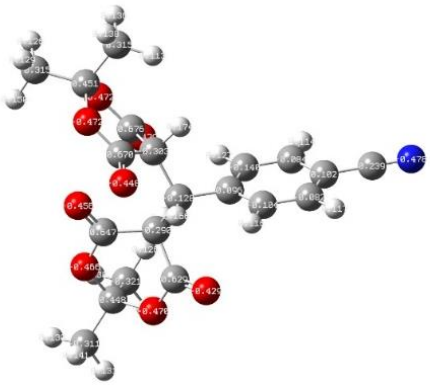
E_{HOMO} reflects the ability of an inhibitor to donate electrons to the vacant 3*d* orbitals of Fe atom which is essential for chemisorption. Based on DFT calculations, the E_{HOMO} values of studied inhibitor followed the order of PYMA (-9.72) < FBMA (-7.07 eV) < THMA (-6.54 eV) < TOMA (-6.36 eV) . A higher HOMO energy indicates that electrons can be donated more easily, whereas a lower HOMO value represents stronger electron confinement within the molecule and reduced electron-donating ability. Therefore, TOMA and THMA possess a greater tendency to donate electron density toward the vacant d-orbitals of iron compared with FBMA and PYMA (Mamand et al., 2023).

The adsorption of FBMA and PYMA exhibit low relative value, this is due FBMA is mainly governed by physical interactions, including electrostatic attraction between protonated inhibitor species and the charged mild steel surface, together with effective surface coverage. This agrees with the Gibbs free energy result, where FBMA exhibited $\Delta G°ads = -19.4$ kJ mol^{-1}, indicating predominantly physisorption behaviour. Meanwhile, the relatively low value for PYMA may be due to differences in the DFT calculation setup. Unlike the other three compounds, which were modelled using crystal structure data, PYMA was calculated using a molecular structure, which may have influenced the computed adsorption properties.

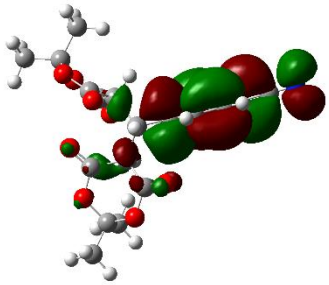
On the other hand, the E_{LUMO} indicates the ability of an inhibitor to accept electron from back donation, strengthening metal inhibitor bonding. The values for FBMA, THMA, TOMA and PYMA are -1.47 eV, -2.58 eV, -0.60 eV and -5.48 eV. The E_{LUMO} values indicate that PYMA possesses the strongest electron-accepting capability due to its significantly lower LUMO energy, followed by THMA, FBMA and TOMA. The low ELUMO value of PYMA suggests that electron transfer from the mild steel surface to the inhibitor molecule is energetically favourable, promoting acceptor–donor interactions during adsorption (Quadri et al., 2022).

The HOMO–LUMO energy gap (ΔE) reflects molecular reactivity and adsorption flexibility. The calculated energy gap (ΔE) values for FBMA, THMA, TOMA and PYMA are 5.60 eV, 3.96 eV, 5.76 eV and 4.24 eV forming an order of THMA< PYMA< FBMA<TOMA. A smaller (ΔE) values implies that less energy is required for electron excitation from the HOMO to the LUMO, in addition, a reduced energy gap lowers the energy barrier for electron transfer, making the interaction between the inhibitor and mild steel surface easier.

THMA has the smallest ΔE (3.96 eV), which facilitates both electron transfer and electrostatic interactions, explaining its mixed chemisorption–physisorption behavior. TOMA, with the largest ΔE (5.76 eV), still undergoes chemisorption due to high E_{HOMO} but requires physisorption to assist surface coverage. PYMA's intermediate ΔE (4.24 eV) supports physical adsorption dominance. The HOMO–LUMO energy gap of the synthesized Meldrum's acid derivatives is shown in Figures 4.38–4.41, which give an insight into their electronic properties and chemical reactivity.

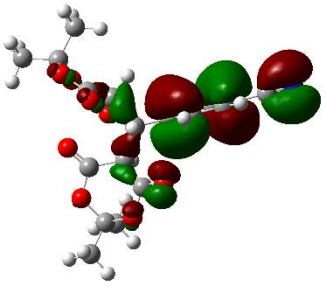


Optimized geometry of FBMA



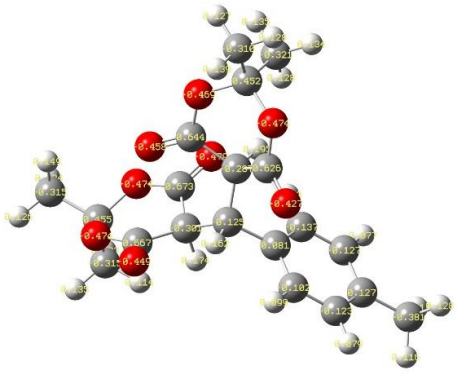
E_{LUMO} = - 1.47eV

ΔE= 5.60 eV

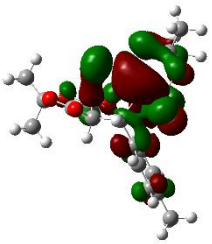


E_{HOMO} = - 7.07eV

Figure 4.35 Energy Band Gap at DFT Level for FBMA

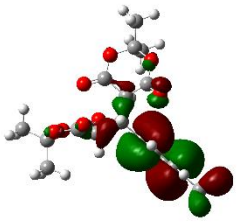


Optimized geometry of TOMA



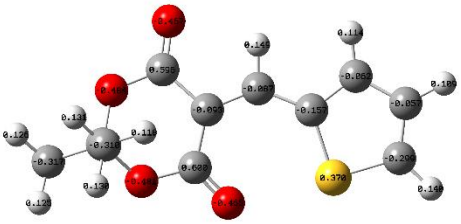
E_{LUMO} = - 0.60eV

ΔE= 5.76 eV

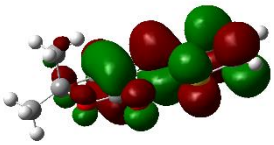


E_{HOMO} = - 6.36eV

Figure 4.36 Energy Band Gap at DFT Level for TOMA



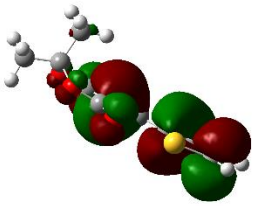
Optimized geometry of THMA



E_{LUMO} = - 2.58 eV

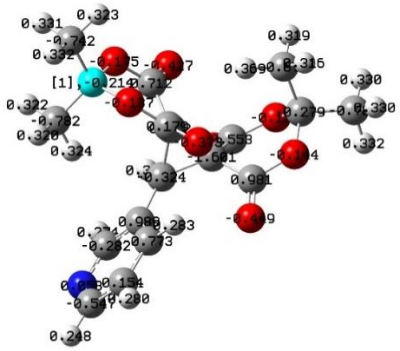


ΔE= 3.96 eV

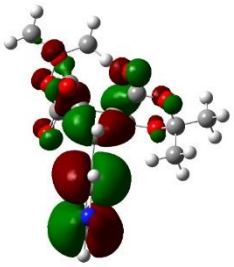


E_{HOMO} = - 6.54 eV

Figure 4.37 Energy Band Gap at DFT Level for THMA

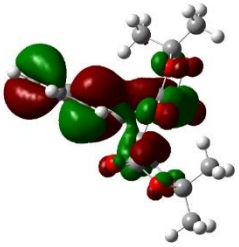


Optimized geometry of PYMA



ELUMO = - 0.20 eV

ΔE= 4.24 eV



EHOMO = - 0.36 eV

Figure 4.38 Energy Band Gap at DFT Level for PYMA

4.5.1.2 Ionization Potential (IP) and Electron Affinity (EA)

Ionization potential (IP) represents the energy required to remove an electron from an inhibitor molecule. A higher IP indicates that the molecule is more stable and less likely to lose electrons (Ferkous et al., 2024). From the Table 4.21 the IP values follow order PYMA (9.72 eV) > FBMA (7.07 eV) > THMA (6.54 eV) > TOMA (6.36 eV). This trend is consistent with E_{HOMO} values, where PYMA show the lowest E_{HOMO} value, indicating stronger electron binding and higher molecular stability.

The high IP of PYMA suggest that it is less prone to electron removal compared to other inhibitors. The presence of a pyridine and two Meldrum acid's rings which were both are electron withdrawing groups. The nitrogen from pyridyl ring pull electron away from nearby parts of molecule through chemical bond and by resonance effect. While the dual carbonyl groups from Meldrum's acid ring stabilize the molecular orbital (Ferkous et al., 2024). These combined effects make PYMA the most electronically stable and least prone to electron loss. FBMA also exhibits a relatively high IP due to the presence of cyano and carbonyl substituents, which reduce electron density across the molecule. This electronic stabilization limits charge transfer to the mild steel surface and supports physisorption-dominated adsorption.

In contrast, THMA has only one Meldrum's acid ring, naturally thiophene ring is electron rich due to the sulfur atom shares extra electron with the rest of the ring. The lower ionization potential is attributed to its higher electron density, which enhances its ability to donate electron readily to the mild steel surface. TOMA also have two Meldrum's rings with the presence of methyl groups on aromatic ring, that donates electron inductively. This slightly enhances electron density, leading to the lowest IP among the studied compounds. Thus, the IP order PYMA > FBMA > THMA > TOMA reflects the balance between the number of Meldrum's acid groups and the electronic nature of the aromatic substituents, with electron-withdrawing groups (pyridyl, cyano, formyl) producing higher IP values and electron-donating groups (thiophene, methyl) lowering them (Verma et al., 2022).

Electron affinity (EA) describes the ability of a molecule to accept electrons and is approximately equal to negative value of the LUMO energy. Higher EA values correspond to lower E_{LUMO} values. The EA values obtained follow the sequence PYMA (5.48) > THMA (2.58 eV) > FBMA (1.47 eV)>TOMA (0.60 eV). This trend shows that a higher EA indicates a greater ability to accept electron to accept electrons favouring chemical adsorption (chemisorption), while lower EA for physical adsorption (physisorption). PYMA show the highest EA (5.48 eV) due to the combined electron withdrawing effects of pyridyl nitrogen and two Meldrum's acid rings. This high electron affinity allows PYMA to easily accept electron.

THMA, with moderate EA (2.58 eV), contains one Meldrum's acid ring and contain sulfur in thiophene ring. The thiophene ring donates electron density, which slightly reduces electron acceptance, but the molecule can still partially adsorb chemically, leading to mixed inhibition. FBMA, despite having moderate EA, lacks

sufficient electron donation capability, resulting in adsorption dominated by physical interaction. Finally, TOMA, with the lowest EA (0.60 eV) due to electron-donating methyl groups, interacts mainly through physical forces, resulting in mixed inhibition. The presence of electron-donating groups has reduced the tendency of TOMA to accept more electrons. Although higher EA and higher IP can predict the efficiency of inhibition and type of adsorption, but from the weight loss and isotherm studies shows that the inhibition efficiency were ranked by FBMA > TOMA > PYMA > THMA.

The conflict-of-interest for this consistency may be due to the difference in molecular model used for DFT calculations. PYMA was optimized using a theoretical molecular structure. While FBMA, THMA and TOMA were modelled using crystallographic data. Crystal derived molecular structures represent more realistic bond lengths, molecular shapes and internal interactions. These features strongly influence how electrons are distributed to the molecule and how the inhibitor approaches and also how it attaches to the mild steel surface (Verma et al., 2022). In contrast, Optimized structures are calculated in isolation and may exaggerate electron-accepting ability and polarity. As a result, DFT parameters such as electron affinity may appear higher than what occurs during adsorption on the mild steel surface.

Steric effects and molecular orientation at the mild steel-solution interface also play an important role. Although PYMA shows high electron affinity and ionization potential, its bulky and rigid structure can limit close contact with the mild steel surface. This reduces effective orbital overlap between PYMA and iron atoms, weakening chemical bonding. On the other hand, FBMA has a more suitable molecular shape that allows better fits to the mild steel surface, stronger electron donation and back-donation and more effective coordination through heteroatoms. This leads to the formation of a stable protective film and explains its higher inhibition efficiency and chemisorption behavior.

Factors such as protonation of inhibitor molecules in acidic media, competition with chloride ions and interactions with solvent molecules can significantly influence adsorption strength and surface coverage. These effects are especially important for PYMA and THMA, which depend partly on electrostatic interactions. Therefore, the actual inhibition performance is controlled by a combination of electronic properties, molecular structure, adsorption orientation and interfacial effects, rather than electron affinity or ionization potential alone (Verma et al., 2022).

4.5.1.3 Dipole Moment (D)

Dipole moment is commonly used to describe the polarity of a molecule and related to its solubility in polar media such as acidic solution. A higher dipole moment usually indicates higher polarity and better solubility, which can enhance interaction with metal surface. Dipole moment plays a major role in physisorption, as it enhances the electrostatic attraction between inhibitor molecules and charged metal surface in acidic medium (Shashirekha et al., 2024; Muhtar et al., 2024).

Based on the calculated values, the dipole moments of the synthesized Meldrum's acid derivatives decrease in the order of PYMA (7.60 D) > THMA (4.56 D) > FBMA (4.27 D) > TOMA (3.48 D). A higher dipole moment generally indicates greater molecular polarity, which can enhance electrostatic interactions between the inhibitor molecules and the charged mild steel surface, thereby favouring physisorption. Accordingly, PYMA, with the highest dipole moment (7.60 D), is expected to exhibit the strongest electrostatic attraction toward the metal surface. THMA, with a relatively high dipole moment (4.56 D), is likely to possess improved solubility in 1 M HCl, facilitating effective transport of the inhibitor molecules to the mild steel surface and promoting both electrostatic and donor–acceptor interactions, consistent with its mixed adsorption behaviour. FBMA (4.27 D) exhibits moderate polarity, which contributes to effective surface coverage and supports its predominantly physisorption mechanism. In contrast, TOMA, with the lowest dipole moment (3.48 D), is comparatively less polar, resulting in weaker electrostatic interactions with the metal surface.

Although PYMA possesses the highest dipole moment, its inhibition efficiency is lower than that of FBMA and TOMA. This indicates that a high molecular polarity alone does not guarantee better corrosion inhibition, which is generally weaker and less stable in aggressive acidic environments (Muhtar et al., 2024). As a result, the protective film formed by PYMA is more susceptible to desorption, or over time, the molecules easily let go and drift away. THMA, with a relatively high dipole moment, also relies on electrostatic interactions. While this enhances its solubility and surface approach, more physisorption limits the stability of its adsorbed layer, explaining its comparatively lower inhibition efficiency observed in weight loss studies. FBMA displays moderate polarity, which favors surface approach and electrostatic interaction without significant charge transfer. This characteristic supports stable physisorption, allowing FBMA molecules to form a uniform protective layer despite limited chemical

bonding. TOMA, with the lowest dipole moment, exhibits weaker electrostatic attraction and relies mainly on surface coverage effects (Shashirekha et al., 2024).

The inconsistency between dipole moment trends and weight loss results highlights that high polarity enhances physisorption but does not guarantee high inhibition efficiency. Instead, effective corrosion inhibition is governed by a balance between molecular polarity, electronic interaction strength, adsorption stability and surface film integrity, with chemisorption playing a dominant role in achieving long-term protection.

4.5.1.4 Electronegativity (χ)

Electronegativity (χ) describes the tendency of an inhibitor molecule to attract electrons toward itself and plays a crucial role in corrosion inhibition by governing the direction and magnitude of charge transfer between the inhibitor and the metal surface. According to the charge-transfer model, when the electronegativity of an inhibitor is lower than that of iron, electrons are preferentially transferred from the inhibitor to the metal surface, thereby promoting chemisorption and the formation of stable chemical bonds (Shashirekha et al., 2024; Obot et al., 2021).

Based on the DFT calculations, the electronegativity values decrease in the order: PYMA (7.60 eV) > THMA (4.56 eV) > FBMA (4.27 eV) > TOMA (3.48 eV). FBMA and TOMA exhibit relatively low electronegativity values, indicating a strong tendency to donate electrons to the vacant *d*-orbitals of iron. FBMA and TOMA, with lower electronegativity values, are more capable of electron donation; however, FBMA's strong internal electron stabilization limits effective charge transfer, resulting in physisorption-dominated adsorption. In contrast, PYMA possesses the highest electronegativity value (7.60 eV), indicating a strong tendency to attract electrons rather than donate them. This pronounced electron-withdrawing character reduces effective electron donation to the mild steel surface and disrupts balanced donor–acceptor interactions. Consequently, PYMA adsorption is dominated by electrostatic attraction and physisorption, which leads to weaker and less stable surface coverage in the aggressive acidic environment (Obot et al., 2021).

THMA exhibit intermediate electronegativity values, suggesting that electron donation to the metal surface is possible; however, their adsorption behavior differs from that of FBMA due to structural effects. THMA contains a thiophene ring, which

is electron-rich and acts as an electron-donating group. Although the sulfur atom can participate in surface adsorption, the electron-donating nature of the thiophene ring reduces the overall electron-accepting ability of the molecule, thereby weakening chemisorption and resulting in mixed adsorption behavior (Obot et al., 2021).

Overall, the electronegativity analysis demonstrates that balanced electronegativity, rather than extreme electron-withdrawing or electron-donating tendencies, is essential for effective corrosion inhibition. PYMA, THMA, FBMA and TOMA are limited by dominant physisorption or mixed adsorption mechanisms.

4.5.1.5 Electronic Chemical Potential (μ)

The electronic chemical potential (μ) represents the tendency of an inhibitor molecule to release or accept electrons during interaction with a metal surface. It is defined as the negative of electronegativity ($\mu = -\chi$) and therefore provides direct insight into the direction of electron flow between the inhibitor and mild steel. In corrosion inhibition, a less negative μ value indicates a higher tendency for electron donation to the metal surface, which favors chemisorption through coordinate bond formation with Fe atoms, while a highly negative μ value reflects stronger electron-withdrawing behavior that promotes physisorption (Obot et al., 2021; Muhtar et al., 2024).

Based on DFT calculations, the electronic chemical potential values follow the order PYMA (−7.60 eV) < THMA (−4.56 eV) < FBMA (−4.27 eV) < TOMA (−3.48 eV). FBMA exhibits a moderately negative μ value, indicating limited electron donation capability and supporting adsorption dominated by physical interactions. This behavior aligns with its positive inhibition efficiency derived mainly from surface coverage and electrostatic attraction rather than chemical bonding.

THMA and TOMA show slightly high negative μ values of −4.56 and −3.48 eV, respectively, indicating that electron donation to the mild steel surface is feasible but less optimally balanced compared to FBMA. As a result, these molecules undergo simultaneous electron donation and electrostatic interaction, leading to mixed adsorption behavior involving both chemisorption and physisorption. This observation agrees well with their moderate ΔN values and experimentally observed intermediate inhibition efficiencies (Muhtar et al., 2024).

In contrast, PYMA exhibits a highly negative electronic chemical potential (−7.60 eV), reflecting a strong tendency to attract electrons rather than donate them.

This behavior is consistent with its negative ΔN value and indicates that electron donation from PYMA to the mild steel surface is energetically unfavorable. The strong electron-withdrawing nature of the pyridyl nitrogen and Meldrum's acid moieties significantly reduces electron density available for donation, resulting in adsorption dominated by electrostatic interactions and physical adsorption, with only a limited contribution from chemisorption.

THMA exhibits mixed adsorption behavior due to the presence of a thiophene ring, which acts as an electron-donating group and increases electron density but weakens effective electron withdrawal, thereby limiting strong chemisorption. Additionally, THMA contains only one Meldrum's acid unit, reducing the number of available adsorption sites.

Similarly, TOMA contains a methyl substituent, a strong electron-donating group that increases electron density on the aromatic ring but raises the LUMO energy, weakening back-donation interactions. Although TOMA has the least negative μ value, its adsorption behavior is governed mainly by enhanced surface coverage and physical adsorption rather than strong chemical bonding.

These findings demonstrate that FBMA adsorption is predominantly physisorption-controlled, while THMA and TOMA exhibit mixed adsorption and PYMA relies heavily on electrostatic interaction. The combined interpretation of FMO parameters, molecular structure and experimental inhibition trends confirms that effective corrosion inhibition arises from a balance between molecular polarity, adsorption stability and surface coverage rather than chemisorption alone (Muhtar et al., 2024).

4.5.1.6 Global Hardness (η) and Softness (S)

Global Hardness(η) and softness (S) are important parameters used to describe the stability and reactivity of molecules. Hardness represents molecules resistance to changes in electron cloud, while softness is the opposite and reflects how easily the electron cloud can be distorted during chemical interaction. Generally, molecules with high hardness are more stable and less reactive, whereas molecules with high softness are more reactive and usually have smaller energy gaps (Shashirekha et al., 2024).

Based on the data in Table 4.21, all inhibitors studied show energy gap (ΔE) values lower than 10 eV, indicating that FBMA, THMA, TOMA and PYMA behave as

soft molecules. This suggests that all inhibitors are reactive enough to participate in electron transfer processes with mild steel. The calculated hardness values follow the order: TOMA > FBMA > PYMA > THMA, while the softness values follow the reverse trend: THMA > PYMA > FBMA > TOMA. Among the studied inhibitors, THMA exhibits the lowest hardness (1.98 eV) and highest softness (0.51 eV^{-1}), indicating the highest intrinsic molecular reactivity, whereas TOMA shows the highest hardness (2.88 eV) and lowest softness (0.35 eV^{-1}).

High softness generally enhances adsorption by facilitating electron cloud deformation and improving interaction with the mild steel surface through both electrostatic attraction and orbital interaction. Accordingly, THMA (0.51 eV^{-1}) and PYMA (0.47 eV^{-1}) exhibit relatively high softness values, favouring adsorption behaviour involving significant physical interaction and limited chemical contribution. In contrast, FBMA (0.36 eV^{-1}) and TOMA (0.35 eV^{-1}) possess lower softness and higher hardness, indicating comparatively reduced tendency for strong orbital overlap with the mild steel surface (Shashirekha et al., 2024).

Despite not being the softest molecule, FBMA exhibits better inhibition efficiency, demonstrating that softness alone does not govern corrosion inhibition performance. The moderate hardness of FBMA arises from the presence of two Meldrum's acid units and multiple carbonyl groups, which enhance molecular polarity and facilitate strong electrostatic interaction with the charged steel surface. These structural features promote effective surface coverage and the formation of a compact adsorbed layer dominated by physisorption (Obot et al.,2021). This behaviour is supported by SEM–EDX analysis, which reveals reduced iron signal intensity and increased carbon and oxygen contents, as well as weight-loss measurements showing the lowest corrosion rate and highest inhibition efficiency, confirming the formation of a stable protective film without the necessity of strong chemical bonding.

TOMA, although exhibiting the highest hardness, shows moderate inhibition efficiency due to the presence of a methyl substituent, which acts as an electron-donating group and enhances surface coverage through increased electron cloud deformability. This moderate softness enables effective physical adsorption; however, the relatively high LUMO energy limits back-donation and strong chemisorption. As a result, TOMA exhibits mixed adsorption behavior, supported by moderate XPS shifts, partial but uniform surface films observed in SEM–EDX, reduced surface roughness in AFM images and intermediate inhibition efficiency from weight-loss measurements.

PYMA displays moderate hardness and relatively high softness, which can be attributed to its conjugated pyridyl system and strong electron-withdrawing groups. Although its electron cloud is highly polarizable, the strong electron-withdrawing nature of the pyridyl nitrogen and Meldrum's acid units reduces effective electron donation to the mild steel surface. Consequently, PYMA can interact with the surface primarily through electrostatic interactions, while stable chemisorption is limited. This behavior is consistent with weight-loss measurements showing lower inhibition efficiency and adsorption dominated by physisorption (Obot et al.,2021).

In contrast, THMA, despite exhibiting the highest softness, shows the lowest inhibition efficiency. This behavior is attributed to its molecular structure, which contains only one Meldrum's acid unit and a thiophene ring. Although the sulfur atom can participate in adsorption, the electron-rich nature of the thiophene ring limits effective donor–acceptor interactions and reduces the stability of chemisorption bonds. As a result, THMA adsorption is dominated by weaker interactions, leading to reduced surface protection and the lowest inhibition efficiency among the studied inhibitors.

Overall, the hardness and softness analysis confirms that corrosion inhibition efficiency depends not only on molecular reactivity but also on structural features that promote stable surface coverage. FBMA achieves optimal performance through moderate softness combined with favourable molecular polarity and surface packing, resulting in effective physisorption-dominated inhibition.

4.5.1.7 Electrophilicity (ω) and Nucleophilicity (ε) Index

Electrophilicity (ω) and nucleophilicity (ε) indices are useful parameters for understanding electron transfer between inhibitor molecules and the metal surface. Electrophilicity measures a molecule's tendency to accept electrons, whereas nucleophilicity represents its tendency to donate electrons (Mamand et al., 2023; Muhtar et al., 2024). These two parameters are inversely related. Based on the calculated values in Table 4.21, the electrophilicity index follows the order: PYMA > TOMA > FBMA > THMA, while the nucleophilicity index shows the reverse trend: THMA > FBMA > TOMA > PYMA. These trends are consistent with the E_{HOMO}, E_{LUMO}, electron affinity and ionization potential values discussed earlier and reflect the strong influence of molecular structure and functional groups on charge-transfer behaviour

TOMA exhibits the highest electrophilicity, indicating a stronger tendency to accept electrons. This is due to the presence of carbonyl groups within the Meldrum's acid rings and the conjugated aromatic system, which can stabilize back-donated electron density (Mamand et al., 2023). However, the methyl substituent in TOMA acts as an electron-donating group (EDG), increasing electron density and raising the LUMO energy, which limits effective back-donation and weakens chemisorption. As a result, despite its relatively high electrophilicity, TOMA exhibits mixed adsorption behaviour dominated by physical interactions.

In contrast, THMA shows the highest nucleophilicity, confirming that it is the most electron rich molecule among the studied inhibitors and has the strongest tendency to donate electrons to the iron surface. This behaviour is due to the thiophene ring, which is rich in π-electrons and acts as a strong electron-donating group (Muhtar et al., 2024). Although this electron donation, it simultaneously reduces the molecule's ability to accept electrons back from the metal surface, resulting in an imbalance in donor–acceptor interactions. Furthermore, THMA contains only one Meldrum's acid unit, limiting the number of available adsorption sites. Consequently, THMA adsorption is weak and largely by mixed or physical interactions, which explains its low inhibition efficiency (Shashirekha et al., 2024).

FBMA exhibits moderate electrophilicity and nucleophilicity, indicating balanced charge-transfer capability. However, the strong electron-withdrawing cyano and carbonyl groups increase molecular polarity rather than promoting stable donor–acceptor bonding. As a result, FBMA adsorption is governed mainly by electrostatic attraction and surface coverage effects, leading to physisorption-dominated inhibition, despite its high experimental efficiency. PYMA exhibits the highest electrophilicity and the lowest nucleophilicity among the studied inhibitors, indicating a strong tendency to accept electrons but a weak ability to donate electrons. This is because of the presence of the pyridyl nitrogen and strong electron withdrawing Meldrum's acid rings, which reduce the electron density for donation (Shashirekha et al., 2024). As a result, PYMA relies on electron acceptance and electrostatic attraction rather than strong donor acceptor chemisorption. This imbalance leads to adsorption dominated by physisorption, weight-loss measurements demonstrate lower inhibition efficiency compared to FBMA and TOMA.

In conclusions, the electrophilicity and nucleophilicity analyses confirm that effective corrosion inhibition requires a balanced donor acceptor interaction rather than

extreme electron-donating or electron-accepting tendencies. Although THMA is highly nucleophilic and PYMA is highly electrophilic, both exhibit inferior inhibition performance due to electronic imbalance and structural limitations. FBMA achieves high inhibition efficiency due to its optimal balance of electrophilicity and nucleophilicity, favourable EWG effects and multiple adsorption sites, while TOMA exhibits intermediate performance by mixed adsorption behaviour. These findings further emphasize that electrophilicity and nucleophilicity must be interpreted alongside molecular structure and experimental surface analyses to accurately explain corrosion inhibition mechanisms.

4.5.1.8 Electron-Donating (ω^-) and Electron-Accepting (ω^+) Power

Electron-donating (ω^-) and electron-accepting (ω^+) powers provide further insight into charge transfer between inhibitors and the metal surface. A lower ω^- value indicates a stronger ability to donate electrons, while a higher ω^+ value indicates a stronger ability to accept electrons (Mamand et al., 2023; Obot et al.,2021). The calculated ω^- values indicate that THMA has the strongest electron-donating ability, followed by FBMA and TOMA. Conversely, TOMA shows the highest ω^+ value, indicating a stronger tendency to accept electrons. These trends are consistent with the E_{HOMO}, E_{LUMO}, electrophilicity and nucleophilicity results. THMA, with its strong electron-donating ability, is expected to interact effectively with the mild steel surface by donating electron density and forming a protective adsorbed layer. However, the experimental inhibition efficiency does not strictly follow this trend, as FBMA still shows better performance. This confirms that electron-donating and electron-accepting power alone do not directly control inhibition efficiency.

PYMA exhibits relatively high ω^+ but very weak ω^-, indicating strong electron-accepting ability but poor electron-donating capability. This behaviour is attributed to the presence of the pyridyl nitrogen and strong electron-withdrawing Meldrum's acid units, which significantly reduce electron density available for donation. Unlike FBMA, TOMA and THMA, the electronic behaviour of PYMA is dominated primarily by its isolated molecular structure rather than collective surface or film-formation effects. As a result, the DFT-calculated parameters for PYMA strongly reflect intrinsic molecular electron withdrawal, leading to excessive electron-accepting character and weak donor–acceptor balance (Mamand et al., 2023). In contrast, FBMA, TOMA and THMA exhibit

adsorption behaviour that is more strongly influenced by surface-driven and condensed-phase effects, including molecular orientation, intermolecular interactions and packing density within the adsorbed film. These crystal- or film-related effects enhance cooperative adsorption and stabilize the protective layer on the mild steel surface, which is not fully captured by isolated-molecule DFT descriptors. Consequently, PYMA adsorption is dominated by electrostatic interactions and physisorption, whereas the other inhibitors benefit from synergistic surface interactions that promote stronger chemisorption.

Overall, the electron-donating and electron-accepting power analysis confirms that neither strong electron donation (as in THMA) nor strong electron acceptance (as in PYMA) alone guarantees effective corrosion inhibition. FBMA achieves better performance due to its balanced ω^- and ω^+ values combined with favourable surface and film-formation effects, while TOMA exhibits intermediate performance due to mixed adsorption behaviour (Obot et al.,2021). The pronounced deviation of PYMA arises from its adsorption being governed primarily by molecular electronic structure rather than collective surface interactions. These findings demonstrate that effective corrosion inhibition requires synergistic charge-transfer interactions supported by appropriate molecular structure and surface-driven stabilization, rather than extreme electronic properties alone.

4.5.1.9 Number of Electrons Transferred (ΔN)

The number of electrons transferred (ΔN) estimates the extent of charge transfer between the inhibitor and iron. Electron transfer occurs from the inhibitor to the metal until their electronegativities reach equilibrium. In this study, a theoretical electronegativity value of 7 eV for iron and zero hardness were used for the calculation (Mamand et al., 2023).

The fraction of electron transfer (ΔN) is a key quantum chemical parameter used to predict both the direction and extent of charge transfer between an inhibitor molecule and a metal surface. A positive ΔN value indicates that electrons are transferred from the inhibitor to the metal, which promotes the formation of coordinate bonds between electron-rich heteroatoms (such as N and O) and Fe atoms (Quadri et al., 2022). This type of interaction is characteristic of chemisorption. Conversely, a negative ΔN value

suggests that electron transfer from the inhibitor to the metal is unfavorable, thereby weakening chemical bonding and favoring physisorption.

The calculated ΔN values follow the order: PYMA < THMA < FBMA < TOMA. All ΔN values are well below the threshold of 3.6, indicating that electron donation from the inhibitors to the iron surface is favourable. PYMA shows the highest ΔN value, suggesting a greater tendency to donate electrons, while THMA shows the lowest. Based on the calculated results, FBMA (ΔN = 0.10), THMA (ΔN = 0.07) and TOMA (ΔN = 0.23) exhibit positive ΔN values, confirming spontaneous electron donation from these inhibitor molecules to the mild steel surface (Quadri et al., 2022). Among them, TOMA shows the highest ΔN value, indicating the strongest electron-donating tendency, however, the relatively small ΔN value of FBMA suggests that charge transfer is weak and insufficient to establish strong chemical bonding. Therefore, FBMA adsorption remains physisorption-dominated, driven by electrostatic interaction rather than coordinate bond formation. THMA, with the smallest positive ΔN value, exhibits weaker electron donation, resulting in a mixed adsorption mechanism involving both chemical and physical interactions (Mamand et al., 2023).

In contrast, PYMA with a negative ΔN value (−0.53), shows that electron donation from PYMA to the iron surface is unfavourable and that the interaction is from electron acceptance to the metal. This is because from the strong electron-withdrawing character of the pyridyl nitrogen and the conjugated Meldrum's acid units, which significantly reduce the availability of electron density for donation. Consequently, PYMA shows limited ability to form stable iron–inhibitor coordinate bonds and its adsorption is governed predominantly by electrostatic attraction and physical adsorption, in agreement with experimental observations.

4.5.1.10 Back-Donation Energy (ΔE Back-Donation)

As shown in Table 4.21, all inhibitors exhibit negative $\Delta E_{back\text{-}donation}$ values, confirming that Fe→inhibitor back-donation is thermodynamically possible for FBMA, THMA, TOMA and PYMA that this interaction plays an important role in adsorption. FBMA and TOMA display strongly negative back-donation energies of −0.70 and −0.72 eV, respectively, which can be attributed to their molecular structures containing extended π-electron systems and multiple electron-accepting functional groups capable of accommodating electron density from Fe *d*-orbitals. This efficient two-way charge

transfer, involving both inhibitor→Fe donation and Fe→inhibitor back-donation, promotes the formation of stable donor–acceptor bonds. This interpretation is strongly supported by XPS analysis, which reveals the presence of and Fe–O bonding peaks and noticeable binding energy shifts, confirming chemical interaction at the steel surface while SEM-EDX results reveal higher C, N and O elemental contents, confirming strong surface coverage. These findings correlate well with weight-loss measurements, where FBMA and TOMA exhibit better inhibition efficiencies due to the formation of stable adsorbed layers (Alamiery, 2021).

THMA exhibits a moderately negative back-donation energy (−0.50 eV), suggesting that Fe→inhibitor back-donation occurs but to a lesser extent. This behavior is related to its molecular structure, which contains electron-donating heteroatoms but comparatively weaker electron-accepting sites, limiting efficient orbital overlap with Fe d-orbitals. As a result, adsorption of THMA involves both chemical bonding and electrostatic interactions, leading to a mixed adsorption mechanism. This conclusion is supported by XPS spectra showing weaker Fe–heteroatom interactions, SEM observations revealing partial surface protection (Quadri et al., 2022). The corresponding weight-loss results further confirm moderate inhibition efficiency, consistent with mixed adsorption behavior.

In contrast, PYMA displays an excessively negative back-donation energy (−14.54 eV), which indicates abnormal and unstable electronic interaction rather than effective chemical bonding. Such an extreme value suggests poor orbital matching and electronic imbalance, leading to weak and unstable adsorption. Consequently, PYMA does not form stable chemical bonds with the Fe surface and relies primarily on physisorption, consistent with its negative ΔN value and high dipole moment. This interpretation is fully consistent with its negative ΔN value, the absence of strong Fe–N or Fe–O bonding features in XPS spectra, higher surface roughness observed in AFM analysis, limited elemental enrichment in SEM-EDX and the lowest inhibition efficiency obtained from weight-loss measurements.

4.5.2 Molecular Electrostatic Potential (MEP)

The molecular electrostatic potential (MEP) diagram of Meldrum's acid derivatives (Figures 4.42 - 4.45) shows the distribution of electron-rich and electron-deficient regions, which determine its adsorption behaviour on the mild steel surface.

4.5.2.1 MEP, Interpretation of FBMA

The MEP map of FBMA (Figure 4.39) shows that the most intense red regions are mainly localized around the oxygen atoms of the carbonyl (C=O) groups in the 1,3-dioxane-4,6-dione rings. These red regions indicate areas with high electron density, identifying the carbonyl oxygen atoms as the primary nucleophilic sites in the molecule (Moradi et al., 2011). A moderate red region is also observed near the nitrile nitrogen (–C≡N), reflecting its electronegative nature and ability to participate in electron donation (Fouda et al., 2021).

In contrast, blue regions are observed around the hydrogen atoms and parts of the aromatic ring, indicating electron-deficient areas. The uneven charge distribution across the molecule arises from resonance and inductive effects, where electron-withdrawing carbonyl and nitrile groups pull electron density toward themselves (Moradi et al., 2011; Fouda et al., 2021). From a DFT perspective, the red regions correspond to areas with higher HOMO contribution, suggesting that the carbonyl oxygen atoms and nitrile nitrogen are the main sites capable of donating electrons to the vacant *d*-orbitals of iron. According to HSAB theory, these oxygen and nitrogen atoms behave as hard Lewis bases, which can still interact effectively with the iron surface through coordinate bonding and electrostatic attraction.

Overall, the MEP analysis indicates that FBMA adsorbs on the mild steel surface predominantly through physisorption, driven by electrostatic attraction between the negatively charged regions (carbonyl oxygen and nitrile nitrogen) and the positively charged metal surface. This adsorption leads to the formation of a protective molecular film that reduces anodic dissolution of mild steel and retards the corrosion process (Fouda et al., 2021; Obot et al., 2021). The absence of strong Fe–O or Fe–N coordinate bond formation confirms that the inhibition mechanism of FBMA is governed mainly by physisorption rather than chemisorption.

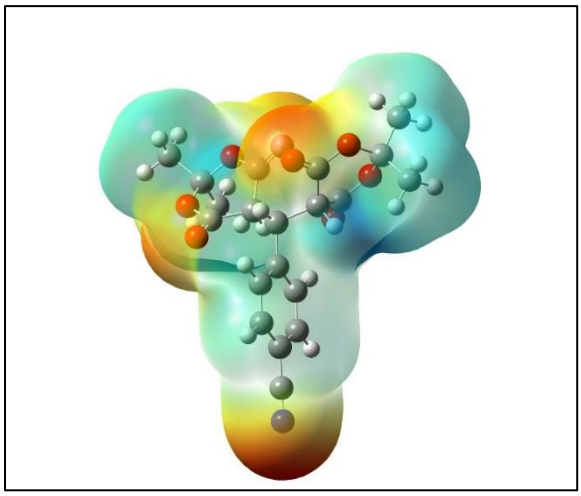


Figure 4.39 MEP Diagram for FBMA

4.5.2.2 MEP, Interpretation of TOMA

The MEP diagram of TOMA (Figure 4.40) reveals strong red regions concentrated around the carbonyl oxygen atoms of both 1,3-dioxane-4,6-dione units. These oxygen atoms show the highest electron density in the molecule, indicating that they are the most reactive nucleophilic sites. The presence of two dione rings increases the number of electron-rich centres, which enhances the adsorption capability of TOMA (Verma et al., 2018; Fouda et al., 2021).

The aromatic *p*-tolyl group displays mainly green to light-yellow regions, suggesting moderate electron density, while blue regions are seen around hydrogen atoms, indicating electron-poor sites (Verma et al., 2018). The electron density distribution is governed by resonance effects between the aromatic ring and the carbonyl groups, as well as inductive electron withdrawal by the carbonyl functionalities. In DFT terms, the carbonyl oxygen atoms correspond to HOMO-dominated regions, enabling efficient electron donation to the iron surface. Based on HSAB theory, although oxygen atoms are relatively hard bases, their high electron density and multiple coordination sites allow strong adsorption through donor acceptor interactions.

As a result, the MEP analysis suggests that TOMA forms a stable adsorbed layer through multiple carbonyl oxygen atoms, leading to improved surface coverage and effective corrosion inhibition of mild steel. The intense red regions around the carbonyl oxygen atoms indicate areas of high electron density, which favour electron donation to the vacant d-orbitals of iron, leading to the formation of coordinate Fe–O bonds

characteristic of chemisorption. In contrast, the green to light-yellow regions over the aromatic p-tolyl ring represent areas of moderate electron density, which promote electrostatic attraction and van der Waals interactions with the charged metal surface, contributing to physisorption (Verma et al., 2018).

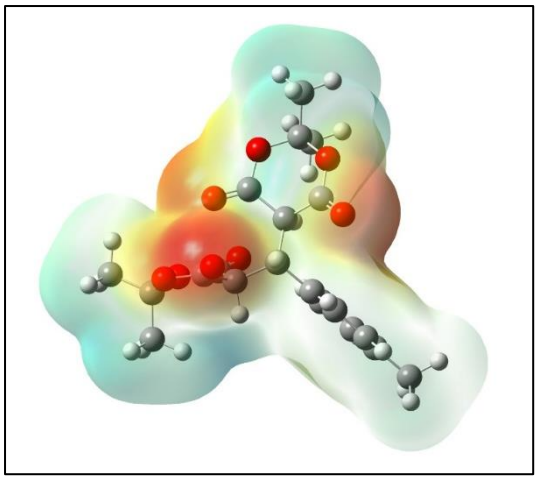


Figure 4.40 MEP Diagram for TOMA

4.5.2.3 MEP, Interpretation of THMA

The MEP map of THMA (Figure 4.41) shows prominent red regions located around the carbonyl oxygen atoms of the dioxane-4,6-dione ring, like FBMA and TOMA. In addition, a distinct red region is also observed around the sulphur atom of the thiophene ring, indicating that this sulphur atom possesses relatively high electron density. Blue regions are mainly found around hydrogen atoms and some carbon atoms, representing electron-deficient sites. The coexistence of oxygen- and sulphur-rich regions is due to resonance interaction between the thiophene ring and the conjugated methylene linkage, which enhances electron delocalization across the molecule. From a DFT viewpoint, the red regions around oxygen and sulphur atoms are associated with high HOMO density, making these atoms effective electron donors (Fouda et al., 2021). According to HSAB theory, the thiophene sulphur behaves as a soft base, which can interact strongly with the soft iron surface, while the carbonyl oxygen atoms provide additional anchoring points.

Therefore, the MEP analysis indicates that THMA adsorbs on mild steel through both sulphur and oxygen atoms, resulting in stronger and more stable adsorption. This synergistic interaction promotes the formation of a compact protective film, leading to

enhanced corrosion inhibition efficiency. The red regions surrounding the oxygen and sulphur atoms correspond to HOMO-dominated areas, enabling electron donation to the vacant *d*-orbitals of iron and leading to the formation of Fe–O coordinate bond, which is characteristic of chemisorption (Gece, 2008; Fouda et al., 2021). Simultaneously, the green/yellow and blue regions facilitate physisorption through electrostatic attraction and van der Waals interactions between the polar regions of THMA and the charged mild steel surface. According to HSAB theory, the thiophene sulphur behaves as a soft Lewis base and interacts strongly with the soft iron surface, while the carbonyl oxygen atoms provide additional anchoring points.

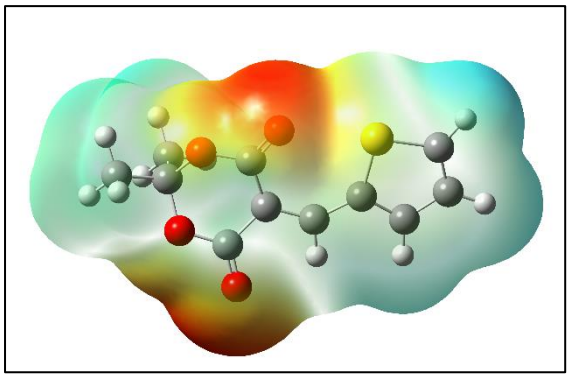


Figure 4.41 MEP Diagram for THMA

4.5.2.4 MEP, Interpretation of PYMA

The MEP map of PYMA (Figure 4.42) shows clear red regions mainly concentrated around the carbonyl oxygen atoms of the dioxane-4,6-dione moiety, indicating that these oxygen atoms possess high electron density and act as the primary nucleophilic sites in the molecule. In addition, a red region is also observed around the nitrogen atom of the pyridine ring, suggesting that this nitrogen atom is another important electron-rich center.

The blue regions are mainly located around hydrogen atoms and some carbon atoms, representing electron-deficient areas that are less involved in adsorption (Gece, 2008). The presence of both oxygen and nitrogen-rich regions is attributed to resonance and conjugation effects between the pyridine ring and the adjacent methylene linkage, which electron delocalization throughout the molecule. From a DFT perspective, the red regions around the oxygen and nitrogen atoms correspond to areas with high HOMO density, indicating strong electron-donating ability. According to HSAB theory, the

pyridine nitrogen can interact effectively with the iron surface, while the carbonyl oxygen atoms provide additional coordination sites, allowing PYMA to adsorb through multiple active centres.

Therefore, the MEP analysis suggests that PYMA adsorbs onto the mild steel surface mainly through its carbonyl oxygen and pyridine nitrogen atoms, leading to stronger interaction and improved surface coverage. This multi-site adsorption promotes the formation of a stable protective layer on the mild steel surface, contributing to effective corrosion inhibition. The intense red regions localized around the carbonyl oxygen atoms of the dioxane-4,6-dione moiety and the pyridine nitrogen atom reflect areas of high electron density, which facilitate electron donation to the vacant *d*-orbitals of iron and lead to the formation of coordinate Fe–O and Fe–N bonds characteristic of chemisorption (Gece, 2008; Fouda et al., 2021). In contrast, the green to light-yellow regions over the conjugated molecular framework and the blue regions surrounding hydrogen atoms represent areas of moderate and low electron density, respectively, which favour electrostatic attraction and van der Waals interactions with the charged mild steel surface, contributing to physisorption.

The charge distribution originates from resonance and conjugation between the pyridine ring and the methylene linkage, enabling electron delocalization and multi-site interaction. Physisorption in PYMA occurs primarily through electrostatic attraction and weak intermolecular forces. In the acidic corrosive environment, the pyridine nitrogen of PYMA can undergo protonation, producing positively charged PYMA species. These protonated molecules are physically attracted to the negatively charged mild steel surface, which is rendered negatively charged due to the adsorption of aggressive anions such as Cl^-. In addition, the conjugated aromatic framework and methylene-linked backbone of PYMA promote van der Waals interactions and π–metal interactions with the iron surface. These weak physical forces enable PYMA molecules to be initially anchored onto the metal surface, facilitating subsequent chemisorption and improving molecular orientation, surface coverage and stability of the protective film. Consequently, PYMA adsorbs on mild steel through a mixed chemisorption–physisorption mechanism, forming a stable and compact protective layer that enhances surface coverage and effectively inhibits the corrosion process.

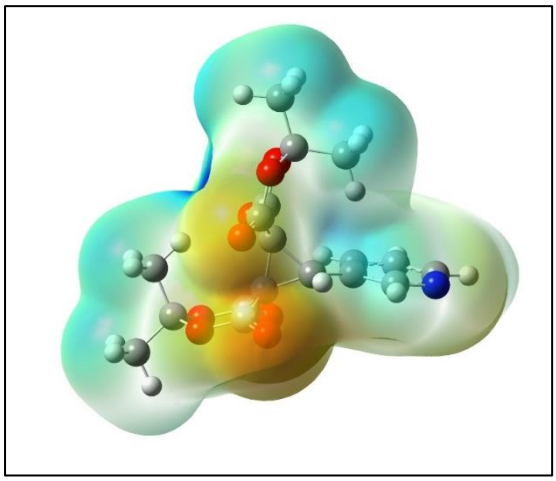


Figure 4.42 MEP Diagram for PYMA

4.5.3 Mulliken Population Analysis

Mulliken population analysis was used to understand the charge distribution within the inhibitor molecules and the possible charge transfer between the inhibitors and the mild steel surface (Figures 4.46 – 4.49). This analysis is important because it helps identify the active atoms responsible for adsorption and predicts which atoms are more likely to donate or accept electrons during corrosion inhibition (Hashim et al., 2020; Gebremeskel et al., 2024).

For FBMA, TOMA, PYMA and THMA, (Figures 4.46 – 4.49). the Mulliken charge results show that the oxygen atoms of the carbonyl (C=O) groups carry significant negative charges value. These negatively charged oxygen atoms are electron-rich and therefore act as nucleophilic sites, making them highly favourable for interaction with the iron surface. This finding agrees well with the MEP analysis, where strong red regions were also observed around the carbonyl oxygen atoms, confirming their high electron density.

In the case of FBMA (Figure 4.43), the nitrile nitrogen atom (–C≡N) also shows a noticeable negative charge value, indicating its ability to participate in electron donation and adsorption on the mild steel surface. For THMA, (Figure 4.45) the sulphur atom in the thiophene ring exhibits a relatively negative Mulliken charge, suggesting that it can act as an additional active site for adsorption. This sulphur atom behaves as a soft electron donor and can interact strongly with the iron surface through chemisorption.

Atoms with positive Mulliken charges, such as hydrogen atoms and some carbon atoms, represent electron-deficient regions. These areas are less likely to donate electrons but may still contribute to electrostatic (physisorption) interactions with negatively charged sites on the metal surface. The planarity of the molecules further enhances adsorption, as flat structures allow closer contact with the mild steel surface, especially through carbonyl oxygen atoms, promoting stronger chemisorption.

To conclude, the Mulliken charge analysis clearly indicates that oxygen atoms are the primary adsorption sites for for all compounds and addition nitrile for FBMA while sulphur for THMA. This result is fully consistent with the MEP findings and confirms the role of these heteroatoms in electron donation to the iron surface. These computational results are in good agreement with the experimental surface analyses, such as SEM and XPS, which show that the mild steel surface becomes smoother in the presence of the inhibitors compared to the blank solution. This smooth surface indicates the formation of a stable protective adsorbed layer, which reduces the attack of aggressive ions.

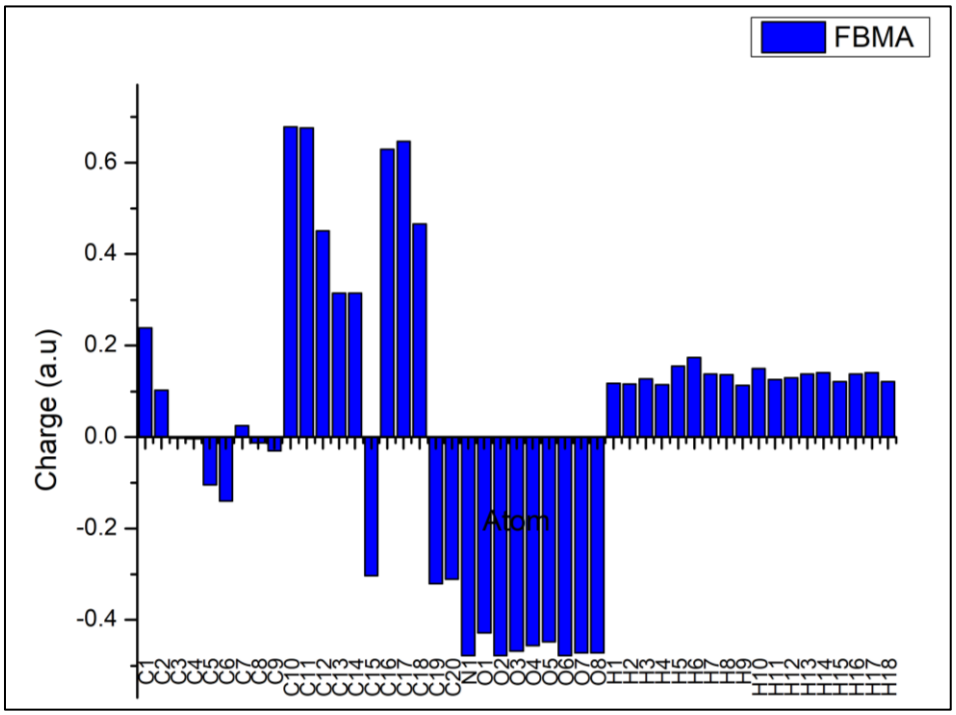


Figure 4.43 Atomic Charge Distribution for Each Atom in FBMA

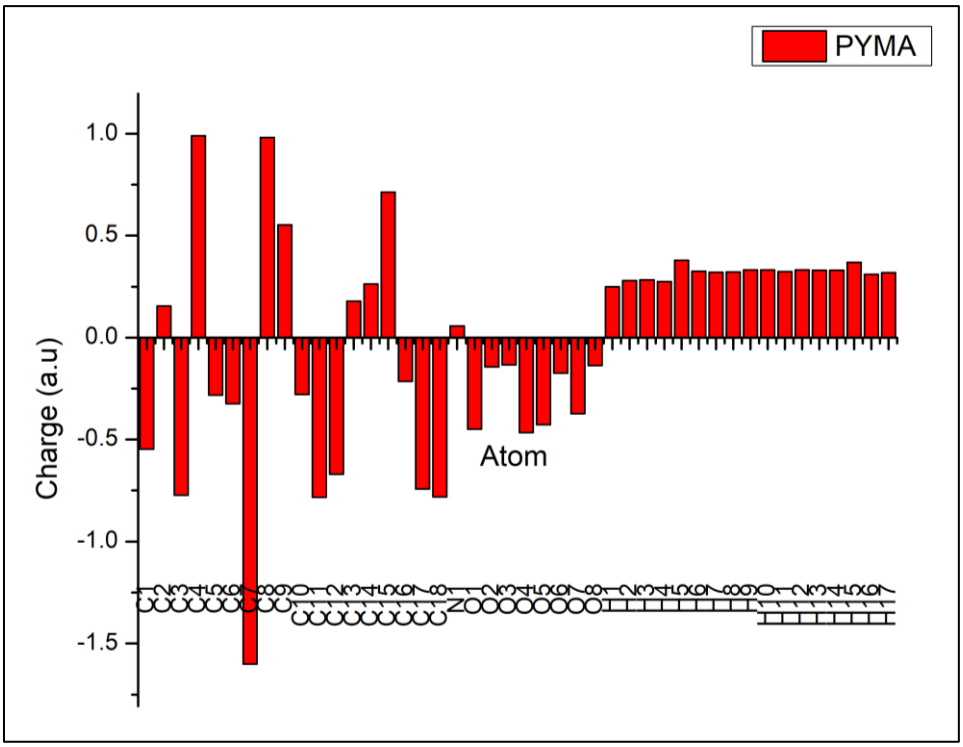


Figure 4.44 Atomic Charge Distribution for Each Atom in PYMA

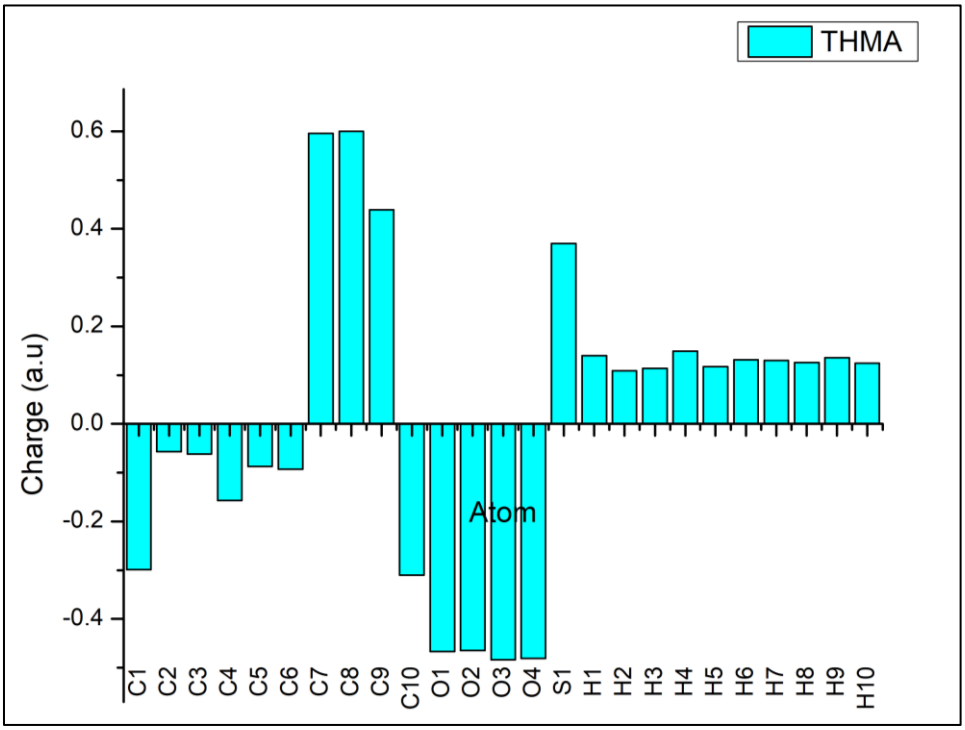


Figure 4.45 Atomic Charge Distribution for Each Atom in THMA

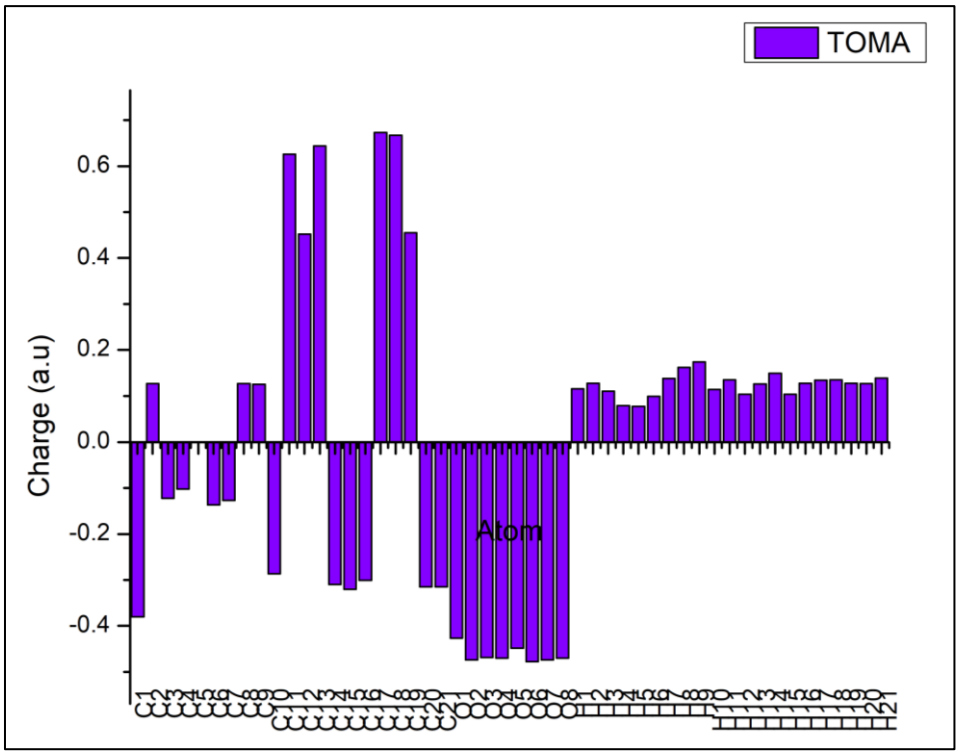


Figure 4.46 Atomic Charge Distribution for Each Atom in TOMA

4.6 Corrosion Inhibition Mechanism

The corrosion mechanism of mild steel in HCl solution is presented in Figure 4.50, in which the aggressive chloride ions and hydrogen ions react with the mild steel surface causing the dissolution of the iron and the corrosion of the mild steel. (Equation 4.5) shows mild steel was immersed in hydrochloric acid (HCl) then the electrochemical begins where it dissociates into highly reactive H^+ and Cl^- ions (Revie & Uhlig, 2011). Where hydrogen ion (H^+) aggressively attacking on mild steel surface, while chloride ion (Cl^-) is small and highly mobile making it easier to penetrate mild steel easily.

$$HCl \rightarrow H^+ + Cl^- \qquad (4.5)$$

This environment initiates a two-part electrochemical reaction consisting of anodic and cathodic processes. At the anodic sites Fe undergo oxidation, losing electrons to become ferrous ions (Fe^{2+}) that dissolve in solution which resulting mild steel to thinning and degrade (anodic reaction) referring to (equation 4.6).

$$Fe \rightarrow Fe^{2+} + 2e^{-} \quad (4.6)$$

Simultaneously, at the cathodic sites (Equation 4.7), the electrons released during iron dissolution are captured by the H^{+} ions. This reduction reaction produces hydrogen gas. When experiment done bubbles occur signifying the product of hydrogen gas. This occurred when the electron release from iron dissolution at cathodic sites by hydrogen ion.

$$2H^{+} + 2e^{-} \rightarrow H_2 \quad (4.7)$$

Meanwhile chloride ion will be adsorbed on the steel surface and it downs protective oxide layer and soluble iron chloride complexes referring to (equation 4.8).

$$Fe^{2+} + 2Cl^{-} \rightarrow FeCl_2 \quad (4.8)$$

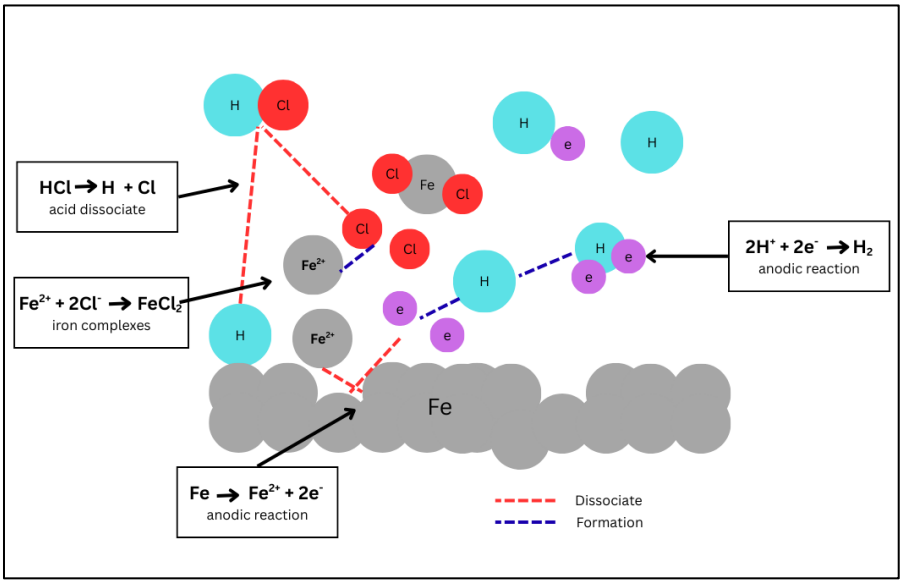


Figure 4.47 Corrosion Mechanism of HCl on Mild Steel Surface

4.6.1 FBMA Inhibition Mechanism

Based on the adsorption isotherm and Gibbs free energy (ΔG°_{ads}) results, the inhibition mechanism of FBMA on mild steel can be clearly predicted. The adsorption behavior of FBMA follows the Langmuir adsorption isotherm, indicating that FBMA

molecules form a uniform monolayer on the mild steel surface with no significant interaction between adsorbed molecules. The negative and sufficiently large $\Delta G°_{ads}$ values suggest that the adsorption process is spontaneous and mainly governed by physisorption. To further support this mechanism, surface analyses (SEM–EDX and XPS) and quantum chemical calculations (DFT) were employed to explain how FBMA interacts with the mild steel surface at the molecular level.

Physisorption arises mainly from electrostatic interactions between the charged mild steel surface and the inhibitor molecules (Figure 4.51). In aqueous acidic media, FBMA molecules can exist in protonated, while the mild steel surface becomes positively charged due to dissolution. DFT results showing a red region (negative electrostatic potential) at the nitrogen and oxygen atoms indicate it is a nucleophilic site (Gece, 2008; Obot et al., 2019). In the acidic solution, the positively charged hydronium (H_3O^+) ions are naturally attracted to this electron-dense molecules become protonated which is oxygen atom at carbonyl. The nitrogen atom in the cyanide group has a lone pair of electrons. When the H^+ ion approaches, it forms a coordinate covalent bond with this lone pair, effectively converting the neutral cyanide (CN) into a protonated nitrilium-like cation (CNH^+). Once protonated, the molecule carries a positive charge. The mechanism for its binding to mild steel as physisorption. In HCl, chloride ions (Cl^-) first adsorb onto the mild steel surface, giving it a net negative charge. The positively charged, protonated compound then attracted to this negatively charged on the steel surface. This electrostatic attraction holds the molecule to the surface without forming a permanent chemical bond, creating a protective barrier against further acid attack (Ferkous et al., 2024).

Quantum chemical calculations provide further insight into this mechanism. DFT results show that FBMA possesses a relatively high HOMO energy and a low LUMO energy, indicating good electron density distribution and molecular polarizability, which favor interaction with the mild steel surface. The molecular electrostatic potential (MEP) map reveals intense red regions localized around the oxygen atoms of the carbonyl groups and the nitrogen atom of the nitrile group, confirming that these sites are electron rich (Sastri, 2011). These regions act as the primary adsorption centres, interacting with the mild steel surface mainly through electrostatic attraction and weak donor–acceptor interactions, rather than the formation of strong coordinate bonds (Guo et al., 2017).

Importantly, although electron density is concentrated on the N and O atoms, the interaction does not involve significant orbital overlap or permanent Fe–N or Fe–O bond formation. Instead, the adsorption is dominated by physical forces, including Coulombic attraction and van der Waals interactions (Finšgar & Jackson, 2014; Verma et al., 2018). The negative $\Delta E_{back\text{-}donation}$ and low E_{LUMO} values suggest that electron exchange between FBMA and the iron surface is weak and reversible, which is characteristic of physisorption. Surface analyses further support this conclusion. SEM images show a smoother and more uniform surface in the presence of FBMA, indicating the formation of a protective film. EDX analysis confirms the presence of nitrogen on the inhibited surface, verifying FBMA adsorption, while XPS spectra show no significant shifts or new peaks indicative of strong Fe–N or Fe–O chemical bond formation. The observed C–N and C=O signals therefore correspond to physically adsorbed FBMA molecules rather than chemisorbed species.

Overall, FBMA inhibits mild steel corrosion primarily through physisorption, forming a compact and uniform protective film on the metal surface. This physically adsorbed layer blocks active corrosion sites and hinders the penetration of aggressive chloride (Cl^-) ions into surface defects such as pores and microcracks. As a result, both anodic metal dissolution and localized corrosion processes are effectively suppressed, leading to enhanced corrosion resistance (Idelfitri et al., 2023).

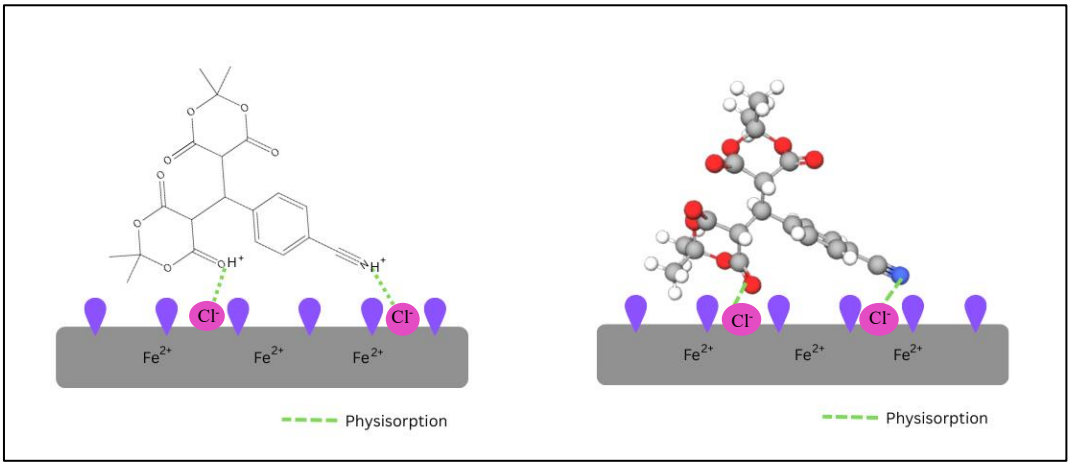


Figure 4.48 Proposed Inhibition Mechanism For FBMA

4.6.2 TOMA Inhibition Mechanism

TOMA inhibits the corrosion of mild steel in acidic solution through a combination of physisorption and chemisorption (Figure 4.52). This mixed adsorption behaviour explains the good inhibition performance observed experimentally.

For physisorption in acidic media, TOMA molecules become protonated which is oxygen atom at carbonyl. At the same time, chloride ions from the acid are adsorbed on the mild steel surface, making the surface negatively charged. This situation causes an electrostatic attraction between the positively charged TOMA molecules and the mild steel surface. As a result, TOMA is physically adsorbed onto the mild steel (Oguzie et al., 2011; Guendouz et al., 2024). The moderate dipole moment of TOMA (3.48 D) helps the molecules to align and spread over the steel surface. When the concentration of TOMA increases, more molecules are physically adsorbed, leading to higher surface coverage (Fouda et al., 2021; Timoudan et al., 2024). This physical adsorption forms the first protective layer, which slows down the attack of aggressive ions such as H^+ and Cl^-. In the MEP analysis it shows Meldrum's acid ring is in blue region which indicates it more likely to protonated compared to carbonyl which red region, thus the physisorption occur at the Meldrum's acid ring (Idelfitri et al., 2023).

Chemisorption occurs due to strong chemical bonding between TOMA and the empty *d*-orbital of Fe on the mild steel surface (Guo et al., 2017). The MEP map shows strong red regions around the carbonyl oxygen atoms of TOMA, indicating areas with high electron density. These oxygen atoms act as the main active sites for adsorption (Obot et al., 2019). The relatively high HOMO energy of TOMA (−6.36 eV) shows that the molecule can easily donate electrons. Electrons from the carbonyl oxygen atoms are transferred to the empty *d*-orbitals of Fe atoms on the mild steel surface, forming coordinate bonds. This confirms the occurrence of chemisorption. In addition, the low LUMO energy (−0.60 eV) allows TOMA to accept electrons from the filled *d*-orbital Fe of the mild steel. This back-donation strengthens the bond between TOMA and Fe, as supported by the favorable back-donation energy (−0.72 eV) (Obot et al., 2019; Gece, 2008). The positive electron transfer value ($\Delta N = 0.23$) also confirms that electrons move from TOMA to the metal.

In summary, TOMA first attaches to the mild steel surface through weak electrostatic forces (physisorption). Then, stronger chemical bonds (chemisorption) are formed through electron donation and back-donation between TOMA and iron atoms.

The combined effect produces a dense and stable protective film that blocks active corrosion sites and effectively reduces the corrosion rate of mild steel in acidic solution.

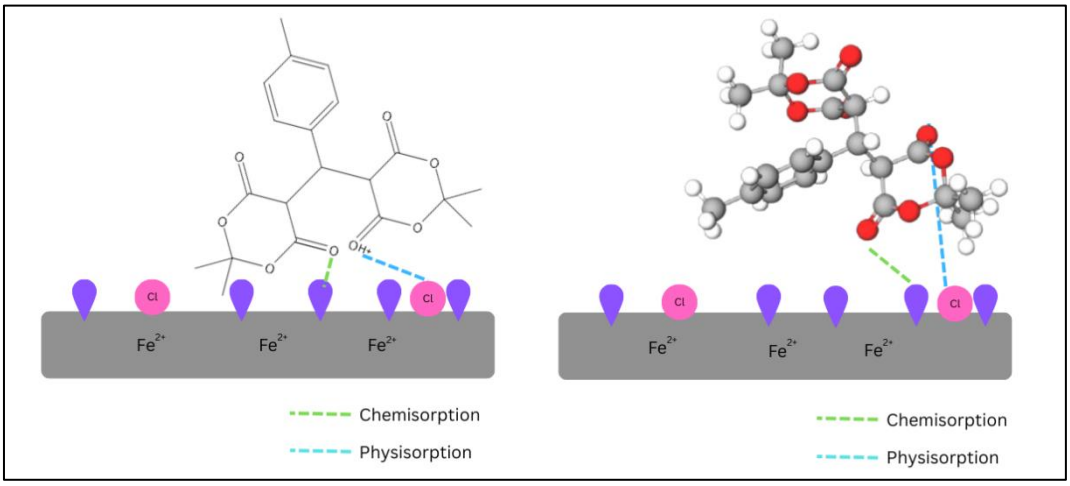


Figure 4.49 Proposed Inhibition Mechanism For TOMA

4.6.3 THMA Inhibition Mechanism

The corrosion inhibition action of THMA on mild steel in acidic medium occurs through a combined physisorption and chemisorption mechanism (Figure 4.53). This mixed adsorption behaviour is responsible for the high inhibition efficiency of THMA.

In acidic solution, THMA molecules become partially protonated, especially at heteroatoms such as sulphur. At the same time, chloride ions (Cl^-) from the acid adsorb onto the mild steel surface, making the surface negatively charged. This condition creates electrostatic attraction between the protonated THMA molecules and the steel surface, leading to physical adsorption (Oguzie et al., 2011; Guendouz et al., 2024). The relatively high dipole moment of THMA (4.56 D) helps the molecules orient and spread over the metal surface, increasing surface coverage. As the concentration of THMA increases, more molecules are physically adsorbed, forming an initial protective layer that reduces the direct contact between the mild steel surface and the corrosive environment (Fouda et al., 2021; Timoudan et al., 2024). From the MEP cloud the sulfur region is blue where it indicates as positive regions, it also supported by Mulliken analysis where the S atom is positive which most likely to protonated (Idelfitri et al., 2023).

Chemisorption plays a major role in stabilizing the adsorbed THMA layer. The MEP map of THMA shows strong red regions around the carbonyl oxygen atoms and

the sulphur atom of the thiophene ring, indicating electron-rich active sites. These atoms are responsible for strong interaction with the mild steel surface. DFT results show that THMA has a relatively high HOMO energy (−6.54 eV), meaning it can easily donate electrons. Electrons from the oxygen and sulphur atoms are transferred to the vacant *d*-orbitals of iron atoms, forming coordinate covalent bonds (Quadri et al., 2022). According to HSAB theory, the thiophene sulphur acts as a soft base and interacts strongly with the soft iron on the mild steel surface, while the oxygen atoms provide additional anchoring points. This multi-site bonding confirms chemisorption. In addition, the low E_{LUMO} value (−2.58 eV) and the negative back-donation energy (−0.50 eV) indicate that THMA can also accept electrons from the filled *d*-orbitals of iron through back-donation. This electron exchange strengthens the inhibitor–metal bond and improves the stability of the protective layer.

In summary, THMA first adsorbs on the mild steel surface through weak electrostatic forces (physisorption). This is followed by strong chemical bonding (chemisorption) through electron donation and back-donation involving oxygen and sulphur atoms. The combined effect leads to the formation of a compact and stable protective film, which blocks active corrosion sites and limits the penetration of aggressive chloride ions, thereby effectively reducing corrosion of mild steel in acidic media.

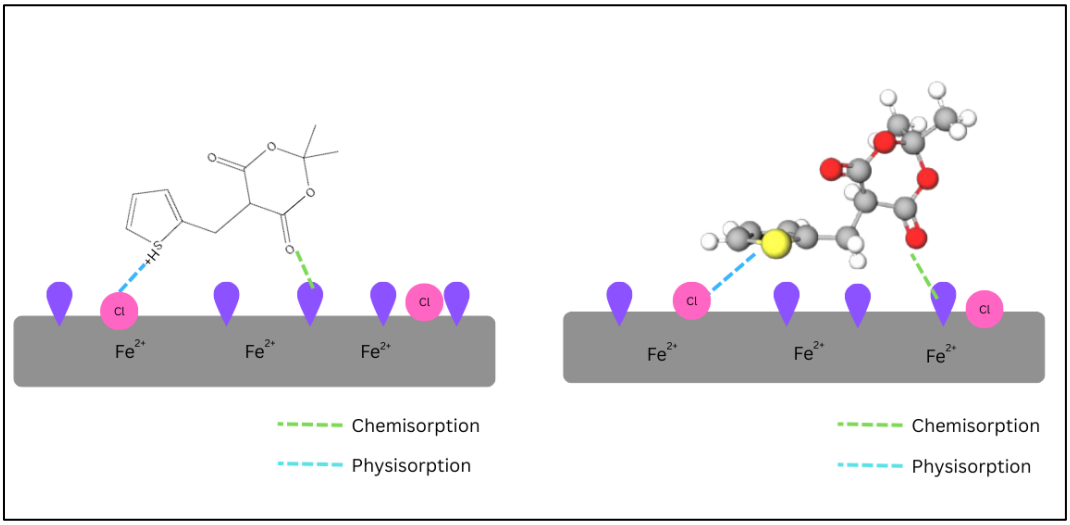


Figure 4.50 Proposed Inhibition Mechanism For THMA

4.6.4 PYMA Inhibition Mechanism

The corrosion inhibition behavior of PYMA on mild steel in acidic medium follows a mixed adsorption mechanism, involving both physisorption and chemisorption (Figure 4.54). This conclusion is supported by the DFT parameters and the molecular electrostatic potential (MEP) map. For physisorption mechanism, in acidic solution, PYMA molecules can become partially protonated, particularly at the nitrogen atom of the pyridine ring this is due referring to MEP region the cloud is blue indicating it was more positive. At the same time, chloride ions (Cl^-) from the acidic medium are adsorbed on the mild steel surface, creating negatively charged sites. This leads to electrostatic attraction between the protonated PYMA molecules and the mild steel surface, resulting in physical adsorption. The moderate dipole moment of PYMA facilitates proper molecular orientation on the mild steel surface, allowing the inhibitor molecules to spread and cover a large surface area (Sastri, 2011; Fouda et al., 2021). As the inhibitor concentration increases, more PYMA molecules are physically adsorbed, forming an initial protective layer that reduces direct contact between the mild steel and the corrosive solution.

Chemisorption occurs through strong chemical interaction between PYMA and iron atoms on the mild steel surface. The MEP map of PYMA shows intense red regions around the carbonyl oxygen atoms of the dioxane-4,6-dione group and a noticeable red region around the nitrogen atom of the pyridine ring, indicating that these atoms are electron-rich and act as the main adsorption canters' results show that PYMA has a relatively high HOMO energy, indicating a good ability to donate electrons (Gece, 2008; Guo et al., 2017). Electrons from the oxygen and nitrogen atoms are transferred to the vacant d-orbitals of iron atoms, forming coordinate covalent bonds, which confirms the presence of chemisorption. In addition, the low LUMO energy and the negative back-donation energy ($\Delta E_{back\text{-}donation}$) indicate that PYMA can also accept electrons from the filled *d*-orbitals of iron through back-donation. This two-way charge transfer strengthens the interaction between PYMA and the mild steel surface. The positive electron transfer value (ΔN) further confirms that electron donation from PYMA to iron is favorable. The aromatic pyridine ring also contributes to adsorption through its π-electron system, which enhances interaction with the mild steel surface and improves the stability of the adsorbed layer (Idelfitri et al., 2023).

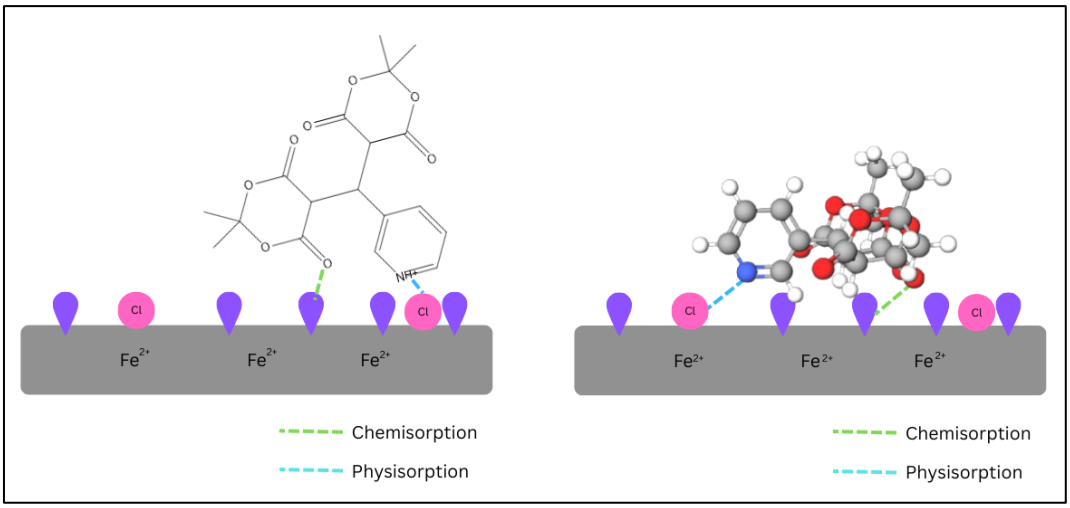


Figure 4.51 Proposed Inhibition Mechanism for PYMA

4.7 Response Surface Methodology (RSM)

For RSM study used a five-level Central Composite Design (CCD) to optimize the corrosion inhibition performance of all compounds FBMA, TOMA, THMA and PYMA on mild steel. Four independent variables were examined: concentration inhibitor (A), concentration acid (B), immersion time (C). and inhibitor to acid ratio (D). These parameters were selected to study their effects on inhibition efficiency and overall corrosion behaviour towards mild steel. Inhibition efficiency was evaluated using the weight loss method, calculated according to Equation (3.1, 3.2, 3.3) (Montgomery, 2020; Myers et al., 2016).

All the best model for this study was selected using statistical analysis by comparing the *F*-value and *p*-value. The *F*-value indicates how strong the effect of a model or factor is compared to random error. A large *F*-value means that the model or factor has a strong effect on the response, while a small *F*-value suggests that the effect may be due to random variation (noise). The *p*-value shows whether the observed effect is statistically significant. A small *p*-value (usually < 0.05) indicates a significantly effect, whereas a large *p*-value (> 0.05) indicates an insignificantly effect (Nor et al., 2022).

Lack of fit is used to determine whether the difference between the experimental and predicted values comes from model inadequacy or random experimental error. When the p-value is less than 0.05, the lack of fit is considered significant, indicating that the model does not properly describe the data. In contrast, when the p-value is

greater than 0.05, the lack of fit is not significant, showing that the model fits the data well and that the observed differences are mainly due to random error.

4.7.1 Optimization for FBMA

The inhibition efficiencies for FBMA obtained under different experimental conditions are shown in Table 4.22 A total of 30 experimental were carried out, although two runs were excluded due to unrelated factors. The highest inhibition efficiency of 90.1% was achieved at an inhibitor concentration of 4 mM (A), an acid concentration of 0.5 M (B), an inhibitor-to-acid ratio of 4 (C) and an immersion time of 24 hours (D) at std 22. In contrast, the lowest inhibition efficiency of 51.5% was recorded at an inhibitor concentration of 6 mM (A), an acid concentration of 0.75 M (B), an inhibitor-to-acid ratio of 4 (C) and an immersion time of 12 hours (D) at std 12.

Table 4.22
Experimental Runs from CCD Design and the Response of the FBMA

Std	Run	Concentration inhibitor (mM)	Concentration acid (M)	Immersion time (h)	Ratio	Inhibition efficiency (%)
1	20	2	0.25	12	3.0	67.94
2	27	6	0.25	12	3.0	64.10
3	21	2	0.75	12	3.0	69.19
4	15	6	0.75	12	3.0	59.98
5	8	2	0.25	20	3.0	52.00
6	26	6	0.25	20	3.0	56.06
7	1	2	0.75	20	3.0	79.17
8	13	6	0.75	20	3.0	78.12
9	24	2	0.25	12	4.0	77.66
10	17	6	0.25	12	4.0	79.80
11	30	2	0.75	12	4.0	53.02
12	9	6	0.75	12	4.0	51.51
13	23	2	0.25	20	4.0	79.28
14	29	6	0.25	20	4.0	87.87
15	25	2	0.75	20	4.0	83.80
16	2	6	0.75	20	4.0	85.92
17	7	0	0.50	16	3.5	-
18	5	8	0.50	16	3.5	67.04
19	19	4	0.00	16	3.5	63.38
20	16	4	1.00	16	3.5	61.09
21	4	4	0.5	8	3.5	65.49
22	3	4	0.5	24	3.5	90.10
23	10	4	0.5	16	2.5	63.38
24	6	4	0.5	16	4.5	81.63
25	11	4	0.5	16	3.5	71.83
26	14	4	0.5	16	3.5	74.65
27	18	4	0.5	16	3.5	71.83
28	12	4	0.5	16	3.5	72.30
29	28	4	0.5	16	3.5	74.65
30	22	4	0.5	16	3.5	73.24

4.7.1.1 Determination of Selected Model

Based on the results in the Table 4.23, the quadratic versus 2FI model showed the highest *F*-value and the lowest *p*-value, indicating that it was the most suitable model compared to the others. The cubic model was found to be aliased, meaning its effects could not be clearly separated from other terms and therefore it was not selected.

Consequently, the quadratic model was chosen as the best and most appropriate model for describing and optimising the response (Nor et al., 2022).

Table 4.23
Sequential Model Sum of Square for FBMA

Source	Sum of squares	df	Mean square	*F*-value	*p*-value	
Mean vs Total	146000	1	146000			
Linear vs Mean	1183.6	4	295.9	3.49	0.0222	
2FI vs Linear	1718.84	6	286.47	16.21	< 0.0001	
Quadratic vs 2FI	295.97	4	73.99	46.9	< 0.0001	Suggested
Cubic vs Quadratic	12.8	8	1.6	1.03	0.4977	Aliased
Residual	9.28	6	1.55			
Total	149000	29	5137.52			

Lack of fit test also concluded to measures the difference between experimental and predicted values is due to model inadequacy or random experimental error. If the lack of fit considered significant indicating that the selected model may be inappropriate or that important factors are not adequately represented in the model. While if the *p*-value > 0.05 it means that not significant lack of fit which indicates that the model explains the data well; errors are just random. Table 4.24 shows the quadratic model with a low *F*-value (0.8566) and a high *p*-value (0.6052), indicating that the lack of fit is not significant. This confirms that the quadratic model fits the experimental data well and that the differences between predicted and experimental values are mainly due to pure experimental error. The cubic model also shows a non-significant lack of fit; however, it is aliased and therefore not suitable for interpretation. Based on these results, the quadratic model was considered the most appropriate model for describing the response (Nor et al., 2022).

Table 4.24
Lack of Fit Test FBMA

Source	Sum of squares	df	Mean square	*F*-value	*p*-value	
Linear	2028.2	19	106.75	61.43	0.0001	
2FI	309.36	13	23.8	13.69	0.0047	
Quadratic	13.4	9	1.49	0.8566	0.6052	Suggested
Cubic	0.5929	1	0.5929	0.3412	0.5845	Aliased
Pure Error	8.69	5	1.74			

The model summary statistics were used to evaluate the accuracy and reliability of the developed models as shown in Table 4.25. The standard deviation (Std. Dev.) indicates the average difference between the experimental and predicted values; a lower value means better model accuracy (Montgomery, 2020; Myers et al., 2016). Among all models, the quadratic model shows a very low standard deviation (1.26), indicating a close agreement between predicted and experimental results. The coefficient of determination (R^2) measures the proportion of variation in the response variable that is explained by the regression model. A higher R^2 value indicates that the model provides a better fit to the experimental data (Montgomery, 2020). The quadratic model shows a very high R^2 value (0.9931), meaning that more than 99% of the response variation is explained by the model. In comparison, the linear model has a very low R^2 value (0.3675), indicating poor performance.

The adjusted R^2 considers the number of model terms and provides a more accurate measure of model quality (Myers et al., 2016). The quadratic model again shows a high adjusted R^2 value (0.9863), confirming that the added quadratic terms significantly improve the model without overfitting. The predicted R^2 indicates the model predicts new experimental data. The quadratic model shows a high predicted R^2 value (0.9689), which is in good agreement with the adjusted R^2, indicating strong predictive capability. In contrast, the linear model has a negative predicted R^2, showing that it is unsuitable for prediction.

The PRESS (Predicted Residual Error Sum of Squares) measures the overall prediction error of the model; a smaller value indicates better predictive performance. The quadratic model has the lowest PRESS value (100.08), confirming its better predictive accuracy. Although the cubic model shows slightly higher R^2 values, it is aliased and therefore unreliable (Montgomery, 2020). Based on these results, the quadratic model was selected as the most appropriate and reliable model for the study.

Table 4.25
Model Summary Statistics for FBMA

Source	Standard deviation	R^2	Adjusted R^2	Predicted R^2	PRESS	
Linear	9.21	0.3675	0.2621	-0.0063	3240.71	
2FI	4.2	0.9012	0.8464	0.8305	545.90	
Quadratic	1.26	0.9931	0.9863	0.9689	100.08	Suggested
Cubic	1.24	0.9971	0.9866		*	Aliased

4.7.1.2 Identification of Model Accuracy

To ensure that the mathematical model accurately represents the corrosion inhibition process, the reliability of the data was checked using diagnostic plots as shown Figures 4.55 - 4.60. This step is crucial to prove that the results are not due to random errors (Salam et al., 2015). The accuracy of the model is first confirmed by the Normal Plot of Residuals. In this study, the data points follow a straight line, which indicates that the experimental errors are normally distributed Figure 4.52. In simple terms, this means that the model is balanced and there is no unusual bias in the data. Because the points do not form an "S-shape," we can conclude that the chosen quadratic model is a perfect fit for this experiment without needing any further mathematical transformations. The model's predictive power is further validated by comparing the values predicted by the software against the actual results obtained in laboratory Figure 4.53. The data points are clustered tightly along a 45° diagonal line. This close alignment shows that the model is highly accurate at identifying the relationship between acid concentration, inhibitor concentration, ratio, time and inhibition efficiency (Dada et al., 2021).

The predicted vs Actual plot as shown in Figure 4.57 deduces that both values are very close to each other and demonstrating good agreement between the model and experimental data. It is concluded that the model has high accuracy and reliability in predicting the response. Since the Predicted R^2 and Adjusted R^2 values are in close agreement (within 0.2 of each other), the model is considered robust and reliable for predicting corrosion behavior even for conditions that were not specifically tested within the design range (Figure 4.58) (Dada et al., 2021).

To ensure that no individual data point unduly influenced the regression results, Cook’s Distance Figure 4.56 was used to identify potential outliers. Data points with large Cook’s Distance values indicate that removing them would noticeably change the model’s estimates, suggesting they may be influential observations. All experimental points fell within the accepted limits (below 1.0), meaning no single test result had an unfair influence on the overall trend. This confirms that the 3D surface generated is a true reflection of the chemical interaction between the inhibitor and the acid (Anadebe et al., 2018).

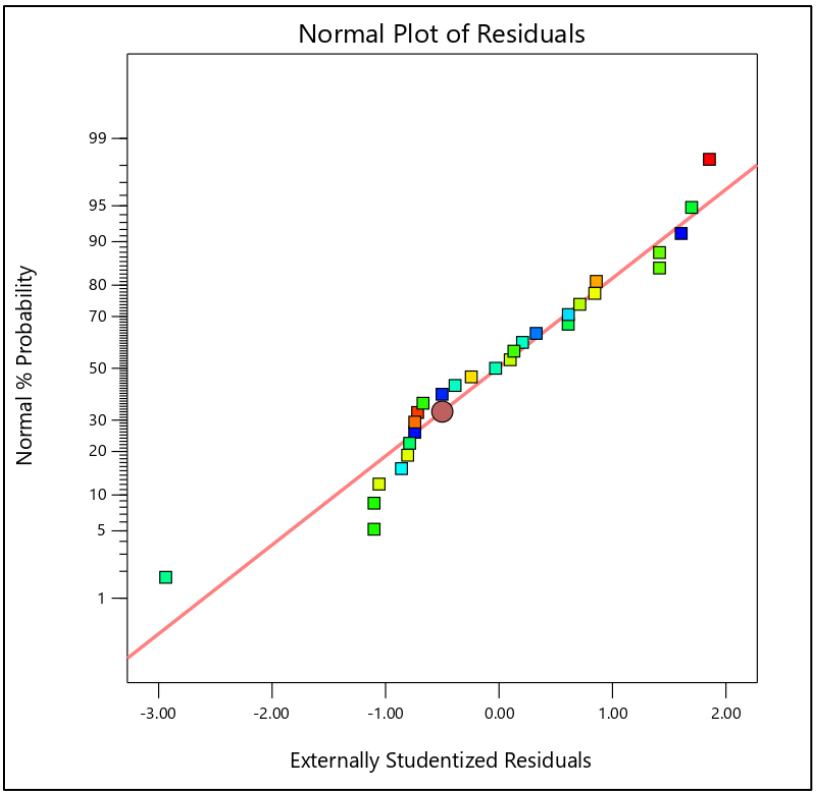


Figure 4.52 Normal Plot for FBMA

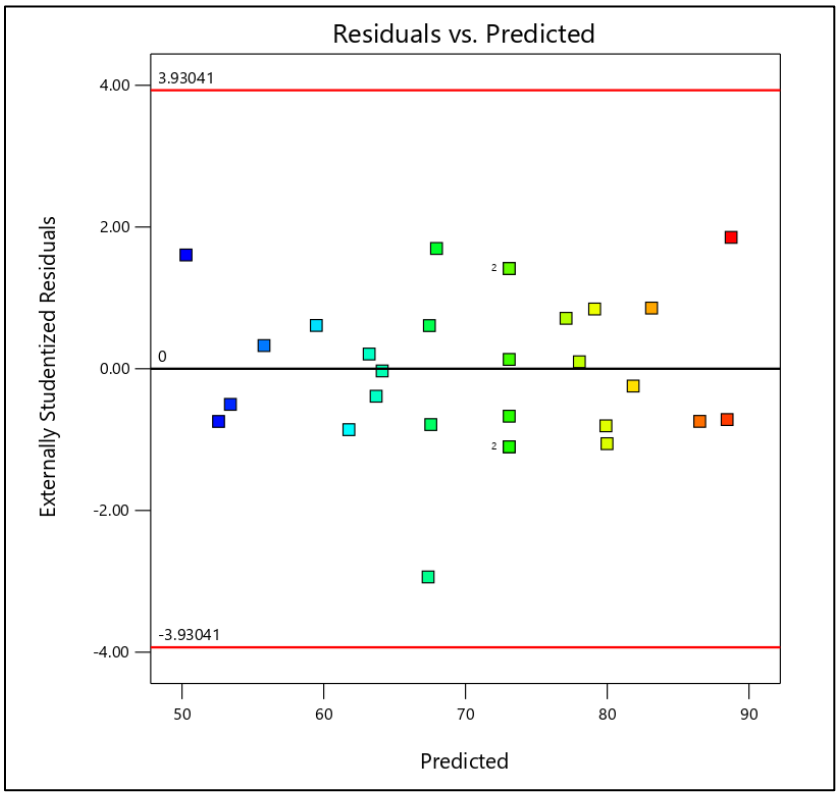


Figure 4.53 Residual vs Predicted for FBMA

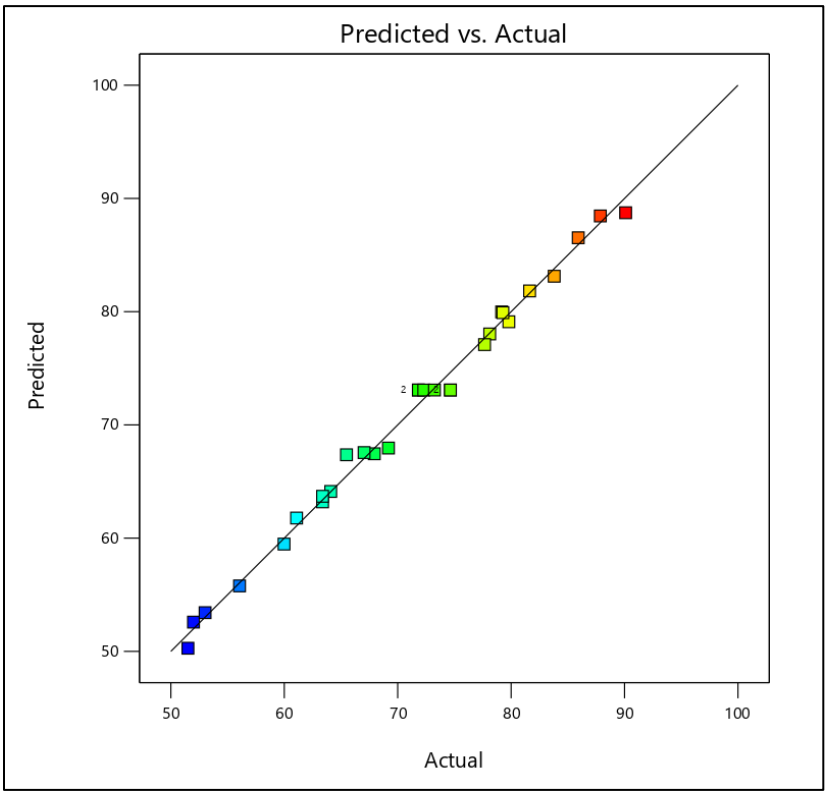


Figure 4.54 Predicted vs Actual for FBMA

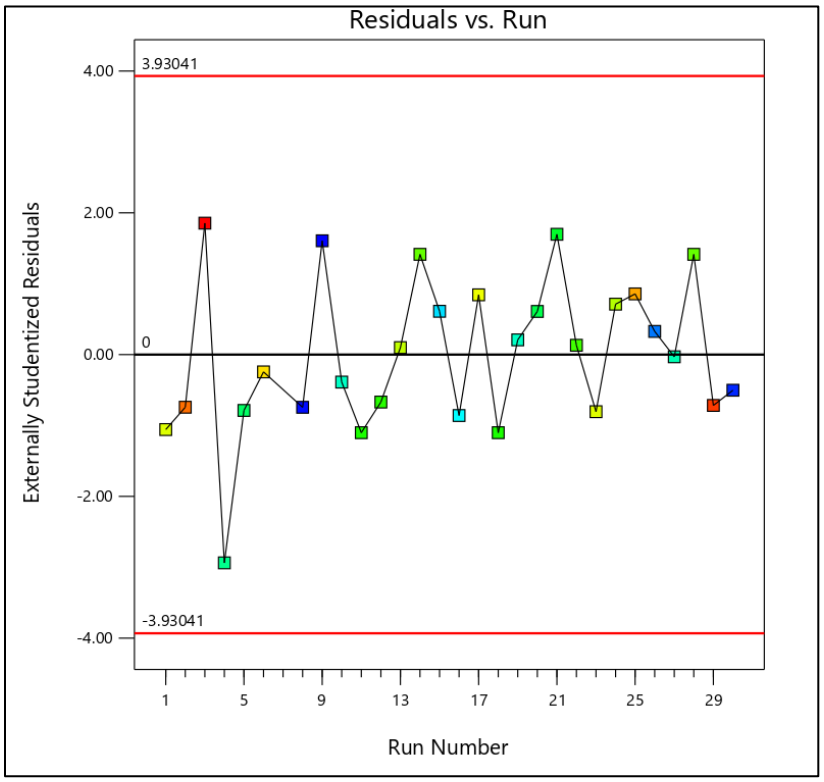


Figure 4.55 Residual vs Run for FBMA

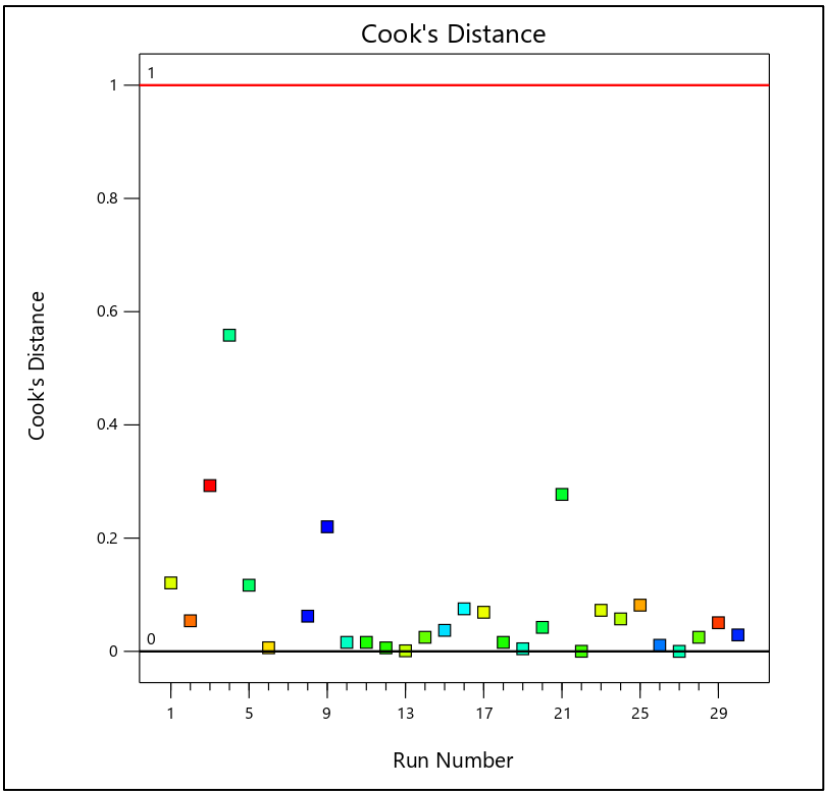


Figure 4.56 Cook's Distance for FBMA

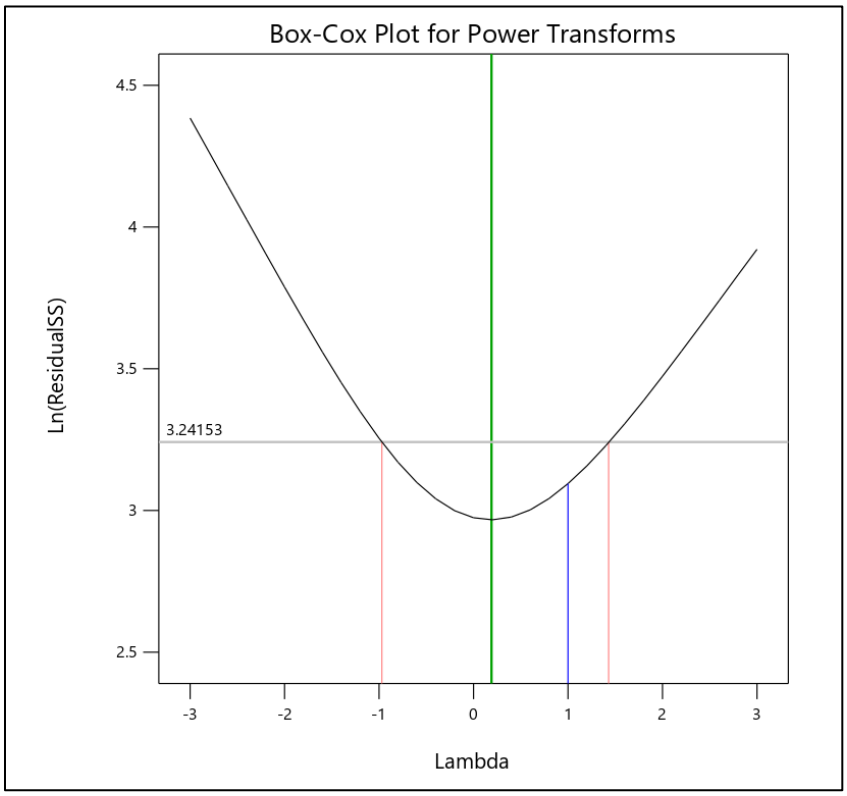


Figure 4.57 Box-Cox Plot for FBMA

4.7.1.3 Analysis of Variance (ANOVA)

Table 4.26 shows the summary of ANOVA analysis for inhibition efficiency FBMA. The model developed to predict the inhibition efficiency of FBMA was found to be highly significant. This is supported by a very low *p*-value (< 0.0001) and a high *F*-value (144.82), showing that the model terms strongly influence the response (Antony, 2014). The lack-of-fit test is not significant (F = 0.6052, p = 0.8566), indicating that the model fits the experimental data well and the differences between predicted and observed values are mainly due to random errors.

The coefficient of determination (R^2 = 0.9931) indicates that 99.31% of the variation in inhibition efficiency is explained by the model (Salam et al., 2015; Tansuğ et al., 2014). The adjusted R^2 (0.9863) and predicted R^2 (0.9689) are also high and in close agreement, suggesting that the model is reliable and can predict new data accurately. The standard deviation (1.26) and coefficient of variation (C.V = 1.83%) are low, confirming that the model predictions are precise and reproducible. Additionally, the adequate precision (42.58), which measures the signal-to-noise ratio, is much higher than the minimum required value of 4, indicating that the model can effectively navigate the design space (Salam et al., 2015).

In this study, the relationship between the inhibition efficiency (Y) and the four variables inhibitor concentration (A), acid concentration (B), immersion time (C) and inhibitor-to-acid ratio (D) including their interactions, is described by Equation 4.1 According to Sarabia & Ortiz (2009), a positive coefficient in the model means the factors work together to improve inhibition, while a negative coefficient means the factors reduce efficiency when combined.

$$\begin{aligned} Y = \; & 140.07 - 3.869A + 112.88B - 13.066C - 5.33D - 2.57AB + 0.204AC \\ & + 1.336AD + 6.725BC - 48.36BD + 2.21CD - 0.347A^2 - 42.357B^2 + \\ & 0.077C^2 - 0.3193D^2 \end{aligned} \tag{4.1}$$

Y is the predicted inhibition efficiency. A, B, C and D are the main (linear) effects of the variables, the squared terms (A^2, B^2, C^2, D^2) show curved or quadratic effects, and the interaction terms (AB, AC, AD, BC, BD, CD) show how two variables together affect the efficiency. By putting specific values of A, B, C and D into Equation

4.1 just now, the predicted inhibition efficiency able to be calculated. These predicted values were then plotted using response surface methodology (RSM) with a central composite design (CCD) and compared to the experimental results to check how well the model predicts the actual behavior.

Table 4.26
ANOVA Analysis of the Model for FBMA

Source	Inhibition efficiency of FBMA
p-value model	< 0.0001
F-value model	144.82
p-value Lack of fit	0.8566
F-value Lack of fit	0.6052
R^2	0.9931
Adjusted R^2	0.9863
Predicted R^2	0.9689
Standard deviation	1.26
Coefficient of Variation (C.V)	1.83
Adequate precision	42.57582

Table 4.27 shows the ANOVA results for the regression model used to predict the inhibition efficiency of FBMA. The table provides important statistical metrics, including *F*-values and *p*-values, which indicate the significance of each variable. The independent variables in the table can be grouped into four categories: linear terms (concentration of inhibitor (A), concentration of acid (B), immersion time (C) and Ratio (D)), quadratic terms (A^2, B^2, C^2, D^2) and interaction terms (AB, AC, AD, BC, BD, CD). By examining the *p*-values, it is possible to identify which variables significantly affect the inhibition efficiency. In this study, concentration inhibitor (A), concentration acid (B), immersion time (C) and Ratio (D), all show highly significant effects, with *p*-values less than 0.05 (specifically <0.0001). Many interaction terms, such as AB, AC, AD, BC, BD and CD, are also significant, indicating that the combined effects of two variables can strongly influence the inhibition efficiency (Tansuğ et al., 2014). In contrast, some terms, like D^2 (p = 0.7476) and A terms (p = 0.9574), were not significant.

Table 4.27
ANOVA Analysis Factor for FBMA

Source	Sum of square	df	Mean square	*F*-value	*p*-value
A- Inhibitor Concentration	0.0047	1	0.0047	0.003	0.9574
B - Acid Concentration	3.07	1	3.07	1.94	0.1849
C - Time	685.23	1	685.23	434.38	< 0.0001
D - Ratio	493.23	1	493.23	312.66	< 0.0001
AB	26.52	1	26.52	16.81	0.0011
AC	42.71	1	42.71	27.07	0.0001
AD	28.57	1	28.57	18.11	0.0008
BC	723.61	1	723.61	458.71	< 0.0001
BD	584.67	1	584.67	370.63	< 0.0001
CD	312.76	1	312.76	198.26	< 0.0001
A^2	30.9	1	30.9	19.58	0.0006
B^2	186.89	1	186.89	118.47	< 0.0001
C^2	41.18	1	41.18	26.1	0.0002
D^2	0.17	1	0.17	0.1077	0.7476

4.7.1.4 Three-Dimensional (3D) Surface

Based on Table 4.27 the interaction effects between the independent variables were evaluated by comparing the *p*-values of each pair variables. The interaction pairs studied concentration of inhibitor and concentration of acid (AB), concentration of inhibitor and time (AC) concentration of inhibitor and ratio (AD), concentration of acid and time (BC) concentration acid and ratio (BD), time and ratio (CD). The *p*-values indicate how strongly each pair of variables influences the inhibition efficiency (Myers et al., 2016; Montgomery, 2020).

To further the understanding, three-dimensional (3D) response surface plots were analysed. These plots were used to study how to independent variables at a time affect the inhibition efficiency while other variables are kept constant (Bezerra et al., 2008; Yamin et al., 2020). Figure 4.58 present the effects of each variable pair using response surface plot. The shape and slope of the response surface plots provide useful information about the contribution of each variable. A steeper surface and a wider red zone indicate a stronger effect on inhibition efficiency. The direction and inclination of the red region also show which variable has a more dominant influence in the interaction. In this study, the effects of the quadratic independent variables on inhibition efficiency were examined by considering their *p*-values together with their interaction patterns observed in both contour and response surface plots. This combined analysis

helps to clearly explain the role of each variable and their interactions in controlling the adsorption process and overall inhibition performance.

Figure 4.58 (a) show 3D plot relationship between the inhibitor concentration (A) and acid concentration (B). Since the data (AB) in ANOVA, Table 4.27 show *p*-value higher than (p<0.001) thus the 3D surface shows less impact. The surface slightly convex shape, which was classic sign of an optimum range. Increasing the inhibitor concentration initially leads to sharp rise in efficiency as more molecules become available to block the active corrosion sites on the mild steel surface. However, at very high inhibitor concentrations combined with high acid levels, the surface flattens slightly indicating that there is an ideal balance point where the mild steel is most protected without wasting excess material (inhibitor).

The flattening of the 3D response surface critical observations in this corrosion study, as they represent the physical and chemical saturation of the mild steel surface. Initially, as the inhibitor concentration (A) increases, the inhibition efficiency (R1) rises sharply because there are numerous active sites on the mild steel surface available for the inhibitor molecules to bond with. These molecules act as a protective barrier, effectively blocking the corrosive acid (B) from attacking the mild steel substrate (Bentiss et al., 2000; Verma et al., 2018). However, the surface eventually flattens because once every available site on the mild steel is occupied by an inhibitor molecule, the surface reaches a state of saturation; at this stage, adding more inhibitors does not further increase efficiency because the protective film is already complete (Hashim et al., 2020; Ahmed et al., 2024).

Referring to Table 4.27, AC also showed *p*-value that higher (p < 0.001) indicating that this factor has less impact making the 3D structure less curvature. The 3D surface plot Figure 4.58 (b) shows how inhibitor concentration (A) and immersion time (C) work together to protect the mild steel. As both concentration and time increase, the surface of the graph rises, which means the inhibition efficiency (R1) gets higher. This increase in efficiency happens through a process called adsorption. When the inhibitor concentration is high, there are more protective molecules available in the solution to find and attach to the mild steel surface. Thus, more time is needed for these molecules to organize themselves into a tight, leak-proof film (Bentiss et al., 2000; Verma et al., 2018). Without enough time, the molecules might be scattered, leaving gaps where the acid can still attack the mild steel. However, as time progresses to 20 hours, the inhibitor molecules could fill all the empty "active sites" on the mild steel,

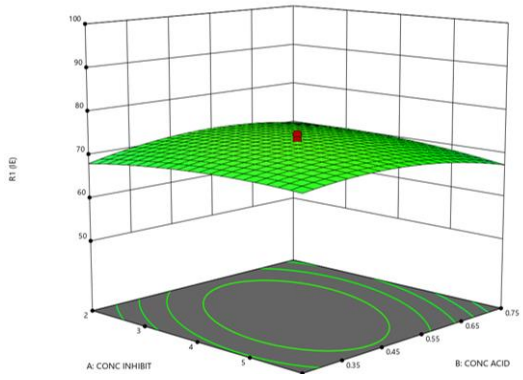
creating a complete barrier. Consequently, the highest efficiency (reaching over 90%) is found at the peak where both concentration and time are at their maximum. The smooth curve of the graph confirms that these two factors support each other; more inhibitors make the film thicker, while more time makes the film more stable and reliable. (Ahmed et al., 2024).

The 3D surface plot Figure 4.58 (c) illustrates the interaction between inhibitor concentration (A) and ratio (D) on the inhibition efficiency (R1). From Table 4.27 it shows that AD *p*-value also higher than ($p < 0.001$) making it less impact. The graph shows a smooth, upward slope, where the efficiency improves as both the concentration and the ratio of the inhibitor increase. This trend occurs because the Ratio represents the proportion of active ingredients within the inhibitor blend. When the ratio is optimized alongside the concentration, it ensures that the most effective molecules are present in high enough numbers to settle on the mild steel surface. This allows the inhibitor to form a thicker and more uniform protective layer, which acts as a physical barrier against the acidic environment (Hashim et al., 2020; Ahmed et al., 2024). The yellow region at the top of the plot represents the optimum spot where the mild steel is most protected. Because the red design points sit directly on the predicted surface, it proves that the model is very accurate.

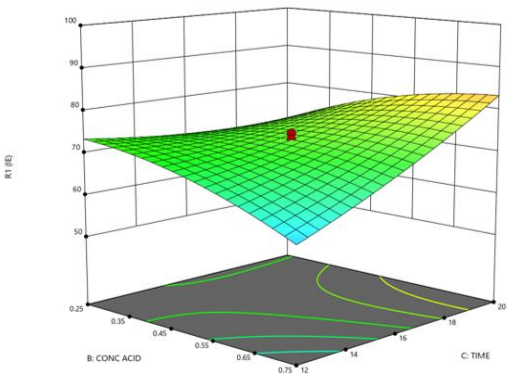
In this corrosion study, the 3D surface plot Figure 4.58 (d) specifically illustrates the interaction between acid concentration (B) and immersion time (C) on the inhibition efficiency (R1). As the immersion time increases from 12 to 20 hours, the surface of the graph rises steadily, indicating that the inhibitor provides much better protection over longer periods (Gece, 2008; Verma et al., 2018). Statistically, the interaction between these two factors is highly significant, as evidenced by a BC *p*-value of less than 0.001 ($p < 0.001$), which confirms that the combined effect of acid strength and time is a critical driver of the model's results. This increase in efficiency occurs because the inhibitor molecules require sufficient time to move through the acid and attach themselves firmly to the mild steel surface (Hashim et al., 2020). As time passes, these molecules organize into a dense, continuous protective film that acts as a physical barrier. The plot also reveals that the inhibitor is chemically durable; even at a high acid concentration (0.75), the efficiency remains very strong and reaching toward 90.1% whereas long the maximum immersion time is achieved. This suggests that the protective layer is robust enough to resist aggressive acidic attacks without breaking down.

In the FBMA system, Figure 4.58 (e) the change in inhibition efficiency with acid concentration and inhibitor-to-acid ratio can be explained by their combined effect on adsorption at the mild steel surface. At low acid concentration and low ratio, the inhibition efficiency is relatively low because fewer inhibitor molecules are available to compete with aggressive acid ions for adsorption sites on the steel surface. As the acid concentration increases to a moderate level, the metal surface becomes more activated, which enhances the interaction between FBMA molecules and the steel, leading to better adsorption and higher inhibition efficiency. At the same time, increasing the inhibitor-to-acid ratio supplies more FBMA molecules, allowing a denser and more stable protective film to form on the surface. However, the curved response surface indicates that beyond an optimum combination of acid concentration and ratio, the inhibition efficiency no longer increases significantly. At higher acid concentration, excessive acid ions can disturb the adsorbed inhibitor layer, while an overly high ratio may lead to saturation of adsorption sites (Verma et al., 2018). Therefore, the observed trend results from a balance between acid activation of the metal surface and effective inhibitor coverage, with the highest inhibition efficiency occurring at an optimal acid concentration and inhibitor-to-acid ratio.

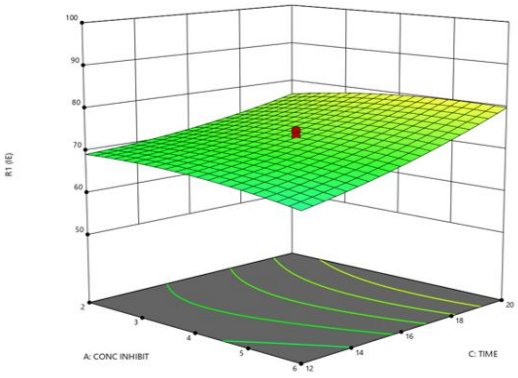
Figure 4.58 (f) indicates the interaction between immersion time (C) and ratio (D) on the inhibition efficiency (R1). The graph displays a significant upward trend toward the orange region as both immersion time and the inhibitor ratio increase, indicating a strong synergistic effect between these two variables. Statistically, the interaction between time and ratio is highly significant, as confirmed by a *p*-value of less than 0.001 ($p < 0.001$), which proves that their combined influence is a primary driver for maximizing corrosion protection (Elebo et al., 2024; Yamin et al., 2020). This significant result occurs because the ratio determines the correct balance of active chemical components needed to bond with the mild steel. When this optimal ratio is combined with a longer time of up to 20 hours, it allows the inhibitor molecules to not only attach to the surface but to pack together tightly into a more organized and impenetrable protective film. Without sufficient time or the correct ratio, the protective barrier would be thin or patchy, leaving the mild steel vulnerable to the acid. However, at the peak of this 3D surface, the combination of maximum time and the highest ratio produces the most effective inhibition.



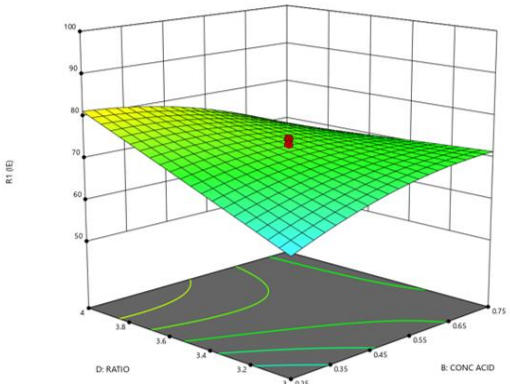
(a) Effect of Concentration Inhibitor (A) and Acid Concentration (B)



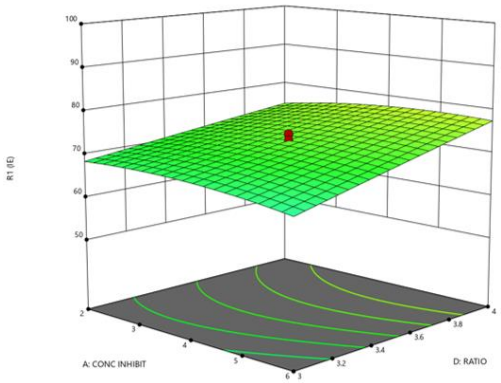
(d) Effect of Concentration Acid (B) and Time (C)



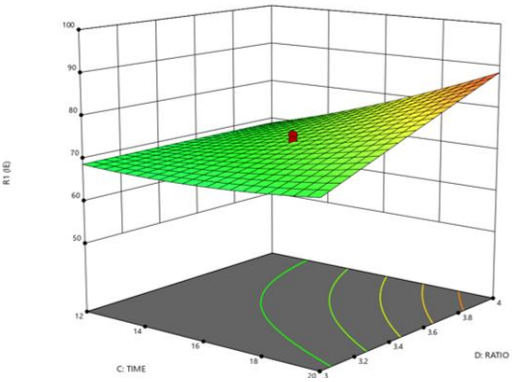
(b) Effect of Concentration Inhibitor (A) and Time (C)



(e) Effect of Concentration Acid (B) and Ratio (D)



(c) Effect of Concentration Inhibitor (A) and Ratio (D)



(f) Effect Of Time (C) and Ratio (D)

Figure 4.58 3D Surface Plot FBMA for (a) AB (b) AC (c) AD (d) BC (e) BD and (f) CD

4.7.1.5 Verification Model

Three experiments were conducted as confirmation tests to verify the accuracy of the model-predicted values. The strong agreement between the experimental and predicted results confirms the validity of the model. The Residual Standard Error (RSE) was used to evaluate the accuracy of the developed RSM model. RSE represents the percentage difference between the experimental and predicted values. Generally, lower RSE values indicate better model accuracy and a closer agreement between experimental and predicted responses. All RSE values were found to be below 5%, indicating a very good fit of the model to the experimental data (Table 4.28) (Odejobi & Akinbulumo, 2019). Consequently, this study demonstrates that the experimental design is a reliable, straightforward and effective approach for determining the optimum conditions for corrosion inhibition using FBMA.

Table 4.28
Table of Verification Model for FBMA

	Independent variables				Response %		
no	A	B	C	D	Predicted	Actual	RSE
1	4	0.50	16	3.5	73.36	73.52	0.21
2	6	0.75	12	3.0	59.25	59.47	0.37
3	2	0.25	12	4.0	77.10	76.88	0.28

4.7.1.6 Optimum Condition for Corrosion Inhibition FBMA

To verify the accuracy of the study, a numerical optimization was performed by setting specific goals and constraints for each factor. The constraint data Table 4.29 shows that the primary objective was to maximize the inhibition efficiency (R1) within a defined experimental range: an inhibitor concentration between 2 and 6, an acid concentration between 0.25 and 0.75, a time of 12 to 20 hours and a ratio between 3 and 4. By assigning an importance level of 3 to all factors, the model ensures a balanced and fair evaluation of these variables interact to protect the mild steel. The optimization results demonstrate the effectiveness of the developed model, as evidenced by a perfect desirability value of 1.000. This indicates that all the objectives and constraints defined in the study were fully satisfied, confirming that the predicted conditions correspond to

the most favorable scenario for corrosion inhibition using FBMA (Salam et al., 2015; Anadebe et al., 2018).

According to the response ramps from Figure 4.59, maximum inhibition is achieved at an inhibitor concentration of 5.96 mM, concentration acid 0.45M an immersion time of 19.98 hours and an inhibitor-to-acid ratio of 3.99. At this concentration, the FBMA molecules are sufficient to form a dense layer on the mild steel surface. The extended immersion time allows FBMA molecules to reach adsorption equilibrium, promoting full coverage of the mild steel surface and enhancing the stability of the protective layer (Bentiss et al., 2000; Verma et al., 2018). This ensures that the inhibition is not only immediate but also sustained over time. Similarly, the inhibitor-to-acid ratio of approximately 4 optimizes the balance between inhibitor availability and the corrosive strength of the medium, preventing excessive inhibitor desorption while maintaining effective protection.

Maintaining the acid concentration at a moderate 0.46 M further supports the inhibitor's efficiency by avoiding overly aggressive conditions that could compromise the protective film. Under these optimized conditions, the predicted inhibition efficiency reaches 90.13%. The validation of the optimum condition was performed by calculating the RSE as shown in Table 4.30, which showed values below 5% for the percentage yield of FBMA. This confirms the reliability and accuracy of the obtained results (Elebo et al., 2024). These conditions provide the most effective scenario for maximizing FBMA adsorption, establishing a stable protective layer through physisorption and minimizing corrosion of mild steel in the acidic environment.

Table 4.29
Constraint Data of FBMA

Parameters	Goal	Lower limit	Upper limit	Lower weight	Upper weight	Importance
A: Inhibitor concentration	Is in range	2	6	1	1	3
B: Acid concentration	Is in range	0.25	0.75	1	1	3
C: Immersion Time	Is in range	12	20	1	1	3
D: Ratio	Is in range	3	4	1	1	3
R1: Inhibition Efficiency	Maximize	51.51	90.1	1	1	3

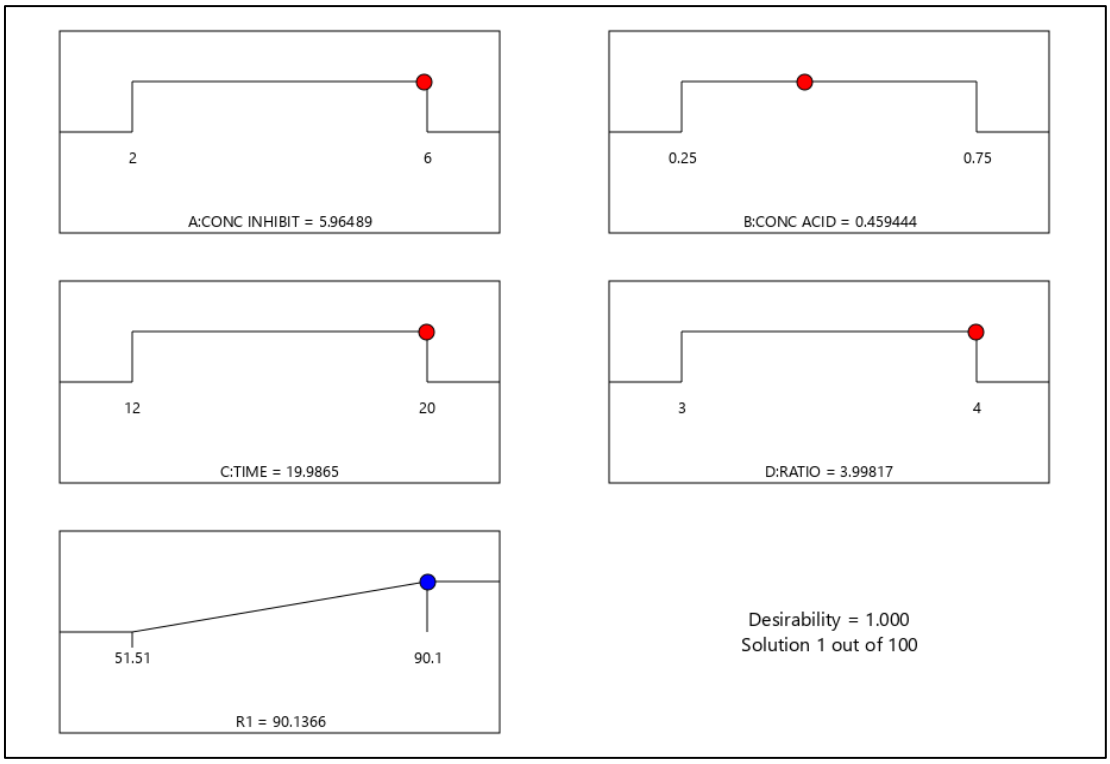


Figure 4.59 Optimum Ramp Data for FBMA

Table 4.30
Actual Predicted Data for Optimum Condition FBMA

Independent variables					Response %		
no	A	B	C	D	Predicted	Actual	RSE
1	5.96	0.45	19.9	3.9	90.13	90.02	0.12

4.7.2 Optimization for TOMA

The inhibition efficiencies values obtained under different experimental conditions are presented in Table 4.31 A total of 30 experiments were carried out, although one run was excluded due to unrelated factors. The highest inhibition efficiency of 82.4 % was achieved at a concentration inhibitor of 6 mM (A), a concentration acid of 0.75 M (B), an inhibitor-to-acid ratio of 4 (C) and an immersion time of 20 hours (D) std 16. In contrast, the lowest inhibition efficiency of 36.09 % was recorded at an inhibitor concentration of 2 mM (A), an acid concentration of 0.75 M (B), an inhibitor-to-acid ratio of 4 (C) and an immersion time of 12 hours (D) std 11.

Table 4.31
Experimental Runs from CCD Design and the Response for TOMA

Std	Run	Concentration inhibitor (mM)	Concentration acid (M)	Immersion time (h)	Ratio	Inhibition efficiency (%)
1	3	2	0.25	12	3.0	64.10
2	7	6	0.25	12	3.0	80.86
3	6	2	0.75	12	3.0	37.22
4	12	6	0.75	12	3.0	63.01
5	25	2	0.25	20	3.0	62.00
6	26	6	0.25	20	3.0	60.00
7	17	2	0.75	20	3.0	67.95
8	14	6	0.75	20	3.0	70.80
10	1	6	0.25	12	4.0	72.30
11	27	2	0.75	12	4.0	36.09
12	28	6	0.75	12	4.0	54.20
13	18	2	0.25	20	4.0	69.70
14	2	6	0.25	20	4.0	67.40
15	10	2	0.75	20	4.0	80.90
16	4	6	0.75	20	4.0	82.40
17	11	0	0.50	16	3.5	55.40
18	21	8	0.50	16	3.5	77.40
19	23	4	0	16	3.5	-
20	15	4	1.00	16	3.5	45.22
21	29	4	0.50	8	3.5	56.00
22	9	4	0.50	24	3.5	77.29
23	22	4	0.50	16	2.5	70.40
24	16	4	0.50	16	4.5	71.86
25	24	4	0.50	16	3.5	58.53
26	8	4	0.50	16	3.5	58.52
27	5	4	0.50	16	3.5	60.00
28	13	4	0.50	16	3.5	58.53
29	20	4	0.50	16	3.5	55.00
30	19	4	0.50	16	3.5	56.00

4.7.2.1 Determination of Selected Model

According to the results shown in the Table 4.32 the quadratic model compared to the 2FI model had the highest F-value and the lowest p-value, showing that it was the most suitable model among those tested. The cubic model was found to be aliased, meaning that its effects could not be clearly distinguished from other model terms and therefore it was not selected. As a result, the quadratic model was chosen as the best and most appropriate model for describing and optimising the response (Nor et al., 2022).

Table 4.32
Sequential Model Sum of Square for TOMA

Source	Sum of squares	df	Mean square	*F*-value	*p*-value	
Mean vs Total	115,300.	1	115300			
Linear vs Mean	1679.72	4	419.93	4.56	0.0070	
2FI vs Linear	1680.36	6	280.06	9.50	< 0.0001	
Quadratic vs 2FI	490.30	4	122.57	42.82	< 0.0001	Suggested
Cubic vs Quadratic	22.17	8	2.77	0.9283	0.5522	Aliased
Residual	17.91	6	2.98			
Total	119200	29	4110.46			

According to Table 4.33 the quadratic model shows a low *F*-value of 0.7170. and a high *p*-value of 0.6874, indicating that the lack of fit is not significant. This confirms that the quadratic model adequately represents the experimental data and the differences between the predicted and experimental values are largely due to pure experimental error (Dada et al., 2021). Although the cubic model also exhibits a non-significant lack of fit, it is aliased and therefore not suitable for further interpretation. Based on these findings, the quadratic model was selected as the most appropriate model for describing the response.

Table 4.33
Lack of Fit Test for TOMA

Source	Sum of squares	df	Mean square	*F*-value	*p*-value	
Linear	2193.23	19	115.43	32.99	0.0005	
2FI	512.87	13	39.45	11.27	0.0073	
Quadratic	22.58	9	2.51	0.7170	0.6874	Suggested
Cubic	0.4128	1	0.4128	0.1180	0.7452	Aliased
Pure Error	17.50	5	3.50			

The standard deviation (Std. Dev.) reflects the average difference between the experimental and predicted values, where a lower value indicates better model accuracy (Antony, 2014; Tansuğ et al., 2014). Among the models studied, the quadratic model shows a low standard deviation of 1.69 (Table 4.34), indicating a close agreement between the predicted and experimental results compared to the linear and 2FI models. The coefficient of determination (R^2) describes how much of the variation in the response is explained by the model. A higher R^2 value indicates a better fit. The quadratic model exhibits a very high R^2 value of 0.9794, meaning that about 99% of the response variation is explained by the model. In contrast, the linear model shows a much lower R^2 value of 0.4318, indicating poor model performance.

The adjusted R^2 accounts for the number of terms in the model and provides a more reliable measure of model quality (Antony, 2014). The quadratic model again shows a high adjusted R^2 value of 0.9794, confirming that the inclusion of quadratic terms significantly improves the model without overfitting. The predicted R^2 evaluates the model's ability to predict new experimental data (Anadebe et al., 2018; Odejobi & Akinbulumo, 2019). The quadratic model has a high predicted R^2 value of 0.9563, which is in good agreement with the adjusted R^2, indicating strong predictive capability. Meanwhile, the linear model shows a very low predicted R^2 value of 0.1184, demonstrating weak predictive performance.

The PRESS (Predicted Residual Error Sum of Squares) represents the overall prediction error, where a smaller value indicates better prediction accuracy (Antony, 2014; Dada et al., 2021). The quadratic model records the lowest PRESS value of 170.00, further confirming its better predictive ability. Although the cubic model shows slightly higher R^2 values, it is aliased and therefore not suitable for interpretation. Based on these results, the quadratic model was selected as the most appropriate and reliable model for this study.

Table 4.34
Model Summary Statistics for TOMA

Source	Standard Deviation	R^2	Adjusted R^2	Predicted R^2	PRESS	
Linear	9.60	0.4318	0.3370	0.1184	3429.78	
2FI	5.43	0.8637	0.7879	0.7511	968.24	
Quadratic	1.69	0.9897	0.9794	0.9563	170.00	Suggested
Cubic	1.73	0.9954	0.9785		*	Aliased

4.7.2.2 Identification of Model Accuracy

To guarantee that the mathematical model appropriately portrays the corrosion inhibition process, the data's reliability was confirmed with specific diagnostic plots. The Normal Plot of Residuals Figure 4.60 supports the model's because the data points follow a very straight line, showing that experimental errors are normally distributed and the model has no major bias. The Residuals vs. Predicted (Figure 4.61) and Residuals vs. Run plots (Figure 4.63). Figure 4.63 demonstrate a random scatter of points within the red control limits of ±3.93, indicating a consistent variance and no time-related mistakes during laboratory run. The model's reliability is further strengthened by the Cook's Distance plot Figure 4.64, where all experimental points remain well below the 1.0 threshold, confirming that no single outlier unfairly influenced the results. Additionally, the Box-Cox Plot Figure 4.65 shows a "Current Lambda" of 1, which sits perfectly within the 95% confidence intervals; since the recommended transformation is "None," it is verified that the original data scale is ideal for this analysis. Statistically, these findings are highly significant, as evidenced by a *p*-value of less than 0.001 ($p<0.001$), which proves that the relationships identified between the variables are robust (Salam et al., 2015; Dada et al., 2021). The predicted vs Actual plot as shown in Figure 4.70 deduces that both values are very close to each other and demonstrating good agreement between the model and experimental data. It is concluded that the model has high accuracy and reliability in predicting the response.

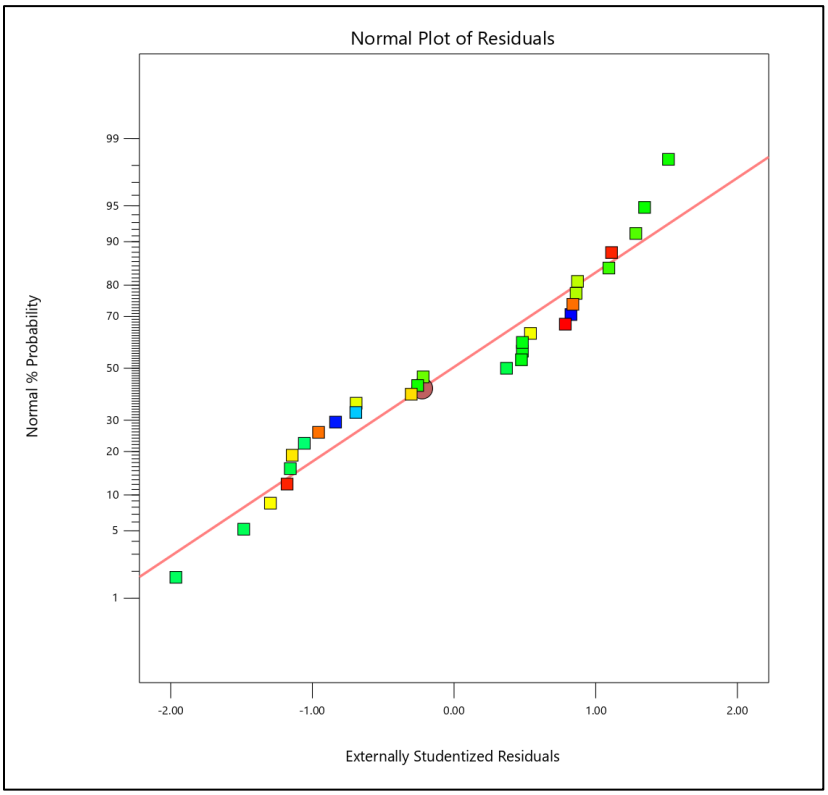


Figure 4.60 Normal Plot for TOMA

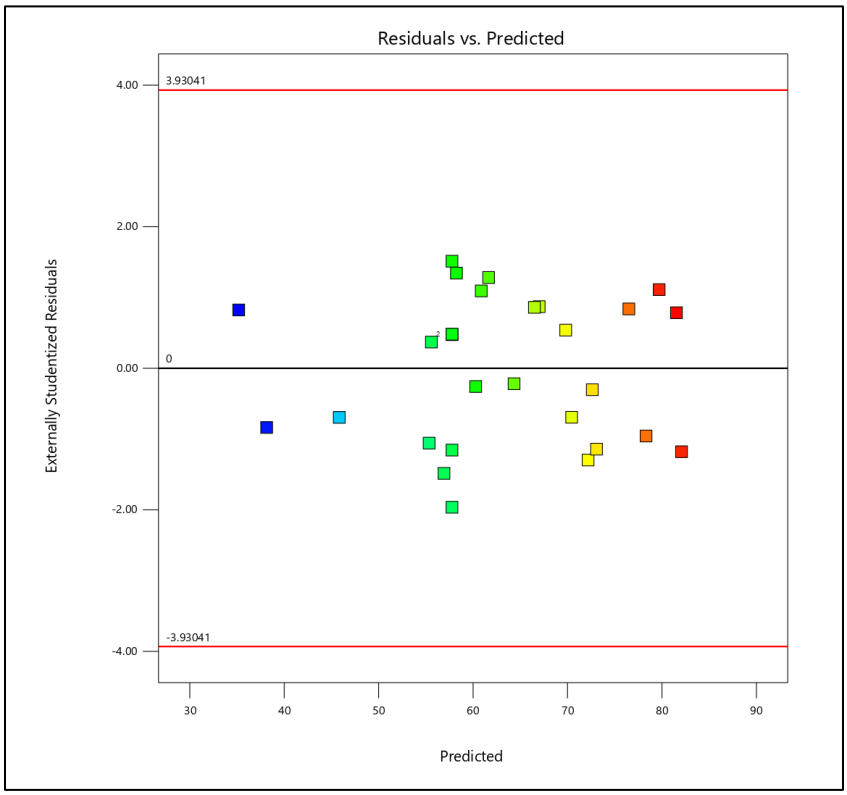


Figure 4.61 Residuals vs Predicted for TOMA

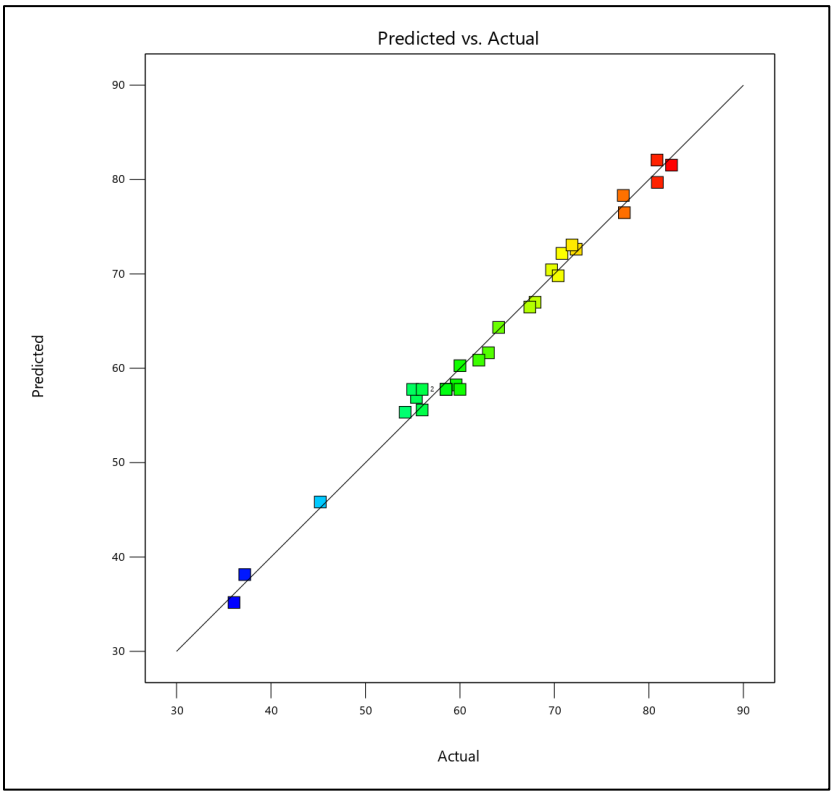


Figure 4.62 Predicted vs Actual for TOMA

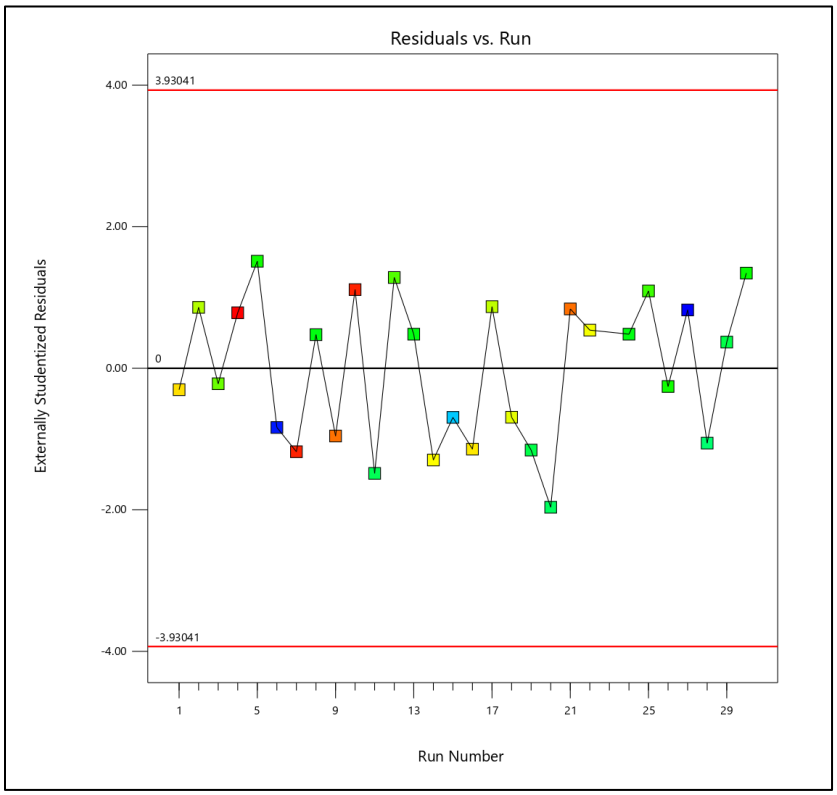


Figure 4.63 Residual vs Run for TOMA

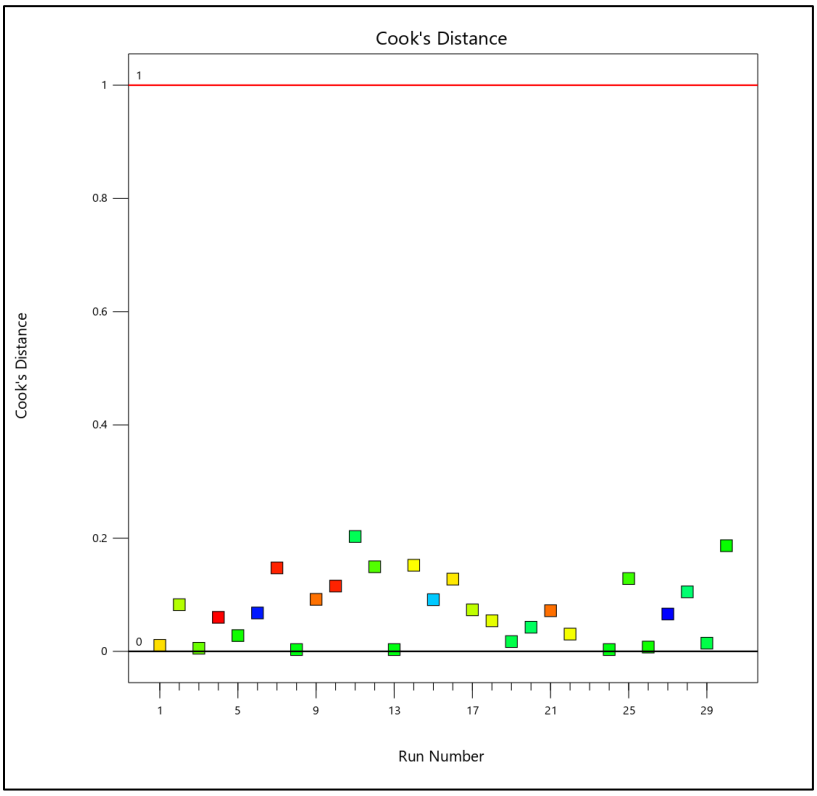


Figure 4.64 Cook's Distance for TOMA

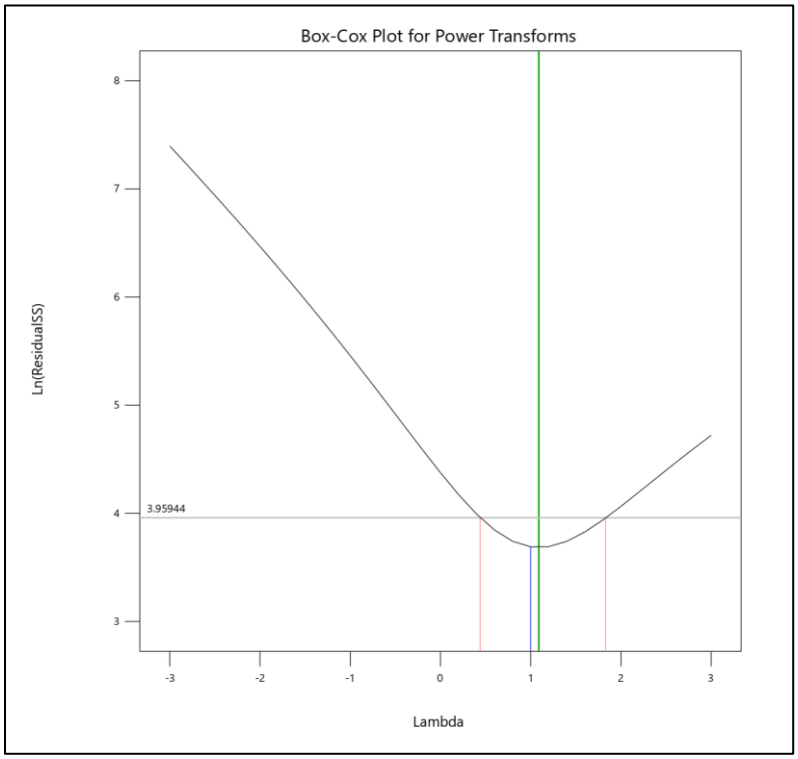


Figure 4.65 Box-Cox Plot for TOMA

4.7.2.3 Analysis of Variance (ANOVA)

Table 4.35 summarizes the ANOVA results for TOMA's inhibitory efficiency. The model for predicting inhibition efficiency is highly significant, with a low *p*-value (< 0.0001) and a high *F*-value (96.08). These findings demonstrate that the selected model terms have a significant and substantial impact on inhibition efficiency (Salam et al., 2015; Tansuğ et al., 2014). The lack-of-fit test returns a high *p*-value (0.6874) but a low *F*-value (0.7110), indicating that the lack of fit is not significant. This demonstrates that the model properly matches the experimental data and the variations between anticipated and experimental values are primarily attributable to random experimental error rather than model inadequacies (Dada et al., 2021). The coefficient of determination ($R^2 = 0.9896$) indicates that approximately 98.96% of the variation in inhibition efficiency is explained by the model.

The adjusted R^2 (0.9793) and predicted R^2 (0.9563) values are also high and in close agreement, confirming that the model is reliable and has strong predictive capability for new experimental data (Anadebe et al., 2018; Odejobi & Akinbulumo, 2019). The low standard deviation value of 1.69 and the low coefficient of variation (C.V = 2.68%) indicate good precision and reproducibility of the experimental results. In addition, the adequate precision value of 38.53, which measures the signal-to-noise ratio, is much higher than the minimum recommended value of 4, showing that the model provides an adequate signal and can be effectively used to explore the design space.

In this study, the relationship between inhibition efficiency (Y) and the four independent variables which were concentration inhibitor (A), concentration acid (B), immersion time (C) and inhibitor-to-acid ratio (D), including their interaction effects, is described by Equation (4.2). A positive coefficient in the model indicates a synergistic effect that enhances inhibition efficiency, while a negative coefficient represents an antagonistic effect that reduces inhibition efficiency when factors were combined.

$$\begin{aligned} Y = {} & 57.76 - 4.89A + 2.79B - 5.68C - 0.814D - 1.44AB - 4.58AC - \\ & 0.8369AD + 8.08BC - 0.7856\,BD + 3.92CD - 2.24A^2 - 1.59B^2 + \\ & 2.30C^2 + 3.42D^2 \end{aligned} \quad (4.2)$$

In this Equation (4.2), Y represents the predicted inhibition efficiency. The terms A, B, C and D correspond to the main (linear) effects of the variables. The squared terms (A^2, B^2, C^2 and D^2) describe the curvature or quadratic effects, while the interaction terms (AB, AC, AD, BC, BD and CD) explain how the combined effect of two variables influences the inhibition efficiency. By substituting specific values of A, B, C and D into Equation 4.2, the predicted inhibition efficiency can be calculated. These predicted values were then analyzed using response surface methodology (RSM) based on a central composite design (CCD) and compared with the experimental results to evaluate how accurately the model represents the actual system behavior.

Table 4.35
ANOVA Analysis of the Model for TOMA

Source	Inhibition efficiency of TOMA
p-value model	< 0.0001
F-value model	96.08
p-value Lack of fit	0.6874
F-value Lack of fit	0.7110
R^2	0.9896
Adjusted R^2	0.9793
Predicted R^2	0.9563
Standard deviation	1.69
Coefficient of Variation (C.V)	2.68
Adequate precision	38.5331

Table 4.36 presents the ANOVA results for the regression model developed to predict the inhibition efficiency of TOMA. The table lists important statistical parameters, including the sum of squares, *F*-values and *p*-values, which are used to evaluate the significance of each model term. The independent variables are linear terms inhibitor concentration (A), concentration acid (B), immersion time (C) and inhibitor-to-acid ratio (D), interaction terms (AB, AC, AD, BC, BD and CD) and quadratic terms (A^2, B^2, C^2 and D^2). Based on the *p*-values, all linear terms (A, B, C and D) show significant effects on inhibition efficiency, with *p*-values less than 0.05. Among these variables, concentration inhibitor (A), immersion time (C) and acid concentration (B) exhibit particularly strong effects, as indicated by their high *F*-values. Several interaction terms, including AC, BC and CD, are also statistically significant ($p < 0.05$), demonstrating that the combined effects of two variables play an important role in influencing inhibition efficiency (Myers et al., 2016; Montgomery, 2020).

However, the interaction terms AD (p = 0.0679) and BD (p = 0.0844) are not significant, suggesting that these variable combinations have a weaker influence on the response. All quadratic terms (A^2, B^2, C^2 and D^2) are statistically significant with p-values below 0.05, indicating the presence of curvature effects in the system and confirming that inhibition efficiency does not change linearly with the studied variables. Overall, these results show that both individual factors and their interactions contribute significantly to the inhibition efficiency of TOMA.

Table 4.36
ANOVA Analysis Factor for TOMA

Source	Sum of square	df	Mean square	F-value	p-value
A- Inhibitor concentration	574.38	1	574.38	200.65	< 0.0001
B- Acid concentration	133.35	1	133.35	46.58	< 0.0001
C- Immersion time	774.64	1	774.64	270.61	< 0.0001
D- Ratio	15.96	1	15.96	5.57	0.0333
AB	33.32	1	33.32	11.64	0.0042
AC	335.90	1	335.90	117.34	< 0.0001
AD	11.21	1	11.21	3.91	0.0679
BC	1044.74	1	1044.74	364.97	< 0.0001
BD	9.88	1	9.88	3.45	0.0844
CD	245.31	1	245.31	85.70	< 0.0001
A^2	133.36	1	133.36	46.59	< 0.0001
B^2	40.30	1	40.30	14.08	0.0021
C^2	140.77	1	140.77	49.17	< 0.0001
D^2	311.68	1	311.68	108.88	< 0.0001

4.7.2.4 Three-Dimensional (3D) surface

The 3D surface plot Figure 4.66 (a) demonstrates the effect of concentration inhibitor (A) and concentration acid (B) on inhibition efficiency (R1). The graph has a distinct increasing trend as the inhibitor concentration increases, demonstrating that the protection level grows as more inhibitor is put into the system. Statistically, the interaction between these two variables is highly significant, as confirmed by F-value of 11.64 and p-value of 0.0042, which is well below the common significance threshold ($p < 0.05$) furthermore, the overall model remains robust with a total p-value of less than 0.0001 ($p < 0.0001$), proving that the combined effects of the variables are fundamental drivers of the model's predictive power (Bezerra et al., 2008). This highly significant result occurs because the inhibitor concentration determines the density of

protective molecules available to coat the mild steel. When the concentration is high, many molecules compete for and occupy the active sites on the mild steel surface, creating a blocking effect that shields the ions from the acid concentration (Finšgar & Jackson, 2014). At the optimal concentration, these molecules form an impenetrable barrier that remains stable even as the environment becomes more corrosive. The red design points resting directly on the surface plot validate the model's precision, showing that the high inhibition efficiency recorded during experiment aligns perfectly with the predicted mathematical trends. This confirms that the synergy between these two factors is essential for maximizing metal preservation and provides a reliable basis for optimizing the chemical dosage in real-world applications.

The 3D surface map Figure 4.66 (b) in this corrosion investigation shows the effect of concentration inhibitor (A) and immersion time (C) on inhibition efficiency (R1). The graph shows a clear and significant rising trend towards the yellow-green region as the inhibitor concentration and immersion time rise. Statistically, the interaction between these two variables is highly significant, as confirmed by a high *F*-value of 117.34 and an extremely low *p*-value of less than 0.0001 ($p < 0.0001$), which proves that their combined effect is a primary driver for maximizing the protection of the metal surface (Elebo et al., 2024). This highly significant result occurs because the inhibitor concentration provides the necessary number of molecules to cover the mild steel surface, while immersion time allows these molecules to settle and bond firmly. As time progresses from 12 toward 20 hours, the inhibitor molecules can organize into a dense, impenetrable protective film that physically blocks corrosive agents (Hashim et al., 2020; Ahmed et al., 2024). The smooth upward slope reaching toward peak efficiency confirms that these two factors work in harmony to create a robust barrier. Furthermore, the red design points sitting directly on the surface validate the model's precision, showing that the laboratory data matches the predicted mathematical trends perfectly. This confirms that maximizing both concentration and time is essential for achieving the highest possible inhibition efficiency in this study.

Figure 4.66 (c) shows the 3D surface plot specifically illustrates the interaction between concentration inhibitor (A) and ratio (D) on the inhibition efficiency (R1). The graph shows a gradual upward trend toward the yellow region as the inhibitor ratio increases, even as the inhibitor concentration remains an influencing factor. Statistically, the interaction between these two variables yielded an *F*-value of 3.91 and a *p*-value of 0.0679. Although this *p*-value is slightly above the conventional 0.05

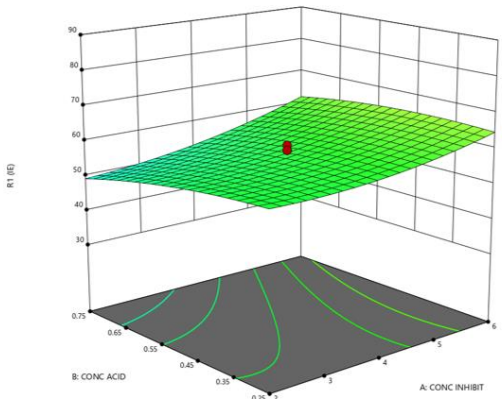
significance threshold, the overall model remains highly significant with a total *p*-value of less than 0.0001 ($p < 0.0001$), confirming that these parameters still contribute meaningfully to the overall protective performance. This interaction occurs because the ratio represents the balance of active components within the inhibitor blend. When the ratio is at its highest value (4.0), it provides the most effective combination of inhibitor molecules, particularly at higher inhibitor concentrations. These molecules adsorb onto the mild steel surface, forming a protective layer that limits the access of corrosive species and suppresses mild steel dissolution (Hashim et al., 2020; Ahmed et al., 2024). As indicated by the red design points closely following the response surface, the experimental results are in good agreement with the model predictions. Overall, the plot demonstrates that maximizing the inhibitor ratio, together with sufficient inhibitor concentration, is a reliable strategy for maintaining high inhibition efficiency, as it promotes the formation of a more stable and robust protective film. A more stable and robust film that can withstand moderate acidic environments.

3D surface plot specifically Figure 4.66 (d) illustrates the interaction between concentration acid (B) and immersion time (C) on the inhibition efficiency (R1). The graph shows a significant upward trend as time increases, indicating that the inhibitor becomes much more effective at protecting the mild steel surface over longer periods. Statistically, this interaction is extremely significant, as confirmed by a high *F*-value of 364.97 and a *p*-value of less than 0.0001 ($p < 0.0001$), which proves that the combined influence of acid strength and immersion time is a primary driver of the corrosion inhibition process. This highly significant result occurs because the inhibitor molecules require sufficient time to move through the solution and attach firmly to the mild steel surface. As time progresses from 12 toward 20 hours, these molecules organize themselves into a dense, continuous protective film. This film acts as a physical barrier that shields the mild steel from the acid concentration, effectively blocking the corrosive agents even at higher acid levels (Ahmed et al., 2024). The smooth curve rising toward the yellow-orange region highlights that peak protection is reached when the inhibitor has had maximum time to stabilize its protective layer. The red design points resting directly on the surface validate the model's accuracy, confirming that these laboratory results are highly reliable.

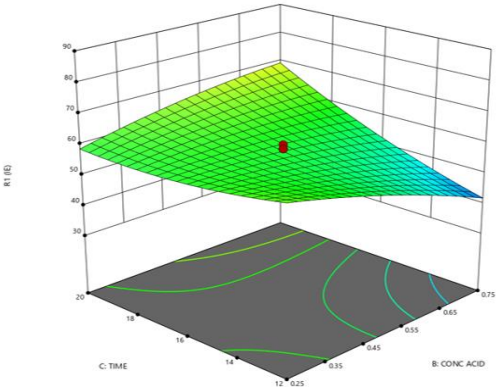
The 3D surface plot Figure 4.66 (e) depicts the relationship of concentration acid (B) and ratio (D) on inhibitory efficiency (R1). The plot shows a gradual trend where the efficiency is maintained or improved as the inhibitor ratio increases, even

when facing different levels of acid. Statistically, the interaction between these two variables yielded an *F*-value of 3.45 and a *p*-value of 0.0844. While this *p*-value is slightly above the strict 0.05 threshold for this specific interaction, the overall model remains exceptionally robust with a total *p*-value of less than 0.0001 ($p < 0.0001$), confirming that the combined experimental factors are highly reliable for predicting corrosion protection. This interaction occurs because the ratio represents the balance of active chemical components within the inhibitor. When the ratio is optimized toward 4.0, it provides a more effective molecular structure that can withstand the corrosive attack of the acid concentration. These molecules work by attaching to the mild steel surface to form a thin but resilient shield that interferes with the chemical reaction between the acid and the substrate (Hashim et al., 2020; Ahmed et al., 2024). As shown by the red design points resting on the surface, the experimental data aligns well with the model's predictions. The plot indicates that maximizing the inhibitor ratio is a reliable strategy for maintaining high efficiency, as it ensures a more stable protective layer that can resist aggressive acidic environments.

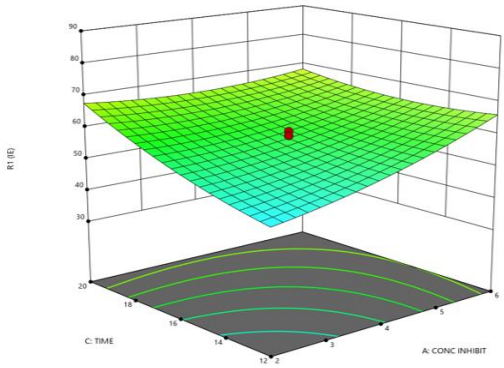
The 3D surface plot Figure 4.66 (f) illustrates the interaction between immersion time (C) and ratio (D) on the inhibition efficiency (R1). The graph displays a significant upward trend toward the yellow-orange region as both immersion time and the inhibitor ratio increase, indicating a strong synergistic effect between these two variables. Statistically, the interaction between immersion time and ratio is exceptionally significant, as confirmed by a high *F*-value of 85.70 and an extremely low *p*-value of less than 0.0001 ($p < 0.0001$), which proves that their combined influence is a primary driver for maximizing corrosion protection. This highly significant result occurs because the ratio determines the correct balance of active chemical components needed to bind with the mild steel surface. When this optimal ratio is combined with a longer immersion time of up to 20 hours, it allows the inhibitor molecules to not only attach to the surface but to pack together tightly into a more organized and impenetrable protective film. Without sufficient time or the correct ratio, the protective barrier would be thin or patchy, leaving the metal vulnerable to the acid. However, at the peak of this 3D surface, the combination of maximum time and the highest ratio produces the most effective inhibition (Shahid, 2011).



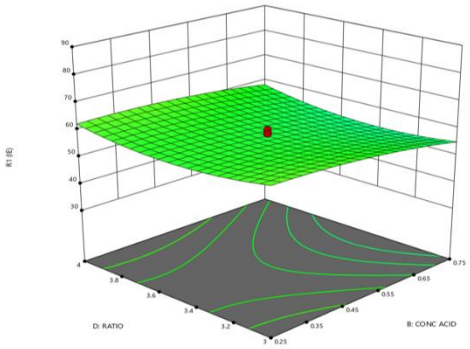
(a) Effect of Concentration Inhibitor (A) and Acid Concentration (B)



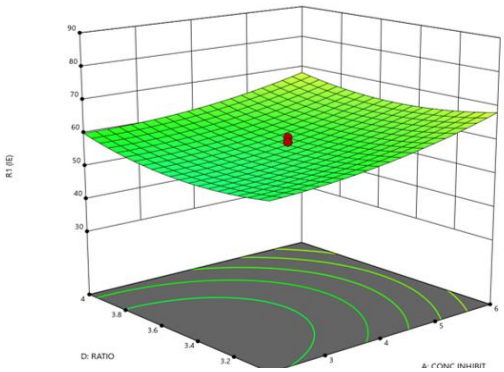
(d) Effect of Concentration Acid (B) and Time (C)



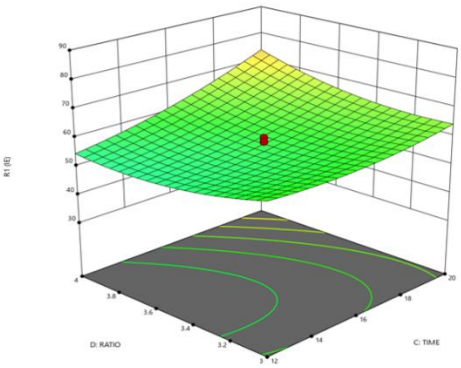
(b) Effect of Concentration Inhibitor (A) and Time (C)



(e) Effect of Concentration acid (B) and Ratio (D)



(c) Effect of Concentration Inhibitor (A)and Ratio (D)



(f) Effect of Time (C) and Ratio (D)

Figure 4.66 3D Surface Plot TOMA for (a) AB (b) AC (c) AD (d) BC (e) BD and (f) CD

4.7.2.5 Verification Model

Three tests were carried out to ensure that the model predictions were accurate. The close agreement between the predicted and experimental results confirms the reliability and validity of the model. RSE values confirmed the value were below 5% indicates the models were suitable to use Table 4.37 (Nor et al., 2022). This demonstrates that the experimental design is robust, simple and effective for determining the optimum conditions for corrosion inhibition using TOMA and that the model can accurately predict inhibitor performance under the specified conditions.

Table 4.37
Table of Verification Model TOMA

	Independent variables				Response %		
no	A	B	C	D	Predicted	Actual	RSE
1	6	0.25	12	3.5	81.97	81.07	1.09
2	6	0.25	20	3.0	60.32	58.88	2.50
3	2	0.25	12	4.0	57.87	57.50	0.63

4.7.2.6 Optimum Condition for Corrosion Inhibition (TOMA)

To verify the accuracy of the corrosion study, the Constraint Table 4.38 show the maximize inhibition efficiency (R1) while keeping the variables within their established ranges: inhibitor concentration (2 to 6), acid concentration (0.25 to 0.75), immersion time (12 to 20 hours) and ratio (3 to 4). By assigning a uniform "importance" level of 3 to every factor, the model ensured a balanced evaluation of how these variables combined to protect the mild steel. The success of the optimisation process is clearly evidenced by the desirability value of 1.000, which represents the maximum achievable desirability within the response surface methodology framework. This value indicates that all predefined optimisation criteria were simultaneously satisfied, confirming that the identified conditions correspond to a true global optimum for corrosion inhibition using TOMA.

Based on the optimisation ramps Figure 4.67, the highest inhibition performance was obtained at an inhibitor concentration (A) of 6mM, concentration acid (B) 0.25M an immersion time (C) of 12 h and an inhibitor-to-acid ratio (D) of 3. At this inhibitor's concentration, an adequate number of TOMA molecules are available to effectively

adsorb onto the mild steel surface. The presence of heteroatoms and π-electron-rich functional groups in the TOMA structure promotes strong interactions with the vacant *d*-orbitals of iron, facilitating chemisorption (Gece, 2008; Obot et al., 2019). Simultaneously, electrostatic interactions between protonated TOMA molecules and the negatively charged steel surface in the acidic medium contribute to physisorption. The coexistence of both adsorption mechanisms leads to the formation of a compact, stable and adherent protective film that efficiently blocks active corrosion sites (Verma et al., 2018). The immersion time of approximately 12 h further enhances the inhibition performance by allowing sufficient time for the adsorption equilibrium to be established. Prolonged exposure enables TOMA molecules to reorganise and strengthen their interaction with the metal surface, resulting in improved surface coverage and increased stability of the protective layer. This behaviour is consistent with adsorption-controlled inhibition mechanisms, where longer contact times favour the formation of a more uniform and persistent inhibitor film.

An inhibitor-to-acid ratio (c) 3 provides an optimal balance between the aggressive acidic environment and the availability of inhibitor molecules. At this ratio, TOMA effectively suppresses the corrosion process without reaching saturation or experiencing competitive desorption effects. Maintaining the acid concentration (B) at a moderate level of 0.25 ensures that the corrosive species remain sufficiently controlled, allowing the inhibitor to dominate the metal–solution interface and maintain its protective function (Revie & Uhlig, 2008). Under these optimised conditions, the model predicts a high inhibition efficiency of 82.07%, highlighting the strong synergistic interaction among the process variables. Table 4.39 shows the optimum condition that validated using RSE analysis, which showed values below 5% for the percentage yield of FBMA, confirming the reliability of the results. The excellent agreement between the optimisation objectives and the predicted response confirms the robustness and reliability of the developed model (Nor et al., 2022).

These mechanisms and state that the selected conditions maximise TOMA adsorption, stabilise the protective film through combined physisorption and chemisorption mechanisms and effectively minimise corrosion of mild steel in the acidic medium.

Table 4.38
Constraint Table Data TOMA

Parameters	Goal	Lower limit	Upper limit	Lower weight	Upper weight	Importance
A: Inhibitor concentration	Is in range	2	6	1	1	3
B: Acid concentration	Is in range	0.25	0.75	1	1	3
C: Immersion time	Is in range	12	20	1	1	3
D: Ratio	Is in range	3	4	1	1	3
R1: Inhibition Efficiency	Maximize	36.09	82.4	1	1	3

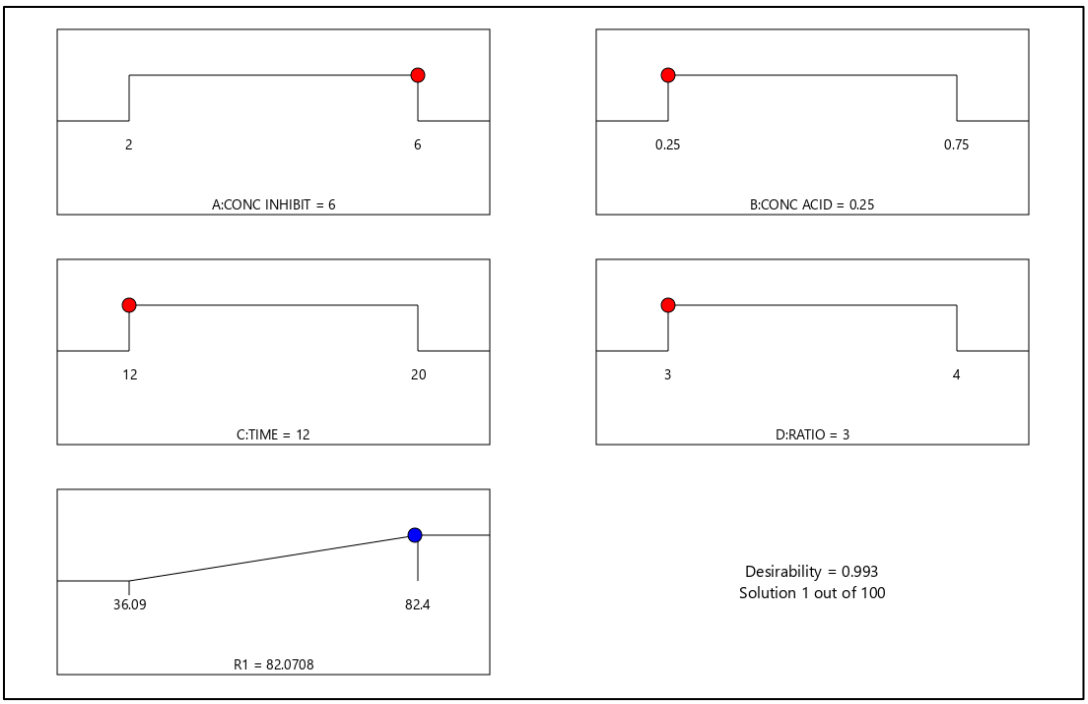


Figure 4.67 Optimum Ramp Data for TOMA

Table 4.39
Actual and Predicted Data for Optimum Condition (TOMA)

	Independent variables				Response %		
no	A	B	C	D	Predicted	Actual	RSE
1	6.00	0.45	12.00	3.0	82.07	81.37	0.85

4.7.3 Optimization for THMA

The inhibition efficiencies obtained under different experimental conditions are shown in Table 4.40 A total of 30 experiments were carried out, although two runs were excluded due to unrelated factors. The highest inhibition efficiency of 82.8% was achieved at a concentration inhibitor of 4 mM (A), a concentration acid of 0.5 M (B), an inhibitor-to-acid ratio of 4 (C) and an immersion time of 24 hours (D) std 22. In

contrast, the lowest inhibition efficiency of 52.3% was recorded at an inhibitor concentration of 2 mM (A), an acid concentration of 0.75 M (B), an inhibitor-to-acid ratio of 4 (C) and an immersion time of 12 hours (D) std 11.

Table 4.40
Experimental Runs from CCD Design and the Response of THMA

Std	Run	Concentration inhibitor (mM)	Concentration acid (M)	Immersion time (h)	Ratio	Inhibition efficiency (%)
1	18	2	0.25	12	3.0	70.16
2	6	6	0.25	12	3.0	76.00
3	25	2	0.75	12	3.0	54.00
4	20	6	0.75	12	3.0	61.37
5	17	2	0.25	20	3.0	70.31
6	12	6	0.25	20	3.0	78.20
7	30	2	0.75	20	3.0	72.90
8	14	6	0.75	20	3.0	81.25
9	9	2	0.25	12	4.0	74.50
10	8	6	0.25	12	4.0	76.90
11	28	2	0.75	12	4.0	52.30
12	22	6	0.75	12	4.0	56.60
13	1	2	0.25	20	4.0	74.20
14	4	6	0.25	20	4.0	77.30
15	29	2	0.75	20	4.0	76.20
16	7	6	0.75	20	4.0	81.80
17	3	0	0.50	16	3.5	-
18	19	8	0.50	16	3.5	63.40
19	10	4	0	16	3.5	-
20	24	4	1.00	16	3.5	72.30
21	5	4	0.50	8	3.5	61.50
22	26	4	0.50	24	3.5	82.80
23	2	4	0.50	16	2.5	72.30
24	27	4	0.50	16	4.5	73.10
25	11	4	0.50	16	3.5	71.00
26	23	4	0.50	16	3.5	72.50
27	16	4	0.50	16	3.5	72.00
28	21	4	0.50	16	3.5	71.90
29	15	4	0.50	16	3.5	73.00
30	13	4	0.50	16	3.5	73.00

4.7.3.1 Determination of Selected Model

Based on the results in the Table 4.41, the quadratic versus 2FI model showed the highest F-value and the lowest p-value, indicating that it was the most suitable model compared to the others. The cubic model was found to be aliased, meaning its effects could not be clearly separated from other terms and therefore it was not selected. Consequently, the quadratic model was chosen as the best and most appropriate model for describing and optimising the response (Nor et al., 2022).

Table 4.41
Sequential Model Sum of Square for THMA

Source	Sum of squares	df	Mean square	*F*-value	*p*-value	
Mean vs Total	151100	1	151100			
Linear vs Mean	683.13	4	170.78	4.88	0.0054	
2FI vs Linear	352.05	6	58.67	2.20	0.0942	
Quadratic vs 2FI	444.94	4	111.24	165.31	< 0.0001	Suggested
Cubic vs Quadratic	7.27	7	1.04	4.23	0.0493	Aliased
Residual	1.47	6	0.2456			
Total	152600	28	5448.60			

. According to the results in Table 4.42, the quadratic model shows a low *F*-value of 4.29 and a high *p*-value of 0.0629, confirming that its lack of fit is not significant. This suggests that the quadratic model provides a good representation of the experimental data and the variation between predicted and observed values is primarily due to pure experimental error. Although the cubic model also exhibits a non-significant lack of fit, it is aliased and therefore cannot be reliably interpreted. Based on these findings, the quadratic model was selected as the most suitable model for describing the response.

Table 4.42
Lack of Fit Test (THMA)

Source	Sum of squares	df	Mean square	*F*-value	*p*-value	
Linear	804.62	18	44.70	200.75	< 0.0001	
2FI	452.58	12	37.71	169.38	< 0.0001	
Quadratic	7.63	8	0.9543	4.29	0.0629	Suggested
Cubic	0.3600	1	0.3600	1.62	0.2595	Aliased
Pure Error	1.11	5	0.2227			

According to the Table 4.43 the quadratic model shows the lowest standard deviation (<0.0001), demonstrating very close agreement between the predicted and experimental results. The coefficient of determination (R^2) indicates the extent to which the model explains the variation in the response. A higher R^2 value reflects a better fit to the data (Bezerra et al., 2008; Myers et al., 2016). The quadratic model presents a high R^2 value of 0.9941, confirming that most of the response variation is captured by the model. In contrast, the linear model exhibits poor performance, as reflected by its low R^2 value.

The adjusted R^2 considers the number of model terms and provides a more dependable assessment of model quality. The quadratic model again shows a high adjusted R^2 value of 0.9878, indicating that the additional quadratic terms significantly improve the model without overfitting. The predicted R^2 evaluates the model's ability to forecast new experimental results (Benyounis, 2019). The quadratic model demonstrates good predictive strength, with a predicted R^2 that is inacceptable agreement with the adjusted R^2, whereas the linear model shows weak predictive capability.

The PRESS value represents the overall prediction error of the model, where smaller values correspond to better predictive performance (Yolmeh & Jafari, 2017). The quadratic model records the lowest PRESS value (< 0.0001), further confirming its better predictive accuracy. Although the cubic model displays relatively high R^2 values, it is aliased and therefore unsuitable for reliable interpretation. Based on these statistical findings, the quadratic model was selected as the most appropriate and dependable model for this study.

Table 4.43
Model Summary Statistics for THMA

Source	Std Dev	R^2	Adjusted R^2	Predicted R^2	PRESS	
Linear	5.92	0.4588	0.3647	0.1537	1260.08	
2FI	5.17	0.6953	0.5160	0.4802	773.95	
Quadratic	0.8203	0.9941	0.9878	0.9628	55.40	Suggested
Cubic	0.4955	0.9990	0.9955		*	Aliased

4.7.3.2 Identification of Model Accuracy

To confirm that the developed mathematical model accurately simulates the corrosion inhibition process, the experimental data was undergone comprehensive diagnostic testing. This validation is for demonstrating that the findings are statistically significant and not the result of random error. The initial accuracy of the model was verified using a normal probability plot of residuals Figure 4.68. The data points in this study follow a linear distribution, which signifies that the experimental errors are normally distributed (Montgomery, 2020). This linearity indicates that the model is unbiased and well-balanced. Furthermore, because the data does not exhibit an "S-shaped" curvature, it can be concluded that the selected quadratic model provides an optimal fit for the experimental data without the necessity for further mathematical transformations. Figure 4.82 shows that the residuals values are randomly scattered around the zero line without any clear pattern indicating the model assumptions are fascinating and there is no significant systematic error.

The predictive capability of the model was further validated by correlating the values estimated by the software against the actual laboratory measurements. The resulting data points are tightly clustered along a 45° diagonal line, demonstrating a high degree of precision in identifying the relationship between acid concentration, immersion time and inhibition efficiency. The robustness of the model is further supported by the close agreement between the Adjusted R^2 and Predicted R^2 values (which differ by less than 0.2 (Figure 4.83). This high correlation confirms that the model is reliable for predicting corrosion behavior even for experimental conditions located between the specifically tested design points. Figure 4.84 displays the residual values are randomly distributed above and below the zero line throughout the experimental runs, with no obvious trend pattern. This deduces there is no time-related bias and confirms the adequacy of the developed model (Benyounis, 2019). Finally, the model was screened for potential outliers using Cook's Distance Figure 4.72. All experimental data points remained within the acceptable limits, specifically falling below the threshold of 1.0, indicating that no single observation exerted a disproportionate or "unfair" influence on the regression analysis. This confirms that the generated 3D response surfaces provide an authentic representation of the chemical interactions occurring between the inhibitor molecules and the acidic environment (Figure 4.86) (Elebo et al., 2024; Mansor et al., 2024).

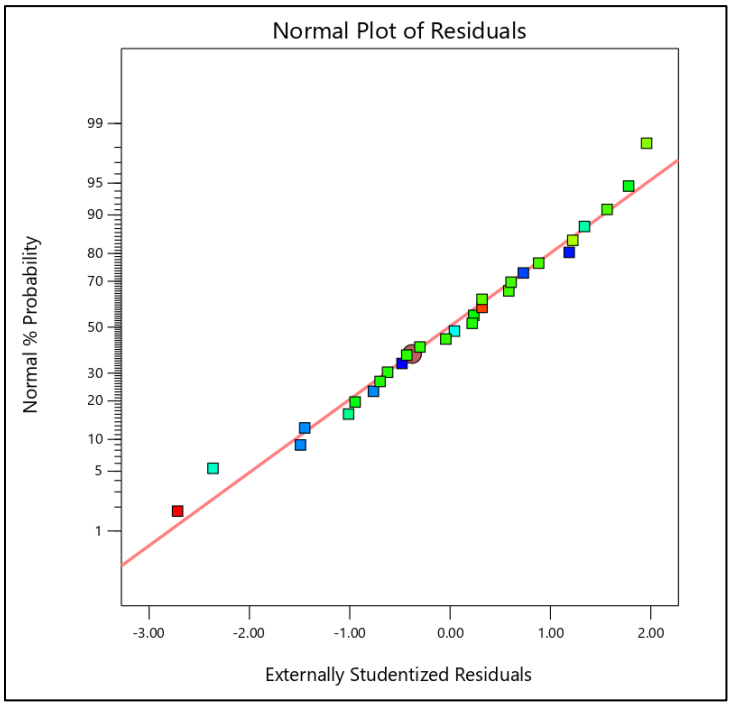


Figure 4.68 Normal Plot for THMA

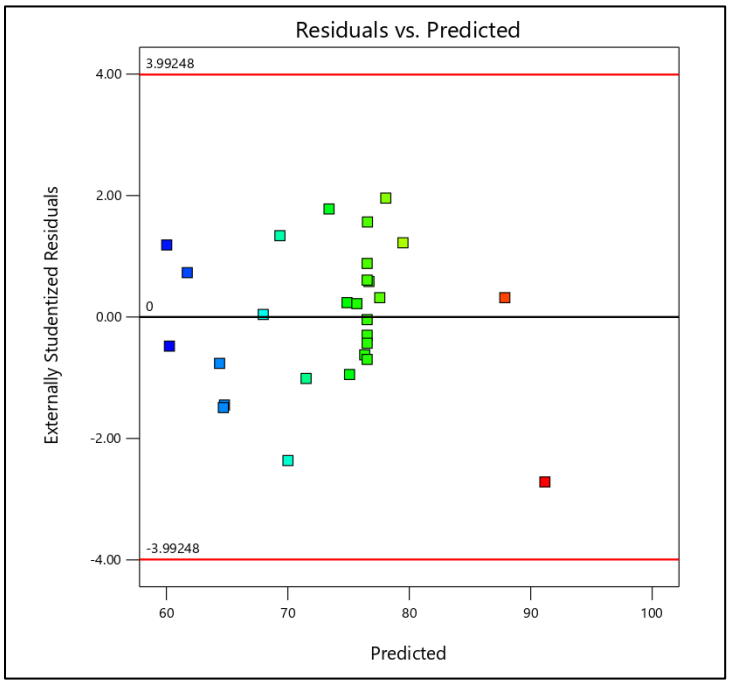


Figure 4.69 Residual vs Predicted for THMA

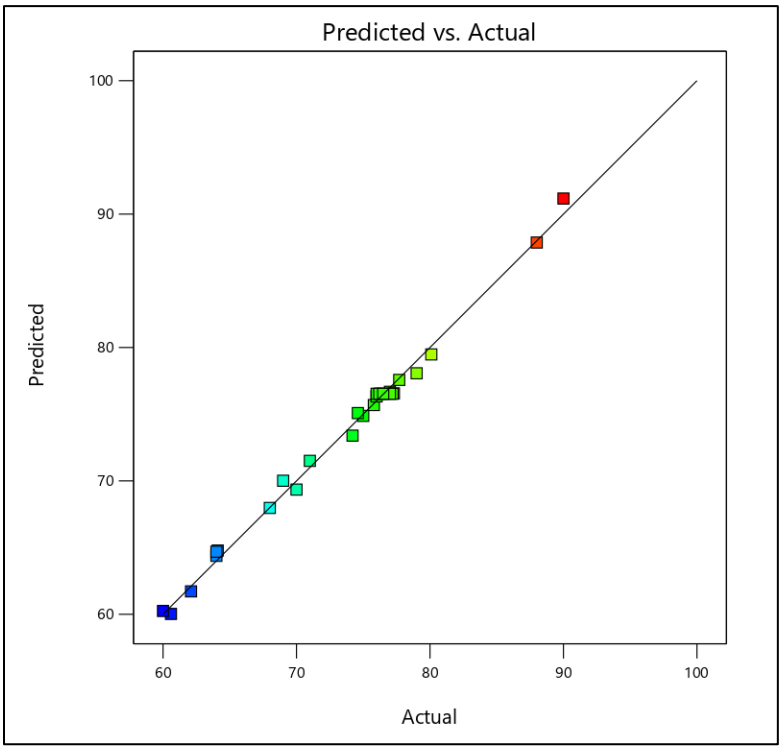


Figure 4.70 Predicted vs Actual for THMA

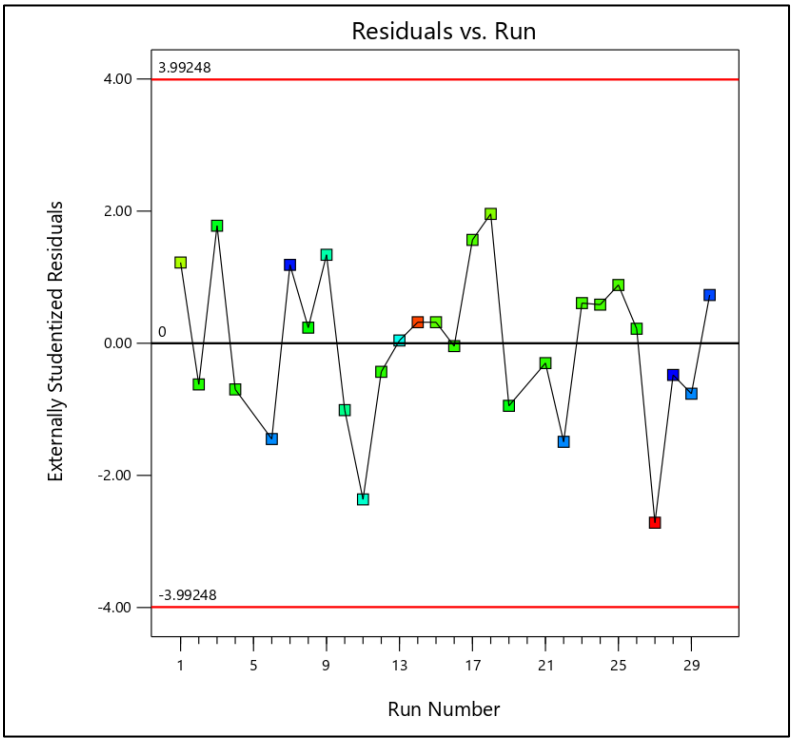


Figure 4.71 Residual vs Run for THMA

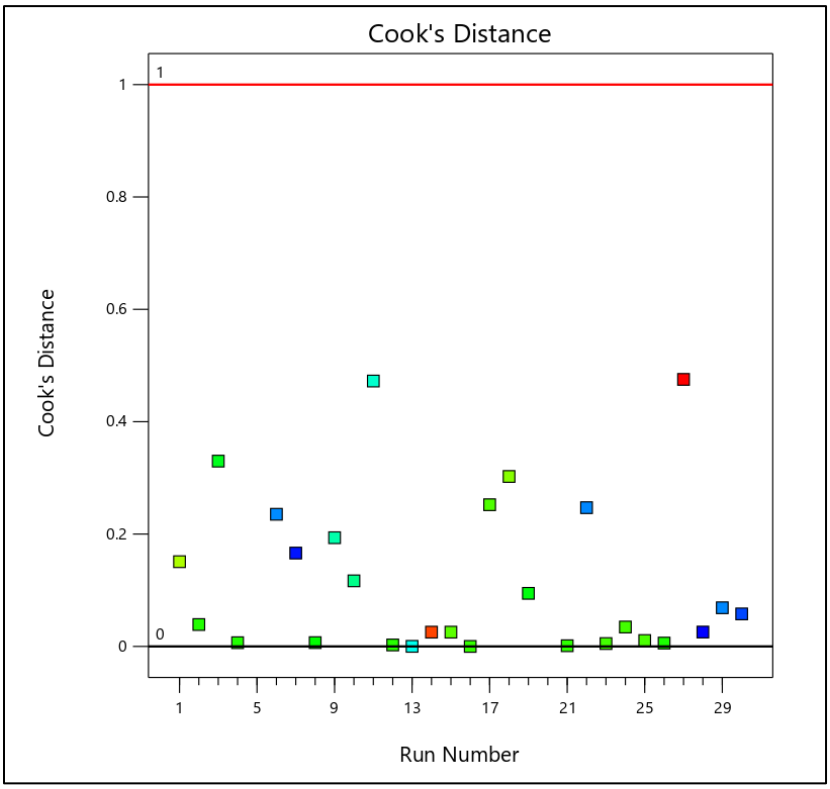


Figure 4.72 Cook's Distance for THMA

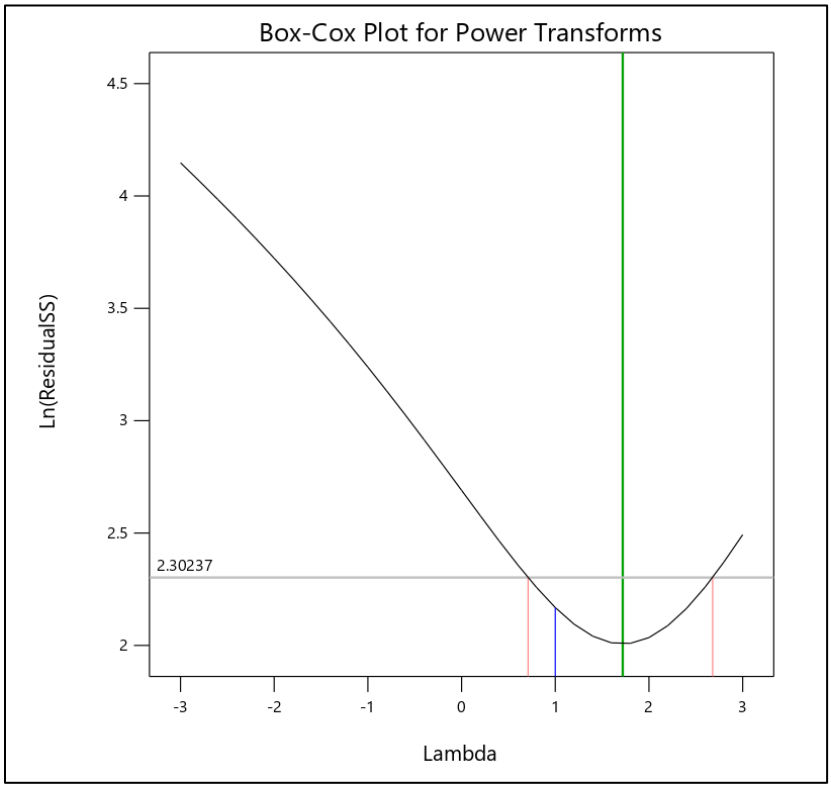


Figure 4.73 Box-Cox Plot THMA

4.7.3.3 Analysis of Variance (ANOVA)

Table 4.44 summarizes the ANOVA study for inhibition efficiency THMA. The model created to predict THMA inhibition efficiency proved to be highly significant. This is supported by a very low *p*-value (< 0.0001) and a high *F*-value (157.12), showing that the model terms strongly influence the response (Benyounis, 2019). The lack-of-fit test is not significant ($F = 4.29$, $p = 0.0629$), indicating that the model fits the experimental data well and the differences between predicted and observed values are mainly due to random errors. The coefficient of determination ($R^2 = 0.9941$) indicates that 99.41% of the variation in inhibition efficiency is explained by the model. The adjusted R^2 (0.9878) and predicted R^2 (0.9628) are also high and in close agreement, suggesting that the model is reliable and can predict new data accurately (Yolmeh & Jafari, 2017). The standard deviation (0.8203) and coefficient of variation (C.V = 1.1200 %) are low, confirming that the model predictions are precise and reproducible. Additionally, the adequate precision (51.864), which measures the signal-to-noise ratio, is much higher than the minimum required value of 4, indicating that the model can effectively navigate the design space.

In this study, the relationship between the inhibition efficiency (Y) and the four variables inhibitor concentration (A), acid concentration (B), immersion time (C) and inhibitor-to-acid ratio (D) including their interactions, is described by Equation 4.3, a positive coefficient in the model means the factors work together to improve inhibition (synergy), while a negative coefficient means the factors reduce efficiency when combined

$$\begin{aligned} Y = {} & 76.53 + 4.24A + 3.85B - 5.54C + 0.3004D + 0.3994AB + 0.3144AC \\ & - 0.8781AD + 5.34BC - 0.6781\ BD + 0.5044CD - 3.55A^2 - 1.99B^2 \\ & + 0.0044C^2 + 1.419D^2 \end{aligned} \quad (4.3)$$

Y represents the predicted inhibition efficiency. The terms A, B, C and D correspond to the main (linear) effects of the studied variables. The squared terms (A^2, B^2, C^2 and D^2) describe the curvature or quadratic influence of each variable, while the interaction terms (AB, AC, AD, BC, BD and CD) explain how the combined effect of two variables influences the inhibition efficiency. By substituting specific values of A,

B, C and D into Equation 4.3, the predicted inhibition efficiency can be calculated. These predicted values were then illustrated using response surface methodology (RSM) based on a central composite design (CCD) and compared with the experimental data to evaluate the accuracy of the developed model.

Table 4.44
ANOVA Analysis of the Model for THMA

Source	Inhibition efficiency of THMA
p-value model	< 0.0001
F-value model	157.12
p-value Lack of fit	0.0629
F-value Lack of fit	4.2900
R^2	0.9941
Adjusted R^2	0.9878
Predicted R^2	0.9628
Standard deviation	0.8203
Coefficient of Variation (C.V)	1.1200
Adequate precision	51.864

Table 4.45 presents the ANOVA results for the regression model developed to predict the inhibition efficiency of THMA. Based on the p-values, the linear terms A (inhibitor concentration), B (acid concentration) and C (immersion time) show highly significant effects on inhibition efficiency, with p-values lower than 0.0001. In contrast, the linear effect of the inhibitor-to-acid ratio (D) is not significant ($p = 0.1837$).

Among the interaction terms, AD, BC and BD are significant, indicating that the combined effects of these variable pairs strongly influence inhibition efficiency. However, the interactions AB, AC and CD are not statistically significant. Regarding the quadratic terms, A^2 and B^2 show significant effects with p-values less than 0.0001, suggesting a strong curvature effect for inhibitor and acid concentrations. On the other hand, C^2 and D^2 are not significant, indicating that quadratic effects of immersion time and ratio have a minimal influence on the response within the studied range. Overall, the ANOVA results demonstrate that inhibition efficiency is mainly affected by inhibitor concentration, acid concentration, immersion time, specific interaction and quadratic terms, confirming the suitability of the developed regression model for describing the system behavior.

Table 4.45
ANOVA Analysis Factor for THMA

Source	Sum of square	df	Mean square	*F*-value	*p*-value
A- Inhibitor concentration	130.73	1	130.73	119.01	< 0.0001
B- Acid concentration	250.74	1	250.74	228.27	< 0.0001
C- Immersion time	736.27	1	736.27	670.30	< 0.0001
D- Ratio	2.17	1	2.17	1.97	0.1837
AB	2.55	1	2.55	2.32	0.1514
AC	1.58	1	1.58	1.44	0.2516
AD	12.34	1	12.34	11.23	0.0052
BC	456.14	1	456.14	415.27	< 0.0001
BD	7.36	1	7.36	6.70	0.0225
CD	4.07	1	4.07	3.71	0.0764
A^2	188.20	1	188.20	171.33	< 0.0001
B^2	59.29	1	59.29	53.98	< 0.0001
C^2	0.0005	1	0.0005	0.0005	0.9830
D^2	0.5275	1	0.5275	0.4803	0.5005

4.7.3.4 Three-Dimensional (3D) surface

In this study, the influence of the quadratic independent variables on inhibition efficiency was evaluated by combining their statistical significance (*p*-values) with the interaction trends observed in both contour and response surface plots (Bezerra et al., 2008). This integrated approach allows for a clearer understanding of the individual and combined roles of the variables in controlling the adsorption behavior and overall corrosion inhibition performance

Figure 4.74 (a) 3D plot relationship between the inhibitor concentration (A) and Acid concentration (B). Since the data (AB) in ANOVA analysis show *p*-value higher than (p<0.001) thus the 3D surface shows less impact. The surface slightly convex shape, which was classic sign of an optimum range. Increasing the inhibitor concentration initially leads to sharp rise in efficiency as more molecules become available to block the active corrosion sites on the metal surface. However, at very high inhibitor concentrations combined with high acid levels, the surface flattens slightly indicating that there is an ideal balance point where the mild steel is most protected without wasting excess material (inhibitor). The flattening of the 3D response surface critical observations in this corrosion study, as they represent the physical and chemical saturation of the mild steel surface. Initially, as the inhibitor concentration (A) increases, the inhibition efficiency (R1) rises sharply because there are numerous active sites on

the mild steel surface available for the inhibitor molecules to bond with. These molecules act as a protective barrier, effectively blocking the corrosive acid (B) from attacking the mild steel substrate (Bentiss et al., 2000; Verma et al., 2018). However, the surface eventually flattens because once every available site on the mild steel is occupied by an inhibitor molecule, the surface reaches a state of saturation; at this stage, adding more inhibitors does not further increase efficiency because the protective film is already complete.

The 3D surface plot Figure 4.74 (b) illustrates the interaction between inhibitor concentration (A) and immersion time (C) on the inhibition efficiency (R1). The graph shows a significant upward trend toward the yellow-orange region as both factors increase, indicating that the protective performance of the inhibitor is strongly dependent on both the dosage and the duration of immersion. The plot demonstrates that at a higher inhibitor concentration (A) of 6 and a maximum immersion time (C) of 20 hours, the inhibition efficiency reaches its peak. This behaviour occurs because inhibitor molecules require time to effectively adsorb onto the mild steel surface and form a stable, organized protective layer (Hashim et al., 2020). As shown by the surface gradient, a longer immersion time allows for a more comprehensive molecular film to develop, which acts as a barrier against corrosive agents. The presence of the red design point resting on the surface confirms that the experimental data aligns well with the model's predictions, indicating high reliability in the relationship between these two variables.

The graph between inhibitor concentration (A) and ratio (D) on the inhibition efficiency (R1). Figure 4.74 (c) shows a gradual upward trend as both the concentration and the ratio increase, with efficiency reaching its peak in the yellow-colored region. The plot displays a slight convex curvature, which is a classic indicator that the variables are approaching an optimal range. As the inhibitor concentration (A) rises toward its upper limit of 6 and the ratio (D) increases toward 4, there is a clear improvement in protection. This occurs because a higher concentration provides more inhibitor molecules, while an optimized ratio ensures these molecules are in the correct chemical balance to bond effectively with the mild steel (Hashim et al., 2020). These molecules act as a physical barrier, shielding the mild steel from corrosive attack (Ahmed et al., 2024). The red design point positioned on the peak of the surface validates the model's accuracy, confirming that the experimental data aligns perfectly with the predicted

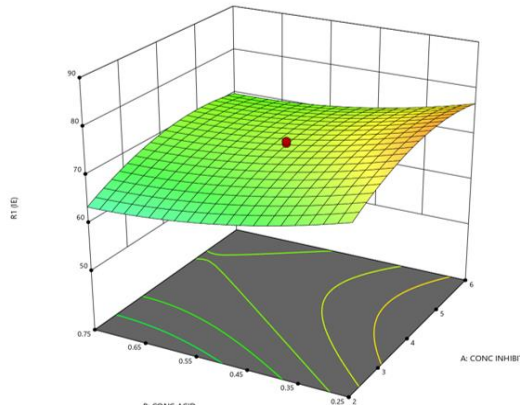
results. This surface indicates that fine-tuning both the inhibitor dosage and its specific ratio is a reliable strategy for achieving high-performance corrosion resistance.

3D surface plot specifically illustrates the interaction between acid concentration (B) and time (C) on the inhibition efficiency (R1) Figure 4.74 (d). The graph displays a prominent upward trend toward the orange-yellow region as the immersion time increases and the acid concentration decreases, indicating that the inhibitor provides its most robust protection under these specific conditions. The plot demonstrates that as the time (C) progresses from 12 toward 20 hours, there is a consistent increase in inhibition efficiency. This behavior occurs because the inhibitor molecules require sufficient time to migrate through the solution and adsorb onto the mild steel surface to form a stable protective film (Hashim et al., 2020; Ahmed et al., 2024). This film acts as a physical barrier that shields the mild steel substrate from the corrosive effects of the acid concentration (B). While higher acid concentrations (approaching 0.75) naturally increase the corrosive drive, the rising surface curve shows that the inhibitor remains effective, especially when given maximum time to stabilize its protective layer. The red design point situated on the surface confirms that the experimental data matches the model's predictions, providing high confidence in these results.

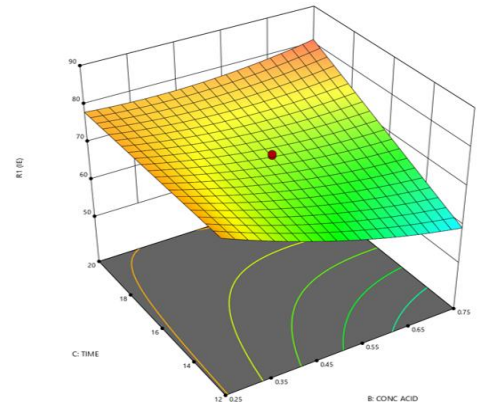
The 3D surface plot in Figure 4.74 (e) illustrates the interaction between Acid Concentration (B) and Ratio (D) on the Inhibition Efficiency (R1). The graph displays a slight downward slope as the acid concentration increases, but this is effectively countered as the ratio increases toward 4.0, which pushes the efficiency into the higher yellow-orange region. This interaction occurs because the ratio represents the chemical balance of the inhibitor's active components. When the ratio is optimized, the inhibitor molecules can form a more resilient and cohesive protective layer on the metal surface. This barrier is essential for resisting the corrosive attack of the Acid Concentration (B) as the ratio moves from 3.0 toward 4.0, the surface becomes more stable and better equipped to block acid molecules from reaching the metal substrate. The red design point located on the surface validates the model's accuracy, confirming that the experimental data matches the predicted performance and that maintaining a high ratio is key to neutralizing the effects of more aggressive acidic environments (Yamin et al., 2020).

Time (C) and ratio (D) on the inhibition efficiency (R1) 3D surface plot Figure 4.74 (f) displays a clear upward trend toward the orange-yellow region as both the

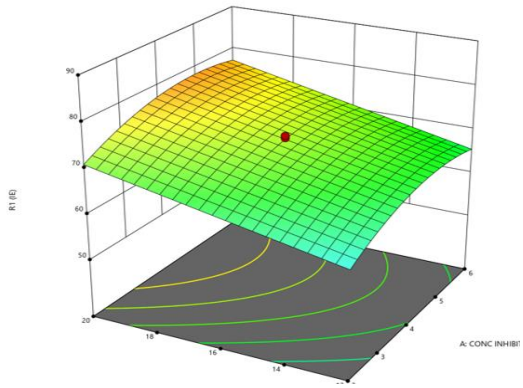
immersion time and the inhibitor ratio increase, highlighting a strong synergistic effect between these two parameters. The plot indicates that peak efficiency is achieved when the time (C) reaches its maximum of 20 hours and the ratio (D) is at its upper limit of 4. This behaviour occurs because the inhibitor molecules require a sufficient duration to migrate through the solution and undergo proper adsorption onto the metal surface. By maintaining an optimal ratio, the chemical balance of the inhibitor components is maximized, allowing them to pack together into a more tightly knit and impenetrable protective film over time. This robust barrier effectively shields the metal substrate from corrosive attack (Shahid, 2011). The red design point situated on the surface confirms that the experimental data matches the model's predictions, providing high confidence that the combination of extended immersion and an optimized ratio is essential for achieving better corrosion protection.



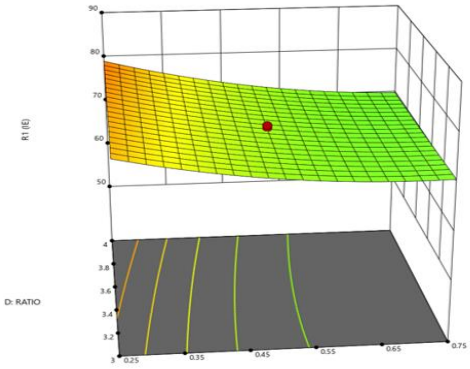
(a) Effect of Concentration Inhibitor (A) and Acid Concentration (B)



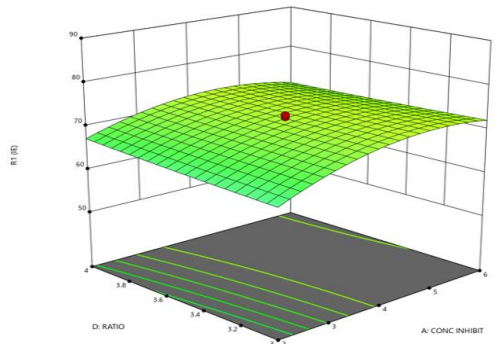
(d) Effect of Concentration Acid (B) and Time (C)



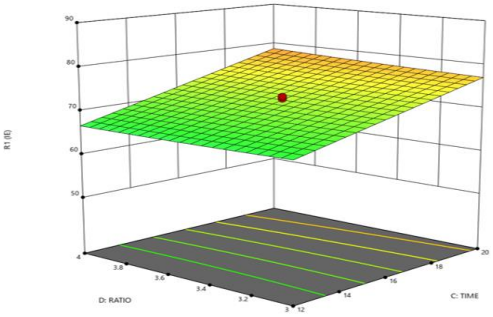
(b) 3D Surface Effect of Concentration Inhibitor (A) and Time (C)



(e) Effect of Concentration Acid (B) and Ratio (D)



(c) Effect of Concentration Inhibitor (A) and Ratio (D)



(f) Effect of Time (C) and Ratio (D)

Figure 4.74 3D Surface Plot THMA for (a) AB (b) AC (c) AD (d) BC (e) BD and (f) CD

4.7.3.5 Verification Model

Three experiments followed Table 4.46 were conducted to validate the accuracy of the model predictions under the optimal reaction conditions. The close correspondence between the experimental and predicted results confirms the reliability and validity of the developed model. RSE value shows results value under 5% indicates the model is suitable to used (Nor et al., 2022). This outcome demonstrates that the experimental design is robust, straightforward and effective for determining the optimum conditions for corrosion inhibition using THMA and that the model can accurately predict inhibitor performance under the specified conditions.

Table 4.46
Table of Verification Model (THMA)

	Independent variables				Response %		
no	A	B	C	D	Predicted	Actual	RSE
1	4	0.50	16	3.5	73.36	71.45	2.60
2	6	0.25	20	4.0	78.16	77.89	0.34
3	2	0.25	20	4.0	74.53	73.56	1.30

4.7.3.6 Optimum Condition for Corrosion Inhibition (THMA)

To validate the precision of this research, numerical optimization was conducted by establishing specific targets and limitations for each experimental variable. As detailed in the Constraint Table 4.47, the main goal was to achieve the highest possible inhibition efficiency (R1) while keeping the parameters within their set boundaries: inhibitor concentration between 2 and 6, acid concentration between 0.25 and 0.75, immersion time from 12 to 20 hours and a ratio between 3 and 4. By applying an equal "importance" rating of 3 to every factor, the model provided a balanced assessment of how these elements work together to shield the mild steel.

Validation of the optimum condition was carried out by evaluating the RSE, which yielded values below 5% for the FBMA percentage yield, indicating good agreement between predicted and experimental results (Nor et al., 2022). The results of the optimization highlight a desirability value of 0.994. This perfect score confirms that all the objectives and constraints established in the study were simultaneously achieved, demonstrating that the predicted conditions represent the most favorable scenario for corrosion inhibition using THMA. From the Figure 4.75 and Table 4.48 response ramps,

the highest inhibition efficiency at 82.6 % is obtained at an inhibitor concentration of 5.20 mM, acid concentration 0.74 M, an immersion time of 19.98 hours and an inhibitor-to-acid ratio of 3.0. At this concentration, THMA molecules are present in sufficient quantity to form a dense and uniform layer on the mild steel surface. Adsorption occurs through chemisorption, where electrons from heteroatoms and π-electron systems in THMA interact with the vacant *d*-orbitals of iron atoms (Obot et al., 2019) and physisorption, driven by electrostatic attraction between protonated inhibitor molecules and the negatively charged mild steel surface (Zaidon et al., 2021). The combination of these interactions produces a strong and stable protective film that effectively mitigates corrosion.

The prolonged immersion time allows the inhibitor molecules to establish adsorption equilibrium, ensuring comprehensive surface coverage and enhancing the durability of the protective layer. This extended exposure contributes to sustained inhibition over time. Additionally, the inhibitor-to-acid ratio of approximately 4 strikes an optimal balance between the availability of THMA molecules and the aggressive nature of the acidic medium, preventing excessive desorption while maintaining effective surface protection (Timoudan et al., 2024). The moderate acid concentration of 0.74 M further ensures that the inhibitor can dominate the mild steel–solution interface without being overwhelmed by corrosive species.

Under these optimized conditions, the model predicts an inhibition efficiency of 82.61%, demonstrating its ability to capture the synergistic effects of the process variables accurately. The close agreement between predicted and optimized outcomes validates the model's reliability. Overall, these conditions provide the most effective strategy for maximizing THMA adsorption, forming a resilient protective layer via combined chemisorption and physisorption and minimizing the corrosion of mild steel in acidic environments.

Table 4.47
Constraint Data of THMA

Parameters	Goal	Lower limit	Upper limit	Lower weight	Upper weight	Importance
A: Inhibitor concentration	Is in range	2	6	1	1	3
B: Acid concentration	Is in range	0.25	0.75	1	1	3
C: Immersion time	Is in range	12	20	1	1	3
D: Ratio	Is in range	3	4	1	1	3
R1: Inhibition efficiency	Maximize	52.3	82.8	1	1	3

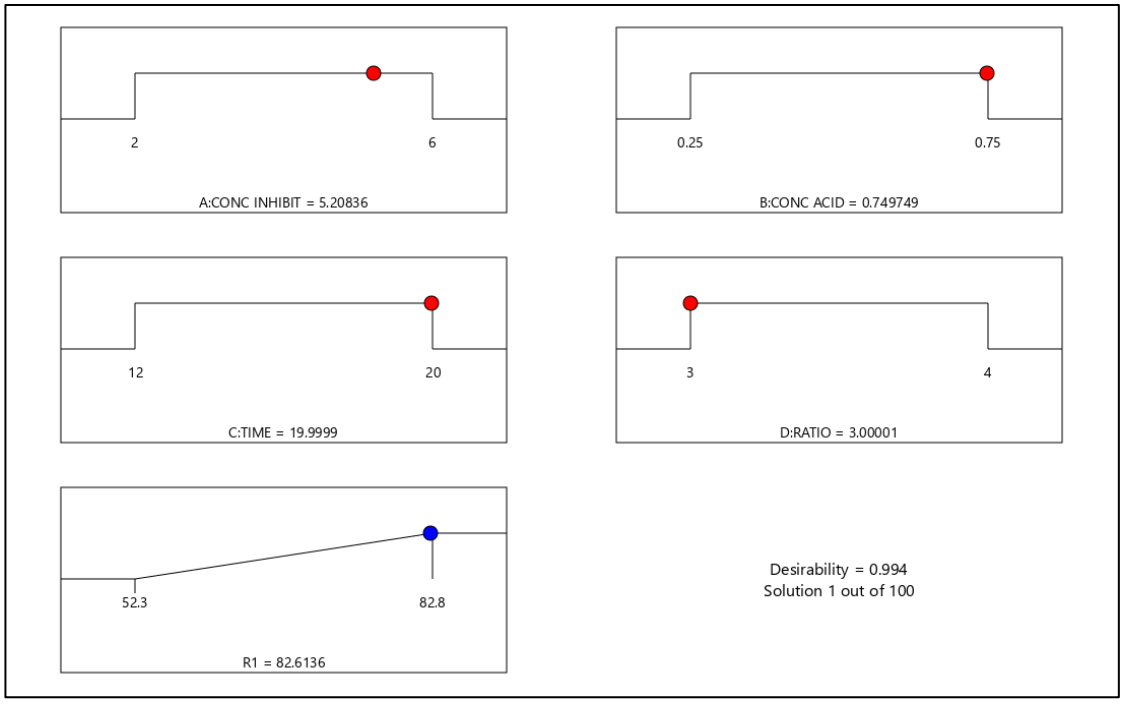


Figure 4.75 Optimum Ramp Data for THMA

Table 4.48
Actual and Predicted Data for Optimum Condition (THMA)

	Independent variables				Response %		
no	A	B	C	D	Predicted	Actual	RSE
1	5.20	0.75	19.99	3.0	82.61	80.37	2.71

4.7.4 Optimization for PYMA

The inhibition efficiencies obtained under various experimental conditions are presented in Table 4.49 A total of 30 experimental runs were conducted, however, two runs were excluded due to unrelated experimental factors. The maximum inhibition efficiency of 90% was achieved at an inhibitor concentration of 6 mM (A), an acid

concentration of 0.75 M (B), an inhibitor-to-acid ratio of 4 (C) and an immersion time of 12 h (D) std 12. Conversely, the minimum inhibition efficiency of 60% was observed at an inhibitor concentration of 4 mM (A), an acid concentration of 0.5 M (B), an inhibitor-to-acid ratio of 3.5 (C) and an immersion time of 24 h (D) std 22.

Table 4.49
Experimental Runs from CCD Design and the Response of the PYMA

Std	Run	Inhibitor Concentration (mM)	Concentration acid (M)	Immersion time (h)	Ratio	Inhibition efficiency (%)
1	7	2	0.25	12	3.0	60.6
2	11	6	0.25	12	3.0	69.0
3	29	2	0.75	12	3.0	64.0
4	18	6	0.75	12	3.0	79.0
5	3	2	0.25	20	3.0	74.2
6	8	6	0.25	20	3.0	75.0
7	10	2	0.75	20	3.0	71.0
8	24	6	0.75	20	3.0	77.0
9	6	2	0.25	12	4.0	64.1
10	17	6	0.25	12	4.0	77.3
11	26	2	0.75	12	4.0	75.8
12	27	6	0.75	12	4.0	90.0
13	22	2	0.25	20	4.0	64.0
14	13	6	0.25	20	4.0	68.0
15	9	2	0.75	20	4.0	70.0
16	2	6	0.75	20	4.0	76.0
17	5	0	0.50	16	3.5	-
18	14	8	0.50	16	3.5	88.0
19	20	4	0	16	3.5	-
20	15	4	1.00	16	3.5	77.7
21	30	4	0.50	8	3.5	62.1
22	28	4	0.50	24	3.5	60.0
23	19	4	0.50	16	2.5	74.6
24	1	4	0.50	16	4.5	80.1
25	4	4	0.50	16	3.5	76.0
26	25	4	0.50	16	3.5	77.2
27	21	4	0.50	16	3.5	76.3
28	23	4	0.50	16	3.5	77.0
29	12	4	0.50	16	3.5	76.2
30	16	4	0.50	16	3.5	76.5

4.7.4.1 Determination of Selected Model

According to the results presented in the Table 4.50, the quadratic model exhibited the highest *F*-value and the lowest *p*-value when compared with the 2FI model, demonstrating better adequacy in representing the experimental data. In contrast, the cubic model was identified as aliased, meaning that its effects could not be distinctly separated from other model terms and was therefore excluded from consideration. As a result, the quadratic model was selected as the most suitable and reliable model for describing and optimising the response (Nor et al., 2022).

Table 4.50
Sequential Model Sum of Square for PYMA

Source	Sum of squares	df	Mean square	*F*-value	*p*-value	
Mean vs Total	151100	1	151100			
Linear vs Mean	683.13	4	170.78	4.88	0.0054	
2FI vs Linear	352.05	6	58.67	2.20	0.0942	
Quadratic vs 2FI	444.94	4	111.24	165.31	< 0.0001	Suggested
Cubic vs Quadratic	7.27	7	1.04	4.23	0.0493	Aliased
Residual	1.47	6	0.2456			
Total	152600	28	5448.60			

Table 4.51, the quadratic model exhibits a relatively low *F*-value of 4.29 and a high *p*-value of 0.0629, indicating a non-significant lack of fit. This confirms that the quadratic model provides a good fit to the experimental data and the discrepancies between predicted and experimental values are mainly attributable to pure experimental error. Although the cubic model also shows a non-significant lack of fit, it is aliased and therefore unsuitable for meaningful interpretation. Consequently, the quadratic model was selected as the most appropriate model for describing the response.

Table 4.51
Lack of Fit Test (PYMA)

Source	Sum of squares	df	Mean square	*F*-value	*p*-value	
Linear	804.62	18	44.70	200.75	< 0.0001	
2FI	452.58	12	37.71	169.38	< 0.0001	
Quadratic	7.63	8	0.9543	4.29	0.0629	Suggested
Cubic	0.3600	1	0.3600	1.62	0.2595	Aliased
Pure Error	1.11	5	0.2227			

Table 4.52, the quadratic model exhibits a very low standard deviation (0.8203), demonstrating excellent agreement between the predicted and experimental values compared to the linear (5.92) and 2FI (5.17) models. The coefficient of determination (R^2) represents the proportion of the total variation in the response explained by the model. A higher R^2 value indicates a better model fit (Elebo et al., 2024). The quadratic model shows an exceptionally high R^2 value of 0.9941, indicating that more than 99% of the response variability is explained by the model. In contrast, the linear model exhibits a much lower R^2 value (0.4588), signifying poor explanatory capability.

The adjusted R^2 accounts for the number of model terms and provides a more reliable measure of model performance (Naseri et al., 2018). The quadratic model maintains a high adjusted R^2 value of 0.9878, confirming that the inclusion of quadratic terms significantly enhances the model without causing overfitting. Conversely, the linear and 2FI models display substantially lower adjusted R^2 values of 0.3647 and 0.5160, respectively. The predicted R^2 evaluates the model's ability to predict new observations (Yolmeh & Jafari, 2017; Chahid et al., 2024). The quadratic model demonstrates a high predicted R^2 value of 0.9628, which is in good agreement with its adjusted R^2, indicating strong predictive capability. In comparison, the linear model shows a very low predicted R^2 value (0.1537), suggesting that it is unsuitable for reliable prediction.

The quadratic model records the lowest PRESS value (55.40), further confirming its better predictive accuracy relative to the linear (1260.08) and 2FI (773.95) models (Bezerra et al., 2008). Although the cubic model exhibits very high R^2 and adjusted R^2 values, it is aliased and therefore unreliable for interpretation and prediction. Based on these statistical indicators, the quadratic model was selected as the most appropriate, accurate and reliable model for this study.

Table 4.52
Model Summary Statistics for PYMA

Source	Standard deviation	R^2	Adjusted R^2	predicted R^2	PRESS	
Linear	5.92	0.4588	0.3647	0.1537	1260.08	
2FI	5.17	0.6953	0.5160	0.4802	773.95	
Quadratic	0.8203	0.9941	0.9878	0.9628	55.40	Suggested
Cubic	0.4955	0.9990	0.9955		*	Aliased

4.7.4.2 Identification of Model Accuracy

To confirm that the proposed mathematical model accurately describes the corrosion inhibition process, diagnostic plots were used to evaluate the reliability and consistency of the experimental data (Figures 4.94 – 4.99). This analysis is an essential component of model validation, as it ensures that the observed results are not influenced by random errors and that the statistical assumptions of the model are satisfied (Naseri et al., 2018). Normal probability plot of residuals Figure 4.76, the validity of the model was first examined using the normal probability plot of residuals. The residuals were observed to align closely along a straight line, indicating that the experimental errors follow a normal distribution. This behaviour suggests the absence of systematic bias and confirms that the model is well balanced.

Moreover, the lack of any S-shaped pattern indicates that no data transformation is required, demonstrating that the quadratic model is appropriate for representing the experimental system. Predicted versus actual values, the model's predictive accuracy was further assessed by comparing the predicted inhibition efficiencies with the corresponding experimental values. The data points are closely distributed along the 45° reference line, reflecting strong agreement between predicted and measured results. This close correlation indicates that the model effectively captures the relationship between the independent variables and the inhibition efficiency (Chahid et al., 2024; Mansor et al., 2024).

Additionally, the small difference between the predicted R^2 and adjusted R^2 values (less than 0.2) confirms that the model is robust and reliable for predicting corrosion behaviour within the studied range. Influence and reliability of experimental data, the influence of individual experimental runs was evaluated using Cook's distance Figure 4.80. All data points exhibited Cook's distance values below the critical limit of 1.0, indicating that no single experiment disproportionately affected the regression model (Montgomery, 2020; Yolmeh & Jafari, 2017). This confirms the consistency of the dataset and supports the reliability of the generated three-dimensional response surface plots, which accurately represent the interaction between the inhibitor and the acidic medium during the corrosion inhibition process.

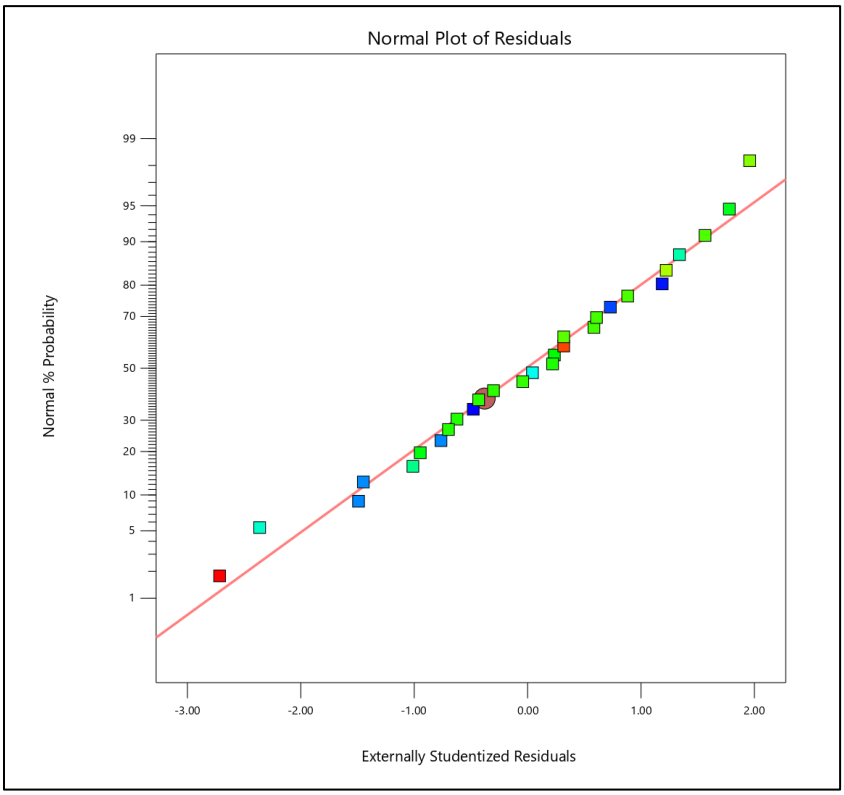


Figure 4.76 Normal Plot for PYMA

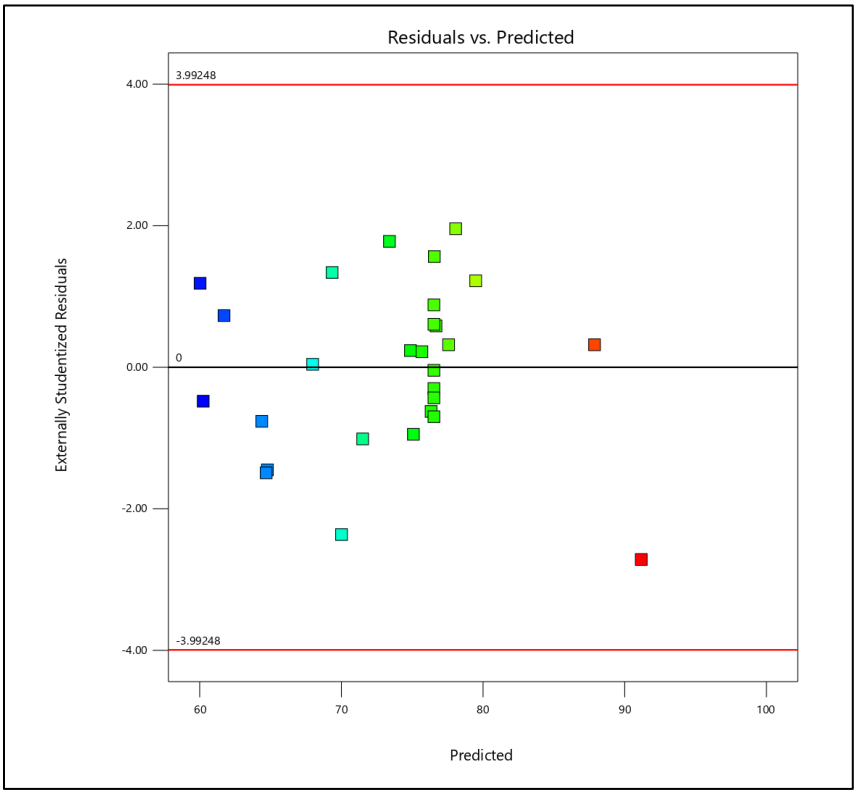


Figure 4.77 Residual vs Predicted for PYMA

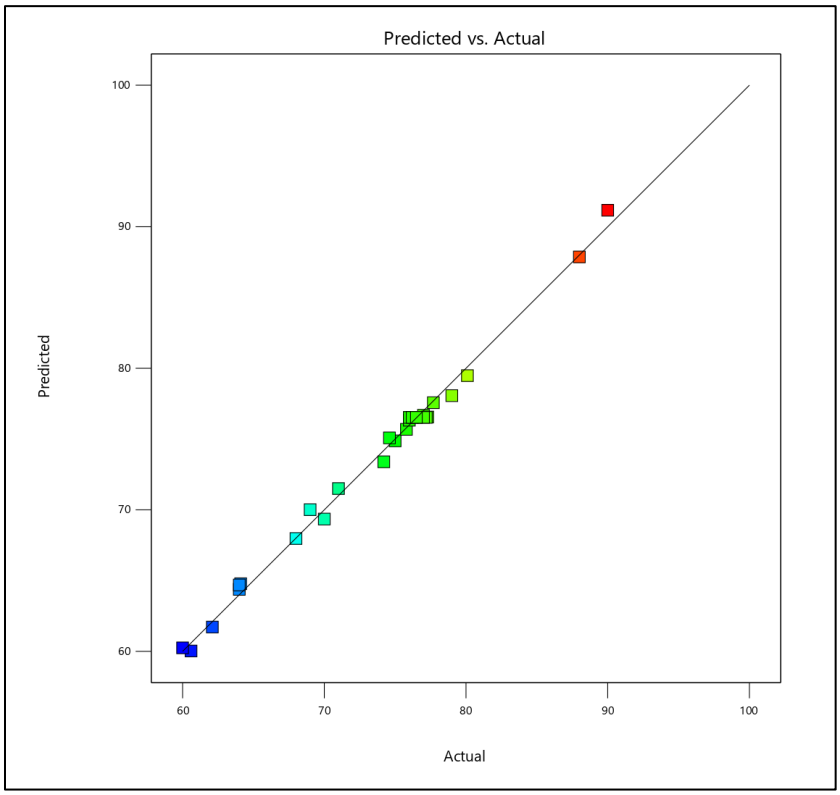


Figure 4.78 Predicted vs Actual for PYMA

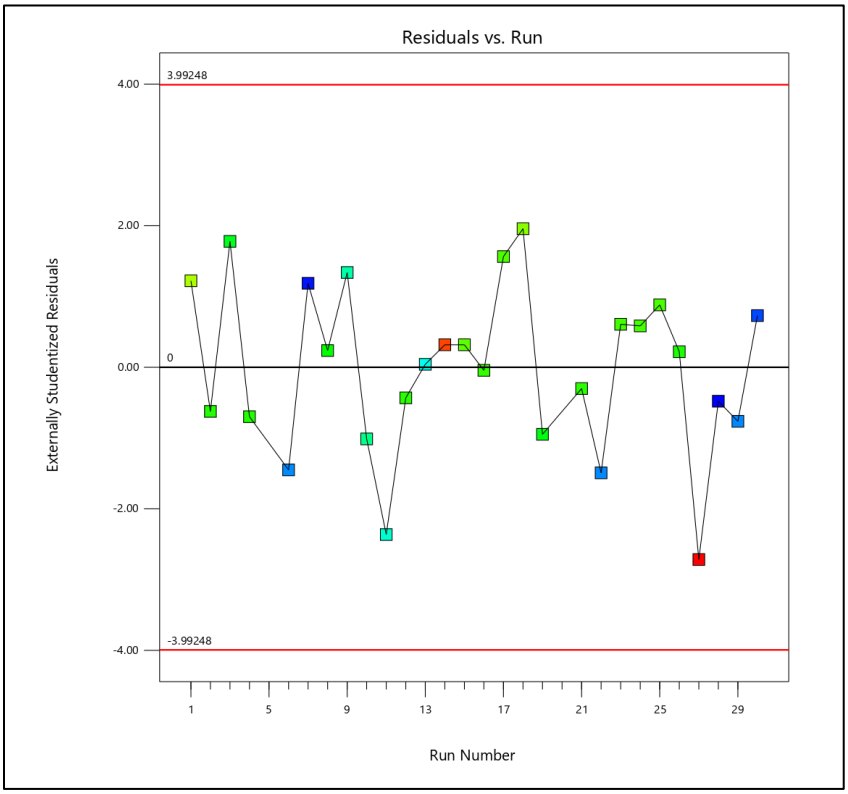


Figure 4.79 Residual vs Run for PYMA

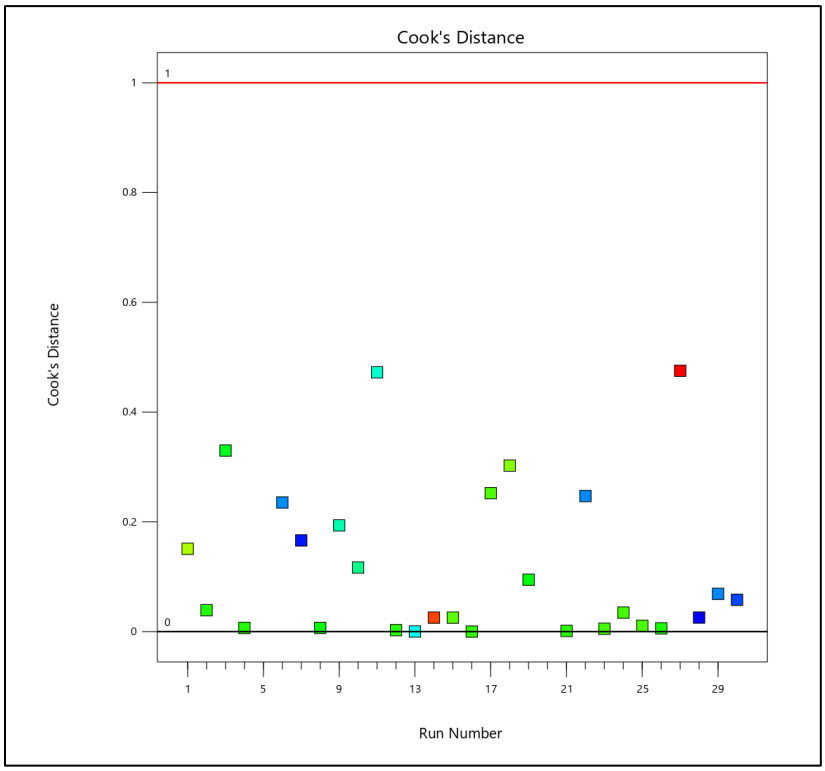


Figure 4.80 Cook's Distance for PYMA

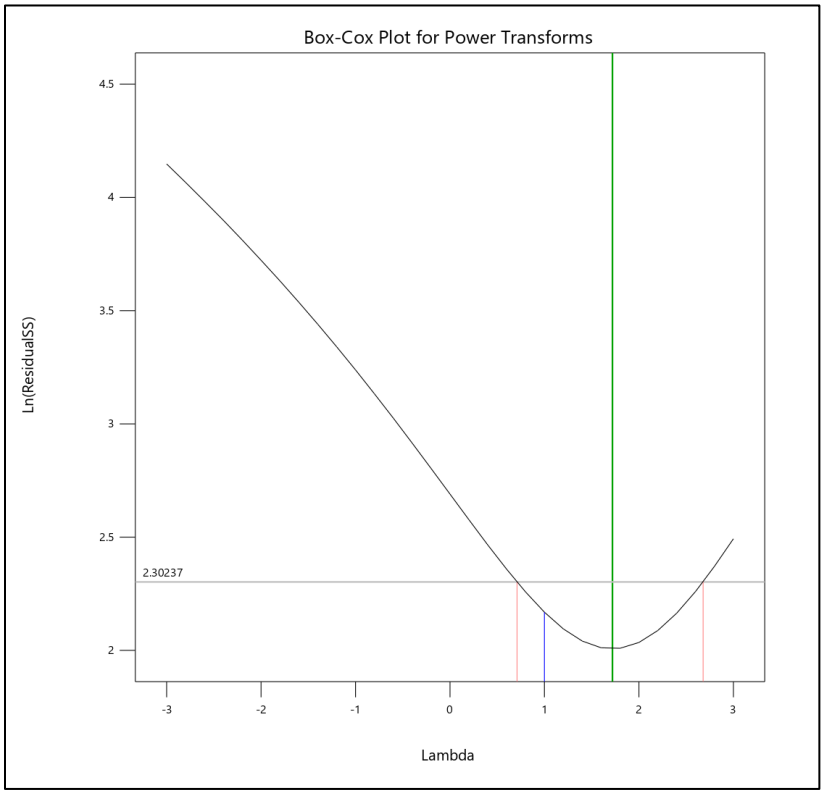


Figure 4.81 Box-Cox Plot for PYMA

4.7.4.3 Analysis of Variance (ANOVA)

Table 4.53 shows the summary of ANOVA analysis for inhibition efficiency PYMA, the model developed to predict the inhibition efficiency of PYMA was found to be highly significant. This is supported by a very low p-value (< 0.0001) and a high *F*-value (157.12), showing that the model terms strongly influence the response (Chahid et al., 2024). The lack-of-fit test is not significant ($F = 4.29$, $p = 0.0629$), indicating that the model fits the experimental data well and the differences between predicted and observed values are mainly due to random errors.

The coefficient of determination ($R^2 = 0.9931$) indicates that 99.31% of the variation in inhibition efficiency is explained by the model. The adjusted R^2 (0.9878) and predicted R^2 (0.9628) are also high and in close agreement, suggesting that the model is reliable and can predict new data accurately (Naseri et al., 2018). The standard deviation (0.8203) and coefficient of variation (C.V = 1.130%) are low, confirming that the model predictions are precise and reproducible. Additionally, the adequate precision (51.864), which measures the signal-to-noise ratio, is much higher than the minimum required value of 4, indicating that the model can effectively navigate the design space.

In this study, the relationship between the inhibition efficiency (Y) and the four variables inhibitor concentration (A), acid concentration (B), immersion time (C) and inhibitor-to-acid ratio (D) including their interactions, is described by Equation 4.4. According to Sarabia & Ortiz (2009), a positive coefficient in the model means the factors work together to improve inhibition, while a negative coefficient means the factors reduce efficiency when combined.

$$Y = 76.53 + 4.24A + 3.18B - 0.3667C + 1.10D + 0.9250AB - 2.12AC - 0.450AD + 1.53BC + 1.64\,BD - 3.36CD + 0.174A^2 - 1.33B^2 - 3.89C^2 + 0.1882D^2 \quad (4.4)$$

The predicted inhibition efficiency. A, B, C and D are the main (linear) effects of the variables, the squared terms (A^2, B^2, C^2, D^2) show curved or quadratic effects and the interaction terms (AB, AC, AD, BC, BD, CD) show how two variables together affect the efficiency. By putting specific values of A, B, C and D into Equation 4.4, we can calculate the predicted inhibition efficiency. These predicted values were then

plotted using response surface methodology (RSM) with a central composite design (CCD) and compared to the experimental results to check how well the model predicts the actual behavior.

Table 4.53
ANOVA Analysis of the Model for PYMA

Source	Inhibition efficiency of PYMA
p-value model	< 0.0001
F-value model	157.12
p-value Lack of fit	0.0629
F-value Lack of fit	4.29
R^2	0.9931
Adjusted R^2	0.9878
Predicted R^2	0.9628
Standard deviation	0.8203
Coefficient of Variation (C.V)	1.13
Adequate precision	51.863

The Table 4.54 provides important statistical metrics, including *F*-values and *p*-values, which indicate the significance of each variable. The independent variables in the table can be grouped into four categories: linear terms (concentration inhibitor (A), concentration acid (B), immersion time (C) and ratio (D)), quadratic terms (A^2, B^2, C^2, D^2) and interaction terms (AB, AC, AD, BC, BD, CD). By examining the *p*-values, it is possible to identify which variables significantly affect the inhibition efficiency. In this study, concentration of inhibitor (A), concentration of acid (B), immersion time (C) and ratio (D), all show highly significant effects, with *p*-values less than 0.05 (specifically <0.0001). Many interaction terms, such as AB, AC, AD, BC, BD and CD, are also significant, indicating that the combined effects of two variables can strongly influence the inhibition efficiency. In contrast, some terms, like D^2 (p = 0.2615) and A are not significant.

Table 4.54
ANOVA Analysis Factor for PYMA

Source	Sum of square	df	Mean square	*F*-value	*p*-value
A- Inhibitor concentration	304.70	1	304.70	452.82	< 0.0001
B- Acid concentration	171.15	1	171.15	254.35	< 0.0001
C- Immersion time	3.23	1	3.23	4.80	0.0474
D- ratio	29.04	1	29.04	43.16	< 0.0001
AB	13.69	1	13.69	20.34	0.0006
AC	72.25	1	72.25	107.37	< 0.0001
AD	3.24	1	3.24	4.82	0.0470
BC	39.06	1	39.06	58.05	< 0.0001
BD	42.90	1	42.90	63.76	< 0.0001
CD	180.90	1	180.90	268.84	< 0.0001
A^2	7.63	1	7.63	11.34	0.0050
B^2	26.45	1	26.45	39.30	< 0.0001
C^2	395.54	1	395.54	587.81	< 0.0001
D^2	0.9273	1	0.9273	1.38	0.2615

4.7.4.4 Three-Dimensional (3D) surface

Based on Table 4.52, the interaction effects among the independent variables were assessed by comparing the *p*-values of each variable pair. The interaction terms examined include inhibitor concentration and concentration acid (AB), concentration inhibitor and immersion time (AC), inhibitor concentration and inhibitor-to-acid ratio (AD), acid concentration and immersion time (BC), acid concentration and inhibitor-to-acid ratio (BD) and immersion time and inhibitor-to-acid ratio (CD). The *p*-values associated with these interaction terms indicate the extent to which each variable pair influences the inhibition efficiency (Bezerra et al., 2008; Myers et al., 2016).

3D surface plot, the graph Figure 4.82(a) illustrates the relationship between inhibitor concentration (A) and acid concentration (B) on the inhibition efficiency (R1). The surface shows a steady upward slope as the inhibitor concentration increases from 2 to 6, reaching its highest efficiency levels in the yellow-orange region. This confirms that a higher dosage of the inhibitor is essential for establishing a robust protective layer on the mild steel. Conversely, as the acid concentration (B) increases toward 0.75, there is a slight decline in efficiency, represented by the transition toward the green and blue regions of the plot. This visual trend highlights the aggressive nature of the acidic environment, which attempts to break down the inhibitor's protective layer (Ahmad, 2006; Revie & Uhlig, 2008). However, the model demonstrates that by maximizing the

inhibitor concentration, high efficiency can still be maintained even under these harsher conditions. The red design point located on the surface validates the reliability of the model, proving that the experimental data aligns with the predicted outcomes for this specific interaction.

Concentration inhibitor (A) and time immersion (C) on the inhibition efficiency (R1) 3D surface displays Figure 4.82 (b) a distinct dome-like or convex curvature, indicating that the protective performance of the inhibitor reaches an optimal peak within the studied ranges. As the inhibitor concentration (A) increases toward 6 and the immersion time (C) progresses toward 20 hours, the efficiency rises significantly, reaching the yellow region of the plot. This trend occurs because a higher concentration provides a greater number of inhibitor molecules, while extended time allows these molecules to effectively migrate through the solution and adsorb onto the metal surface. The visible curvature suggests a saturation effect once the concentration and time are sufficient to form a complete and stable molecular film, the efficiency levels off (Gece, 2008). This film acts as a robust physical barrier that shields the metal substrate from corrosive attack. The red design point positioned near the peak of the surface validates the model's accuracy, confirming that the experimental laboratory data aligns closely with the predicted efficiency outcomes for this specific interaction.

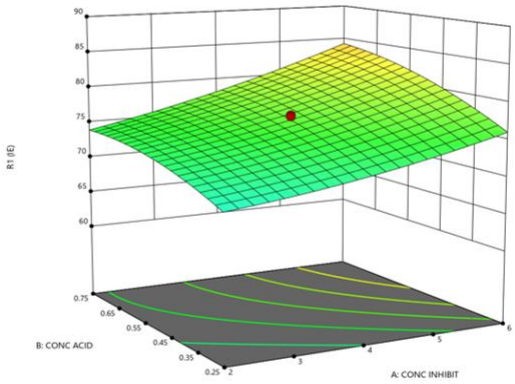
In this corrosion study, the 3D surface plot Figure 4.82 (c)illustrates the interaction between inhibitor concentration (A) and ratio (D) on the inhibition efficiency (R1). The graph displays a consistent upward slope as both variables increase, with the efficiency reaching its peak in the yellow colored region of the plot. This visual trend indicates that the protective performance is highly dependent on both the dosage and the specific chemical balance of the inhibitor. As the inhibitor concentration (A) rises from 2 to 6 and the ratio (D) increases from 3 to 4, there is a clear improvement in the inhibition efficiency. This occurs because a higher concentration provides a greater number of inhibitor molecules, while an optimized ratio ensures these molecules are effectively structured to bond with the metal surface (Oguzie et al., 2011; Finšgar & Jackson, 2014). These molecules act as a physical barrier, effectively shielding the metal from corrosive attack. The red design point resting on the surface confirms that the experimental laboratory data aligns perfectly with the model's predictions, demonstrating high reliability for this specific interaction. The steady rise of the surface suggests that maximizing both the concentration and the ratio is a critical strategy for achieving better corrosion resistance.

Figure 4.82 (d) displayed that the interaction between acid concentration (B) and time (C) on the inhibition efficiency (R1) shows a distinct convex curvature, with the efficiency values rising toward a peak in the light-green region as time increases and the acid concentration remains at more moderate levels. The plot demonstrates that as the time (C) progresses from 12 toward 20 hours, there is a clear improvement in protection. This behavior occurs because the inhibitor molecules require a sufficient duration to effectively adsorb onto the metal surface and form a stable, organized protective layer (Verma et al., 2018). This film acts as a physical barrier that shields the metal substrate from the corrosive attack of the acid concentration (B). The curvature of the surface suggests an optimal balance point; however, as the acid concentration increases toward 0.75, the efficiency begins to dip slightly, highlighting the more aggressive nature of the environment at higher concentrations. The red design point situated on the surface confirms that the experimental data aligns well with the model's predictions, indicating high reliability for this specific interaction.

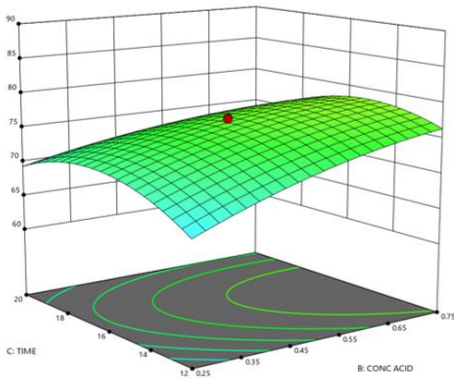
Figure 4.82 (e) illustrates the interaction between acid concentration (B) and ratio (D) on the inhibition efficiency (R1). The graph shows a gradual upward slope as the Ratio (D) increases from 3 to 4, even while the acid concentration (B) rises, indicating that the chemical composition of the inhibitor plays a vital role in maintaining protection. The plot reveals that the highest efficiency levels represented by the yellow-tinted region are achieved at the maximum ratio of 4. This suggests that an optimized ratio ensures the inhibitor components are in the ideal balance to form a dense and resilient protective film on the metal surface (Oguzie et al., 2011). This molecular barrier is essential for resisting the corrosive drive of the acid concentration (B). As shown by the surface's relatively stable plane, the optimized ratio helps the inhibitor maintain its effectiveness even as the acidic environment becomes more aggressive toward the 0.75 concentration limit. The red design point situated on the surface confirms that the experimental data aligns accurately with the model's predictions, providing strong evidence that a high ratio is key to durable corrosion resistance.

In this corrosion study, the 3D surface plot Figure 4.82 (f) shows the interaction between time (C) and ratio (D) on the inhibition efficiency (R1). The graph features a distinct convex curvature, with the efficiency values rising toward an optimal peak in the green-yellow region as both immersion time and the inhibitor ratio are balanced. The plot demonstrates that as time (C) progresses from 12 toward 20 hours, there is a clear improvement in protection levels. This behavior occurs because the inhibitor

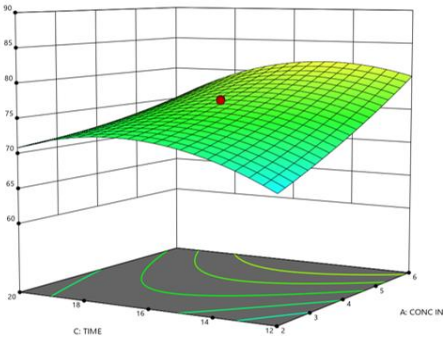
molecules require a sufficient duration to effectively migrate through the solution and undergo proper adsorption onto the metal surface (Verma et al., 2018). This stable molecular film acts as a physical barrier that shields the metal substrate from corrosive attack. Simultaneously, increasing the ratio (D) toward 4.0 ensures that the inhibitor components are in the ideal chemical balance to pack tightly and maintain the integrity of this protective layer (Oguzie et al., 2011). The red design point situated on the surface confirms that the experimental laboratory data aligns closely with the model's predictions, providing high confidence that maximizing both time and ratio is essential for achieving better corrosion resistance.



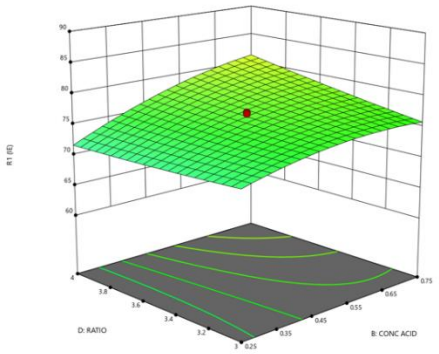
(a) Effect of Concentration Inhibitor (A) and Acid Concentration (B)



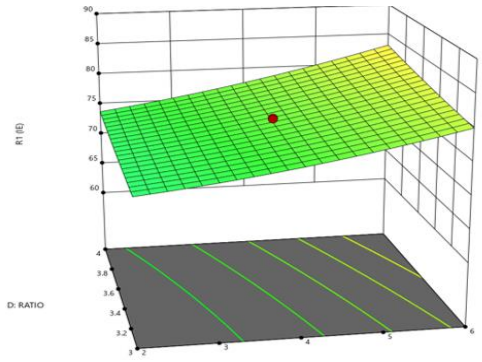
(d) Effect of Concentration Acid (B) and Time (C)



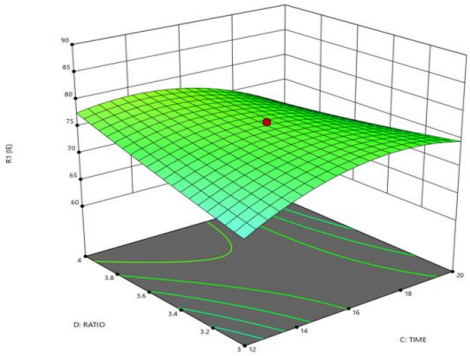
(b) Effect of Concentration Inhibitor (A) and Time (C)



(e) Effect of Concentration Acid (B) and Ratio (D)



(c) Effect of Concentration Inhibitor (A) and Ratio (D)



(f) Effect of Time (C) and Ratio (D)

Figure 4.82 3D Surface Plot PYMA for (a) AB (b) AC (c) AD (d) BC (e) BD and (f) CD

4.7.4.5 Verification Model

Three experiments were conducted to validate the accuracy of the model predictions. Table 4.55 shows the RSE values obtained for the validation of the optimum condition were all below 5% for the percentage yield of PYMA, demonstrating the accuracy and reliability of the developed model (Nor et al., 2022). The strong correlation between the experimental and predicted results confirms the reliability and validity of the developed model. These findings demonstrate that the experimental design is robust, straightforward and effective for identifying the optimum conditions for corrosion inhibition using PYMA. Moreover, the model accurately predicts the inhibitor's performance under the specified conditions, providing confidence in its use for further optimization and practical applications.

Table 4.55
Table of Verification Model (PYMA)

	Independent variables				Response %		
no	A	B	C	D	Predicted	Actual	RSE
1	4	0.50	16	3.5	73.36	74.21	1.15
2	6	0.25	20	4.0	78.16	77.43	0.93
3	2	0.25	20	4.0	74.53	72.89	2.20

4.7.4.6 Optimum Condition for Corrosion Inhibition (PYMA)

As shown in the Constraint Table 4.56, the main goal was to maximize the inhibition efficiency (R1) within the experimental ranges: an inhibitor concentration of 2 mM, an acid concentration of 0.25 M, an immersion time of 12 hours and an inhibitor-to-acid ratio of 3 By giving each factor equal importance (rating of 3), the model was able to evaluate how these variables work together to protect the metal surface (Benyounis, 2019).

The success of this optimization is confirmed by a desirability score of 1.000, the highest possible value, indicating that the software identified the best combination that meets all requirements at the same time. According to the ramp plots Figure 4.83 the predicted optimum performance occurs at an inhibitor concentration (A) of 5.99 mM, an immersion time (C) of 13.39 hours and an inhibitor-to-acid ratio (D) of 3.93. Even at a relatively high acid concentration (B) of 0.74 M, the model predicts a high

inhibition efficiency of 90.03%. Then the model optimum was confirmed by RSE, Table 4.57 which value in not less or more than 5% (Nor et al., 2022).

These conditions are considered the most optimum because they allow enough inhibitor molecules to cover the metal surface completely, forming a strong protective layer that blocks corrosive species. The immersion time is long enough for the inhibitor to attach and stabilize on the surface without causing desorption or uneven coverage. The inhibitor-to-acid ratio ensures a good balance between inhibitor availability and the strength of the acidic solution, so the protective film remains effective (Quadri et al., 2022; Timoudan et al., 2024). Maintaining a moderate acid concentration prevents the solution from being too aggressive, allowing the inhibitor to dominate the metal surface (Revie & Uhlig, 2008; Ahmad, 2006). Overall, these optimized conditions provide the best combination of factors for maximum inhibition efficiency, ensuring a stable and effective protective layer and reliable corrosion protection under the tested conditions.

Table 4.56
Constraint Table for PYMA

Parameters	Goal	Lower limit	Upper limit	Lower weight	Upper weight	Importance
A: Inhibitor concentration	Is in range	2	6	1	1	3
B: Acid concentration	Is in range	0.25	0.75	1	1	3
C: Immersion time	Is in range	12	20	1	1	3
D: Ratio	Is in range	3	4	1	1	3
R1 (Inhibition Efficiency)	Maximize	60	90	1	1	3

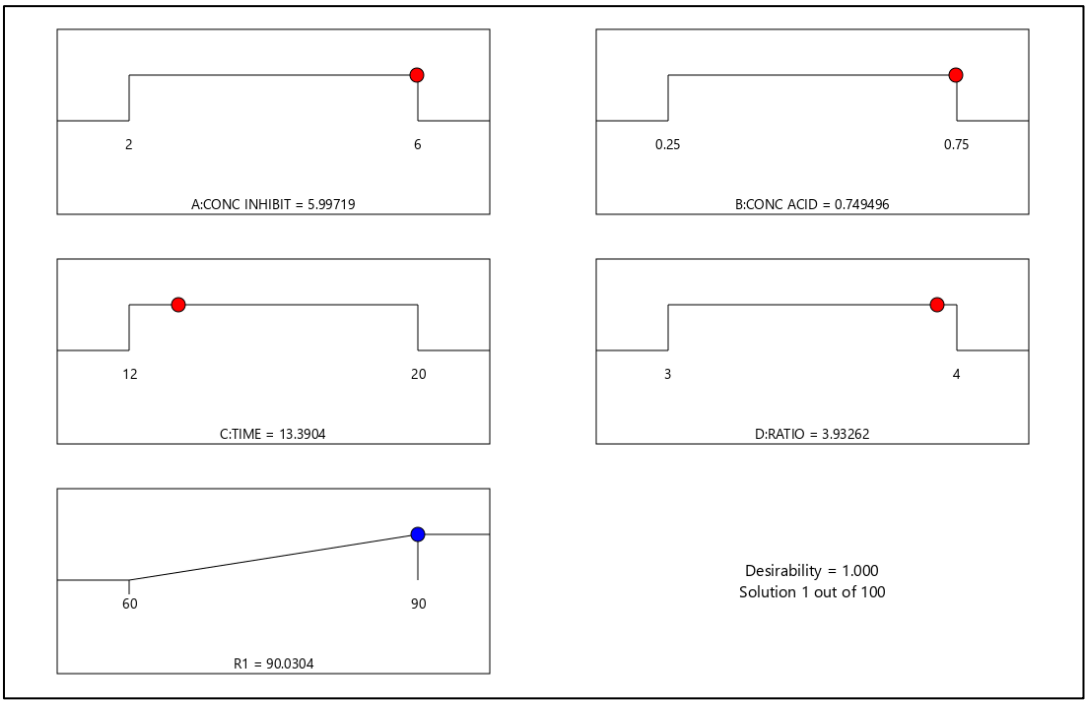


Figure 4.83 Optimum Ramp Data for PYMA

Table 4.57
Actual and Predicted Data for Optimum Condition (PYMA)

	Independent variables				Response %		
no	A	B	C	D	Predicted	Actual	RSE
1	5.99	0.74	13.39	3.99	90.03	88.76	1.41

CHAPTER 5
CONCLUSION

5.1 Conclusion

Four Meldrum's acid derivatives 4-Formylbenzonitrile Meldrum's acid (FBMA), *p*-Tolualdehyde Meldrum's acid (TOMA), 4-Thiophenecarboxyaldehyde Meldrum's acid (THMA) and 2-Pyridinecarboxyaldehyde Meldrum's acid (PYMA) were successfully synthesised through Knoevenagel condensation followed by Michael addition reactions. The prepared compounds were confirmed using elemental analysis, melting point determination and spectroscopic techniques including FTIR, NMR and SC-XRD. The spectroscopic results clearly showed the successful interaction of Meldrum's acid with the corresponding aldehyde derivatives. FTIR spectra showed the disappearance of the aldehyde C=O stretching band and the appearance of characteristic C=C and carbonyl vibrations of the Meldrum's acid derivatives, confirming successful condensation. The ^{1}H and ^{13}C NMR spectra further verified the molecular structures through the disappearance of aldehydic proton signals and the presence of characteristic olefinic and carbonyl carbon resonances. SC-XRD analysis confirmed the molecular geometry and crystal packing of the synthesised compounds, providing definitive structural evidence for the successful formation of the target Meldrum's acid derivatives.

The corrosion inhibition performance of all synthesised compounds was evaluated using weight loss measurements and response surface methodology (RSM). The results demonstrate that all four compounds exhibit strong corrosion inhibition ability in 1 M HCl. The inhibition efficiency increased consistently with increasing inhibitor concentration (1–7 mM), indicating that higher concentrations promote better surface coverage on mild steel. Based on weight loss and RSM results, the inhibition efficiency follows the order: FBMA > TOMA > PYMA > THMA, confirming FBMA as the most effective inhibitor among the studied derivatives.

Adsorption studies revealed that all inhibitors obey the Langmuir adsorption isotherm, indicating monolayer adsorption on the mild steel surface. The calculated Gibbs free energy of adsorption (ΔG°_{ads}) values suggests different adsorption behaviours. FBMA exhibited strong physisorption, with ΔG°_{ads} values lower than −20

kJ mol^{-1}, while TOMA, PYMA and THMA showed mixed adsorption mechanisms in which chemisorption dominates over physisorption.

Surface analysis using SEM-EDX and AFM confirmed the formation of a protective adsorbed layer on the mild steel surface in the presence of inhibitors. These techniques showed a clear reduction in surface roughness compared to the uninhibited sample, with FBMA producing the smoothest surface, further supporting its better inhibition performance. XPS analysis provided direct evidence of inhibitor adsorption, where Fe–O bonds observed in the Fe 2p and O 1s spectra confirmed interaction between the inhibitors and the mild steel surface through oxygen atoms.

DFT calculations suggested PYMA as a promising corrosion inhibitor based on its quantum chemical parameters. However, experimental results showed that FBMA performed better in practice. This enhanced performance of FBMA is attributed to its larger molecular size, the presence of two Meldrum's acid units, a strong electron-withdrawing nitrile group and multiple oxygen and nitrogen atoms, which provide more active adsorption sites and stronger surface coverage. The difference between theoretical and experimental findings arises because DFT calculations were performed in a neutral environment, whereas experimental measurements were conducted in acidic conditions, where protonation effects play a significant role. In addition, factors such as molecular planarity, electron-withdrawing and electron-donating groups and the number of adsorption sites also influence inhibition efficiency.

RSM optimisation studies successfully predicted the optimum conditions for maximum inhibition efficiency. For FBMA, the highest inhibition was achieved at an inhibitor concentration of 5.96 mM, an immersion time of 19.98 h and an inhibitor-to-acid ratio of 3.99, where a dense protective film forms on the steel surface. Similar optimum conditions were observed for TOMA at the same inhibitor concentration and immersion time. For THMA, maximum inhibition occurred at 5.20 mM inhibitor concentration, 0.74 M acid concentration, 19.98 h immersion time and an inhibitor-to-acid ratio of 3.0. PYMA showed optimum performance at 5.99 mM inhibitor concentration, 13.39 h immersion time and an inhibitor-to-acid ratio of 3.93, achieving a high inhibition efficiency of 90.03% even at 0.74 M HCl.

Overall, the combined experimental, surface, theoretical and statistical analyses confirm that the synthesised Meldrum's acid derivatives are effective corrosion inhibitors for mild steel in acidic media, with FBMA showing the highest overall performance.

5.2 Recommendations

To gain more understanding of the inhibitory performance of Meldrum's acid derivatives, future studies should test effectiveness across a broader time immersion. Such investigations will provide valuable insights towards stability and adsorption behaviour under extreme conditions. Further recommendations include examining the temperature effect on inhibition efficiency to assess the thermal stability of the inhibitors and to distinguish more clearly between physisorption and chemisorption mechanisms. Electrochemical techniques such as electrochemical impedance spectroscopy (EIS) and potentiodynamic polarization could also be employed to provide real-time information on charge transfer resistance and corrosion kinetics.

Moreover, studying the performance of these inhibitors in different acidic media and in the presence of other aggressive ions would help evaluate their practical applicability in industrial environments. Finally, structural modification of the Meldrum's acid derivatives, such as introducing different electron-donating or electron-withdrawing substituents, may further enhance inhibition efficiency and should be explored in future research.

In addition, Molecular Dynamics (MD) simulations are strongly recommended to further clarify the adsorption mechanisms and the formation of protective films at the atomic and molecular levels. MD simulations can offer detailed insights into adsorption configurations, binding energies, surface coverage and the dynamic behaviour of inhibitor molecules on the metal surface under realistic conditions.

REFERENCES

Adamu, A. A., Iyun, O. R. A., & Habila, J. D. (2025). Adsorption and thermodynamic studies of the corrosion Inhibition effect of Desmodium adscendens (Swartz) extract on carbon steel in 2 M HCl. BMC *Chemistry, 19*(1), 163.

Adindu, B., Ogukwe, C., Eze, F., & Oguzie, E. (2016). Exploiting the anticorrosion effects of vernonia amygdalina extract for protection of mild steel in acidic environments. *Journal of Electrochemical Science and Technology, 7*(4), 251–262.

Adnan, A. I., Pungot, N. H., & Ash'ari, N. A. N. (2021). A convenient synthesis of 5-arylidene Meldrum's acid derivatives via Knoevenagel condensation. *Journal of Academia, 9*(1), 80–84.

Aghamajidi, F., Khalili, M. R., Masumi, S. (2026). Structure–activity relationship and adsorption behavior of a thiazole-derived Schiff base corrosion inhibitor for mild steel: Integrated experimental and theoretical study. *Environmental Science and Pollution Research, 33*, 5731–5746.

Ahmad, Z. (2006). Principles of corrosion engineering and corrosion control. In *Principles of corrosion engineering and corrosion control* (1st ed., pp. 1–635). Elsevier.

Ahmed, M. A., Amin, S., & Mohamed, A. A. (2024). Current and emerging trends of inorganic, organic and eco-friendly corrosion inhibitors. *RSC Advances, 14*(43), 31877–31920.

Akalezi, C. O., Enenebaku, C. K., & Oguzie, E. E. (2013). Inhibition of acid corrosion of mild steel by biomass extract from the petersianthus macrocarpus plant. *Journal of Materials and Environmental Science, 4*(2), 217–226.

Al-Amiery, A. A., Isahak, W. N. R. W., & Al-Azzawi, W. K. (2023). Corrosion inhibitors: Natural and synthetic organic inhibitors. *Lubricants, 11*(4), 170.

Alamiery, A. A. (2021). Anticorrosion effect of thiosemicarbazide derivative on mild steel in 1 M hydrochloric acid and 0.5 M sulfuric acid: Gravimetrical and theoretical studies. *Materials Science for Energy Technologies, 4,* 263–273.

Alamri, A. H. (2020). Localized corrosion and mitigation approach of steel materials used in oil and gas pipelines - An overview. *Engineering Failure Analysis, 116*, 104735.

Al Bahir, A., Imen, B., & Alqarni, N. (2024). Advancing imine metal chelates for corrosion inhibition across diverse environments: A novel perspective. *Results in Chemistry, 7*, 101455.

Ali, H., Khan, E., & Ilahi, I. (2019). Environmental chemistry and ecotoxicology of hazardous heavy metals: Environmental persistence, toxicity, and bioaccumulation. *Journal of Chemistry,* 2019, 6730305.

Anadebe, V. C., Onukwuli, O. D., Omotioma, M., & Okafor, N. A. (2018). Optimization and electrochemical study on the control of mild steel corrosion in hydrochloric acid solution with bitter kola leaf extract as inhibitor. *South African Journal of Chemistry, 71*, 51–61

Ani, J. U., Obi, I. O., Akpomie, K. G., Eze, S. I., & Nwatu, G. (2022). Corrosion inhibition studies of metals in acid media by fibrous plant biomass extracts and density functional theory: a mini review. *Journal of Natural Fibers, 19*(7), 2391–2401.

Antony, J. (2014). A systematic methodology for design of experiments. In J. Antony (Ed.), *Design of experiments for engineers and scientists* (2nd ed., pp. 33–50). Elsevier.

Baharin, N. A. N., Sheikh Mohd Ghazali, S. A. I., Sirat, S. S., Mohd Tajuddin, A., Pungot, N. H., Normaya, E., Mohd Kamarudin, S. R., & Dzulkifli, N. N. (2024). In-depth investigation of corrosion inhibition mechanism: Computational, electrochemical, and theoretical studies of vanillin Meldrum's acid on mild steel surface in 1 M HCl. *Journal of Molecular Liquids, 416*, 126097.

Barrahi, A., Mekhzoum, M. E. M., Thakur, A., Qaiss, A. E. K., Kaichouh, G., El Faydy, M., Benhiba, F., Dikici, B., Bouhfid, R., Abuelizz, H. A., Warad, I., & Zarrouk, A. (2025). An investigation of benzothiazole ionic compound as corrosion inhibitor for carbon steel in acidic media using electrochemical research, surface techniques, DFT, and MD simulation studies. *International Journal of Electrochemical Science, 20*(1), 100980.

Baskar, P., Annadurai, S., Panneerselvam, S., Prabakaran, M., & Kim, J. (2023). An outline of employing metals and alloys in corrosive settings with ecologically acceptable corrosion inhibitors. *Surfaces, 6(4),* 380–409.

Benyounis, K. Y. (2019). Procedure of conducting an experiment using response surface methodology for manufacturing process modelling and optimization. *Reference Module in Materials Science and Materials Engineering*, 1–11.

Bezerra, M. A., Santelli, R. E., Oliveira, E. P., Villar, L. S., & Escaleira, L. A. (2008). Response surface methodology (RSM) as a tool for optimization in analytical chemistry. *Talanta, 76*(5), 965–977.

Biesinger, M. C. (2017). Advanced analysis of copper X-ray photoelectron spectra. *Surface and Interface Analysis, 49(*13), 1325–1334.

Brosge, F., Singh, P., Almqvist, F., & Bolm, C. (2021). Selected applications of Meldrum's acid – A tutorial. *Organic & Biomolecular Chemistry, 19*(23), 5014–5027

Bukhari, S. N. A., Abdelgawad, M. A., Ahmed, N., Amjad, M. W., Hussain, M. A., Elsherif, M. A., Ejaz, H., Alotaibi, N. H., Filipović, I., & Janković, N. (2023). Synthesis, characterization, and biological evaluation of Meldrum's acid derivatives: dual activity and molecular docking study. *Pharmaceuticals, 16*(2), 281.

Chahid, A., Chafi, M., Essahli, M., Alrashdi, A. A., & Lgaz, H. (2024). Exploring the efficacy of Congo red dye as a corrosion inhibitor for aluminum in HCl solution: An interdisciplinary study with RSM modeling and theoretical simulations. *Arabian Journal of Chemistry, 17*(7), 105970.

Cherif, M., et al. (2024). A review on corrosion inhibitors: Types, mechanisms, electrochemical analysis, corrosion rate and efficiency of corrosion inhibitors on mild steel in an acidic environment. *Results in Surfaces and Interfaces, 16*, 100258.

Cooper, M. M., & Klymkowsky, M. W. (2020). Chapter 9: A return to the carbonyl. *OCLUE: Organic Chemistry, Life, the Universe & Everything*.

Dada, M., Popoola, P., Aramide, O., Mathe, N., & Pityana, S. (2021). Optimization of the corrosion property of a high entropy alloy using response surface methodology. *Materials Today: Proceedings, 38*, 1024–1030.

De Toledo, T. A., da Silva, L. E., Teixeira, A. M. R., Freire, P. T. C., & Pizani, P. S. (2015). Characterization of Meldrum's acid derivative 5-(5-ethyl-1,3,4-thiadiazol-2-ylamino)methylene-2,2-dimethyl-1,3-dioxane-4,6-dione by Raman and FT-IR spectroscopy and DFT calculations. *Journal of Molecular Structure,* 1091, 37–42.

Dey, T., Ghosh, S., Ghosh, S., & Mukherjee, A. K. (2015). 5-Arylidene derivatives of Meldrum's acid: Synthesis, structural characterization using single crystal and

powder crystal X-ray diffraction, and electronic properties. *Journal of Molecular Structure,* 1092, 51–62.

Elebo, A., Uba, S., Adamma Ekwumemgbo, P., & Ajibola, V. O. (2024). Unravelling adsorption potential of expired clindamycin as corrosion inhibitor at mild steel/HCl interface via response surface methodology, artificial neural network, electrochemical, and computational strategies. *Current Research in Green and Sustainable Chemistry, 8*, 100462.

Ferkous, H., Sedik, A., Delimi, A., Redjemia, R., Abdesalem, K., Boulechfar, C., Abdennouri, A., Madaci, A., Berredjem, M., Boublia, A., Sajid Ali, M., Jeon, B. H., Kumar Yadav, K., & Benguerba, Y. (2024). A comparative study of novel synthesised sulfamide compounds: Electrochemical, morphological, XPS, and theoretical investigations on copper corrosion inhibition in 1.0 M HCl. *Journal of Molecular Liquids, 394*, 123685.

Filho, M. A. M., de Santana, L. L. B., Rivelino, R., & Cunha, S. (2020). A theoretical investigation on the nucleophilic behavior of Meldrum's acid linked to experimental evidences. *Chemical Physics Letters, 738*, 136908.

Finšgar, M., & Jackson, J. (2014). Application of corrosion inhibitors for steels in acidic media for the oil and gas industry: A review. *Corrosion Science, 86,* 17–41.

Fouda, A. E. A. S., El-Askalany, A. H., Molouk, A. F. S., Elsheikh, N. S., & Abousalem, A. S. (2021). Experimental and computational chemical studies on the corrosion inhibitive properties of carbonitrile compounds for carbon steel in aqueous solutions. *Scientific Reports, 11*(1), 17865.

Gece, G. (2008). The use of quantum chemical methods in corrosion inhibitor studies. *Corrosion Science, 50*(11), 2981–2992.

Gokhale, M., & Mantri, R. (2017). API solid-form screening and selection. In H. G. Brittain (Ed.), *Developing Solid Oral Dosage Forms* (2nd ed.). Elsevier.

Guendouz, A., Ettahiri, W., Adardour, M., Lazrak, J., Assiri, E. H. El, Taleb, A., Hammouti, B., Rais, Z., Baouid, A., & Taleb, M. (2024). New benzimidazole derivatives as efficient organic inhibitors of mild steel corrosion in hydrochloric acid medium: Electrochemical, SEM/EDX, MC, and DFT studies. *Journal of Molecular Structure, 1305*, 139901.

Harsimran, S., Santosh, K., & Rakesh, K. (2021). Overview of corrosion and its control: a critical review. *Proceedings on Engineering Sciences, 3*(1), 13–24.

Hashim, F., Al-Azawi, K., Al-Bghdadi, S. B., Shaker, L. M., & Al-Amiery, A. (2020). Experimental and theoretical approach to the corrosion inhibition of mild steel in HCl solution by a newly coumarin. *International Journal of Electrochemical Science, 15*, 11871–11884.

Hohenstein, E. G., & Sherrill, C. D. (2009). Effects of heteroatoms on aromatic π–π interactions: Benzene–pyridine and pyridine dimer. *Journal of Physical Chemistry A, 113*(5), 878–886.

Hussein Khalaf, A., Xiao, Y., Xu, N., Wu, B., Li, H., Lin, B., Nie, Z., & Tang, J. (2024). Emerging AI technologies for corrosion monitoring in oil. *Engineering Failure Analysis, 155*, 107730.

Idelfitri, N. I. F., Dzulkifli, N. N., Ash'ari, N. A. N., Sapari, S., Abdul Razak, F. A., & Pungot, N. H. (2023). Synthesis, characterisation and corrosion inhibitory study of Meldrum's acid derivative on mild steel in hydrochloric acid. *Inorganic Chemistry Communications, 150*, 110518.

Ju, H., & Li, Y. (2007). Nicotinic acid as a nontoxic corrosion inhibitor for hot dipped Zn and Zn-Al alloy coatings on steels in diluted hydrochloric acid. *Corrosion Science, 49*(11), 4185–4201.

Kathirvel, K., Thirumalairaj, B., & Jaganathan, M. (2014). Quantum chemical studies on the corrosion inhibition of mild steel by piperidin-4-one derivatives in 1 M HCl. Open *Journal of Metal, 4*(4), 73–85.

Komkov, A. V., Sukhanova, A. A., Menchikov, L. G., & Zavarzin, I. V. (2022). O-aminopyrimidine aldehydes and ketones: synthesis and use as precursors to fused pyrimidines. *Chemistry of Heterocyclic Compounds, 58*(11), 547–566.

Mamand, D. M., Anwer, T. M. K., & Qadr, H. M. (2024). Electronic structure and quantum chemical analysis of the corrosion inhibition efficiency of quinoxalines. *Journal of the Indian Chemical Society, 101*, 101018.

Mansor, M. A. A., Zainal Abidin, N. A., Yasin, Y., Sheikh Mohd Ghazali, S. A. I., & Dzulkifli, N. N. (2024). Optimisation of the corrosion inhibition performance of isatin 4-ethyl-3-thiosemicarbazone for mild steel in sulfuric acid medium using response surface methodology. *Chemical Papers, 78*(13), 7409–7422.

Mert, M. E., Güngör, C., & Doğru Mert, B. (2025). Analytical study on mild steel corrosion inhibition in acidic environment: DFT modeling and RSM optimization. *Fuel, 381*, 133682.

Montgomery, D. C. (2019). Design and analysis of experiments. In *Design and analysis of experiments* (10th ed., pp. 1–549). Wiley.

Moradi, M., Duan, H., & Jiang, Y. (2011). Quantitative structure activity relationships of some pyridine derivatives as corrosion inhibitors of steel in acidic medium. *Journal of Molecular Modeling,* 17, 1887–1897.

Muhtar, H., Darmawan, A., & Bima, D. N. (2024). Corrosion Inhibition of Mild Steel in 1.0 M HCl from Thiadiazole Derivative Schiff Bases and Their Complexes with Co(II) and Ni(II): Synthesis, Characterization, DFT Study, and Monte Carlo Simulation. *Journal of Bio- and Tribo-Corrosion*, *10*(3).

Myers, R. H., Montgomery, D. C., & Anderson-Cook, C. M. (2016). Response Surface Methodology. In *Response Surface Methodology* (4th ed., pp. 1–783). Wiley

Naseri, E., Hajisafari, M., Kosari, A., Talari, M., Hosseinpour, S., & Davoodi, A. (2018). Inhibitive effect of clopidogrel as a green corrosion inhibitor for mild steel; statistical modeling and quantum Monte Carlo simulation studies. *Journal of Molecular Liquids,* 269, 193–202.

Nor, N. M., Salih, N., & Salimon, J. (2022). Optimization and lubrication properties of Malaysian crude palm oil fatty acids based neopentyl glycol diester green biolubricant. *Renewable Energy,* 200, 942–956.

Obot, I. B., Haruna, K., & Saleh, T. A. (2019). Atomistic simulation: A unique and powerful computational tool for corrosion inhibition research. *Arabian Journal for Science and Engineering, 44*(1), 1–32.

Odejobi, O. J., & Akinbulumo, O. A. (2019). Modeling and optimization of the inhibition efficiency of *Euphorbia heterophylla* extract as a corrosion inhibitor for mild steel in HCl medium using response surface methodology. *Journal of Chemical Technology and Metallurgy, 54*(1), p. 217–232.

Oguzie, E. E., Li, Y., Wang, S. G., & Wang, F. (2011). Understanding corrosion inhibition mechanisms - experimental and theoretical approach. *RSC Advances, 1*(5), 866–873.

Okewale, A. O., Omoruwuo, F., & Adesina, O. A. (2019). Comparative studies of response surface methodology (RSM) and predictive capacity of artificial neural network (ANN) on mild steel corrosion inhibition using water hyacinth as an inhibitor. *Journal of Physics: Conference Series, 1378(2).*

Quadri, T. W., Olasunkanmi, L. O., Fayemi, O. E., Lgaz, H., Dagdag, O., Sherif, E.-S. M., Alrashdi, A. A., Akpan, E. D., Lee, H.-S., & Ebenso, E. E. (2022).

Computational insights into quinoxaline-based corrosion inhibitors of steel in HCl: Quantum chemical analysis and QSPR-ANN studies. *Arabian Journal of Chemistry, 15*(7), 103870.

Revie, R. W., & Uhlig, H. H. (2008). Corrosion and corrosion control: An introduction to corrosion science and engineering (4th ed.,pp. 1-331). Wiley.

Salam, K. K., Agarry, S. E., Arinkoola, A. O., & Shoremekun, I. O. (2015). Optimization of operating conditions affecting microbiologically influenced corrosion of mild steel exposed to crude oil environments using response surface methodology. *Biotechnology Journal International, 7*, 68–78.

Serpini, E., Vitu, T., Rota, A., Polcar, T., & Valeri, S. (2021). Friction-Induced chemical and structural modifications of molybdenum disulphide thin films. *Journal of Materials Engineering and Performance, 30*(6), 4117–4125.

Schulz, T., Ahrens, S., Meyer, D., Allolio, C., Peritz, A., & Strassner, T. (2011). Electronic effects of para-substitution on the melting points of TAAILs. Chemistry - *An Asian Journal, 6*(3), 863–867.

Shaabani, A., Yavari, I., Teimouri, M. B., Bazgir, A., & Bijanzadeh, H. R. (2001). New and efficient synthesis of dialkyl 2-[1-p-nitrophenyl-2-(alkylamino)-2-oxoethyl]malonates. *Tetrahedron, 57*(7), 1375–1378.

Shahid, M. (2011). Corrosion protection with eco-friendly inhibitors. Advances in Natural *Sciences: Nanoscience and Nanotechnology, 2*(4).

Sharma, S., & Kumar, A. (2021). Recent advances in metallic corrosion inhibition: A review. *Journal of Molecular Liquids, 322*, 114862.

Shashirekha, K., Aithal, S., BM, P., MK, P., Guruprasad, A., Devendra, B. K., & Rathod, M. R. (2024). Experimental, electrochemical and DFT simulation studies of a novel Schiff base derivative as an efficient mild steel corrosion inhibitor in acidic environments. *Results in Surfaces and Interfaces*, *16*, 100246.

Silverstein, R. M., Webster, F. X., Kiemle, D. J., & Bryce, D. L. (2014). Spectrometric identification of organic compounds. In *Spectrometric identification of organic compounds* (6th ed., pp. 71–274). John Wiley & Sons.

Sokov, S. A., Raskildina, G. Z., Vologzhanina, A. V., Zlotskii, S. S., & Golovanov, A. A. (2024). Michael reaction of enamine derivatives of Meldrum's acid in water: Synthetic approach for creating C–N/C–S bonds with low-reactive nucleophiles. *Tetrahedron, 169*, 134369.

Solomon, M. M. (2023). Effective inhibition of T95 steel corrosion in 15 wt% HCl solution by aspartame, potassium iodide, and sodium dodecyl sulphate mixture. *Scientific Reports, 13*(1), 11126.

Tansuğ, G., Tüken, T., Kıcır, N., & Erbil, M. (2014). Investigation of 2-aminoethanethiol as corrosion inhibitor for steel using response surface methodology (RSM). *Ionics, 20*(2), 287–294.

Timoudan, N., Al-Gorair, A. S., Foujji, L. E., Warad, I., Safi, Z., Dikici, B., Benhiba, F., Qaiss, A. E. K., Bouhfid, R., Bentiss, F., Al-Juaid, S. S., Abdallah, M., & Zarrouk, A. (2024). Corrosion inhibition performance of benzimidazole derivatives for protection of carbon steel in hydrochloric acid solution. *RSC Advances, 14*(41), 30295–30316.

Vaidya, N. R., Aklujkar, P., & Rao, A. R. (2022). Modification of natural gums for application as corrosion inhibitor: a review. *Journal of Coatings Technology and Research, 19*(1), 223–239.

Vashishth, P., Bairagi, H., Narang, R., Shukla, S. K., Olasunkanmi, L. O., Ebenso, E. E., & Mangla, B. (2023). Experimental investigation of sustainable corrosion inhibitor albumin on low-carbon steel in 1N HCl and 1N H_2SO_4. *Results in Surfaces and Interfaces, 13, 100155.*

Verma, C., Lgaz, H., Verma, D. K., Ebenso, E. E., Bahadur, I., & Quraishi, M. A. (2018). Molecular dynamics and Monte Carlo simulations as powerful tools for study of interfacial adsorption behavior of corrosion inhibitors in aqueous phase: A review. *Journal of Molecular Liquids,* 260, 99–120.

Vinutha, M. R., Venkatesha, T. V., & Nagaraja, C. (2018). Anticorrosive ability of electrochemically synthesized 2,2′-disulfanediyldianiline for mild steel corrosion: electrochemical and thermodynamic studies. *International Journal of Industrial Chemistry, 9*(2), 185–197.

Yamin, J. A. A., Ali Eh Sheet, E., & Al-Amiery, A. (2020). Statistical analysis and optimization of the corrosion inhibition efficiency of a locally made corrosion inhibitor under different operating variables using RSM. *International Journal of Corrosion and Scale Inhibition, 9*(2), 502–518.

Yolmeh, M., & Jafari, S. M. (2017). Applications of response surface methodology in the food industry processes. *Food and Bioprocess Technology, 10(3), 413–433.*

Yu. X., Jiahui, K., Jian, H., Kaili, L., Jihui, L., Huixin, Z., & Jianxin, Chen. (2024). Synthesis, scale and corrosion inhibition evaluation and mechanism of 2-

aminobenzimidazole modified polyaspartic acid. *Journal of Environmental Chemical Engineering, 12*(3),112950.

Zaidon, F. H., Kassim, K., Mohd Zaki, H., Embong, Z., Anouar, E. H., & Nor Hashim, N. Z. (2021). Adsorption and corrosion inhibition accomplishment for thiosemicarbazone derivatives for mild steel in 1.0 M HCl medium: Electrochemical, XPS and DFT studies. *Journal of Molecular Liquids, 329*, 115531.

APPENDICES

APPENDIX 1

Bond Length [A], Bond and Torsion Angles [°] for FBMA

Bond	Bond length [Å]	Bond	Bond length [Å]
O1_1—C9_1	1.344 (2)	C7_1—C8_1	1.545 (2)
O1_1—C10_1	1.445 (2)	C7_1—C13_1	1.559 (2)
O2_1—C11_1	1.338 (2)	C7_1—H7_1	0.9800
O2_1—C10_1	1.441 (2)	C8_1—C9_1	1.516 (2)
O3_1—C14_1	1.339 (2)	C8_1—C11_1	1.523 (2)
O3_1—C15_1	1.442 (2)	C8_1—H8_1	0.9800
O4_1—C16_1	1.344 (2)	C10_1—C17_1	1.500 (3)
O4_1—C15_1	1.442 (2)	C10_1—C18_1	1.506 (3)
O5_1—C9_1	1.196 (2)	C13_1—C14_1	1.514 (2)
O6_1—C11_1	1.194 (2)	C13_1—C16_1	1.515 (2)
O7_1—C14_1	1.199 (2)	C13_1—H13_1	0.9800
O8_1—C16_1	1.200 (2)	C15_1—C19_1	1.501 (3)
N1_1—C12_1	1.132 (3)	C15_1—C20_1	1.509 (3)
C1_1—C2_1	1.385 (2)	C17_1—H17A_1	0.9600
C1_1—C6_1	1.385 (2)	C17_1—H17B_1	0.9600
C1_1—C7_1	1.525 (2)	C17_1—H17C_1	0.9600
C2_1—C3_1	1.380 (3)	C18_1—H18A_1	0.9600
C2_1—H2_1	0.9300	C18_1—H18B_1	0.9600
C3_1—C4_1	1.381 (3)	C18_1—H18C_1	0.9600
C3_1—H3_1	0.9300	C19_1—H19A_1	0.9600
C4_1—C5_1	1.385 (3)	C19_1—H19B_1	0.9600
C4_1—C12_1	1.445 (3)	C19_1—H19C_1	0.9600
C5_1—C6_1	1.387 (3)	C20_1—H20A_1	0.9600
C5_1—H5_1	0.9300	C20_1—H20B_1	0.9600
C6_1—H6_1	0.9300	C20_1—H20C_1	0.9600

Bond	Bond length [Å]	Bond	Bond length [Å]
C9_1—O1_1-C10_1	121.04 (14)	O2_1—C11_1—C8_1	116.27 (15)
C11_1—O2_1-C10_1	121.35 (14)	N1_1—C12_1—C4_1	177.6 (3)
C14_1—O3_1—C15_1	121.14 (13)	C14_1—C13_1—C16_1	112.89 (14)
C16_1—O4_1—C15_1	121.53 (14)	C14_1—C13_1—C7_1	115.45 (14)
C2_1—C1_1—C6_1	118.98 (16)	C16_1—C13_1—C7_1	111.92 (14)
C2_1—C1_1—C7_1	117.28 (15)	C14_1—C13_1—H13_1	105.2
C6_1—C1_1—C7_1	123.45 (15)	C16_1—C13_1—H13_1	105.2
C3_1—C2_1—C1_1	120.86 (18)	C7_1—C13_1—H13_1	105.2
C3_1—C2_1—H2_1	119.6	O7_1—C14_1—O3_1	119.03 (16)
C1_1—C2_1—H2_1	119.6	O7_1—C14_1—C13_1	123.69 (16)
C2_1—C3_1—C4_1	119.67 (17)	O3_1—C14_1—C13_1	117.28 (14)
C2_1—C3_1—H3_1	120.2	O3_1—C15_1—O4_1	110.27 (14)

C4_1—C3_1—H3_1	120.2	O3_1—C15_1—C19_1	105.90 (15)
C3_1—C4_1—C5_1	120.35 (17)	O4_1—C15_1—C19_1	106.14 (17)
C3_1—C4_1—C12_1	119.08 (18)	O3_1—C15_1—C20_1	110.18 (16)
C5_1—C4_1—C12_1	120.56 (19)	O4_1—C15_1—C20_1	110.05 (15)
C4_1—C5_1—C6_1	119.42 (18)	C19_1—C15_1—C20_1	114.15 (19)
C4_1—C5_1—H5_1	120.3	O8_1—C16_1—O4_1	118.61 (16)
C6_1—C5_1—H5_1	120.3	O8_1—C16_1—C13_1	124.57 (17)
C1_1—C6_1—C5_1	120.70 (17)	O4_1—C16_1—C13_1	116.79 (15)
C1_1—C6_1—H6_1	119.6	C10_1—C17_1—H17A_1	109.5
C5_1—C6_1—H6_1	119.6	C10_1—C17_1—H17B_1	109.5
C1_1—C7_1—C8_1	113.60 (14)	H17A_1—C17_1—H17B_1	109.5
C1_1—C7_1—C13_1	107.95 (13)	C10_1—C17_1—H17C_1	109.5
C8_1—C7_1—C13_1	116.20 (13)	H17A_1—C17_1—H17C_1	109.5
C1_1—C7_1—H7_1	106.1	H17B_1—C17_1—H17C_1	109.5
C8_1—C7_1—H7_1	106.1	C10_1—C18_1—H18A_1	109.5
C13_1—C7_1—H7_1	106.1	C10_1—C18_1—H18B_1	109.5
C9_1—C8_1—C11_1	110.02 (14)	H18A_1—C18_1—H18B_1	109.5
C9_1—C8_1—C7_1	111.35 (14)	C10_1—C18_1—H18C_1	109.5
C11_1—C8_1—C7_1	113.64 (14)	H18A_1—C18_1—H18C_1	109.5
C9_1—C8_1—H8_1	107.2	H18B_1—C18_1—H18C_1	109.5
C11_1—C8_1—H8_1	107.2	C15_1—C19_1—H19A_1	109.5
C7_1—C8_1—H8_1	107.2	C15_1—C19_1—H19B_1	109.5
O5_1—C9_1—O1_1	119.14 (17)	H19A_1—C19_1—H19B_1	109.5
O5_1—C9_1—C8_1	124.48 (16)	C15_1—C19_1—H19C_1	109.5
O1_1—C9_1—C8_1	116.38 (14)	H19A_1—C19_1—H19C_1	109.5
O2_1—C10_1—O1_1	109.44 (14)	H19B_1—C19_1—H19C_1	109.5
O2_1—C10_1—C17_1	111.11 (17)	C15_1—C20_1—H20A_1	109.5
O1_1—C10_1—C17_1	111.53 (15)	C15_1—C20_1—H20B_1	109.5
O2_1—C10_1—C18_1	104.88 (16)	H20A_1—C20_1—H20B_1	109.5
O1_1—C10_1—C18_1	106.30 (17)	C15_1—C20_1—H20C_1	109.5
C17_1—C10_1—C18_1	113.25 (17)	H20A_1—C20_1—H20C_1	109.5
O6_1—C11_1—O2_1	119.10 (16)	H20B_1—C20_1—H20C_1	109.5
O6_1—C11_1—C8_1	124.63 (16)		

Bond Length [A], Bond and Torsion Angles [°] for TOMA

Bond	**Bond length [Å]**	**Bond**	**Bond length [Å]**
O1—C3	1.347 (2)	C6—H9	0.9800
O1—C2	1.434 (2)	C8—C13	1.498 (3)
O2—C7	1.354 (2)	C8—C9	1.506 (3)
O2—C8	1.440 (2)	C9—H7	0.9600
O3—C3	1.194 (2)	C9—H8	0.9600
O4—C11	1.343 (2)	C9—H2	0.9600
O4—C2	1.436 (2)	C10—H3	0.9600
O5—C11	1.205 (2)	C10—H21	0.9600

O6—C12	1.343 (2)	C10—H22	0.9600
O6—C8	1.442 (2)	C13—H4	0.9600
O7—C12	1.194 (2)	C13—H5	0.9600
O8—C7	1.192 (2)	C13—H6	0.9600
C1—C2	1.509 (2)	C14—C15	1.372 (3)
C1—H19	0.9600	C14—C19	1.391 (2)
C1—H20	0.9600	C15—C16	1.394 (2)
C1—H1	0.9600	C15—H16	0.9300
C2—C10	1.512 (3)	C16—C17	1.386 (3)
C3—C4	1.517 (2)	C16—H15	0.9300
C4—C11	1.512 (2)	C17—C18	1.375 (3)
C4—C5	1.564 (2)	C17—C20	1.513 (2)
C4—H18	0.9800	C18—C19	1.392 (3)
C5—C14	1.529 (2)	C18—H11	0.9300
C5—C6	1.549 (2)	C19—H10	0.9300
C5—H17	0.9800	C20—H12	0.9600
C6—C7l	1.516 (2)	C20—H13	0.9600
C6—C12	1.521 (2)	C20—H14	0.9600

Bond	**Bond length [Å]**	**Bond**	**Bond length [Å]**
C3—O1—C2	121.38 (14)	C8—C9—H8	109.5
C7—O2—C8	121.00 (14)	H7—C9—H8	109.5
C11—O4—C2	120.77 (13)	C8—C9—H2	109.5
C12—O6—C8	120.88 (13)	H7—C9—H2	109.5
C2—C1—H19	109.5	H8—C9—H2	109.5
C2—C1—H20	109.5	C2—C10—H3	109.5
H19—C1—H20	109.5	C2—C10—H21	109.5
C2—C1—H1	109.5	H3—C10—H21	109.5
H19—C1—H1	109.5	C2—C10—H22	109.5
H20—C1—H1	109.5	H3—C10—H22	109.5
O1—C2—O4	110.23 (14)	H21—C10—H22	109.5
O1—C2—C1	105.66 (16)	O5—C11—O4	118.42 (15)
O4—C2—C1	105.80 (14)	O5—C11—C4	124.32 (16)
O1—C2—C10	110.76 (14)	O4—C11—C4	117.26 (14)
O4—C2—C10	110.55 (15)	O7—C12—O6	118.65 (14)
C1—C2—C10	113.62 (18)	O7—C12—C6	125.21 (15)
O3—C3—O1	118.41 (17)	O6—C12—C6	116.14 (15)
O3—C3—C4	125.11 (17)	C8—C13—H4	109.5
O1—C3—C4	116.47 (14)	C8—C13—H5	109.5
C11—C4—C3	112.61 (13)	H4—C13—H5	109.5
C11—C4—C5	115.66 (14)	C8—C13—H6	109.5
C3—C4—C5	112.26 (14)	H4—C13—H6	109.5
C11—C4—H18	105.0	H5—C13—H6	109.5
C3—C4—H18	105.0	C15—C14—C19	118.34 (16)
C5—C4—H18	105.0	C15—C14—C5	123.75 (15)
C14—C5—C6	112.50 (13)	C19—C14—C5	117.78 (16)

C14—C5—C4	108.74 (13)	C14—C15—C16	121.16 (17)
C6—C5—C4	115.69 (12)	C14—C15—H16	119.4
C14—C5—H17	106.4	C16—C15—H16	119.4
C6—C5—H17	106.4	C17—C16—C15	120.7 (2)
C4—C5—H17	106.4	C17—C16—H15	119.6
C7—C6—C12	109.52 (13)	C15—C16—H15	119.6
C7—C6—C5	112.10 (13)	C18—C17—C16	117.96 (16)
C12—C6—C5	113.75 (14)	C18—C17—C20	121.5 (2)
C7—C6—H9	107.0	C16—C17—C20	120.5 (2)
C12—C6—H9	107.0	C17—C18—C19	121.59 (17)
C5—C6—H9	107.0	C17—C18—H11	119.2
O8—C7—O2	118.80 (17)	C19—C18—H11	119.2
O8—C7—C6	125.41 (16)	C14—C19—C18	120.23 (19)
O2—C7—C6	115.79 (13)	C14—C19—H10	119.9
O2—C8—O6	109.31 (14)	C18—C19—H10	119.9
O2—C8—C13	112.07 (15)	C17—C20—H12	109.5
O6—C8—C13	111.04 (17)	C17—C20—H13	109.5
O2—C8—C9	106.20 (16)	H12—C20—H13	109.5
O6—C8—C9	104.75 (15)	C17—C20—H14	109.5
C13—C8—C9	113.10 (17)	H12—C20—H14	109.5
C8—C9—H7	109.5	H13—C20—H14	109.5

Bond	**Bond length [Å]**	**Bond**	**Bond length [Å]**
C3—O1—C2—O4	-42.27 (19)	C12—O6—C8—O2	-43.3 (2)
C3—O1—C2—C1	-156.14 (16)	C12—O6—C8—C13	80.9 (2)
C3—O1—C2—C10	80.41 (19)	C12—O6—C8—C9	-156.71 (17)
C11—O4—C2—O1	42.5 (2)	C2—O4—C11—O5	172.41 (16)
C11—O4—C2—C1	156.28 (17)	C2—O4—C11—C4	-7.9 (2)
C11—O4—C2—C10	-80.3 (2)	C3—C4—C11—O5	151.86 (17)
C2—O1—C3—O3	-171.34 (16)	C5—C4—C11—O5	20.9 (2)
C2—O1—C3—C4	7.4 (2)	C3—C4—C11—O4	-27.8 (2)
O3—C3—C4—C11	-153.40 (17)	C5—C4—C11—O4	-158.71 (14)
O1—C3—C4—C11	28.0 (2)	C8—O6—C12—O7	-175.14 (17)
O3—C3—C4—C5	-20.8 (2)	C8—O6—C12—C6	4.6 (2)
O1—C3—C4—C5	160.62 (13)	C7—C6—C12—O7	-143.32 (19)
C11—C4—C5—C14	-94.84 (15)	C5—C6—C12—O7	-17.0 (3)
C3—C4—C5—C14	134.05 (14)	C7—C6—C12—O6	36.9 (2)
C11—C4—C5—C6	32.86 (19)	C5—C6—C12—O6	163.24 (15)
C3—C4—C5—C6	-98.25 (16)	C6—C5—C14—C15	-52.2 (2)
C14—C5—C6—C7	-63.48 (18)	C4—C5—C14—C15	77.3 (2)
C4—C5—C6—C7	170.72 (14)	C6—C5—C14—C19	132.07 (17)
C14—C5—C6—C12	171.58 (14)	C4—C5—C14—C19	-98.44 (18)
C4—C5—C6—C12	45.78 (19)	C19—C14—C15—C16	0.2 (3)
C8—O2—C7—O8	-178.44 (16)	C5—C14—C15—C16	-175.50 (18)
C8—O2—C7—C6	1.5 (2)	C14—C15—C16—C17	0.3 (3)
C12—C6—C7—O8	140.06 (18)	C15—C16—C17—C18	-0.6 (3)

C5—C6—C7—O8	12.8 (2)	C15—C16—C17—C20	-177.8 (2)
C12—C6—C7—O2	-39.9 (2)	C16—C17—C18—C19	0.3 (3)
C5—C6—C7—O2	-167.16 (14)	C20—C17—C18—C19	177.5 (2)
C7—O2—C8—O6	39.8 (2)	C15—C14—C19—C18	-0.5 (3)
C7—O2—C8—C13	-83.7 (2)	C5—C14—C19—C18	175.48 (17)
C7—O2—C8—C9	152.30 (17)	C17—C18—C19—C14	0.2 (3)

Bond Length [A], Bond and Torsion Angles [°] for THMA

Bond	**Bond length [Å]**	**Bond**	**Bond length [Å]**
S1—C2	1.6975 (15)	C4—H4	0.9300
S1—C1	1.7406 (12)	C5—C6	1.3631 (17)
O1—C7	1.3529 (16)	C5—H5	0.9300
O1—C8	1.4364 (16)	C6—C9	1.4644 (16)
O2—C9	1.3543 (15)	C6—C7	1.4807 (16)
O2—C8	1.4367 (17)	C8—C11	1.508 (2)
O3—C7	1.2010 (16)	C8—C10	1.513 (2)
O4—C9	1.2033 (16)	C10—H10A	0.9600
C1—C4	1.3836 (18)	C10—H10B	0.9600
C1—C5	1.4292 (17)	C10—H10C	0.9600
C2—C3	1.365 (2)	C11—H11A	0.9600
C2—H2	0.9300	C11—H11B	0.9600
C3—C4	1.4013 (19)	C11—H11C	0.9600
C3—H3	0.9300		

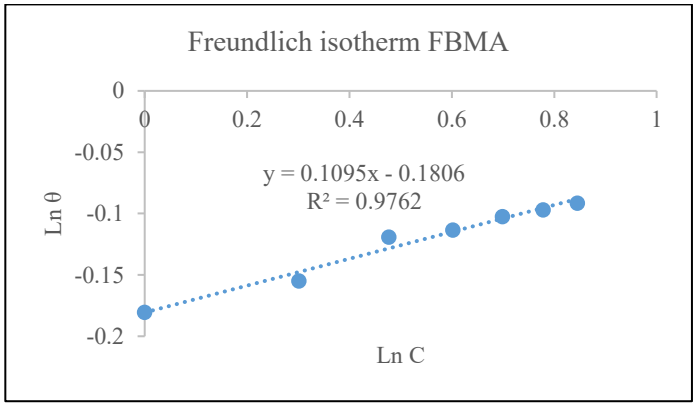
Bond	**Bond length [Å]**	**Bond**	**Bond length [Å]**
C2—S1—C1	91.55 (6)	O1—C7—C6	116.83 (10)
C7—O1—C8	118.92 (10)	O1—C8—O2	110.40 (11)
C9—O2—C8	118.92 (10)	O1—C8—C11	110.13 (12)
C4—C1—C5	120.35 (11)	O2—C8—C11	109.93 (12)
C4—C1—S1	109.78 (10)	O1—C8—C10	106.06 (12)
C5—C1—S1	129.85 (9)	O2—C8—C10	105.94 (12)
C3—C2—S1	113.19 (10)	C11—C8—C10	114.24 (13)
C3—C2—H2	123.4	O4—C9—O2	117.89 (11)
S1—C2—H2	123.4	O4—C9—C6	125.28 (12)
C2—C3—C4	111.66 (13)	O2—C9—C6	116.79 (11)
C2—C3—H3	124.2	C8—C10—H10A	109.5
C4—C3—H3	124.2	C8—C10—H10B	109.5
C1—C4—C3	113.82 (12)	H10A—C10—H10B	109.5
C1—C4—H4	123.1	C8—C10—H10C	109.5
C3—C4—H4	123.1	H10A—C10—H10C	109.5
C6—C5—C1	135.10 (11)	H10B—C10—H10C	109.5
C6—C5—H5	112.5	C8—C11—H11A	109.5
C1—C5—H5	112.5	C8—C11—H11B	109.5
C5—C6—C9	124.84 (11)	H11A—C11—H11B	109.5
C5—C6—C7	116.51 (10)	C8—C11—H11C	109.5

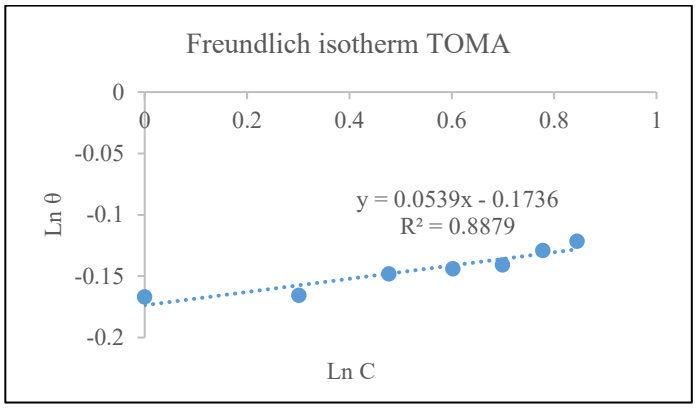
C9—C6—C7	118.56 (11)	H11A—C11—H11C	109.5
O3—C7—O1	118.22 (12)	H11B—C11—H11C	109.5
O3—C7—C6	124.87 (12)		

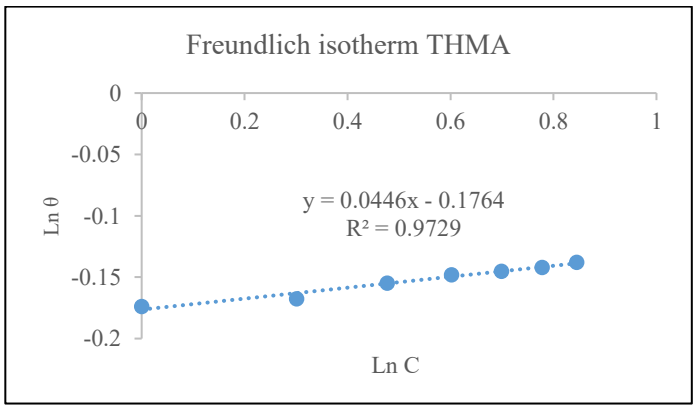
Bond	**Bond length [Å]**	**Bond**	**Bond length [Å]**
C2—S1—C1—C4	-0.04 (10)	C5—C6—C7—O1	-174.75 (11)
C2—S1—C1—C5	-178.26 (12)	C9—C6—C7—O1	8.48 (17)
C1—S1—C2—C3	0.33 (12)	C7—O1—C8—O2	-47.54 (16)
S1—C2—C3—C4	-0.53 (17)	C7—O1—C8—C11	74.04 (15)
C5—C1—C4—C3	178.16 (12)	C7—O1—C8—C10	-161.87 (13)
S1—C1—C4—C3	-0.26 (15)	C9—O2—C8—O1	48.73 (16)
C2—C3—C4—C1	0.51 (19)	C9—O2—C8—C11	-72.97 (15)
C4—C1—C5—C6	-172.89 (14)	C9—O2—C8—C10	163.14 (13)
S1—C1—C5—C6	5.2 (2)	C8—O2—C9—O4	160.18 (13)
C1—C5—C6—C9	-2.4 (2)	C8—O2—C9—C6	-22.12 (17)
C1—C5—C6—C7	-178.95 (13)	C5—C6—C9—O4	-6.5 (2)
C8—O1—C7—O3	-162.98 (13)	C7—C6—C9—O4	170.02 (12)
C8—O1—C7—C6	20.14 (17)	C5—C6—C9—O2	176.03 (11)
C5—C6—C7—O3	8.61 (19)	C7—C6—C9—O2	-7.48 (17)
C9—C6—C7—O3	-168.17 (13)		

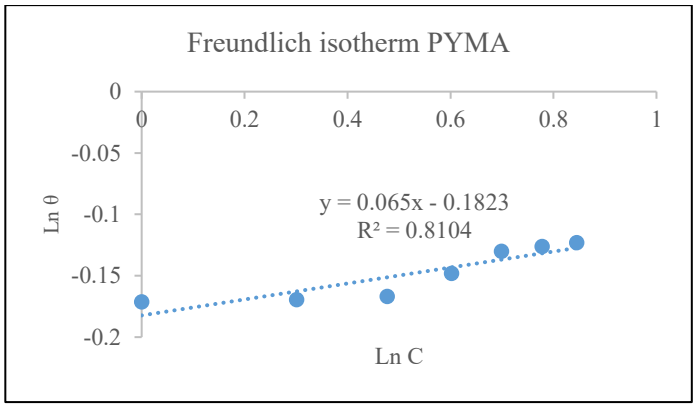
APPENDIX 2

Freundlich isotherms plots

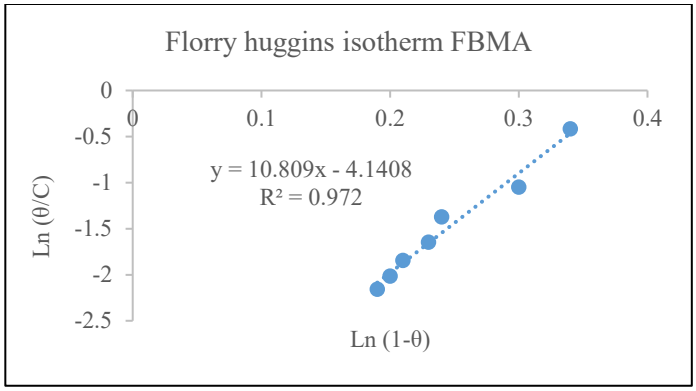


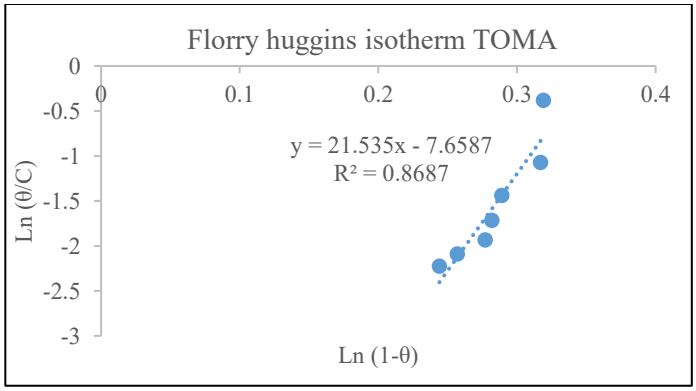


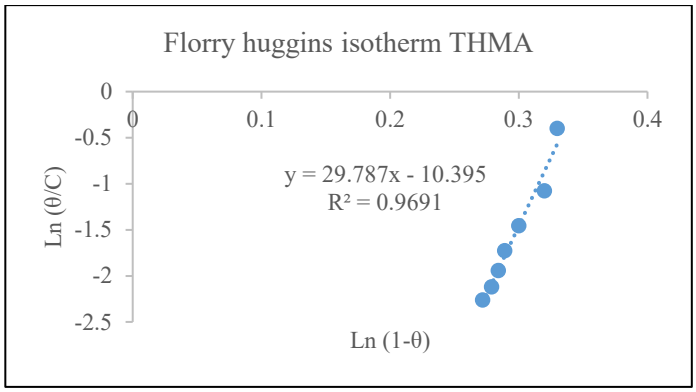


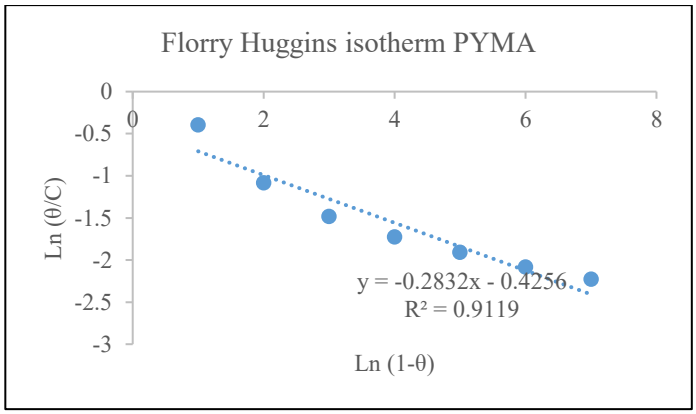


Florry huggins isotherm plot

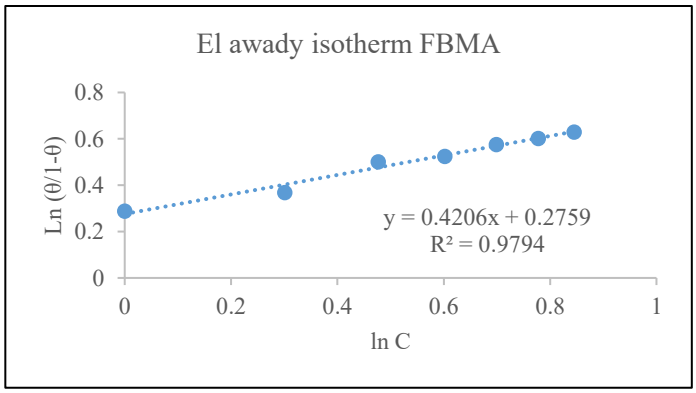


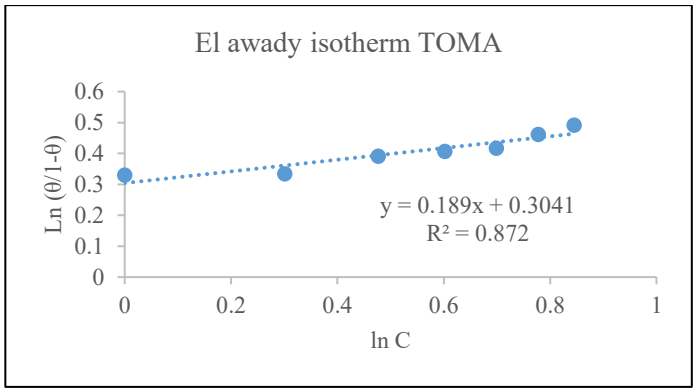


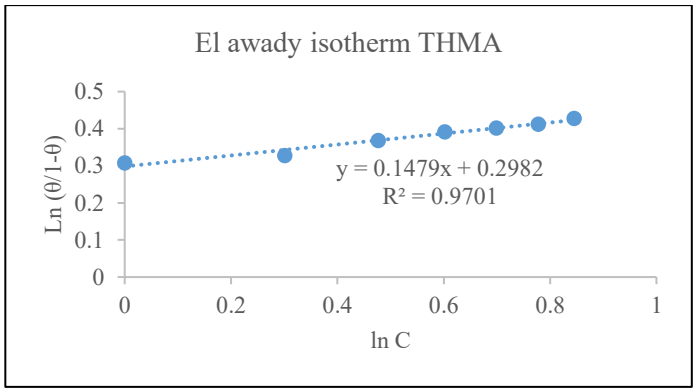


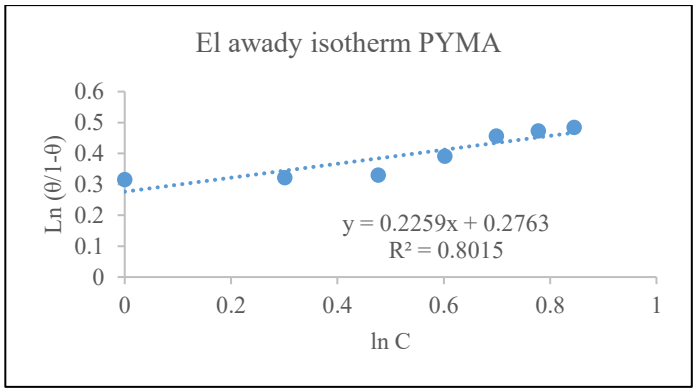


El Awady isotherms plot

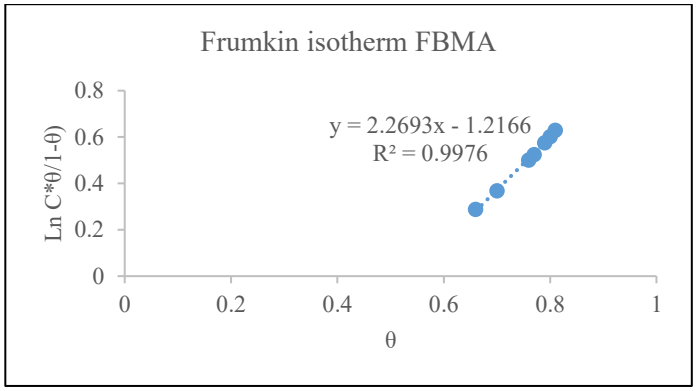


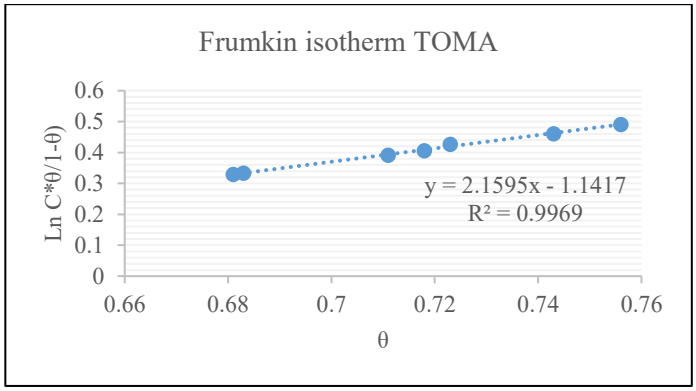

El awady isotherm TOMA
Ln (θ/1-θ)
0.6
0.5
0.4
0.3
0.2
0.1
0
0
0.2
0.4
0.6
0.8
1
ln C
y = 0.189x + 0.3041
R² = 0.872

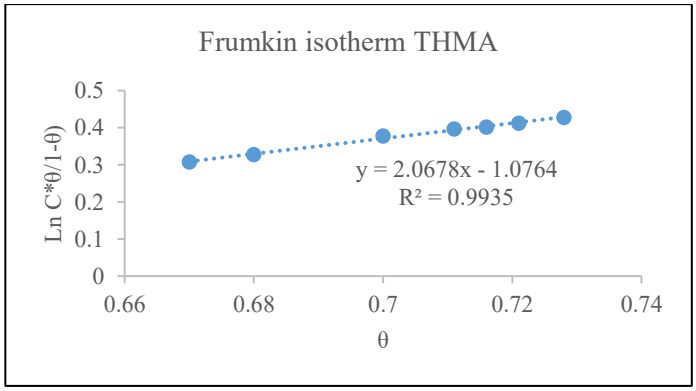

El awady isotherm THMA
Ln (θ/1-θ)
0.5
0.4
0.3
0.2
0.1
0
0
0.2
0.4
0.6
0.8
1
ln C
y = 0.1479x + 0.2982
R² = 0.9701

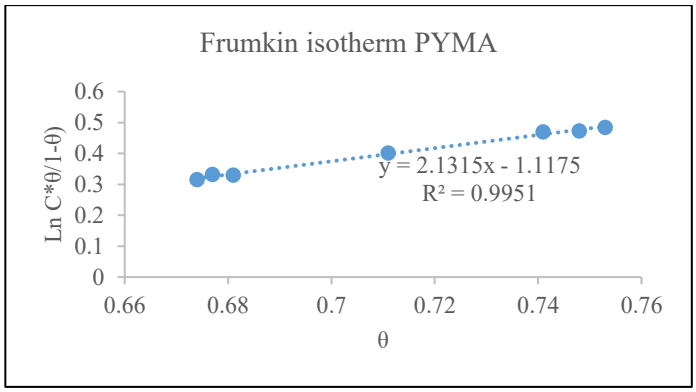

El awady isotherm PYMA
Ln (θ/1-θ)
0.6
0.5
0.4
0.3
0.2
0.1
0
0
0.2
0.4
0.6
0.8
1
ln C
y = 0.2259x + 0.2763
R² = 0.8015

Frumkin Isotherms plot

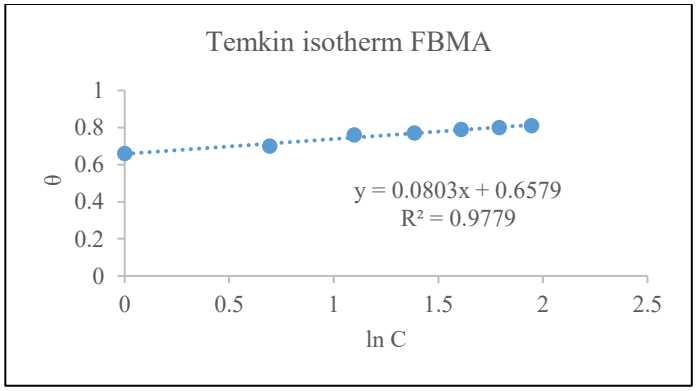


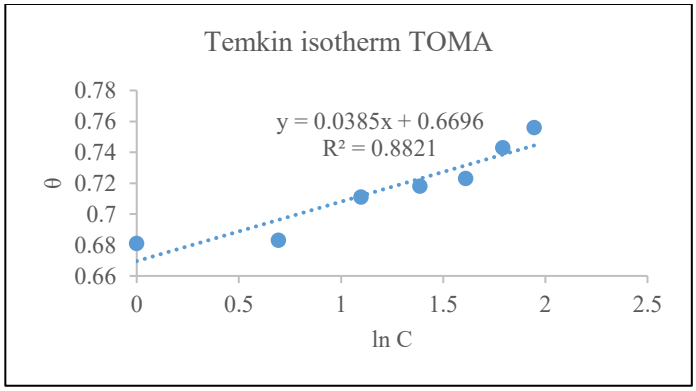


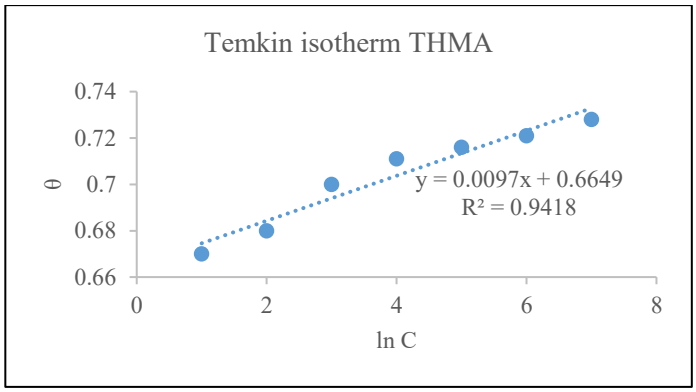


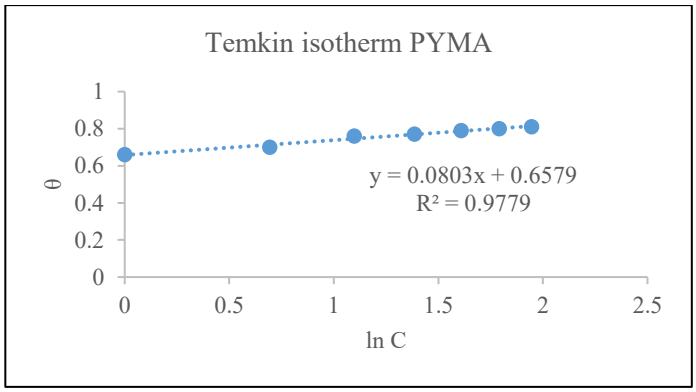


Temkin isotherm plot






Temkin isotherm THMA
0.74
0.72
0.7
0.68
0.66
θ
0
2
4
6
8
ln C
y = 0.0097x + 0.6649
R² = 0.9418


Temkin isotherm PYMA
1
0.8
0.6
0.4
0.2
0
θ
0
0.5
1
1.5
2
2.5
ln C
y = 0.0803x + 0.6579
R² = 0.9779

AUTHOR'S PROFILE



Muhammad Azhan Arif bin Mansor obtained Bachelor of Science in Chemistry and Management (Hons.) in 2024 from University Teknologi MARA (UITM), MSc in Chemistry (2025) from Universiti Teknologi MARA (UITM). His Master thesis involves characterization of new Meldrum's acid derivatives and corrosion study.

LIST OF PUBLICATION:

Muhammad Azhan Arif Mansor., Nur Aiman Najwa Kamarul Baharin., Sheikh Ahmad Izaddin Sheikh Mohd Ghazali., Nurul Auni Zainal Abidin., Tuan Norhafizah Tuan Zakaria., & Nur Nadia Dzulkifli (2025). Corrosion inhibition pre-screening of Nitrobenzaldehyde Meldrum's acid using response surface methodology (RSM) and Pearson correlation analysis. *Pure and Applied Chemistry*.

LIST OF CONFERENCE:

1. International union of pure and applied chemistry (IUPAC) 2025 Kuala Lumpur title : Corrosion inhibition pre-screening of Nitrobenzaldehyde Meldrum's acid using response surface methodology (RSM) and Pearson correlation analysis **(Presenter)**

LIST OF INNOVATIONS:

1. International Thinker Innovation & Entreprenuership Challenge (i-TIEC) 2025. Title : VanMa A Green Solution For stronger Steel in Acidic Environments (**GOLD**)
2. Malaysia Japan innovation Competition 2025. Title : VanishRust VanMa Pinnacle Corrosion Protection (**GOLD**)
3. Malaysia Japan innovation Competition 2025. Title : Nano Verde Herbicide : The Green Nanohybrid Herbicide (**GOLD**)
4. Malaysia Japan innovation Competition 2025. Title : Corroblock Meldrum acid Aluminium air Battery (**SILVER**)
5. Innogen 2026. Title : Organic corrosion inhibition in Battery Using Thiophenecarboxyaldehyde Meldrum acid (THMA) (**GOLD**)

LIST OF COPYRIGHT:

1. Corroblock Meldrum acid Acid Aluminium Air battery
2. Vanishrust VANMA : Ultimate Corrosion Protection